Electronic, excitonic and polaronic properties of organic systems within the many-body GW and Bethe-Salpeter formalisms : towards organic photovoltaics

Carina Faber

UNIVERSITÉ DE GRENOBLE

THÈSE

Pour obtenir le grade de

DOCTEUR DE L'UNIVERSITÉ DE GRENOBLE

Spécialité : **PHYSIQUE THEORIQUE**

Arrêté ministériel : 7 août 2006

Présentée par

Carina FABER

Thèse dirigée par **Dr. Xavier BLASE**
et codirigée par **Dr. Thierry DEUTSCH**

préparée au sein **de l'Institut Néel, CNRS**
et de **l'Ecole Doctorale de Physique (Grenoble)**

Electrons, excitons et polarons dans les systèmes organiques: approches ab initio à N-corps de type GW et Bethe-Salpeter pour le photovoltaïque organique

Thèse soutenue publiquement le **26 novembre 2014**,
devant le jury composé de :

M. Mairbek CHSHIEV
Professeur Université de Grenoble 1 (France), Président

Mme Silke BIERMANN
Professeur École Polytechnique de Palaiseau (France), Rapporteur

M. Gian-Marco RIGNANESE
Professeur Université Catholique de Louvain (Belgique), Rapporteur

M. David BELJONNE
Directeur de Recherche Université de Mons (Belgique), Examinateur

M. Xavier BLASE
Directeur de Recherche CNRS Grenoble (France), Directeur de thèse

M. Thierry DEUTSCH
Directeur de Recherche CEA Grenoble (France), Co-Directeur de thèse

Acknowledgement

Concerning my colleagues at the Néel Institut, I want to thank Valerio Olevano, who is always ready to pull out a pencil for a derivation. Moreover, there is also Claudio Attaccalite, who is not only of great help in physical questions, but who is also more than talented in connecting people. For really interesting discussions in the L_sim group, special thanks goes to my co-supervisor Thierry Deutsch and Ivan Duchemin at CEA. Most importantly, I want to thank my supervisor Xavier Blase, who accompanied and guided my work for the last three years in a very responsible and reassuring manner. I am thankful that he gave me the opportunity to work on this highly interesting topic and to be involved in the FIESTA project since the beginning. It was a really multifaceted subject and it was great to have an insight into programming, code testing and physics applications, all at the same time. It was a big pleasure to work with him on this project and his enthusiastic and motivating manner resulted in very fruitful discussions. There is just one major issue with him, namely that he refused eating my daily prepared cakes at the end of the first year. Just as Paul Boulanger pointed out so tellingly today: "A mind is such a terrible thing to waste, a waist is a terrible thing to mind". This is just one of Paul's pieces of wisdom and I will surely miss our lunch breaks. There, "on a toujours craint le pire" and we discussed everything from black holes to shamanism (which is, in the end, probably the same). In this context, special thanks for his support, helpfulness and most didactic explanations.

The three years of my doctorate in Grenoble represent one of the periods, which influenced me the most in my life. It has been a challenge, but at the same time a great possibility to get in touch with another cultural background and to integrate into the French system (it counts probably as a kind of success that the carefully collected bumps and scrapes in my car do not bother me anymore). Moreover, with Grenoble being a small, but quite international melting pot, I had the great opportunity to meet very interesting people, coming as far as Argentina (even though mainly from Italy). This group of internationals (and some few courageous French) has grown to be a family and is, due to its openness and cordiality, a real enrichment for me. I do not want to pick out specific persons, I just want to thank all of you for the nice moments we spent together. With your diverse and fascinating ways of life, you definitely influenced mine. I learned a lot about me and gained important insights (the recipe of spaghetti carbonara - where cream and even onions are strictly forbidden! - is just one example).

Apart from the Grenoble mafia, which is now establishing as a well-connected European network with headquarters in Paris, Barcelona and London, I want to devote special thanks

to my landlords and friends, the Hottebart family. It is a real pleasure to see you growing up, Romane, Eliette and Gabrielle, and you are an important factor making my stay in Grenoble so enjoyable (even though I am a bit jealous that Gabrielle now speaks better French than me and that you all have more "etoiles" in skiing). I was always "bienvenue chez les Schti" and even though hundreds of kilometers away from my family, I felt at home. Thank you very much for the exceptional experiences and your warm and caring manner. Also, I do not want to forget Franzi and our weakly "Abendbroten". I will definitely miss these evenings, full of laughter, happiness and funny ideas. You even went so far as to have a surgery in order to bear me company – this makes it nearly impossible to express my gratefulness in words. Last, but not least, I want to thank, along with Christoph and Martina, of course my parents and my grandmother who have always been a great support. You surely know me the best and as such, you also know that I am a blink away from the deadline (and a "Abendbrot" with Franzi). There is thus not enough time left for a profound contemplation, however, this last sentence of a three years work is devoted to you.

For job offers in the Grenoble region, please contact me at ☎(0,1,1,1,0,0,1).
[strangers to second quantization call the hotline for redirection]

Résumé

Cette thèse se propose d'explorer les mérites d'une famille d'approches de simulation quantique ab initio, les théories de perturbation à N-corps, pour l'exploration des propriétés électroniques et optiques de systèmes organiques [1, 2]. Nous avons étudié en particulier l'approximation dite de GW et l'équation de Bethe-Salpeter, très largement utilisées dès les années soixante pour les semiconducteurs de volume [3, 4, 5], mais dont l'utilisation pour les systèmes organiques moléculaires est très limitée. L'étude de quelques cas d'intérêt pour le photovoltaïque organique, et en particulier de petites molécules pour lesquelles sont disponibles des données expérimentales ou des résultats issus d'approches de chimie quantique, nous ont permis de valider ces approches issues de la physique du solide.

Ce doctorat s'inscrit dans le cadre du développement d'un outil de simulation quantique spécifique (le projet FIESTA) dont l'objectif est de combiner les formalismes GW et Bethe-Salpeter avec les techniques de la chimie quantique, c'est-à-dire en particulier l'utilisation de bases localisées analytiques (bases gaussiennes) et des approches de type «résolution de l'identité» pour le traitement des intégrales Coulombiennes [6, 7, 8]. Ce code est aujourd'hui massivement parallélisé, permettant, au delà des études de validation présentées dans ce travail de thèse, l'étude de systèmes complexes comprenant plusieurs centaines d'atomes. En cours de développement, l'incorporation d'approches hybrides combinant mécanique quantique et écrantage à longue portée par des approches modèles de milieu polarisable m'a permis d'une part de me familiariser avec le code et le développement méthodologique, et permet d'autre part d'envisager l'étude de systèmes réalistes en couplage avec leur environnement.

Le manuscrit s'ouvre sur une introduction au photovoltaïque organique afin de mettre en lumière les questionnements spécifiques qui requièrent le développement de nouveaux outils théoriques à la fois fiables en terme de précision et suffisamment efficaces pour traiter des systèmes de grande taille. Le premier chapitre est d'ordre méthodologique et rappelle les fondements des techniques ab initio de type champ-moyen (Hartree, Hartree-Fock et théorie de la fonctionnelle de la densité). En partant des principes de la photoémission, les théories de perturbation à N-corps et la notion de quasi-particule sont ensuite introduites, conduisant aux équations de Hedin et aux approximations GW et COHSEX [9]. De même, à partir de la compréhension d'une expérience d'optique, le traitement des interactions électron-trou est présenté, menant à l'équation de Bethe-Salpeter. Le chapitre 2 introduit brièvement les spécificités techniques liées à l'implémentation des formalismes GW et Bethe-Salpeter. Les propriétés analytiques des bases gaussiennes et les principes mathématiques derrière les techniques de type «résolution de l'identité» et «déformation de contour», sont brièvement

décrites. Le troisième chapitre présente les résultats scientifiques obtenus durant cette thèse. Le cas paradigmatique d'un polypeptide model nous permettra de discuter des spécificités de l'approche GW appliquée à des systèmes moléculaires afin d'obtenir des énergies de quasi-particule de bonne qualité [10]. De même, l'utilisation de l'équation de Bethe-Salpeter pour l'obtention du spectre optique de ce système sera présentée, ainsi que le cas d'une famille de colorants [11] d'importance pour les cellules de Graetzel (les coumarines). Finalement, nous explorons dans le cas du fullerène C_{60} [12] et du graphène le calcul des termes de couplage électron-phonon dans le cadre de l'approche GW, c'est-à-dire au delà des approches standards de type théorie de la fonctionnelle de la densité. Notre étude vise à vérifier si une approximation statique et à écrantage constant au premier ordre permet de garder la qualité des résultats GW pour un coût numérique réduit. Après la conclusion, les appendices donnent le détail de certaines dérivations.

Abstract

The present thesis aims at exploring the properties and merits of the ab initio Green's function many-body perturbation theory (MBPT) *GW* and Bethe-Salpeter formalisms [1, 2], in order to provide a well-grounded and accurate description of the electronic and optical properties of condensed matter systems. While these approaches have been developed for extended inorganic semiconductors and extensively tested on this class of systems since the 60s [3, 4, 5], the present work wants to assess their quality for gas phase organic molecules, where systematic studies still remain scarce. By means of small isolated study case molecules, we want to progress in the development of a theoretical framework, allowing an accurate description of complex organic systems of interest for organic photovoltaic devices. This represents the main motivation of this scientific project and we profit here from the wealth of experimental or high-level quantum chemistry reference data, which is available for these small, but paradigmatic study cases.

This doctoral thesis came along with the development of a specific tool, the FIESTA package [6, 7, 8], which is a Gaussian basis implementation of the *GW* and Bethe-Salpeter formalisms applying resolution of the identity techniques with auxiliary bases and a contour deformation approach to dynamical correlations. Initially conceived as a serial *GW* code, with limited basis sets and functionalities, the code is now massively parallel and includes the Bethe-Salpeter formalism. The capacity to perform calculations on several hundreds of atoms to moderate costs clearly paves the way to enlarge our studies from simple model molecules to more realistic organic systems. An ongoing project related to the development of discrete polarizable models accounting for the molecular environment allowed me further to become more familiar with the actual implementation and code structure.

The manuscript at hand is organized as follows. In an introductory chapter, we briefly present the basic mechanisms characterizing organic solar cells, accentuating the properties which seek for an accurate theoretical description in order to provide some insight into the factors determining solar cell efficiencies. The first chapter of the main part is methodological, including a discussion of the principle features and approximations behind standard mean-field techniques (Hartree, Hartree-Fock, density functional theory). Starting from a description of photoemission experiments, the MBPT and quasiparticle ideas are introduced, leading to the so-called Hedin's equations, the *GW* method and the COHSEX approach [9]. In order to properly describe optical experiments, electron-hole interactions are included on top of the description of inter-electronic correlations. In this context, the Bethe-Salpeter formalism is introduced, along with an excursus on time-dependent density functional theory. Chapter 2

briefly presents the technical specifications of the *GW* and Bethe-Salpeter implementation in the FIESTA package. The properties of Gaussian basis sets, the ideas behind the resolution of the identity techniques and finally the contour deformation approach to dynamical correlations are discussed. The third chapter deals with the results obtained during this doctoral thesis. On the electronic structure level, a recent study on a paradigmatic dipeptide molecule [10] will be presented. Further, also its optical properties will be explored, together with an in-depth discussion of charge-transfer excitations in a family of coumarin molecules [11]. Finally, by means of the Buckminster fullerene C_{60} [12] and the two-dimensional semi-metal graphene, we will analyze the reliability of two many-body formalisms, the so-called static COHSEX and constant-screening approximation, for an efficient calculation of electron-phonon interactions in organic systems at the MBPT level. After a short conclusion, the Appendix containing details and derivations of the formalisms presented before closes this work.

Contents

Many-body perturbation theory: towards organic photovoltaics

The present doctoral thesis was initiated having in mind a computational framework which would allow to simulate properties important for organic photovoltaics and to steer experimental research in this field. As such, in order to understand the challenges organic photovoltaics represents to computational physicists, we first briefly discuss the basic principles of organic photovoltaic cells. For a comprehensive overview, the reader is referred to Refs. [13, 14, 15]. This is followed by a short comparison of standard ab initio methods, where we focus on approaches available to calculate electronic structure and optical absorption properties. The presented computational techniques will be compared with special emphasis on accuracy and efficiency. In this context, we define accuracy through the comparison to experimental or correlated quantum chemistry results. Concerning efficiency, we take a pragmatic view, where we attempt to find a proper ratio between accuracy and computing time in the light of the complexity of the targeted systems. Subsequent to the paragraph on computational methods, the organization of the present manuscript follows.

Organic photovoltaics: basic concepts

Photovoltaics: a promising renewable energy source

The search for sustainable and unlimited energy sources is one of the key challenges of the 21st century. Among diverse renewable energy sources, such as wind power, biomass and hydroelectricity, photovoltaics takes a prominent place. In photovoltaic cells, sun light is directly converted into electricity. This is basically achieved through the following working principle: a semiconducting material absorbs photons, which have an energy exceeding the semiconductor's gap. This creates pairs of bound positive and negative charges, so-called excitons. These bound pairs then dissociate, yielding free charges that drift to the respective electrodes through a built-in potential. This provides a closed circuit with direct current flow.

Solar cells of the first generation utilize bulk crystalline silicon as absorbing semiconducting material. Most commercial solar cells to date belong to this type and power conversion efficiencies of over 20% are provided. However, the production process is complicated and material costs of perfectly crystalline silicon are high. Therefore, much research effort is spent on the exploration of novel solar cell concepts. Among the most promising ones are

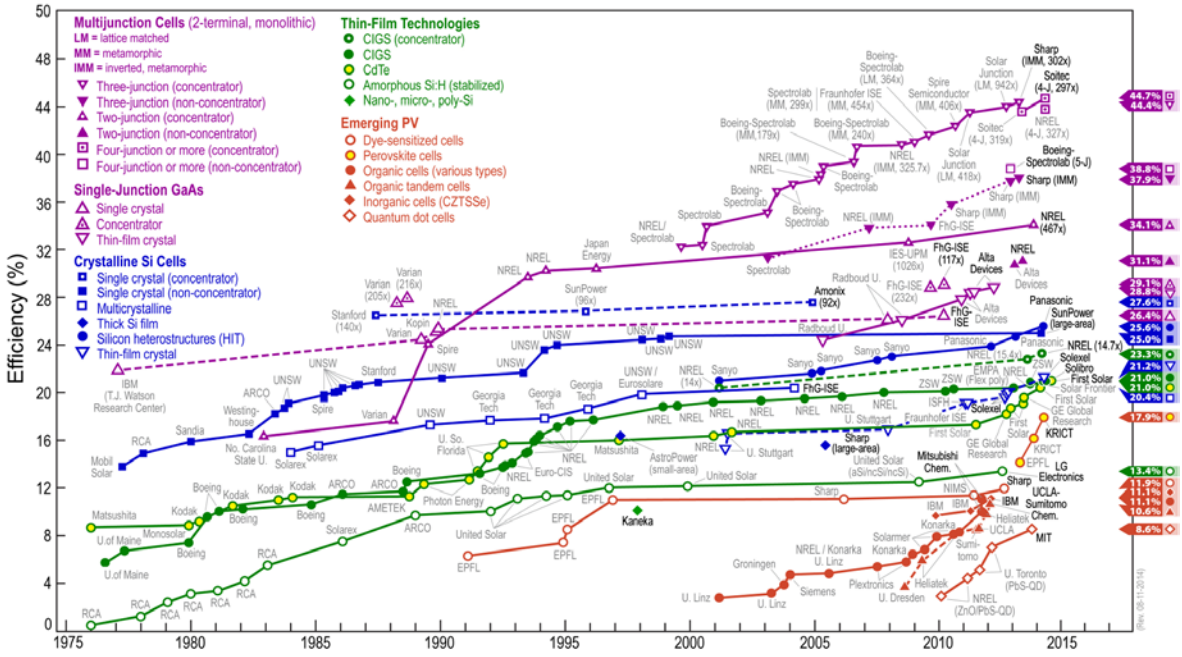

Figure 0.1.: Recent compilation of the best research power conversion efficiencies of diverse solar cell types, reaching from standard single-junction silicon cells to emerging quantum dot cells. Record efficiencies of up to 45% are achieved with multi-junction cells, while single-junction silicon cells approach 28%. From 2001 to 2014, an impressive increase by a factor of around 4 can be noted for organic solar cells, reaching a laboratory efficiency of 11%. Figure provided by the American National Renewable Energy Laboratory (NREL) at http://www.nrel.gov/ncpv/.

e.g. low-cost thin-film solar cells, where the use of very efficiently absorbing direct band gap semiconductors, such as e.g. amorphous silicon or chalcopyrite compound semiconductors (CIS, CIGS), allows for thinner layers and thus production time and material savings. Another example are multijunction concepts, which harvest, through the stacking of several single-junction sub-cells with varying gaps, a broader range of the solar spectrum and thereby obtain record power conversion efficiencies of up to 45%. A compilation of to date power conversion efficiencies for various types of solar cells is provided by Fig. (0.1). Among these trend-setting directions which have risen much attention recently are organic solar cells. It is these types of cells, which we will focus on in the following.[1]

Organic photovoltaic cells: functional principle and characteristics

Perspectives and challenges In organic photovoltaic cells, the traditional silicon absorbing layer is replaced by organic semiconducting materials. In particular, thin-films of polymers or molecules, mainly composed of carbon, hydrogen, oxygen and nitrogen, are applied. The utilization of organic materials as absorbers offers different advantages compared to standard silicon cells. First of all, a low-cost mass production seems possible. This is due to the fact that the needed raw materials are abundantly available and that material costs are low. In

[1] For a comprehensive introduction into solar cells concepts and technology, see Ref. [16].

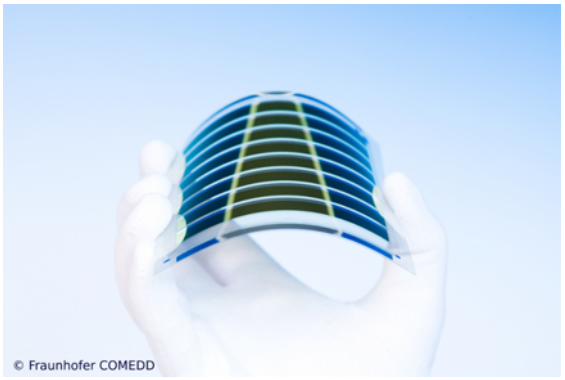

Figure 0.2: Organic solar cells can be not only light and semitransparent, but also flexible. Innovative applications, such as organic solar cell sheets adhered at vitreous building fronts or car roofs, come into reach. Figure reproduced by courtesy of Fraunhofer Center for Organic Materials and Electronic Devices Dresden (COMEDD).

addition, large area thin films can be easily produced without technological difficulties. By way of example, polymer films are usually deposited from the liquid using printing technologies from the already commercialized organic light emitting diode (OLED) sector. Films of organic molecules are instead grown using physical vapor deposition (PVD) techniques. This necessitates high vacuum conditions, however, these procedures are industrially deployed and high quality films can be produced in a very controlled way. In both cases, processing temperatures are of the order of room temperature and thus much lower as compared to the processing of inorganic materials. This allows to freely choose the substrate. Provided that plastic sheets are used, the resulting solar cells can be not only light-weight, but also flexible (see Fig. 0.2). In addition, the lower-temperature manufacturing reduces the energy needs during production [14], which significantly diminishes the solar cell energy pay back time.[2]

Apart from these production related advantages, another important point is that most of the organic compounds used can be chemically tailored with ease. This allows to optimize their physical and chemical properties and makes a variety of interesting organic semiconductors available. By way of example, the miscibility of organic molecules can be improved by adding specific side groups or semitransparent solar cells can be created by choosing the size of the gap such that part of the visible radiation is too low in energy to be absorbed [15, 17]. Another striking advantage is the simple and low-cost installation of organic solar cells, where no robust supporter constructions are necessary as in the case of silicon solar cells. Instead, e.g. deposited on adherent plastic substrates, they can be simply attached.

Organic solar cells are an environmentally safe and cheap alternative compared to classical solar cells, which provide, due to their low weight and mechanical flexibility, completely new scopes of application. The goal is not to replace traditional silicon cells, but to enrich the variety by benefiting from their unique properties. That way, totally different markets are accessible, such as e.g. the integration of organic solar cells in clothes or vitreous facades. However, for a full-scale commercialization, two main challenges have to be tackled. First, much research effort is still needed to increase the lifetime and stability of such cells [15]. Second, power conversion efficiencies, which are to date of about 11% for the best cells in the laboratory, have to be improved. Nevertheless, the rapid increase from around 3% in 2001 to the up-to-date value of 11% is more than promising (see Fig. 0.1).

[2]The energy payback time is the operating time a solar cells needs to produce the amount of energy which was spent during its production, installation and maintenance [14].

Functional principle and characteristics The utilization of organic semiconductors as active absorbing layers in organic photovoltaic cells provides the possibility of cheap, light-weight and flexible end products, entering new emerging consumer markets as compared to standard inorganic solar cells. Apart from these application related advantages, the organic materials used represent a highly interesting challenge for fundamental research. Consisting of weakly interacting molecular units rather than strongly covalently bound atoms, organic semiconductor crystals are at the interface between solid state physics and quantum chemistry theories, urging for new concepts. Organic semiconductors, which are characterized by delocalized π-conjugated electrons, possess inherent characteristics distinguishing them from their inorganic analogues. In order to mention only a small excerpt of properties, one deals with:

- narrow electronic bands, high effective masses,
- strong electron-phonon coupling,
- a high degree of structural disorder,
- discrete and narrow absorption peaks,
- and strongly bound electron-hole pairs.

These aspects significantly influence the semiconductor properties. By way of example, the strong electron-phonon coupling in these materials, i.e. the interplay between the electronic and the atomic structure [14], is one of the reasons leading to charge localizations. As a consequence, free charge carrier transport may rather be described in terms of a hopping of polarons than by standard band models of nearly free electrons. Likewise, the strong electron-hole binding energy necessitates new concepts in order to efficiently separate the electron and the hole and to create free charge carriers. For the sake of comparison, the electron-hole binding energy in inorganic semiconductors[3] is usually of the order of some few meV and consequently room temperature, corresponding to 25 meV, is sufficient to immediately dissociate the exciton after its creation. In organic semiconductors, however, the excitonic binding energy is one order of magnitude larger, typically around 0.5-1 eV [15]. This reflects the fact that organic semiconductors usually have a low dielectric constant [15], namely $\varepsilon =$ 3-4, and thus the electron-hole interaction is not as efficiently screened by the surrounding medium as in inorganic semiconductors. Moreover, due to weak intermolecular interactions, the excited electron and hole have a tendency to stay on the molecule they have been created on. This results in short distances between the charges and consequently a strong Coulomb interaction. As a consequence, an additional driving force is needed to separate the electron and the hole. To date, organic solar cells therefore apply donor-acceptor interfaces consisting of two different materials. One of these materials, the so-called donor, is characterized by a low ionization energy (IE), i.e. it easily gives electrons and stabilizes holes. The second material, the so-called acceptor, has a high electron affinity (EA) and thus efficiently takes up electrons. A simplified scheme of such a bilayer organic solar cell is provided by Fig. (0.3),

[3] By way of example, the excitonic binding energy of silicon is around 15 meV [18].

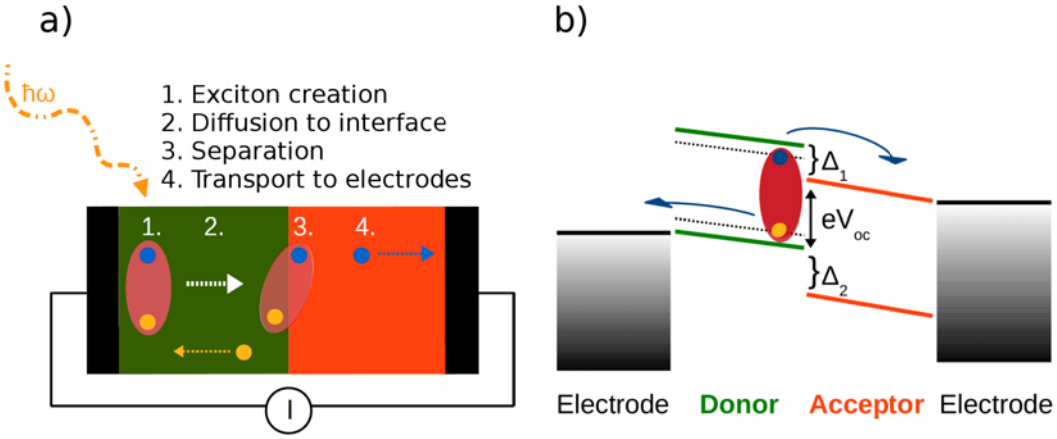

Figure 0.3.: Simplified scheme of the basic functional principle of a bilayer organic solar cell: a) The two organic semiconductors (green, orange) are sandwiched between two different metal leads (black). Absorption of electro-magnetic radiation creates an excited electron (blue) and hole (yellow), bound together by Coulomb attraction. The sun faced electrode is semitransparent and typically made out of a conducting oxide, such as indium-tin oxide (ITO). b) Simplified band scheme of a bilayer organic cell, where a built-in potential is created by the different chemical potentials of the metal leads. The highest occupied (HOMO) and the lowest unoccupied molecular orbital (LUMO), which characterize the fundamental electronic gap of the two semiconductors, are depicted. Electron-hole attraction reduces the energy amount actually needed to excite the lowest-lying optical transition. This defines the optical gap (dotted lines). The driving force for exciton dissociation is the energy gain Δ, which can be increased by shifting the HOMO of the donor upwards in energy and the LUMO of the acceptor downwards. This, however, decreases the open circuit voltage V_{oc}.

where the conversion process of electromagnetic radiation into electricity is basically divided into four steps:

1. Absorption: sunlight is absorbed in the donor material, creating a tightly bound electron-hole pair (exciton).

2. Exciton diffusion: in the ideal case, the created exciton diffuses to the donor-acceptor interface without recombination.

3. Exciton dissociation: the electron and hole are separated at the interface by an electron transfer from the donor to the acceptor.

4. Charge carrier transport: the free electron and the hole drift to the two corresponding electrodes, resulting in a closed current circuit.

The energy level diagram as depicted in Fig. (0.3b) helps to rationalize the photon-to-electron conversion process in organic solar cells, which is highly non-trivial and includes a variety of physical aspects. In the present thesis, we focus on the calculation of the electronic structure and optical properties and thus basically on step 1 and 3 of the photovoltaic process. In order

to understand the associated challenges for computational methods, a discussion of these two steps is provided in the following.

Absorption In general, there are two main losses related to the absorption step in solar cells, both directly connected to the optical gap. First, energy is lost through the thermalization of excess photon energy. Instead of creating electrons and holes in the highest occupied (HOMO) and the lowest unoccupied molecular orbital (LUMO), radiation with an energy overcoming the optical gap excites electrons from lower occupied to higher unoccupied states. These higher excited states usually relax extremely fast in the lowest excitonic state, releasing the excess energy as heat through lattice vibrations. Consequently, the maximum electrical energy which one can gain per electron corresponds to the optical gap, favoring wide band gap semiconductors. This condition, however, disagrees with the second source of energy losses, namely the non-absorption of low-energy photons. Since only photons with an energy higher than the optical gap contribute to the electron-hole pair generation, small gaps would be desirable in order to maximize the amount of created electron-hole pairs. One sees that the choice of an appropriate gap size is very complicated and a careful balance between thermalization and absorption losses has to be found. As a rough estimate, the Shockley-Queisser limit predicts for single-junction cells an optimum gap of 1.4 eV, yielding a maximum theoretical efficiency of around 30% [16, 19]. Since the maximum is rather broad, materials with gaps ranging from 0.8-1.7 eV are usually suitable for single-junction solar cells [20]. Organic semiconductors have fundamental gaps which are typically significantly larger and, even though the electron-hole binding energy can amount to some hundreds of meV, the optical gaps are often too large to capture the low-energy part of the visible radiation. Therefore, much effort is put in the reduction of the optical gap. From a theoretical point of view, these considerations call for an accurate calculation of the fundamental gap and optical absorption spectra, in order to discriminate more or less suited organic systems.

Exciton dissociation For an effective charge separation, the energy which is "gained" by transferring the electron from the donor to the acceptor should be as high as possible.[4] This can be favored by maximizing the band offset Δ between the LUMO (HOMO) of the donor and the LUMO (HOMO) of the acceptor (see Fig. 0.3b). Consequently, an efficient exciton dissociation necessitates a small energy difference between the HOMO of the donor and the LUMO of the acceptor. However, it is exactly this difference which determines the open circuit voltage V_{oc}, which in turn is directly related to the power conversion efficiency. An opening of the two gaps could cure the problem and increase both $\triangle$ and V_{oc}. This, however, would imply that a smaller part of the solar spectrum is absorbed.

Clearly, the presented energy level diagram is a strong simplification of real photovoltaic devices, since one should compare excitonic energy offsets. Nevertheless, this simple model already points out the importance of band offsets and gaps, and the difficulty to find an ideal trade-off between the different requirements. One sees that the design of efficient organic solar

[4] Of course, energy has to be conserved in the system. The exact role of the electronic excess energy in driving the dissociation is still very debated [21, 22, 23].

cells represents a very complex optimization problem and that the choice of high-performance material combinations is a major challenge. Here, calculations could offer a guideline and help experiment to sort out appropriate semiconductors without actually testing every material in the laboratory. This calls for an accurate theoretical description of the electronic structure and optical absorption properties and is, as it will be discussed below, a demanding objective for ab initio theories.

Organic solar cells: devices

In order to concretize the difficulties for theory arising from organic photovoltaic cells, two of the most successful realizations of organic-based solar cells are shortly presented in the following: all-organic bulk heterojunction cells and dye-sensitized solar cells (DSSCs). For a complete overview, the reader is referred to Refs. [13, 14, 15, 24]. In the case of all-organic bulk heterojunction cells, the organic semiconductor serves for light absorption and charge carrier transport, whereas for DSSCs the organic material is only used as absorber. The cell structures are quite different, however, they have in common that light absorption creates bound electron-hole pairs, which have to be dissociated. Therefore, diverse types of organic solar cells are often grouped together and called exciton solar cells.

All-organic bulk heterojunction cells The first all-organic solar cells, which applied the concept of an active donor-acceptor interface for the exciton dissociation, were so-called *bilayer* cells. Even though their device structure is of course more complex, it nevertheless resembles very much the extremely simplified scheme presented in Fig. (0.3a). The first bilayer cell, as realized by Tang in 1986 [25], was based on copper phthalocyanine and a perylene tetracarboxylic derivative as donor and acceptor materials, respectively, resulting in a power conversion efficiency of 1%. The respective molecular structures are depicted in Fig. (0.5b).

As discussed in the following, bilayer structures are not ideal to provide an efficient light absorption and exciton dissociation at the same time. Instead, all-organic *bulk heterostructure* solar cells are most popular device structures at present (see Fig. 0.4). The number of excitons which actually diffuse to the donor-acceptor interface before recombination is crucial for the power conversion efficiency. In organic materials, the diffusion length, i.e. the average distance between excitation and recombination, is only around 10 nm, while usual device structures apply 100-200 nm thick donor/acceptor layers in order to avoid an incomplete absorption [15]. As a result, light is indeed absorbed in the whole layer, however, only absorption in a thin region around the interface actually contributes to the photon-to-electron conversion, whereas most of the incident light remains unused. Bulk heterojunction cells tackle this problem by both allowing for an effective absorption through 100-200 nm thick absorption layers and by reducing the average distance an exciton has to travel in order to reach the donor-acceptor interface. This is achieved by replacing the two flat donor/acceptor layers by a single bulk absorption layer consisting of a blend of the donor and the acceptor material (see Fig. 0.4b). That way, not only the interfacial area is greatly enlarged, but also the average exciton travel distance to the interface is of the order of the diffusion length. A percolation pathway for

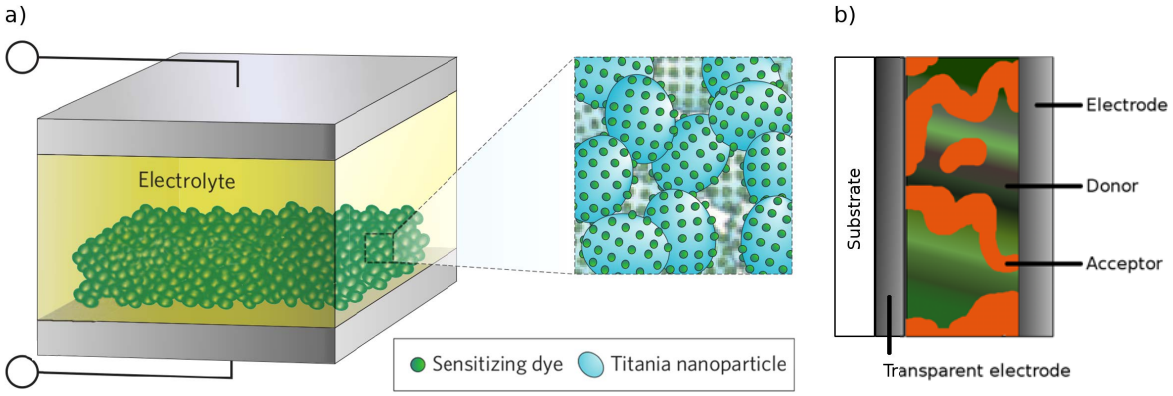

Figure 0.4.: Solar cell device schematic: a) Dye-sensitized solar cell: a monolayer of a sensitized dye (green) serves as absorption medium. The dye molecules are attached to a porous film of TiO_2 (blue) nanoparticles. After light absorption, the photoelectron transfers from the dye to the conduction band of TiO_2 (lower in energy) and finally proceeds in the electrode. The circuit is closed through the reduction of the oxidized dye by the liquid redox electrolyte and the subsequent reduction of the electrolyte by the metal electrode. Figure taken from Ref. [26] and modified. b) All-organic bulk heterojunction cell: instead of a bilayer system with two separated flat donor/acceptor layers, the active absorption medium is composed of an interpenetrating network of donor and acceptor domains (orange and green). This greatly enhances the interfacial area and reduces the donor-acceptor distance.

the free charge carrier transport to the electrodes is provided by the interpenetrating donor-acceptor network. As an acceptor material, fullerene derivatives are typically used, since they have one of the highest electron affinities [15]. A popular compound is e.g. $PC_{61}BM$, which is based on the Buckminster fullerene C_{60} and which has an additional side group improving its aggregation properties (see Fig. 0.5c). In combination with $PC_{61}BM$, polymers such as poly(3-hexylthiophene) (P3HT) are commonly chosen as donor material [17].

Dye-sensitized solar cells The second type of organic solar cells we will present are dye-sensitized solar cells (DSSCs). Here, a monolayer of an organic dye is anchored to an inorganic wide band gap semiconductor, such as e.g. titanium dioxide TiO_2 (see Fig. 0.4a). Through light absorption in the dye, electrons are promoted in unoccupied molecular states and then rapidly transfer in the conduction band of the semiconductor (lower in energy), where they are transported to one of the electrodes. Subsequently, the oxidized dye molecules are reduced to their neutral state by a surrounding redox couple electrolyte, typically iodide/triiodide (I^-/I_3^-). The latter transports positive charges from the dyes to the electrode [26] and thus closes the circuit.

In 1991, the group of Grätzel [27] revolutionized the DSSC approach by introducing a porous film of TiO_2 nanoparticles. That way, the available TiO_2 surface area where dye molecules can be deposited was enlarged by more than a factor of a thousand as compared to a flat structure [26]. This led to a significant increase in light absorption and, for the first time, efficiencies which proved DSSCs to be a promising candidate for low-cost solar cells were obtained. To

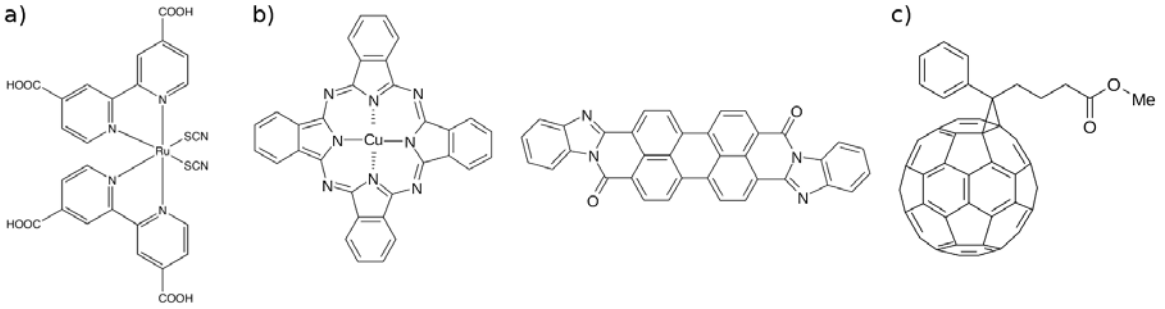

Figure 0.5.: Atomic representation of molecules commonly used in exciton solar cells: a) Ruthenium dye b) Copper phthalocyanine (left) and the perylene tetracarboxylic derivative PTC (right), as applied as donor and acceptor materials in the first organic solar cell with a donor/acceptor interface. c) In bulk heterojunction cells, typically $PC_{61}BM$, a derivative of the Buckminster fullerene C_{60}, is used as acceptor, combined with a semiconducting polymer as donor. The added side group of $PC_{61}BM$ enhances its miscibility compared to C_{60} [13, 17]. Figures taken from Ref. [17].

date, Grätzel's approach is commonly applied and DSSCs are therefore often termed Grätzel cells. Efficiencies of up to 12% are reached (see Fig. 0.1), where mainly ruthenium-based organometallic complexes are used as absorbers (see Fig. 0.5a). Nevertheless, there is a trend towards pure organic absorbers, which are cheaper, easier to synthesize and free from resource limitations. Intense research is conducted in this direction, since solar cell efficiencies are to date usually smaller as compared to cells based on organo-metallic complexes [26]. Later in this work, a study on the optical properties of all-organic coumarin dyes is presented, a family of molecules which recently led to DSSCs with very promising efficiencies [28, 29, 30, 31].

This sections clearly demonstrates that organic photovoltaics makes high demands on computational methods. Apart from the usually experimentally targeted accuracy of 0.1-0.2 eV for electronic levels and optical excitation energies, one has to tackle:

- a huge number of atoms,
- hybrid systems (e.g. TiO_2 nanoparticles/dye molecules/liquid electrolyte),
- complex bulk and interface morphologies showing non-negligible disorder,
- and a complex interplay between electron-electron, electron-hole and electron-vibrations coupling with similar magnitude.

In the following, the merits and limitations of ab initio computational method available to predict electronic and absorption properties are briefly described.

Computational aspects

The photon-to-electron conversion process in organic solar cells is very complex and includes a variety of physical aspects. In this work, and as a first step into the field of organic photovoltaics, we concentrate on the calculation of the electronic structure and optical properties of

small molecules in the gas phase. We seek an *ab initio* computational method able to reliably predict these properties, where only fundamental physical constants and the molecular structures are given as input, whereas no reference data from experiment enters. The above listed aspects imply that the sought computational method responds to the following requirements, by being:

- accurate (within an 0.1-0.2 eV error range as compared to experimental or high level quantum chemistry reference data),
- efficient (both molecules with up to 100 atoms on a standard computer within one day and several hundreds of atoms on large-scale computers should be feasible),
- parameter-free,
- and system-independent.

The two last issues ask for an universal formalism, which works equally well for extended, finite, semiconducting or metallic systems. Universalism is a necessary condition having in mind hybrid systems, such as e.g. inherent to Grätzel cells, or donor-acceptor interfaces in general.

Status report: ab initio electronic structure theories Concerning electronic structure calculations, density functional theory (DFT), particularly in combination with standard (semi)local exchange-correlation functionals, is an efficient and widely applied tool [32, 33]. However, errors of the order of several eVs on the electronic energy levels, namely as large as the visible range of the solar spectrum, are not unusual. On the contrary, correlated quantum chemistry methods [34] yield an excellent agreement with experiment, though they are computationally too demanding to treat systems with more than a few tens of atoms.

In this work, we rely on the many-body perturbation theory GW method [1], which has proven to be a reliable electronic structure theory formalism for extended systems. For finite systems, however, systematic studies remain scarce. This is due to the high computational costs related to the straightforward application of periodic boundary condition codes to molecules, necessitating the development of finite-system-specific packages. The FIESTA code [6] attempts to address this issue and is conceived as an efficient mean to treat the electronic structure of molecular systems at the many-body perturbation theory GW level. It provides a real-space atom-centered Gaussian function basis set implementation, which is very suited for the description of molecular systems. Further, Gaussian basis sets are most popular in computational quantum chemistry and thus allow a direct comparison to higher level quantum chemistry reference data. Finally, even though this is beyond the scope of the present thesis, the proposed real-space basis approach straightforwardly opens the way to embedding techniques, where the electronic structure of a single molecule is evaluated by taking into account the surrounding molecules of the organic crystal. Here, space is divided in an active region around the molecule of interest, which is treated with the highest available accuracy, whereas the ambient medium is included at a lower level of theory to reduce the

computational effort. This allows to go beyond the gas phase description and to simulate organic semiconductors in a more realistic way.

In this context, we want to point out that a trade-off between accuracy and efficiency is inevitable. Conceiving the FIESTA package and choosing input parameters such as e.g. a specific basis set, we deliberately accept certain approximations in order to reduce computational costs, however, always adhering to the targeted maximum 0.1-0.2 eV error range.

Status report: optical absorption formalisms Concerning the calculation of optical absorption properties from first principles, TDDFT [35, 36], the time-dependent extension to DFT, is very popular. TDDFT provides a computationally feasible scheme and yields, for standard (local) optical excitations, energies and oscillator strengths in very close agreement with experiment and correlated quantum chemistry methods. In the present work, however, we want to particularly address the problem of non-local charge-transfer optical excitations. The latter are neutral excitations of great conceptual importance, where the promoted electron and the respective hole are spatially separated, but still interacting. Even though the exact microscopic mechanisms of the exciton dissociation at the donor/acceptor interface are still strongly debated [21, 37, 38], the charge separation process from bound to free carriers is supposed to take place through an intermediate charge-transfer excited state [39, 40, 41]. There is still no clear picture about the exact process, hence calling for the accurate calculation of the excited state properties with respect to the electron-hole distance. Unfortunately, standard TDDFT approaches with (semi)local exchange-correlation functionals fail in correctly describing these excitations by largely underestimating the electron-hole binding energy with increasing separation. Most recently, it has been suggested that a combined GW/BSE approach [2, 42, 43], where first the underlying GW electronic structure is calculated and then electron-hole interactions are included through the Bethe-Salpeter equations, cures the problem. In this context, we recently obtained, together with other groups, promising results for *intermolecular* charge-transfer systems, where the excited electron and the hole are located on different molecules [8, 44]. In this work, we go further and explore the most common case of *intramolecular* charge-transfer excitations by means of the GW/BSE approach [10, 11].

Organization of the present thesis

The present thesis is organized as follows. First, in order to set up a common framework, concepts and definitions are briefly recapitulated in Chapter 1. The latter is divided into two parts, where the first one is devoted to electronic structure theory and the second one to optical absorption. We try to establish a clear connection between experimentally and theoretically accessible quantities in order to clarify which properties are calculable with the respective formalisms and which features are not captured.

The chapter starts with a short introduction to photoemission spectroscopy (PES), an experimental technique directly accessing the electronic structure [45, 46]. The latter is a complex many-particle quantity, where the particle number of the interacting-particle system changes through the ejection/injection of single electrons during the PES measurement. As

it will be pointed out in the subsequent section of Chapter 1, the electronic structure can in principle be exactly treated in terms of the many-body Schrödinger equation. Due to the enormous number of correlated particles in solids or molecules, an analytic or exact numerical solution is out of reach and approximating electronic structure theories have to be introduced. The key problem is the inclusion of the Coulomb interaction, which correlates the particles on a long-range scale. As important representatives of ab initio electronic structure methods, the Hartree, Hartree-Fock and density-functional theory (DFT) formalisms will be briefly discussed. These are mean-field approaches, i.e. the Coulomb interaction is taken into account only in an averaged way. The many-body problem of interacting particles is reduced to the description of a single particle moving in an effective Coulomb field created by the others. Particularly DFT is an efficient and widely applied tool to calculate structural properties. However, as it will be demonstrated many times in this work, it can lead to non-negligible errors of the order of some eV on the energy of electronic levels. In order to go beyond the mentioned mean-field approaches, we present in detail the electronic many-body problem from the view point of many-body perturbation theory, where lies the main emphasis of the present thesis. The central quantity of this formalism are Green's functions G, which describe the propagation of electrons and holes in the environment of an interacting many-body system and which are thus perfectly suited to model the PES process. To be precise, the added charges are considered as quasiparticles, i.e. bare electrons/holes surrounded by a positively/negatively charged screening cloud created by interactions with the system. Due to this screening, quasiparticles only weakly interact via the screened Coulomb potential W, rather than via the bare Coulomb potential. Similar to mean-field approaches, one arrives at an effective single-particle problem, the so-called quasiparticle eigenvalue equation, whose solution gives access to the electronic energies measured in PES experiments. The main ingredient of this equation is the self-energy, an operator which accounts for all interactions beyond Hartree and which is energy-dependent and non-local. In principle, the self-energy can be exactly calculated through the self-consistent solution of a closed set of five integro-differential equations, namely the Hedin's equations [1]. In practice, however, this is not feasible. Following perturbation theory, where the screened Coulomb potential W is taken as perturbation, one retrieves the so-called GW method and the static COHSEX approximation [9].

The second part of the Chapter 1 deals with optical absorption. We first shortly comment on optical absorption experiments and then focus on the fundamental physical differences between electronic structure and optical absorption measurements. Whereas in PES, one considers charged excitations, electrons are promoted from occupied to *bound* unoccupied states in optical absorption experiments. The excited electron and the created hole attract each other through Coulomb forces and, as it will be demonstrated in detail by means of simple absorption models, it is crucial to take into account this interaction in order to accurately describe the absorption process. This implies that, within many-body perturbation theory, one has to go beyond the single quasiparticle (GW) picture towards an interacting quasielectron-quasihole description. This is achieved by first calculating the underlying electronic (GW) structure and then solving the Bethe-Salpeter equations to add electron-hole interactions. Within

the domain of *DFT*, time-dependent *DFT* is a popular method to directly access optical absorption properties. Since it is, in addition to correlated quantum chemistry approaches, the most commonly used technique, a short review of this formalism closes Chapter 1.

Chapter 2 describes the technical specifications of the FIESTA code. General details on Gaussian basis sets with emphasis on auxiliary basis sets are given, along with the introduction of contour deformation techniques. Beyond formalisms and theories, the accuracy of actual calculations may suffer from e.g. convergency issues related to the chosen basis sets or e.g. from an inadequate treatment of dynamical correlations through plasmon-pole models. Such technical concerns have taken an important part in the present doctoral thesis. In the subsequent Chapter 3, namely "*GW and BSE in practice*", we will constantly refer to Chapter 2 in regard to technical terms.

Chapter 3 is divided in three parts. First, we will comment on recent *GW* results which we obtained for a model dipeptide molecule, a paradigmatic system for which large discrepancies on the optical absorption level arise between the different quantum chemistry and TDDFT approaches [10, 47]. Already at the electronic structure level, the chosen molecule is a highly interesting study case. We will demonstrate that the standard "*GW* Scissor" approach of calculating the many-body *GW* correction to the underlying *DFT-LDA* electronic structure for the HOMO and LUMO only, while correspondingly shifting the remaining states, is not enough. It will be pointed out that for a correct ordering and spacing of the frontier orbitals, it is indispensable to go beyond the Scissor approach by explicitly correcting several states around the gap. This is similar to results we previously obtained within the scope of my Master thesis for the DNA/RNA nucleobases (for details see Ref. [7]). In addition, we will propose a reliable alternative to the standard single-shot G_0W_0 approach, which suffers from non-negligible starting point dependencies [48]. Within G_0W_0, the many-body correction to the *DFT* eigenvalues is calculated in a single step. This implies much lower computational costs than self-consistent schemes, however, the choice of an appropriate starting point has a large impact on the resulting many-body electronic structure. In the present work, we carry out inexpensive self-consistent COHSEX calculations on top of *DFT-LDA* electronic structure. We will show that, even though overestimating fundamental gaps, the self-consistent COHSEX approach readily yields the correct level spacing and ordering. This makes self-consistent COHSEX calculations a reliable starting point for G_0W_0 (Scissor) calculations, offering the possibility to treat also large systems on the many-body level.

The second section of Chapter 3 deals with the study of optical absorption properties by means of a combined *GW/BSE* approach, where we mainly focus on the problem of intramolecular charge-transfer excitations. We will present two interesting systems characterized by low-lying charge-transfer excitons, one of them being the already introduced model dipeptide. The other one is a family of coumarin dyes [11], which are both from the fundamental, but also from the applicatory point of view, highly attractive. Apart from the possibility to study charge-transfer excitations, these molecules recently earned much attention due to the high efficiencies obtained when applied as all-organic, transition metal free absorbers in Grätzel cells. Moreover, this family of molecules is an impressive example of molecular design through chemical engineering, where the stacking properties and the gap

have been systematically optimized [28, 29]. Both for the dipeptide and for the coumarin molecules, TDDFT with inexpensive (semi)local exchange-correlation functionals has problems to reproduce charge-transfer excitation energies and only parametrized range-separated exchange-correlation functionals cure the problem [49, 50]. In this work, we will show that our combined GW/BSE approach turns out to be a reliable alternative. It succeeds in describing intramolecular charge-transfer excitations in good agreement with the quantum chemistry reference data, while being parameter-free and system independent.

The third issue we address in Chapter 3 is the accurate calculation of electron-phonon coupling strengths from first principles. The latter takes a prominent place in organic semiconductors, as in various fields of condensed matter physics, and for a realistic modeling of these materials a reliable estimation is indispensable. As this quantity is sensitive to the quality of the underlying electronic structure, it necessitates the accurate calculation of the latter. DFT and especially density functional perturbation theory ($DFPT$) provide a most efficient way to access electron-phonon coupling matrix elements. However, recent studies show a significant underestimation of up to 50% as compared to experiment when using (semi)local exchange-correlation functionals. Further, it has been demonstrated that a many-body treatment on the GW level cures the problem and yields results in close agreement with experiment [12, 51, 52]. However, due to the lack of efficient techniques as in the case of $DFPT$, a frozen-phonon approach with step-wise atomic displacements along the phonon modes has to be carried out. This makes the evaluation of electron-phonon coupling matrix elements within GW very expensive. In this work, we propose two alternative many-body approaches, namely the static COHSEX and the constant screening approximation, yielding a much less demanding frozen-phonon framework as compared to a full GW treatment. We will assess their accuracy by means of the Buckminster fullerene C_{60} and the most popular two-dimensional semi-metal graphene. Concerning the static COHSEX approach, we will show that it leads, especially in the case of graphene, to non-negligible discrepancies as compared to the GW reference. However, the constant screening approach, where we neglect the variation of the screened Coulomb potential with respect to the atomic displacements, yields results in excellent agreement with the corresponding GW and static COHSEX reference. Even though this approach has still to be validated for a larger variety of systems, the obtained results are promising and open the door to an inexpensive and reliable man-body treatment of the electron-phonon coupling.

After a short summary of the presented results and the discussion of future perspectives in Chapter 4, the Appendix, comprising detailed information on derivations and theorems, and a list of publications and conference contributions, closes the present thesis.

1 Methodology

1.1. Accessing the electronic structure experimentally: Photoemission spectroscopy

Photoemission spectroscopy has evolved to become one of the most established experimental techniques, playing a central role in probing the electronic structure of materials [45, 46]. Various quantities related to the electronic structure are accessible, e.g. the chemical composition of materials, the Fermi surface or the electron-phonon coupling strength, leading to major progresses in the understanding of fundamental processes in solid state physics, chemistry and material sciences.

The physical origin of photoemission spectroscopy (PES) is the photoelectric effect [53, 54]. Discovered in 1887 by Hertz and Hallwachs, it describes the ejection of electrons from a sample due to irradiation with light. Today's measurement setups are still very similar to the pioneering experiments: monochromatic and polarized photons from a light source – most commonly UV, X-Ray or synchrotron radiation – hit the sample under a certain angle and cause electrons to be ejected. The kinetic energy of these photoelectrons is detected via an electrostatic analyzer. Due to the relation between the momentum $\mathbf{p}$ of a photoelectron and the wave vector $\mathbf{k}$ of the corresponding Bloch state in the crystal, an angular resolved measurement of the kinetic energy gives access to the electronic dispersion relation, i.e. the band structure (ARPES: angular resolved photoelectron spectroscopy).

The microscopic processes underlying PES experiments constitute a manifold of complicated many-particle interactions. The ejected photoelectron leaves the sample with a maximum kinetic energy, if the remaining electronic system is completely relaxed. However, in the case where the ionized many-body system is left in an excited state, with neutral excitations such as e.g. electron-hole pairs, the kinetic energy of the photoelectron is lowered and so-called satellite peaks occur in the measured spectrum. This will be discussed in more detail later in this chapter. Apart from these intrinsic losses, the photoelectron can also loose energy on its way to the surface by creating secondary electrons through inelastic scattering processes [42, 55]. In order to facilitate the theoretical description of the photoemission process, one usually neglects these extrinsic losses and assumes the *sudden approximation*, where the interaction between the escaping photoelectron and the remaining electrons is not taken into account. In other words, the photoelectron and the ionized system are completely decoupled. Moreover, the response of the system to the ionization, i.e. to the creation of a positive "potential"

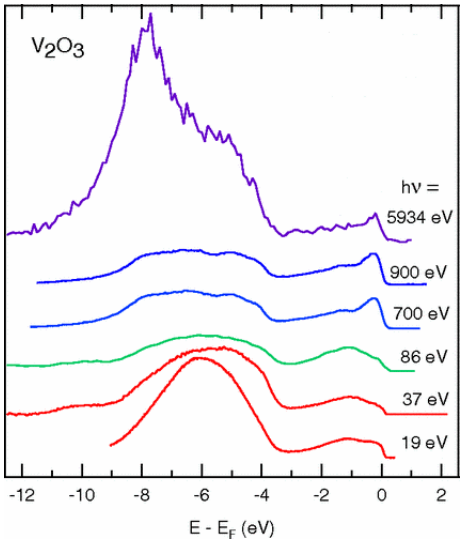

Figure 1.1.: Experimental valence band PES spectra of V_2O_3, measured at different incident photon energies. The spectrum significantly changes going from small photon energies to the high energy limit. This is due to the energy dependence of the electron-photon cross section. Moreover, extrinsic processes, such as inelastic scattering with secondary electrons, are more effective for low kinetic energy photoelectrons. Figure taken from Ref. [56].

or photohole, is assumed to be instantaneous. An additional approximation consists of the neglect of frequency dependent effects in the PES spectrum, i.e. the energy dependence of the electron-photon scattering cross section and the more effective scattering between low-energy photoelectrons and the system's electrons is not taken into account (see Fig. 1.1). In consideration of the assumptions made, a direct comparison of theory and experimental data is complicated and one has to choose wisely the data one compares with. By way of example, one should prefer e.g. spectra measured at sufficiently high frequencies, expecting here the sudden approximation to be more likely valid (see Fig. 1.1).

In order to get a first rough idea of the microscopic mechanisms, one can further simplify the scheme by considering a single electron only to be involved in the PES process. Within this *single-particle picture* (see Fig. 1.2a), an electron is promoted from a bound single-particle state with energy ε_i into an unbound continuum state with energy ε_f by the absorption of a photon of energy $\hbar\omega$. The electronic structure of the initial N-particle ground state and the final (ionized) system are taken to be equal. In other words, the ejection of the electron and the related creation of a positive potential is assumed to have no influence on the remaining electrons. According to energy conservation, simple relations between the measured kinetic energy E_{kin} of the photoelectron and the orbital energy ε_i can be established (see Fig. 1.2a):

$$-\varepsilon_i + E_{kin} = \hbar\omega,$$

$$E_b = \hbar\omega - E_{kin} \equiv -\varepsilon_i.$$

This is known as *Koopmans* or *frozen-orbital approximation* and the binding energy E_b, i.e.

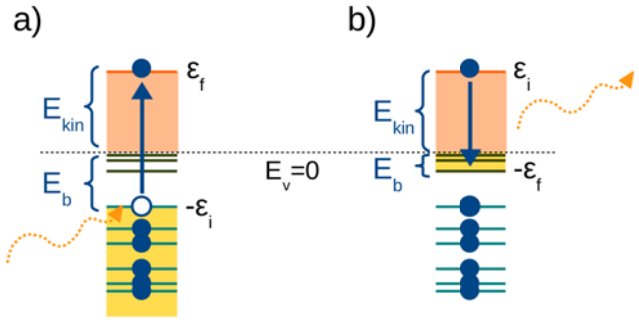

Figure 1.2.: Single-particle picture of the (inverse) photoemission spectroscopy process: a) In a PES experiment, an electron is ejected by photon absorption from one of the occupied states into the continuum (orange); the electronic structure of the ionized system is assumed to be not affected, i.e. the binding energy E_b is approximated by the negative value of the single-particle orbital energy ε_i. b) In IPES experiments, the energy of unoccupied bound states is probed. An incoming electron with defined kinetic energy is inserted into one of the continuum states. The system in turn relaxes under photon emission, whereby the energy needed to insert an electron into the system is approximated by the negative value of ε_f. E_v represents the vacuum level. States which are probed in PES/IPES are highlighted in yellow. This depicts the complementarity of the two methods.

the energy needed to eject an electron from the system, is approximated by the negative value of the orbital energy, $E_b \approx -\varepsilon_i$. Since the ground state and the excited state electronic levels are taken to be equal, the binding energy is equated with a single-particle ground-state property. For a system of non-interacting electrons, this description is valid. However, for interacting systems, this denotes a very simplified picture, where a relaxation of the excited $(N-1)$ system through interactions is neglected (see Fig. 1.3). That points out the fact that orbital energies ε_i represent purely theoretical tools to approximate binding energies, which are the actually measured quantities. This clearly signifies a strong simplification of the PES process, however, often provides a qualitative estimate of the electronic structure.

In order to go beyond this picture, not only a single electron has to be considered, but the PES experiment has to be described as a process, where all N particles are involved and coupled through interactions. As a result, the created positive hole potential influences the ionized $(N-1)$ electron system, which in turn can lead to distinct differences between the initial ground state and the final ionized state. These differences occur both due to the reorganization of electronic levels in form of a relaxation and due to neutral excitations, such as electron-hole pairs, collective electronic oscillations (plasmons) or atomic vibrations (phonons). To state it generally, PES accesses the energy difference between the total energy of a system of N interacting electrons in the ground state E_0^N and the total energy E_i^{N-1} of a $(N-1)$ system, where an electron has been ejected from state i. According to energy conservation, one obtains for the total system:

$$\hbar\omega + E_0^N = E_{kin} + E_i^{N-1},$$

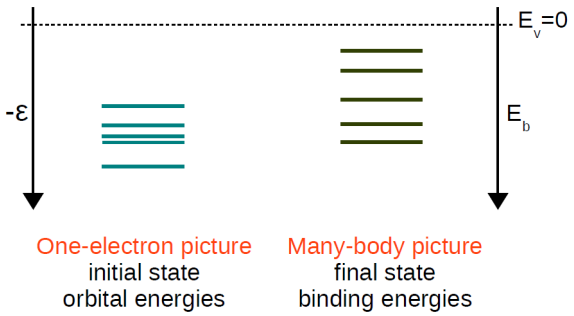

Figure 1.3.: Comparison between a one-electron and a many-body picture of the PES process: The photoelectric effect creates a system reduced by one electron with respect to the initial one. Consequently, PES accesses final state energies (after the ejection of the photoelectron), where the relaxation of the system due to the created hole is taken into account. These so-called binding energies are depicted on the right-hand side, whereas on the left hand side single-electron ground state orbital energies are represented. The relation between initial ground state orbital energies and final state energies is highly nontrivial, being a fingerprint of many-body interactions in the system. The energy levels are not only shifted in energy with respect to each other, but also the level spacings change. For the sake of clarity, broadening effects and satellites are not depicted. The only measurable quantities are binding energies, whereas orbital energies represent purely theoretical tools.

$$E_b = \hbar\omega - E_{kin} \equiv E_i^{N-1} - E_0^N.$$

The binding energy E_b for occupied states is thus the energy needed to eject an electron from a system of N interacting electrons, where the creation of a positive potential and its influence on the electronic structure of the remaining electrons is taken into account. By way of example, the ionization energy (IE), i.e. the energy needed to eject an electron from the highest occupied (ho) state is given by:

$$IE \equiv E_{ho}^{N-1} - E_0^N.$$

The measured binding energy E_b, i.e. the electronic structure, is consequently a complicated many-body quantity, necessitating to go beyond single particle orbital energies.

In order to obtain information about unoccupied states, i.e. to get a complete view of the electronic structure of the system, a complementary method to PES is usually used, called inverse PES (IPES). The measurement principle of IPES is the following: an electron with a fixed energy E_{kin} is inserted into the $i-$th unoccupied state of the N electron system, which in turn relaxes to the charged $(N+1)$ ground state under photon emission (see Fig. (1.2b)). The energy E_b needed to insert an electron in state i of a system of N interacting electrons is given by:

$$E_{kin} + E_0^N = \hbar\omega + E_i^{N+1},$$

$$E_b = \hbar\omega - E_{kin} \equiv E_0^N - E_i^{N+1},$$

and can consequently easily be obtained by measuring the energy distribution of the outgoing photons. By way of example, the energy needed to insert an electron into the lowest unoccupied (lu) state of the N electron system, i.e. the so-called electron affinity (EA), is defined as:

$$EA = \hbar\omega - E_{kin} \equiv E_0^N - E_{lu}^{N+1}.$$

To conclude, the described underlying microscopic mechanisms of PES/IPES are complicated many-body processes involving not only the ejection/insertion of a single electron, but also the associated creation of an additional positive/negative potential. The obtained electronic structure represents thus an excited state property, where an added charge interacts with the whole many-body system. This explains why the electronic structure is very difficult to calculate and usually approximations are needed. In the subsequent sections, we explore different levels of electronic structure theory and discuss both microscopic processes they describe and their range of validity. We focus on ab initio theories, i.e. approaches where no adjustable parameters enter. We further do not account for extrinsic effects, i.e. we limit our considerations on the intrinsic spectrum related to the excitation of a photoelectron and the response of the $(N-1)$ system, whereas energy losses the photoelectron suffers from on its way out of the target are neglected. Including extrinsic effects clearly goes beyond the scope of this work and the reader is referred to Ref. [55] for a comprehensive discussion.

1.2. Electronic structure theory: a many-body problem

The many-body problem Atoms, molecules and solids are systems composed of positively charged atomic cores and the respective electrons. In quantum mechanics, assuming non-relativistic and time-independent problems, the behavior of interacting electrons and nuclei is governed by the following Schrödinger equation:

$$\hat{H}\Psi\left(\mathbf{x},\mathbf{R}\right) = E\Psi\left(\mathbf{x},\mathbf{R}\right),$$

where $\Psi\left(\mathbf{x},\mathbf{R}\right)$ is the many-particle wave function depending on the spatial coordinates $\mathbf{R} \equiv (\mathbf{R}_1 \dots \mathbf{R}_n)$ of the K ion cores with nuclear charge Z_I. The spatial coordinates $\mathbf{r} \equiv (\mathbf{r}_1 \dots \mathbf{r}_N)$ and the spin coordinates $\{s_i\}$ of the N electrons are regrouped in the generalized coordinate $\mathbf{x}$, while the total energy of the system is represented by E. The Hamiltonian $\hat{H}$ is composed as follows:

$$\hat{H} = -\frac{1}{2}\sum_{i=1}^{N}\nabla_i^2 - \frac{1}{2}\sum_{I=1}^{K}\frac{\nabla_I^2}{M_I} + \sum_{i=1}^{N}\sum_{j>i}^{N}\frac{1}{|\mathbf{r}_i - \mathbf{r}_j|} + \sum_{I=1}^{K}\sum_{J>i}^{K}\frac{Z_I Z_J}{|\mathbf{R}_I - \mathbf{R}_J|} - \sum_{i=1}^{N}\sum_{I=1}^{K}\frac{Z_I}{|\mathbf{r}_i - \mathbf{R}_I|},$$

where the first two terms are kinetic energy contributions. The remaining terms originate from the electron-electron, core-core and electron-core Coulomb interaction, respectively. Here and in the following, atomic units are used, i.e. the mass m_e and the charge e of an electron, the Planck constant $\hbar$ and the permittivity of the vacuum $4\pi\varepsilon_0$ are set to unity.

The electronic problem Since the mass M of the nuclei is essentially larger than the electronic mass m_e, the velocity of the ion cores is much smaller and one supposes that electrons adjust immediately to changes in the core positions. Following Born and Oppenheimer [57, 58], the Hamiltonian can be expanded in terms of the mass ratio $(m_e/M)^{1/4}$, resulting in a decoupling of the Schrödinger equation in an electronic and an ionic part. For now, we focus on the electronic Schrödinger equation, where the ion cores are kept frozen at fixed positions $\mathbf{R}^0$. As a result, their kinetic energy contribution vanishes and the repulsive ion-ion Coulomb potential becomes a constant:

$$\hat{H}^e\left(\mathbf{R}^0\right)\Psi^e\left(\mathbf{x},\mathbf{R}^0\right) = E\left(\mathbf{R}^0\right)\Psi^e\left(\mathbf{x},\mathbf{R}^0\right), \tag{1.1}$$

$$\hat{H}^e\left(\mathbf{R}^0\right) = -\frac{1}{2}\sum_{i=1}^{N}\nabla_i^2 + \sum_{i=1}^{N}\sum_{j>i}^{N}\frac{1}{|\mathbf{r}_i-\mathbf{r}_j|} - \sum_{i=1}^{N}\sum_{I=1}^{K}\frac{Z_I}{|\mathbf{r}_i-\mathbf{R}_I^0|}. \tag{1.2}$$

The last term in equation (1.2), a constant potential originating from the interaction of the electrons with the fixed ion cores, is from now on termed external potential $\hat{V}_{ext}$, even though $\hat{V}_{ext}$ is not necessarily restricted to the electron-core potential and can in principle contain any applied external field. In the following, except for some special cases, the electronic spin degree of freedom is not explicitly considered, i.e. we limit ourselves to systems with spin paired electrons and thus no magnetization. Moreover, we omit the explicit notation of the nuclear positions $\mathbf{R}^0$, only representing parameters. The electronic kinetic energy contribution and the external potential are grouped together in $\hat{h}_0$,

$$\hat{h}_0 = -\frac{1}{2}\nabla^2 + \hat{V}_{ext},$$

which is the so-called single-particle Hamiltonian, only containing operators acting on a single electron. On the contrary, the electron-electron Coulomb interaction term in equation (1.2) is a two-particle operator, correlating the motion of the electrons and making the electronic problem very difficult to solve for a larger number of particles.

Correlation means that the behavior of a single electron is affected by the motion of all the other electrons. In crystals, where a 1 cm^3 volume contains roughly 10^{23} electrons, the enormous complexity of solving the Schrödinger equation becomes obvious. Calculating total energies, such as $E(N)$ and $E(N\pm1)$, in order to obtain the electronic structure amounts thus to a complex many-body problem, too difficult to be solved exactly. For realistic systems, approximations are consequently inevitable. Since the Coulomb interaction constitutes a clearly non-negligible contribution, low-order perturbation theories have to be manipulated with care.[1] In principle, there is no controlled way to treat these correlations and one usually chooses approximations including the most important features of the strong Coulomb interaction. Only in very few cases mathematical error estimates can be made and approximations have rather to be justified through systematic comparisons with experiments.

An often used starting point to deal with correlations is to find an appropriate set of one-

[1] By way of example, the electrostatic energy between two electrons placed at one Bohr radius a_0 apart from each other, amounts to around $\frac{e^2}{a_0} = 27$ eV.

electron orbitals, obtained using reasonable approximative single-particle expressions for the Coulomb term. Among these approaches are so-called mean-field theories, where the many-body system is reduced to the problem of a single electron moving in an averaged (effective) interaction field of the other electrons. Two important representatives, the Hartree-Fock approach (HFA) and density functional theory (DFT) are introduced in the following.

1.2.1. The Hartree-Fock Approach

The variational principle Solving the electronic Schrödinger equation (1.1) allows to predict the properties of any electronic system. Due to its complexity, an exact solution of the problem is, however, out of reach. Nevertheless, one can formulate strategies, where not a full solution is obtained, but where at least the ground state wave function Ψ_0 and the ground state energy E_0 are accessible. In this context, the total energy E_{trial} is calculated using an arbitrary trial many-body wave function Ψ_{trial}. The variational principle then states that E_{trial} is always larger than the ground state energy, except the case, where Ψ_{trial} equals the ground state wave function:

$$\begin{aligned} E_{trial} &= \langle \Psi_{trial} | \hat{H}^e | \Psi_{trial} \rangle , \\ E_0 &= \langle \Psi_0 | \hat{H}^e | \Psi_0 \rangle , \\ E_{trial} &\geq E_0 . \end{aligned}$$

Consequently, searching through all admissible many-body wave functions represents a way to systematically minimize the total energy and thus to find the ground state energy and wave function:

$$E_0 = \min \; E \left[\Psi_{trial} \right] .$$

Possible trial wave functions have to fulfill certain conditions, characteristic to fermionic wave functions. An important criterion is anti-symmetry, i.e.

$$\Psi \left(\mathbf{r}_1 \dots \mathbf{r}_i \mathbf{r}_j \dots \mathbf{r}_N \right) = -\Psi \left(\mathbf{r}_1 \dots \mathbf{r}_j \mathbf{r}_i \dots \mathbf{r}_N \right) .$$

This is nothing else than a generalization of the *Pauli exclusion principle*, which states that two fermions are not allowed to occupy the same state. In addition, a physical meaning can only be associated to the absolute square of a wave function. In particular, one is usually interested in averaged quantities, such as the charge density $n(\mathbf{r})$ and the pair density $\varrho(\mathbf{r}, \mathbf{r}')$:

$$\begin{aligned} n(\mathbf{r}_1) &= N \int \cdots \int \left| \Psi \left(\mathbf{r}_1 \dots \mathbf{r}_N \right) \right|^2 d\mathbf{r}_2 \dots d\mathbf{r}_N , \\ \varrho(\mathbf{r}_1, \mathbf{r}_2) &= N(N-1) \int \cdots \int \left| \Psi \left(\mathbf{r}_1 \dots \mathbf{r}_N \right) \right|^2 d\mathbf{r}_3 \dots d\mathbf{r}_N . \end{aligned}$$

The former represents the probability to find one of the N electrons at $\mathbf{r}$, while the latter describes the probability that one electron is at $\mathbf{r}$ and another one at $\mathbf{r}'$.[2] Since the probability

[2] Following Ref. [59], we introduced a normalization factor of $N(N-1)$ for the pair density, corresponding to the total number of *non-distinct* pairs. However, also the prefactor $N(N-1)/2$ is common, corresponding to the total number of *distinct* pairs [60].

of finding the N electrons anywhere in space has to be 1, one imposes

$$\int\cdots\int |\Psi(\mathbf{r}_1 \ldots \mathbf{r}_N)|^2 \, d^3\mathbf{r}_1 \ldots d^3\mathbf{r}_N = 1$$

as a normalization condition to the wave function.

From the mentioned physical properties, important mathematical characteristics of wave functions can be derived, such as continuity and quadratic integrability. Nevertheless, the manifold of possible functions is enormous and in practice a complete search through all elements is, except for very small systems, not feasible. Instead, one has to limit the search on subsets which are both physically meaningful and manageable.

The Hartree approximation The many-electron wave function Ψ depends on $3N$ spatial electronic coordinates and is consequently highly non-trivial. Several approaches exist, where functions depending on the known single-electron orbitals are taken as a subset. One of the most straightforward ways is to approximate the many-body wave function by a simple product of orthonormal single-particle orbitals:

$$\Psi(\mathbf{r}_1 \ldots \mathbf{r}_N) \approx \Psi_H = \phi_1(\mathbf{r}_1) \ldots \phi_N(\mathbf{r}_N).$$

This denotes a drastic approximation and e.g. the anti-symmetry condition is not fulfilled. Instead, the Hartree wave function Ψ_H represents the exact solution for a system of N non-interacting bosons. Nevertheless, the simplicity of the approximated many-body wave function invites to apply the mentioned minimization scheme. The degrees of freedom to vary are the N single-electron orbitals, under the constraint to remain orthonormal. This boundary condition introduces Lagrange multipliers ε_i, resulting in:

$$\left[\hat{h}_0 + \tilde{V}_{H,i}\right] \phi_i(\mathbf{r}) = \varepsilon_i \phi_i(\mathbf{r}). \tag{1.3}$$

The complex many-body problem thus reduced, by the introduction of an approximated Hartree wave function, to an effective single-particle eigenvalue equation. Here, the state-dependent Hartree operator is introduced,

$$\tilde{V}_{H,i}(\mathbf{r}) = \int d^3\mathbf{r}' \frac{\rho_i(\mathbf{r}')}{|\mathbf{r} - \mathbf{r}'|},$$

corresponding to a classical electrostatic potential at point $\mathbf{r}$ generated by a charge distribution $\rho_i(\mathbf{r}')$. The latter is obtained by $\rho_i(\mathbf{r}') = \sum_{j \neq i} |\phi_j(\mathbf{r}')|^2$, where the absolute square of the wave function for the particle i under study is explicitly not considered in order to avoid an unphysical self-interaction. Since only the N states lowest in energy are occupied in the ground state, only these contribute to $\rho_i(\mathbf{r}')$.

To conclude, the many-body problem expressed in terms of the many-body Schrödinger equation is reduced to a subproblem, where a single particle moves in an averaged repulsive field, compensated by the attractive background of the positive ion cores. Concerning the total ground state energy of the system, it equals the sum of the eigenvalues ε_i, where the

Coulomb repulsion energy is counted twice for each (ij) pair and thus has to be subtracted:

$$E_0 = \sum_i^N \varepsilon_i - \sum_i^N \int d^3\mathbf{r}\, \phi_i^* (\mathbf{r})\, \tilde{V}_{H,i} \phi_i (\mathbf{r}) \,.$$

The self-consistent field scheme A priori, the Hartree potential is not known, since it depends through $\rho_i (\mathbf{r}')$ on the single-particle orbitals ϕ_j, i.e. on the solutions itself. Consequently, the problem has to be solved in an iterative way, where one starts with an initial guess for the orbitals. From the latter, the Hartree potential, the missing ingredient to set up the Hartree equations, is constructed. As a solution, updated single-particle orbitals ϕ_j and thus a corrected Hartree potential are obtained. This procedure is continued until reaching a defined convergency limit for the input and the updated potential. Since the resulting Hartree potential is finally consistent with the generating orbitals, this scheme is called self-consistent field approach. The mathematical algorithms associated with the fast convergence to the fixed point solution, such as Lanczos method [61] or direct inversion of the iterative subspace (DIIS) [62], will be not detailed here.

The Hartree-Fock approximation Even though the Hartree approach denotes a strong simplification to the many-body problem, some important physical trends are already covered by the effective electrostatic potential. However, in order to also account for antisymmetry, the many-body wave function is approximated as an antisymmetric product of one-electron orbitals:

$$\Psi (\mathbf{x}_1 \ldots \mathbf{x}_N) \approx \Psi_{SD} = \frac{1}{\sqrt{N!}} \begin{vmatrix} \phi_1 (\mathbf{x}_1) & \ldots & \phi_N (\mathbf{x}_1) \\ \vdots & \ddots & \vdots \\ \phi_1 (\mathbf{x}_N) & \ldots & \phi_N (\mathbf{x}_N) \end{vmatrix} .$$

This is the popular Hartree-Fock approach (HFA) and the resulting wave functions are so-called Slater determinant Ψ_{SD} [63, 64]. Anti-symmetry and hence the Pauli exclusion principle are respected, since Ψ_{SD} changes sign under the exchange of two rows or columns and vanishes for two equal rows/columns. Again, the introduced variational scheme can be applied, where the total energy is minimized with respect to the one-electron orbitals. This leads to single-particle effective equations, the Hartree-Fock equations:

$$\left[\hat{h}_0 + \hat{V}_{HF}\right] \phi_i (\mathbf{x}) = \varepsilon_i \phi_i (\mathbf{x}) \,. \tag{1.4}$$

The above relation is very similar to the Hartree result, however, due to the anti-symmetry of the wave function, a more complex operator occurs, the Hartree-Fock operator $\hat{V}_{HF}$. It is composed of two contributions, whose physical meaning can be made clear considering the corresponding total Hartree-Fock energy:

$$E_{HF} \;=\; \textstyle\sum_i^N \langle \phi_i | \, \hat{h}_{0,i} \, | \phi_i \rangle + \frac{1}{2} \sum_i^N \sum_j^N (ii|jj) - (ij|ji) \,,$$

where

$$(ii|jj) = \iint d\mathbf{r}d\mathbf{r}' \frac{|\phi_i(\mathbf{x})|^2 |\phi_j(\mathbf{x}')|^2}{|\mathbf{r}-\mathbf{r}'|}$$

and

$$(ij|ji) = \iint d\mathbf{r}d\mathbf{r}' \frac{\phi_i(\mathbf{x}) \phi_j^*(\mathbf{x}) \phi_j(\mathbf{x}') \phi_i^*(\mathbf{x}')}{|\mathbf{r}-\mathbf{r}'|}.$$

The first term in the Hartree-Fock total energy arises from $\hat{h}_0$, i.e. from the kinetic energy and the external potential. The second one, the so-called Hartree energy, plays the role of a classical averaged electrostatic repulsion. It corresponds to the energy $\langle\phi_i| \tilde{V}_{H,i} |\phi_i\rangle$ introduced in Hartree theory, differing only in the fact that here the considered particle can be included in the sum. The Hartree operator within HF theory is defined as:

$$V_H(\mathbf{r}) = \int d\mathbf{r}' \frac{n(\mathbf{r}')}{|\mathbf{r}-\mathbf{r}'|},$$

where the charge density $n(\mathbf{r})$ is expressed in terms of single-particle orbitals:

$$\begin{aligned} n(\mathbf{r}) &= N \int |\Psi_{SD}(\mathbf{r} \ldots \mathbf{r}_N)|^2 d\mathbf{r}_2 \ldots d\mathbf{r}_N, \\ &= \sum_j^N |\phi_j(\mathbf{r})|^2. \end{aligned}$$

In the following, it is always this potential we refer to as Hartree potential and not the state-dependent potential $\tilde{V}_{H,i}$ from Hartree theory. Analogue, we introduce the so-called Hartree energy contribution, corresponding to $\frac{1}{2}(ii|jj)$, as follows:

$$E_H = \frac{1}{2} \int d\mathbf{r}d\mathbf{r}' \frac{n(\mathbf{r}) n(\mathbf{r}')}{|\mathbf{r}-\mathbf{r}'|}.$$

The third contribution in equation (1.4), $(ij|ji)$, is governed by the Fock operator $\hat{V}_F$, which is defined by its effect on an orbital ϕ_i:

$$V_{F,j}(\mathbf{r}) \phi_i(\mathbf{r}) = \int \phi_j^*(\mathbf{r}') \phi_i(\mathbf{r}') \frac{1}{|\mathbf{r}-\mathbf{r}'|} d\mathbf{r}' \phi_j(\mathbf{r}).$$

It is called exchange contribution and has no classical analogue, since it emanates from the fermionic nature of electrons. It cancels for electrons with opposite spin and only electrons with the same spin are subject to it. Since the result of the application of $\hat{V}_F$ on a orbital depends on the value of the latter in the entire space, this operator is called non-local.

For the case $(i = j)$, the Hartree and the exchange term cancel ($(ii|jj) = (ij|ji)$), i.e. an unphysical self-interaction of the electron with itself is automatically avoided. Analogue to the Hartree equations, the Hartree-Fock equations (1.4) have to be solved self-consistently. The obtained eigenvalues have an important physical interpretation. It can be easily demonstrated that the orbital energies ε_i obtained in the presented single determinant approximation correspond to the already introduced Koopmans binding energies, i.e. to a frozen orbital approximation.

Electron correlation Even though a single Slater determinant captures important physical effects present in many-body systems, it does not represent an exact solution to the many-body wave function. As a consequence, this approach covers only part of the electron correlation, i.e. the effect an electron has on the others. In this context, the so-called correlation energy is introduced as the difference between the exact ground state energy and the Hartree-Fock energy. However, some correlations are already governed within the Hartree-Fock approach, namely exchange interactions originating from the anti-symmetric nature of the fermionic wave function.[3] On the contrary, correlations due to the charge of the electrons are completely neglected within Hartree-Fock theory. By way of example, the probability $\varrho(\mathbf{r},\mathbf{r}')$ of finding one electron at $\mathbf{r}$ and another one at $\mathbf{r}'$ is not simply $\varrho^{cl}(\mathbf{r},\mathbf{r}') = [N/(N-1)]\, n(\mathbf{r})\, n(\mathbf{r}')$, as it would be the case for classical non-interacting charge distributions, but the electrons try to avoid each other.[4] The region around an electron is thus depleted of other electrons and a screening hole is formed around, reducing the interaction between electrons and thus the Coulomb energy. Within Hartree-Fock, $\varrho(\mathbf{r}s;\mathbf{r}'s')$ differs from a simple product only for equal spin electrons through the introduction of an exchange correlation f_x:

$$\varrho^{HF}_{\uparrow\uparrow}\left(\mathbf{r},\mathbf{r}'\right) = n(\mathbf{r},\uparrow)\, n\left(\mathbf{r}',\uparrow\right) + f_x\left(\mathbf{r},\mathbf{r}'\right).$$

However, electrons with opposite spins move completely uncorrelated, following:[5]

$$\varrho^{HF}_{\downarrow\uparrow}\left(\mathbf{r},\uparrow;\mathbf{r}',\downarrow\right) = n(\mathbf{r},\uparrow)\, n\left(\mathbf{r}',\downarrow\right).$$

As a result, two electrons of opposite spin are even allowed to be simultaneously at $\mathbf{r}$. Consequently, in average electrons come too close together, giving rise to an overestimation of the electron-electron repulsion term.

In order to account for correlation effects beyond the exchange interaction f_x, an approach based on a single *ground state* Slater determinant is not sufficient. Instead, the exact solution for an interacting electron system requires an infinite sum of Slater determinants, including also determinants with excitations of one, two, three etc. electrons:

$$\Psi(\mathbf{x}_1 \ldots \mathbf{x}_N) = \sum_{i=0}^{\infty} \Psi_{SD,i}.$$

This approach is known as *Full Configuration Interaction Method* (Full CI). Since one works with the exact Hamiltonian and the full wave function space, correlation is in principle completely taken into account [65, 66]. However, the number of determinants included in the sum scales exponentially with the system's size and therefore, one usually limits the sum to single or double excitations ($CISD$). Thereby, the scaling reduces to N^6. Besides CI, different kinds of post-Hartree-Fock ab initio methods exist, where the most popular ones are e.g. Møller–Plesset perturbation theory and Coupled Cluster *(CC)* approaches. These

[3] Later in this work, we adopt the common notation to restrict the word "correlation" to correlation effects beyond exchange interactions present in HF.

[4] The factor $N/(N-1)$ accounts for the fact that the particles are identical and indistinguishable.

[5] Here, the factor $N/(N-1)$ disappears, since the two considered electrons are distinguished by their spin.

methods are widely used in quantum chemistry electronic structure calculations, however, their detailed discussion is beyond the scope of this thesis and the reader is referred to Refs. [34, 67, 68, 69].

1.2.2. Density Functional Theory

Density Functional Theory (DFT) represents a powerful alternative to Hartree-Fock and post-Hartree-Fock approaches [59, 60, 70]. The already introduced electron density $n(\mathbf{r})$ constitutes the central quantity in this method, bearing the advantage of being much easier to handle than the complicated many-body wave function $\Psi(\mathbf{x}_1 \dots \mathbf{x}_N)$. Even though representing a much simpler object depending only on 3 instead of $3N$ spatial variables, very intuitive arguments demonstrate that it provides all necessary information to set up the many-body Hamiltonian and consequently to determine the properties of the N-electron system. The Hamiltonian is completely determined by the number of electrons N, and by the charge Z_i and the position of the ions $\{\mathbf{R}_0\}$, which enter in the external potential. These quantities are readily available through the ground state density. Integrating the density over the whole volume gives the number of electrons N. Moreover, due to Coulomb attraction, the core positions $\{\mathbf{R}_0\}$ can be identified through finite maxima of the ground state density. Here, the gradient of the density has a discontinuity, resulting from the singularity of the electron-ion potential for $\mathbf{r} \to \mathbf{R}_0$. The cusp can be directly related to the nuclear charge Z_i. The actual physical proof of these plausibility arguments is provided by the Hohenberg-Kohn theorems.

The Hohenberg-Kohn theorems The basis of DFT has been set in 1964 by Hohenberg and Kohn who introduced, in two theorems, the charge density as main ingredient to describe a many-body system [32]. The first theorem states that the external potential $V_{ext}(\mathbf{r})$, the only system dependent ingredient of the Hamiltonian, is uniquely defined within an additive constant by the ground state density $n_0(\mathbf{r})$. Two external potentials, differing by more than a constant and providing the same ground state density, do thus not exist. Accordingly, $n_0(\mathbf{r})$ contains all important information to uniquely determine the full many-body Hamiltonian and hence the true total ground state energy:

$$n_0(\mathbf{r}) \to V_{ext}(\mathbf{r}) \to \hat{H} \to E_0.$$

The latter is a functional of $n_0(\mathbf{r})$ and can be expressed as follows:

$$\begin{aligned} E[n_0] &= F_{HK}[n_0(\mathbf{r})] + \int d^3\mathbf{r}\, V_{ext}(\mathbf{r})\, n_0(\mathbf{r}), \\ F_{HK}[n_0] &= T[n_0] + E_{ee}[n_0]. \end{aligned}$$

The introduced Hohenberg-Kohn functional $F_{HK}[n_0]$ is universal and accounts for the kinetic energy $T[n_0]$ and the electron-electron interaction $E_{ee}[n_0]$, whereas the specifications of the system under study are completely governed by the external potential term. The explicit form of $F_{HK}[n_0]$ is not known, however, it is possible to divide E_{ee} into the electrostatic Hartree

energy E_H and a non-classical energy E_{ncl}, accounting for exchange and correlation:

$$E_{ee}[n_0] = \frac{1}{2}\int d^3\mathbf{r}d^3\mathbf{r}' \frac{n_0(\mathbf{r})\, n_0(\mathbf{r}')}{|\mathbf{r}-\mathbf{r}'|} + E_{ncl}.$$

The second Hohenberg-Kohn theorem introduces the variational principle for the energy functional with respect to the charge density. It states that $E[n]$ has its minimum at the ground state equilibrium density $n_0(\mathbf{r})$,

$$\begin{aligned} n_0(\mathbf{r}) &= N\int |\Psi_0(\mathbf{r}\ldots\mathbf{r}_N)|^2\, d^3\mathbf{r}_2\ldots d^3\mathbf{r}_N, \\ E_0 &= \min_n E[n] = E[n_0], \end{aligned}$$

and provides thus a systematic way to obtain the ground state energy from trial densities. It is important to mention that the variational principle only holds for the exact Hohenberg-Kohn functional. As soon as approximations to this functional are made, total energies lower than the true ground state energy can be obtained.

The Kohn-Sham approach The first Hohenberg-Kohn theorem proves that the the ground state density provides all necessary information of the system, while the variational principle provides a systematic way to obtain it. However, the explicit form of the Hohenberg-Kohn functional $F_{HK}[n]$ is not known. After many trails and errors, the Kohn-Sham ansatz turns DFT into a widely used practical method [33]. The idea is to introduce an auxiliary reference system of N non-interacting electrons whose density $n_s(\mathbf{r})$ equals the density $n(\mathbf{r})$ of the corresponding interacting system. Since the many-body wave function of the non-interacting electron gas is a single Slater determinant, the non-interacting density $n_s(\mathbf{r})$ is completely determined by single-electron orbitals, the so-called Kohn-Sham wave functions $\phi_{KS,i}(\mathbf{r})$:

$$n_s(\mathbf{r}) = \sum_i^N |\phi_{KS,i}(\mathbf{r})|^2 \equiv n(\mathbf{r}).$$

Also the kinetic energy T_s of the reference system can be readily obtained from the Kohn-Sham orbitals:

$$T_s[n] = -\sum_i^N \int d^3\mathbf{r}\, \phi^*_{KS,i}(\mathbf{r}) \frac{\nabla^2}{2} \phi_{KS,i}(\mathbf{r}).$$

The latter is supposed to constitute the major fraction of the kinetic energy of the interacting system. As a consequence, the Hohenberg-Kohn functional can be rewritten as follows:

$$F_{HK}[n] = T_s[n] + E_H[n] + E_{xc}[n],$$

where the so-called exchange-correlation functional E_{xc} contains all unknown contributions, i.e. the residual part of the kinetic energy, repulsive exchange interactions due to Pauli's exclusion principle and correlation effects due to repulsive Coulomb interactions between charged particles:

$$E_{xc} = (T - T_s) + (E_{ee} - E_H).$$

A priori, its exact form is not known and finding appropriate approximative functionals represents a challenging field of research.

Minimizing the energy functional $E[n]$ with respect to the density leads to a density-only Euler eigenvalue equation:

$$\frac{\partial F[n]}{\partial n(\mathbf{r})} + V_{ext}(\mathbf{r}) = \mu,$$

where μ is the chemical potential. Taking the one-particle Kohn-Sham orbitals $\phi_{KS,i}$ as variational parameters finally gives the Kohn-Sham (KS) equations:

$$\left[-\frac{1}{2}\nabla^2 + \hat{V}_{eff}\right]\phi_{KS,i}(\mathbf{r}) = \varepsilon_{KS,i}\phi_{KS,i}(\mathbf{r}). \tag{1.5}$$

The latter represent a single-particle problem, where an electron moves in an effective one-particle potential V_{eff},

$$V_{eff}(\mathbf{r}) = V_H(\mathbf{r}) + V_{ext}(\mathbf{r}) + V_{xc}(\mathbf{r}).$$

In this context, the exchange-correlation potential V_{xc} is introduced as:

$$V_{xc}(\mathbf{r}) = \frac{\partial E_{xc}[n]}{\partial n(\mathbf{r})}.$$

The effective one-particle potential V_{eff} apparently depends on the density and thus on the solution of the problem itself. Therefore, a self-consistent field scheme starting from an initial guess density has to be applied in order to solve the Kohn-Sham eigenvalue problem.

The DFT Kohn-Sham (1.5) and Hartree-Fock equations (1.4) appear very similar, however, important conceptual differences have to be noted. First, in contrast to the Hartree-Fock scheme which is conceived to find the best *approximative* many-body wave function, *DFT-KS* is in principle an exact theory, provided that the correct exchange-correlation energy is known. Moreover, the *DFT-KS* effective potential and thus the exchange correlation functional are local in space, compared to the non-local Fock exchange term in Hartree-Fock. Formally, the *DFT-KS* scheme seems thus less complicated, however, the true exchange-correlation functional is supposed to show a very complicated non-local dependence on n. This points out the challenge in finding a suitable approximation for V_{xc}, covering both as many correlation effects as possible and being at the same time computationally feasible.

A manifold of different exchange-correlation functionals have been elaborated and merits and limitations of the diverse functionals have been studied in detail for diverse materials [59]. The *Local Density Approximation* (LDA) to V_{xc} represents the pioneering exchange-correlation functional [33, 71, 72]. It has been proposed by Kohn and Sham and is based on the assumption that the charge density of the system only slowly varies. As a consequence, each volume element is described by the density $n(\mathbf{r})$ of a uniform electron gas. Based on the exchange-correlation energy $\epsilon_{xc}(n)$ per electron in a homogeneous gas, a quantity that has been calculated using Quantum Monte Carlo techniques [73], one deduces for the exchange-

correlation energy of the whole volume:

$$E_{xc}^{LDA}[n] = \int d^3\mathbf{r}\, \epsilon_{xc}(n)\; n(\mathbf{r})\,.$$

The LDA represents one of the simplest approaches, however, it proved to yield ground state properties in excellent agreement with experiment for a large class of systems, in particular due to the satisfaction of important sum rules.

A possible improvement can be achieved by also including information about the density gradient. This leads to semi-local generalized gradient approximations (GGA), among which the functional of Perdew, Burke and Ernzerhof (PBE) is the most popular [74]. However, (semi)local functionals seem not appropriate for molecules, which are characterized by extremely inhomogeneous and localized densities. Moreover, from equation (1.5) one can readily see that self-interaction effects, which can be dramatic for localized orbitals, are not avoided within (semi)local functionals. In order to tackle these issues, so-called hybrid functionals have been designed. They are based on (semi)local functionals such as LDA or PBE, but also include a certain percentage of exact exchange from Hartree-Fock theory. These functionals, especially the so-called $B3LYP$ functional [75], have been shown to yield satisfying results and have been established as functionals of choice for e.g. the optimization of ground state molecular structures [76]. Within the DFT community, the development of exchange-correlation functionals represents a vivid field of research of its own. A detailed discussion is clearly beyond the scope of this work and the reader is referred to Ref. [59].

Physical interpretation of the Kohn-Sham eigenvalues The quantities accessible through the DFT-KS scheme are first of all ground state related properties, i.e. ground state densities, total energies or structural properties such as lattice constants. For various classes of systems, such as atoms [77], molecules [77], metals [78] and insulators [79], more than satisfactory result have been obtained at favorable computational costs.

Corresponding to the Hohenberg-Kohn theorem, the ground state density contains the entire information needed to construct the exact Hamiltonian. Consequently, also excited state properties should, in principle, be accessible. However, so far it is not known how to extract this information from the Kohn-Sham formalism. By way of example, Kohn-Sham eigenvalues enter the equations as Lagrange multipliers in order to ensure orthogonality of the Kohn-Sham wave functions during the minimization of the energy functional. This is analogue to the derivation of the Hartree-Fock equations, where the HF eigenvalues guarantee orthogonality of the Hartree-Fock single-particle wave functions. Provided that the electronic structure is unaffected by changing the number of electrons in the system (frozen orbital approximation), the HF eigenvalues gain a direct physical meaning through Koopmans theorem, associating them with electron removal/addition energies $\varepsilon_{i,j}^{HF}$:

$$\varepsilon_{i,j}^{HF} = \begin{cases} E^N(n_1,\ldots,n_N) - E^{N-1}(n_1,\ldots n_i-1,\ldots,n_N) \\ \\ E^{N+1}(n_1,\ldots,n_N,\ldots n_j+1,\ldots) - E^N(n_1,\ldots,n_N)\,. \end{cases}$$

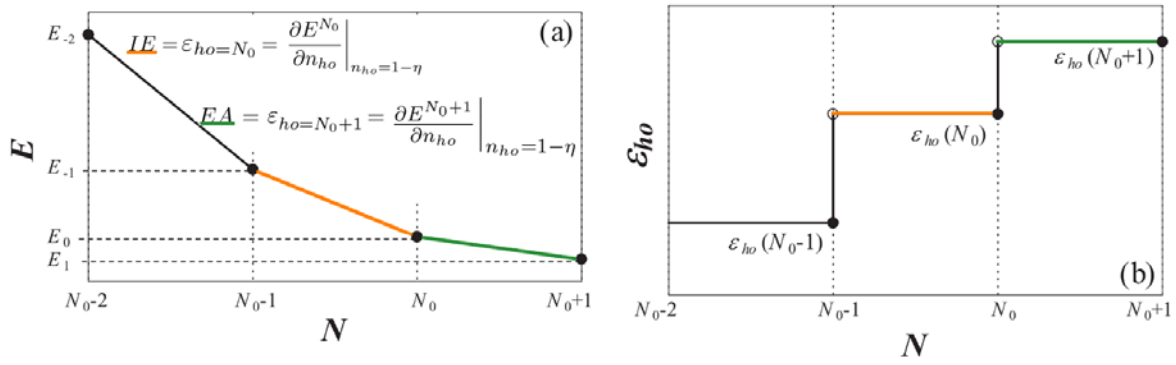

Figure 1.4.: (a) Schematic plot of the total energy E: The exact exchange correlation functional is assumed, for which the total energy is piecewise linear. Moreover, it is supposed that the series $E(N_0)$ with $N_0 \in \mathbb{N}$ is convex and monotonously decreasing. This implies that the ionization energies $IE(N_0) \equiv E_{ho}^{N_0-1} - E^{N_0}$ and electron affinities $EA(N_0) \equiv E^{N_0} - E_{lu}^{N_0+1}$, which correspond to the slopes between two integer values differing by 1, are always positive. In addition, higher ionizations are always greater in magnitude than lower ones, i.e. $IE(N_0 - 1) > IE(N_0)$. (b) Schematic representation of the energy ε_{ho} of the highest occupied level with respect to the fractional number of particles N. Figure taken from Ref. [83] and modified.

Here, E denote total energies of the N and $(N-1)$ electron system, respectively, and $(n_i = 1)$ and $(n_j = 0)$ are occupation numbers. On the contrary, the DFT-KS scheme does, even for the exact exchange-correlation potential, not provide a straightforward mapping between excitation energies and Kohn-Sham eigenvalues. Since the Kohn-Sham system is a fictitious model, the latter are, strictly speaking, pure mathematical tools to obtain the correct ground state density. However, in DFT-KS, there is Janak's theorem [80, 81]:

$$\varepsilon_i^{DFT} = \left.\frac{\partial E^{N_0}}{\partial \tilde{n}_i}\right|_{\tilde{n}_i=1},$$

connecting the Kohn-Sham eigenvalues ε_i^{DFT} to the derivative of the total energy with respect to the *fractional* occupation number $\tilde{n}_i \in [0,1]$. Moreover, it can be shown that the ground-state energy E for fractional numbers of electrons $(N \equiv N_0 + \alpha)$, with $N_0 \in \mathbb{N}$ and $\alpha \in [0,1]$, is a linear combination of the ground state energies at the closest integer values [82, 83]:

$$E(N) = (1-\alpha)\,E(N_0) + \alpha E(N_0+1)\,.$$

This implies that the function $E(N)$ is piecewise linear, as it is depicted in Fig. (1.4a). Within *exact* DFT, i.e. in the case where the exact exchange-correlation functional is used for the Kohn-Sham equations, this piecewise linear behavior of the total energy is reproduced. In this case, based on Janak's theorem, one can show that the negative eigenvalue of the highest occupied (ho) level of a N-particle system corresponds to the ionization energy IE [82, 83, 84, 85, 86, 87], representing the energy needed to remove an electron from the highest

occupied level:

$$-IE\left(N_0\right) = E^{N_0} - E_{ho}^{N_0-1} = \varepsilon_{ho=N_0}^{DFT} = \left.\frac{\partial E^{N_0}}{\partial n_{ho}}\right|_{n_{ho}=1-\eta}, \tag{1.6}$$

where $\eta = 0^+$. This is known as the ionization potential theorem and is illustrated in Fig. (1.4a). Even though only assigning a physical meaning to the highest occupied level, it is nevertheless stronger than Koopmans theorem, since relaxation effects, i.e. the reaction of the remaining electrons on the ejection of the photoelectron, are included. The electron affinity EA, i.e. the energy needed to insert an electron in the lowest unoccupied (lu) level, can be accessed in the same manner. In this case, one has to carry out an exact DFT calculation on a $(N+1)$ electron system, making again use of the ionization potential theorem:

$$-EA\left(N_0\right) = E_{lu}^{N_0+1} - E^{N_0} \quad = \quad \varepsilon_{ho=N_0+1}^{DFT} = \left.\frac{\partial E^{N_0+1}}{\partial n_{ho}}\right|_{n_{ho}=1-\eta}. \tag{1.7}$$

In general, it follows from Janak's theorem that the energy of the highest occupied eigenvalue is a stair-step function with respect to the particle number N, jumping at the integer points (see Fig. 1.4b). This is physically sound, since e.g. the energy needed to eject an electron (IE) or to insert one (EA) are different, i.e. the fundamental gap is non-zero.

It is important to note that for the majority of approximate exchange-correlation functionals, the presented relations are not forced to hold. Moreover, only the highest occupied Kohn-Sham eigenvalue is directly associated with a physical quantity, whereas there is no conclusion for the remaining eigenvalue spectrum. Despite these discoveries, in practice, the whole Kohn-Sham eigenvalue spectrum is usually associated with excitation energies. This is due to the fact that more accurate and at the same time inexpensive ab initio alternatives are rare. The consequences on the quality of the resulting electronic structures will be discussed in detail in subsequent chapters. A comprehensive overview of excited states in DFT is provided by Refs. [82, 83, 87].

1.3. Many-body perturbation theory

The key feature of the so far introduced electronic structure theories, namely the HF approximation and DFT, is to map the many-body system onto an effective single-particle problem. Concerning excitation energies, these approaches have the conceptual disadvantage that only the N particle ground state enters, whereas the ionized electronic configuration is not explicitly considered. The HFA is limited to the single particle picture (Koopmans binding energies) and standard DFT calculations on N particles access only the ionization energy IE. In order to model the microscopic processes occurring when removing (adding) an electron from the system in PES/ IPES experiments, a formalism connecting a system of N interacting electrons to one with $(N \pm 1)$ would be desirable.

Many-particle physics [88, 89, 90] provides quantities which can be directly related to the mentioned process, namely single-particle Green's functions. As it will be discussed in the following, the latter are propagators, which describe the motion of an additional charge in

an interacting many-body system. Here, the many-body problem can be also transformed into an effective one-particle problem. In contrast to the *HF* or Kohn-Sham equations, not a bare particle, but a so-called quasiparticle is considered. The latter behaves like a non-interacting electron or hole subject to an external potential, however, its mass and energy are renormalized due to Coulomb interactions with the remaining particles. Based on one-particle Green's functions, a closed set of equations, the Hedin's equations, will be set up. From these, spectroscopic quantities such as excitation energies are, in theory, exactly accessible from first principles. Representing a set of five integro-differential equations which have to be solved self-consistently, this denotes a very demanding problem. Therefore, practical approaches to the Hedin's equations, namely the so-called *GW* and COHSEX approximation, will be discussed.

Real experimental measurements can not be carried out at absolute zero, but at very low temperatures. Since many physical quantities only weakly depend on temperature in this low temperature regime, calculations at absolute zero can often be helpful describing real systems. Moreover, from a theoretical point of view, the ground state of an interacting system $|\Psi_0\rangle$, a property at zero temperature or at small thermal energies not sufficient to excite the system, is of great conceptual importance. Therefore, we limit the description to zero-temperature single-particle Green's functions in the following and refer the reader to Appendix A.2 for more detailed information.

1.3.1. Green's functions as propagators

Our starting point is a system of N interacting electrons in a static external potential V_{ext}. In order to study the electronic structure, we introduce the single-electron Green's function $G^e(\mathbf{r}t,\ \mathbf{r}'t')$, defined such that $i\hbar G^e(\mathbf{r}t,\ \mathbf{r}'t')$ is the probability amplitude to detect an electron at $(\mathbf{r}t)$ after the insertion of an electron to the interacting many-body system at $(\mathbf{r}'t')$. Similarly, we can define a single-hole Green's function $G^h(\mathbf{r}'t',\ \mathbf{r}t)$, describing the probability amplitude to find a hole at $(\mathbf{r}t)$ subsequent to its creation at $(\mathbf{r}'t')$ [91]. These quantities represent thus theoretical tools to describe electron injection (ejection) and the induced reaction of the system. It is important to note that despite their name, single-particle Green's functions are true many-body quantities, characterizing the propagation of a single particle in an interacting many-particle system.

Using the field operator description in the Schrödinger picture, the one-electron Green's function is defined as follows:

$$G^e(\mathbf{r}t,\ \mathbf{r}'t') = -\frac{i}{\hbar}\ \left\langle \Psi_0^N(t)\right|\hat{\Phi}(\mathbf{r})\ S(t,t')\ \hat{\Phi}^\dagger(\mathbf{r}')\left|\Psi_0^N(t')\right\rangle\ \theta\left(t-t'\right). \tag{1.8}$$

Hence, a process is described which adds an electron at time t' and position $\mathbf{r}'$ to the N-electron ground state $\left|\Psi_0^N(t')\right\rangle$, through the application of the field operator $\hat{\Phi}^\dagger(\mathbf{r})$:

$$\left|\Psi^{N+1}(\mathbf{r}'t')\right\rangle = \hat{\Phi}^\dagger(\mathbf{r}')\left|\Psi_0^N(t')\right\rangle.$$

Subsequently, the evolution operator $S(t,t') = e^{-i\hat{H}(t-t')}$ propagates the system from time t'

to t,

$$S(t,t')\,\hat{\Phi}^{\dagger}(\mathbf{r}')\left|\Psi_0^N(t')\right\rangle \;=\; e^{-i\hat{H}(t-t')}\,\left|\Psi^{N+1}(\mathbf{r}'t')\right\rangle = \left|\Psi^{N+1}(\mathbf{r}'t)\right\rangle,$$

where interactions of the added electron and its environment are considered via the many-body Hamiltonian $\hat{H}$. By means of the annihilation field operator $\hat{\Phi}(\mathbf{r})$, the process is finalized at time t by verifying whether there is an electron at position $\mathbf{r}$:

$$\hat{\Phi}(\mathbf{r})\,S(t,t')\,\hat{\Phi}^{\dagger}(\mathbf{r}')\left|\Psi_0^N(t')\right\rangle.$$

Except the case where an electron is at $\mathbf{r}$, the above expression vanishes. The probability amplitude is then obtained by calculating the overlap of the final state with the N-particle ground state $\left|\Psi_0^N(t)\right\rangle$ at time t. The right time order is ensured by including the step function θ:

$$\theta\left(t-t'\right) = \begin{cases} 1 & \text{for } t > t' \\ 0 & \text{for } t < t', \end{cases}$$

i.e. an electron is first added and then annihilated. Transforming equation (1.8) from the Schrödinger representation into the Heisenberg picture, one obtains an equivalent description. Here, the time-dependence is governed by field operators instead of wave functions, following:

$$\hat{\Phi}^{(\dagger)}(\mathbf{r},t) = e^{i\hat{H}t}\,\hat{\Phi}^{(\dagger)}(\mathbf{r})\,e^{-i\hat{H}t}.$$

This leads to:

$$\begin{aligned} G^e(\mathbf{r}t,\,\mathbf{r}'t') \;&=\; -\tfrac{i}{\hbar}\left\langle\Psi_0^N(0)\,e^{i\hat{H}t}\right|\hat{\Phi}(\mathbf{r})\,e^{-i\hat{H}(t-t')}\,\hat{\Phi}^{\dagger}(\mathbf{r}')\left|e^{-i\hat{H}t'}\Psi_0^N(0)\right\rangle\,\theta\left(t-t'\right) \\ &=\; -\tfrac{i}{\hbar}\left\langle\Psi_0^N\right|\hat{\Phi}(\mathbf{r},t)\,\hat{\Phi}^{\dagger}(\mathbf{r}',t')\left|\Psi_0^N\right\rangle\,\theta\left(t-t'\right). \end{aligned} \tag{1.9}$$

The inverse process of first ejecting and then reinjecting an electron to the system can be formulated in a similar way. It is considered as the propagation of a hole from $(\mathbf{r}t)$ to $(\mathbf{r}'t')$, i.e. of a particle possessing the same mass and opposite charge than an electron and moving opposite in time:

$$G^h(\mathbf{r}'t',\,\mathbf{r}t) = -\frac{i}{\hbar}\left\langle\Psi_0^N\right|\hat{\Phi}^{\dagger}(\mathbf{r}',t')\,\hat{\Phi}(\mathbf{r},t)\left|\Psi_0^N\right\rangle\,\theta\left(t'-t\right). \tag{1.10}$$

For the sake of convenience, equations (1.9) and (1.10) are combined to one time-ordered Green's function $G^T \equiv G^e(\mathbf{r}t,\,\mathbf{r}'t') - G^h(\mathbf{r}'t',\,\mathbf{r}t)$ using Wick's time-ordering operator $\hat{T}$. The latter arranges time-dependent operators $\hat{O}$ with earliest times to the right giving rise to a factor (-1) for each permutation in the fermionic case:

$$\hat{T}\left[\hat{O}_1(t_1)\hat{O}_2(t_2)\right] \;=\; \hat{O}_1(t_1)\hat{O}_2(t_2)\,\theta\left(t_1-t_2\right) - \hat{O}_2(t_2)\hat{O}_1(t_1)\,\theta\left(t_2-t_1\right),$$

$$G^T(\mathbf{r}t,\,\mathbf{r}'t') = -\frac{i}{\hbar}\left\langle\Psi_0^N\right|\hat{T}\left[\hat{\Phi}(\mathbf{r},t)\,\hat{\Phi}^{\dagger}(\mathbf{r}',t')\right]\left|\Psi_0^N\right\rangle. \tag{1.11}$$

Depending on the time order, this equation describes either the propagation of an electron ($t > t'$) or a hole ($t < t'$).

Besides the time-ordered Green's function, it is very useful to introduce the retarded Green's function G^R,

$$G^R(\mathbf{r}t,\ \mathbf{r}'t') = -\frac{i}{\hbar}\ \left\langle \Psi_0^N \right|\left\{\hat{\Phi}(\mathbf{r},t)\ \hat{\Phi}^\dagger(\mathbf{r}',t')\right\}\left|\Psi_0^N\right\rangle \theta\left(t-t'\right),$$

where $\{\ldots\}$ denotes the anticommutator. Analogously, the advanced Green's function G^A is defined as:

$$G^A(\mathbf{r}t,\ \mathbf{r}'t') = \frac{i}{\hbar}\ \left\langle \Psi_0^N \right|\left\{\hat{\Phi}(\mathbf{r},t)\ \hat{\Phi}^\dagger(\mathbf{r}',t')\right\}\left|\Psi_0^N\right\rangle \theta\left(t'-t\right).$$

Strictly speaking, among the time-ordered, the retarded and the advanced Green's function, only G^R is physically meaningful, since it is directly related to experimental quantities. Nevertheless, G^T and G^A are mathematical tools which facilitate calculations and which are connected to G^R via simple relations.

1.3.2. The Lehmann representation of the Green's function

The power of the Green's function formalism for describing PES/IPES experiments can be made clear by rewriting the time-ordered Green's function G^T (1.11) in its Lehmann representation. The latter is a reformulation of the problem in terms of the eigenfunctions $\left\{\left|\Psi_n^N\right\rangle\right\}$ of the many-body Hamiltonian $\hat{H}$, solutions to $\hat{H}\left|\Psi_n^N\right\rangle = E_n^N\left|\Psi_n^N\right\rangle$. As it is explicitly demonstrated in Appendix A.2, G^T can be written in the complete $\left\{\left|\Psi_n^N\right\rangle\right\}$ basis as follows:

$$G^T(\mathbf{r},\mathbf{r}',\tau) = -\frac{i}{\hbar}\sum_m^{unocc} e^{-i\varepsilon_m\tau}\ f_m^*(\mathbf{r})f_m(\mathbf{r}')\ \Theta(\tau) + \frac{i}{\hbar}\sum_l^{occ} e^{-i\varepsilon_l\tau}\ g_l^*(\mathbf{r}')g_l(\mathbf{r})\ \Theta(-\tau), \quad (1.12)$$

where we defined the Lehmann amplitudes for the $(N+1)$ system,

$$f_m(\mathbf{r}) = \left\langle \Psi_m^{N+1}\right|\hat{\Phi}^\dagger(\mathbf{r})\left|\Psi_0^N\right\rangle \qquad f_m^*(\mathbf{r}) = \left\langle \Psi_0^N\right|\hat{\Phi}(\mathbf{r})\left|\Psi_m^{N+1}\right\rangle,$$

and the $(N-1)$ system:

$$g_l(\mathbf{r}) = \left\langle \Psi_l^{N-1}\right|\hat{\Phi}(\mathbf{r})\left|\Psi_0^N\right\rangle \qquad g_l^*(\mathbf{r}) = \left\langle \Psi_0^N\right|\hat{\Phi}^\dagger(\mathbf{r})\left|\Psi_l^{N-1}\right\rangle.$$

The excitation energy needed to insert an electron into an unoccupied state of an interacting N particle system in its ground state with total energy E_0^N, creating a $(N+1)$ system with total energy E_m^{N+1}, is here defined as $\varepsilon_m = E_m^{N+1} - E_0^N$. The excitation energy needed to remove an electron from an occupied state of the N particle system, creating a $(N-1)$ system with total energy E_l^{N-1}, is $\varepsilon_l = E_0^N - E_l^{N-1}$ [55]. The notation (l-occupied, m-unoccupied) in the above equations serves to distinguish these two cases. The excitation energies $\varepsilon_{m,l}$ correspond to the negative value of the binding energy E_b as defined before in the discussion of PES experiments. Since the Hamiltonian does not explicitly depend on time, the problem is translationally invariant and the Green's function only depends on the time difference

$\tau = t - t'$. Consequently, a Fourier transformation from time to frequency space is suitable, following:

$$G(\mathbf{r}, \mathbf{r}', \omega) = \int_{-\infty}^{\infty} d\tau \, e^{i\omega\tau} G(\mathbf{r}, \mathbf{r}', \tau),$$

$$G(\mathbf{r}, \mathbf{r}', \tau) = \frac{1}{2\pi} \int_{-\infty}^{\infty} d\omega \, e^{-i\omega\tau} G(\mathbf{r}, \mathbf{r}', \omega).$$

For the time-ordered Green's function, the Fourier transformation yields:

$$G^T(\mathbf{r}, \mathbf{r}', \omega) = \frac{1}{\hbar} \sum_{m}^{unocc} \frac{f_m^*(\mathbf{r}) f_m(\mathbf{r}')}{\omega - \varepsilon_m + i\eta} + \frac{1}{\hbar} \sum_{l}^{occ} \frac{g_l^*(\mathbf{r}') g_l(\mathbf{r})}{\omega - \varepsilon_l - i\eta}, \tag{1.13}$$

where the small imaginary part η appears to ensure convergence (see Appendix A.2). When not explicitly needed in the following, i.e. except for integrals, we set η to zero. Likewise, we can derive an expression for the retarded Green's function:

$$G^R(\mathbf{r}, \mathbf{r}', \omega) = \frac{1}{\hbar} \sum_{m}^{unocc} \frac{f_m^*(\mathbf{r}) f_m(\mathbf{r}')}{\omega - \varepsilon_m + i\eta} + \frac{1}{\hbar} \sum_{l}^{occ} \frac{g_l^*(\mathbf{r}') g_l(\mathbf{r})}{\omega - \varepsilon_l + i\eta}. \tag{1.14}$$

In this representation, one can easily see that G^T and G^R have poles at the excitation energies $\varepsilon_{m/l}$ measured as binding energies in PES/IPES experiments. This suggests that these quantities are, in principle, accessible. However, this is a highly non-trivial problem, since all many-body interactions are taken into account.

A suitable starting point from which the interacting system can be modeled is a system of N non-interacting particles, governed by $\hat{h}_0 = -\frac{1}{2}\nabla_{\mathbf{r}}^2 + \hat{V}_{ext}$. In this case, the excitation energies are simply the single-particle energies $\varepsilon_{m/l}^0$ and the many-electron states are single Slater determinants constructed from single-particle wave functions $\phi_{m/l}$, simplifying the Lehmann amplitudes to $\phi_{m/l}$. Thus, the Green's function G_0^T for a system of N non-interacting particles denotes in the Lehmann representation:

$$G_0^T(\mathbf{r}, \mathbf{r}', \omega) = \sum_n \frac{\phi_n^*(\mathbf{r}) \, \phi_n(\mathbf{r}')}{\omega - \varepsilon_n^0 + i\eta \, \mathrm{sgn}(\mu - \varepsilon_n^0)}, \tag{1.15}$$

where we introduced the chemical potential μ to distinguish between occupied and unoccupied states regrouped in the index n. For the retarded Green's function one finds:

$$G_0^R(\mathbf{r}', \mathbf{r}, \omega) = \sum_n \frac{\phi_n(\mathbf{r}) \phi_n(\mathbf{r}')}{\omega - \varepsilon_n^0 + i\eta}. \tag{1.16}$$

Besides one-particle excitation spectra, important ground state properties are accessible through the single-particle Green's function. By way of example, the ground state expectation value of any one-particle operator, such as e.g. the density operator $\hat{n}(\mathbf{r}, t) = \hat{\Phi}^\dagger(\mathbf{r}, t) \, \hat{\Phi}(\mathbf{r}, t)$, can be obtained:

$$n(\mathbf{r}, t) = -iG\left(\mathbf{r}, \mathbf{r}, t, t^+\right).$$

Moreover, also the exact total ground state energy can be calculated by means of the one-

particle Green's function using e.g. the Galitskii-Migdal relation [92]:

$$E_0^N = -\frac{i}{2}\int d^3\mathbf{r} \lim_{t'\to t^+}\lim_{\mathbf{r}'\to\mathbf{r}}\left(\frac{i\partial}{\partial t} - h_0(\mathbf{r})\right) G\left(\mathbf{r},\mathbf{r}',t,t'\right).$$

1.3.3. The Dyson equation and the self-energy

The equation of motion technique As depicted in the previous section, the Green's function enters in many observables. Studying its time-dependence represents a powerful tool to explore these quantities. Different approaches exist, where one of which is the equation of motion technique. Here, the quantity of interest, e.g. the single-particle Green's function, is differentiated several times, creating a series of coupled differential equations. Provided that this series constitutes a closed set of equations, the problem is in principle exactly solvable. However, if it is not a closed, physical arguments have to be carefully selected in order to truncate the series in a physically meaningful manner.

As elaborated in Appendix A.3, the derivation of the equation of motion (EOM) of the time-ordered Green's function starts by differentiating G with respect to one of its two time arguments, yielding:

$$i\hbar\tfrac{\partial G(\mathbf{r}t,\mathbf{r}',t')}{\partial t} = \delta\left(\mathbf{r}-\mathbf{r}'\right)\delta\left(t,t'\right) + \left\langle\Psi_0^N\middle|\, T\left[\tfrac{\partial\hat{\Phi}(\mathbf{r},t)}{\partial t}\hat{\Phi}^\dagger(\mathbf{r}',t')\right]\middle|\Psi_0^N\right\rangle.$$

The time-derivative of the annihilation operator $\hat{\Phi}(\mathbf{r},t)$ reads:

$$i\hbar\frac{\partial\hat{\Phi}(\mathbf{r},t)}{\partial t} = \left\{\hat{\Phi}(\mathbf{r},t),\hat{H}\right\} = h_0\left(\mathbf{r}\right)\hat{\Phi}(\mathbf{r},t) + \int d^3\mathbf{r}''\, v\left(\mathbf{r},\mathbf{r}''\right)\hat{\Phi}^\dagger(\mathbf{r}'',t)\hat{\Phi}(\mathbf{r}'',t)\hat{\Phi}(\mathbf{r},t), \quad (1.17)$$

where $v\left(\mathbf{r},\mathbf{r}''\right) = \frac{1}{|\mathbf{r}-\mathbf{r}''|}$ is the bare Coulomb potential and where $h_0\left(\mathbf{r}\right)$ accounts for the kinetic and the ionic potential. Inserting the time-derivative results in:

$$\begin{aligned}&\left(i\hbar\tfrac{\partial}{\partial t} - h_0\left(\mathbf{r}\right)\right) G(\mathbf{r}t,\ \mathbf{r}'t')\\ &+\tfrac{1}{i\hbar}\int d^3\mathbf{r}''\, v\left(\mathbf{r},\mathbf{r}''\right)\left\langle\Psi_0^N\middle|\, T\left[\hat{\Phi}(\mathbf{r},t)\hat{\Phi}(\mathbf{r}'',t)\,\hat{\Phi}^\dagger(\mathbf{r}'',t)\hat{\Phi}^\dagger(\mathbf{r}',t')\right]\middle|\Psi_0^N\right\rangle \;=\; \delta\left(\mathbf{r}-\mathbf{r}'\right)\delta\left(t,t'\right).\end{aligned}$$

The above equation consists of a single-particle expression and an expectation value containing four field operators accounting for electron-electron interactions. This expectation value can be associated with a two-particle Green's function G_2 at zero temperature, in general defined as [2, 90]:

$$G_2\left(\mathbf{r}_1t_1;\mathbf{r}_2t_2;\mathbf{r}_1't_1';\mathbf{r}_2't_2'\right) = \frac{1}{(i\hbar)^2}\left\langle\Psi_0^N\middle|\, T\left[\hat{\Phi}(\mathbf{r}_1,t_1)\hat{\Phi}(\mathbf{r}_2,t_2)\,\hat{\Phi}^\dagger(\mathbf{r}_2't_2')\hat{\Phi}^\dagger(\mathbf{r}_1't_1')\right]\middle|\Psi_0^N\right\rangle.$$

Analogue to the one-particle Green's function G_1, it represents the probability amplitude of finding simultaneously two particles at $(\mathbf{r}_1,t_1)$ and $(\mathbf{r}_2,t_2)$, which have been added to the system at $(\mathbf{r}_1't_1')$ and $(\mathbf{r}_2't_2')$. It thus contains information about two-particle processes and the involved interactions. Depending on the time order it either describes the propagation of two electrons, two holes or an electron-hole pair. In terms of the two-particle Green's function, the EOM in its differential form is represented by:

$$\left(i\hbar\frac{\partial}{\partial t} - h_0\left(\mathbf{r}_1\right)\right) G(11') + i\hbar \int d2\, v\left(\mathbf{r}_1, \mathbf{r}_2\right)\; G_2\left(12, 1'2^+\right) = \delta\left(1, 1'\right). \tag{1.18}$$

Concerning the introduced shorthand notation, natural numbers regroup both space and time arguments. In this specific case, we defined $1 \equiv (\mathbf{r}_1, t)$, $1' \equiv (\mathbf{r}_1', t_1')$, $2 \equiv (\mathbf{r}_2, t)$ and $2^+ \equiv (\mathbf{r}_2, t + \eta)$, where the infinitesimal parameter η ensures the right time order.

Provided that the Hamiltonian does not explicitly depend on time, the Green's function G only depends on the time difference $\tau = t - t'$. Hence, it is very useful to transform equation (1.18) to frequency space via a Fourier transformation. Using the fact that the Fourier transformation of a derivative $\frac{\partial}{\partial t}$ becomes $(-i\omega)$ and that δ-functions $\delta(\tau)$ give unity, one arrives at:

$$\left(\hbar\omega - h_0\left(\mathbf{r}_1\right)\right) G(\mathbf{r}_1, \mathbf{r}_1'; \omega) + i\hbar \int d^3\mathbf{r}_2\, v\left(\mathbf{r}_1, \mathbf{r}_2\right)\; G_2\left(\mathbf{r}_1\mathbf{r}_2, \mathbf{r}_1'\mathbf{r}_2; \omega\right) = \delta\left(\mathbf{r}_1, \mathbf{r}_1'\right). \tag{1.19}$$

Equations (1.18) and (1.19) provide a possibility to calculate the single-particle Green's function from the known single-particle potential $h_0(\mathbf{r})$ and the two-body Green's function G_2. This is an important result, however, of little practical use. In order to obtain the two-particle Green's function, a solution to an EOM containing a three particle Green's function is needed. The latter in turn is obtained by solving an EOM involving a four-particle Green's function. That means, in order to calculate the single-particle Green's function, a hierarchy of equations of motions for higher order Green's functions has to be solved. This is not astonishing regarding the fact that equation (1.18) is an exact reformulation of the many-body problem implying all kinds of complex many-particle correlations.

The Dyson equation A useful reformulation of the the single-particle Green's function EOM is to map the complicated many-body system onto an effective one-particle problem. This can be achieved by introducing a one-particle quantity, the so-called self-energy Σ, pushing the two-particle Green's function out of the EOM. Following Ref. [4], we first introduce the mass operator M, accounting for electron-electron interactions both at the classical Hartree level and beyond:

$$\int d2\, M(12)\, G(21') = -i\hbar \int d2\, v\left(\mathbf{r}_1, \mathbf{r}_2\right)\; G_2\left(12, 1'2^+\right).$$

Inverting the above equation using the inverse Green's function G^{-1},

$$\int d2\, G(12) G^{-1}(21') = \int d2\, G^{-1}(12) G(21') = \delta(1, 1'),$$

yields the explicit definition of the mass operator:

$$M(12) = -i\hbar \int d4 \int d3\, v\left(\mathbf{r}_1, \mathbf{r}_3\right)\; G_2\left(13, 43^+\right) G^{-1}(42). \tag{1.20}$$

Consequently, the equation of motion (1.18) can be written as follows:

$$\left(i\hbar\frac{\partial}{\partial t} - h_0\left(\mathbf{r}_1\right)\right) G(11') - \int d2\, M(12)\, G(21') = \delta\left(1,1'\right), \tag{1.21}$$

i.e. we reformulated the many-body problem in terms of the mass operator. In frequency space, we consequently obtain:

$$\left(\hbar\omega - h_0\left(\mathbf{r}_1\right)\right) G(\mathbf{r}_1,\mathbf{r}_1';\omega) - \int d\omega' \int d^3\mathbf{r}_2\, M\left(\mathbf{r}_1\mathbf{r}_2;\omega'\right)\, G\left(\mathbf{r}_2,\mathbf{r}_1';\omega+\omega'\right) = \delta\left(\mathbf{r}_1,\mathbf{r}_1'\right).$$

Even though representing a one-particle quantity, the latter is a highly non-trivial object being not only non-local and non-Hermitian, but also implying a self-consistent solution scheme for the EOM due to its dependence on G. Nevertheless, it constitutes a suited starting point for perturbative approaches.

Tackling the equation of motion by means of perturbation theory (see Appendix A.3) can be achieved by starting from an exactly solvable problem, such as the case of non-interacting particles subject to a classical Hartree potential V_H. For the latter, the non-interacting single-particle Green's function G_0 can be readily calculated following equation (1.21) via:

$$\left(i\hbar\frac{\partial}{\partial t} - H_0\left(\mathbf{r}_1\right)\right) G_0(11') = \delta\left(1,1'\right),$$

where we introduced the Hamiltonian $\hat{H}_0$:

$$\hat{H}_0 = \hat{h}_0 + \hat{V}_H = -\frac{1}{2}\nabla^2 + \hat{V}_{ext} + \hat{V}_H.$$

Due to the choice to include the operator of the classical Hartree potential in the latter, this kind of electron-electron interaction has to be removed from the mass operator in order to not counting it twice. This leads to the definition of the self-energy operator Σ,

$$\Sigma = M - \hat{V}_H,$$

governing all interactions beyond Hartree. Reformulating the EOM (1.21) in terms of G_0 and Σ leads to:

$$\left(i\hbar\frac{\partial}{\partial t_1} - H_0\left(\mathbf{r}_1\right)\right) G(11') - \int d3\, \Sigma\left(13\right) G\left(31'\right) = \delta\left(1,1'\right), \tag{1.22}$$

which can be reformulated to the so-called Dyson equation for the single-particle Green's function [93, 94]:

$$G(11') = G_0(11') + \int d2 \int d3\, G_0(12)\Sigma(23)G(3'1). \tag{1.23}$$

Rewriting the latter in a separated form with respect to the particular contributions, following:

$$G^{-1}\left(54\right) = G_0^{-1}\left(54\right) - \Sigma\left(54\right),$$

facilitates the Fourier transformation of equation (1.22) to frequency space:

$$[\hbar\omega - H_0(\mathbf{r})]\, G(\mathbf{r},\mathbf{r}',\omega) - \int d\mathbf{r}''\, \Sigma(\mathbf{r},\mathbf{r}'',\omega)\, G(\mathbf{r}'',\mathbf{r}',\omega) = \delta(\mathbf{r},\mathbf{r}')\,.$$

Dyson's equation (1.23) represents an infinite series in the perturbation Σ based on the known building blocks G_0 and can be symbolically written as:

$$G = G_0 + G_0\Sigma G_0 + G_0\Sigma G_0\Sigma G_0 + \dots\,.$$

Truncating the series at zero order simply results in the propagation of a non-interacting particle. Including higher order terms provides more and more interactions and finally the infinite series describes the full many-body problem correctly. Equation (1.23) offers thus a systematic way to include correlation effects with the challenge to find both physically meaningful and feasible truncations.

It is often of high practical use and repeatedly applied in the subsequent sections to express the Dyson equation within a non-interacting Hartree basis ϕ_i, in which G_0 is diagonal:

$$\begin{aligned} G^T_{0,ii} &\equiv \langle\phi_i|\, G_0\, |\phi_i\rangle \\ &= \iint d^3\mathbf{r}\, d^3\mathbf{r}' \sum_n \tfrac{\phi^*_n(\mathbf{r})\phi_i(\mathbf{r})\phi^*_i(\mathbf{r}')\phi_n(\mathbf{r}')}{\omega-\varepsilon^0_n\pm i\eta} = \sum_n \tfrac{\delta_{in}}{\omega-\varepsilon^0_n\pm i\eta} = \tfrac{1}{\omega-\varepsilon^0_i\pm i\eta}. \end{aligned}$$

Assuming that the self-energy is diagonal in this basis, namely that Hartree and quasiparticle wave functions strongly overlap, it follows for the interacting Green's function:

$$G^T_{ii} \equiv \langle\phi_i|\, G\, |\phi_i\rangle = \langle\phi_i|\left(G_0^{-1} - \Sigma\right)^{-1}|\phi_i\rangle = \frac{1}{\omega - \varepsilon^0_i - \Sigma_{ii}}, \tag{1.24}$$

with $\Sigma_{ii} = \langle\phi_i|\,\Sigma\,|\phi_i\rangle$.

1.3.4. The spectral function and the quasiparticle picture

The spectral function Coming back to the actual problem of accurately calculating PES/IPES spectra, we search a formalism which directly connects the Green's function as presented in the preceding sections to experimentally accessible quantities such as the measured photocurrent. As already commented on, the accurate theoretical description of PES/IPES experiments requires many-body concepts, however, approximations are inevitable.

One of these is the sudden approximation, where the measured photocurrent I directly results from the excitation of an electron from an initial state Ψ_i to a final state Ψ_f due to the interaction of the electronic system with a photon field. Losses on its way out to the surface are not considered. Within Fermi's Golden Rule and the dipole approximation, the transition rate Ω, i.e. the probability of a transition per unit time, can be written as follows [95, 96]:

$$\Omega \approx \frac{2\pi}{\hbar}\left|\langle\Psi_f|\,\mathbf{r}\,|\Psi_i\rangle\right|^2 \delta(E_f - E_i - \hbar\omega)\,.$$

The main ingredients are the matrix element of the perturbation and a δ-function ensuring energy conservation. The matrix element is further simplified within a single-electron picture,

where the initial state is described by a single-particle orbital $\phi_{i,m}$, from which the electron is ejected, and the decoupled remaining electronic system $\Psi_{i,m}^{N-1}$:

$$\Psi_i^N \approx \hat{C}\,\phi_{i,m}\Psi_{i,m}^{N-1}.$$

Antisymmetry of the state is guaranteed by the operator $\hat{C}$. Likewise, the final state is characterized by the single-particle orbital of the free photoelectron $\phi_{f,Ekin}$ and the left over electrons $\Psi_{f,m}^{N-1}$:

$$\Psi_f^N \approx \hat{C}\,\phi_{f,Ekin}\Psi_{f,m}^{N-1}.$$

Within the single-electron approximation, the matrix element thus reduces to:

$$\langle\Psi_f|\,\mathbf{r}\,|\Psi_i\rangle = \langle\phi_{f,Ekin}|\,\mathbf{r}\,|\phi_{i,m}\rangle\left\langle\Psi_{f,m}^{N-1}\middle|\;\Psi_{i,m}^{N-1}\right\rangle,$$

i.e. it is given by the overlap of the initial and final state of the $(N-1)$ electron system and the matrix element consisting of the perturbation between the single-electron orbitals. Within Koopmans approximation, these states are supposed to be equal, $\Psi_{f,m}^{N-1} = \Psi_{i,m}^{N-1}$, yielding:

$$\langle\Psi_f|\,\mathbf{r}\,|\Psi_i\rangle = \langle\phi_{f,Ekin}|\,\mathbf{r}\,|\phi_{i,m}\rangle\,.$$

The relaxation of the remaining electronic system is thus completely neglected and the final state $\Psi_{f,m}^{N-1}$ corresponds to the frozen ground state electronic configuration, where one electron in state m is missing.

In order to go beyond Koopmans approximation, first one has to allow the electronic system to react on the creation of a charge in state m. This results in a relaxed many-body state labeled $\Psi_{f,m,0}^{N-1}$, where an electron is still missing in state m, but where the remaining energy levels are renormalized. Moreover, one also has to consider final state configurations, where the electronic system not only relaxes, but where the system also reacts in form of neutral excitations, such as the creation of e.g. electron-hole pairs or plasmon excitations. The manifold of all possible final excited states, including $\Psi_{f,m,0}^{N-1}$, is labeled with the index s, $\Psi_{f,m,s}^{N-1}$, and assigned the energy $E_{f,m,s}^{N-1}$. The electronic system can thus react in many different ways to the ionization, provided that the particle number $(N-1)$ remains fixed and that energy conservation is respected, i.e. the sum of the kinetic energy of the outgoing electron and the energy of the final state is constant. The above matrix element then reads:

$$\langle\Psi_f|\,\mathbf{r}\,|\Psi_i\rangle = \langle\phi_{f,Ekin}|\,\mathbf{r}\,|\phi_{i,m}\rangle\sum_s\left\langle\Psi_{f,m,s}^{N-1}\middle|\;\Psi_{i,m}^{N-1}\right\rangle.$$

The measured photocurrent I, which is proportional to the transition rate Ω, becomes:

$$I \approx \sum_{fim}|\langle\phi_{f,Ekin}|\,\mathbf{r}\,|\phi_{i,m}\rangle|^2\sum_s\left|\left\langle\Psi_{f,m,s}^{N-1}\middle|\;\Psi_{i,m}^{N-1}\right\rangle\right|^2\delta\left(\hbar\omega - E_{f,kin} - E_b\right), \tag{1.25}$$

where $E_{i,0}^N$ is the total energy of the initial (neutral) electronic system. E_b represents the binding energy, which has been already defined as $E_b \equiv E_{f,m,s}^{N-1} - E_{i,0}^N$, i.e. it is always

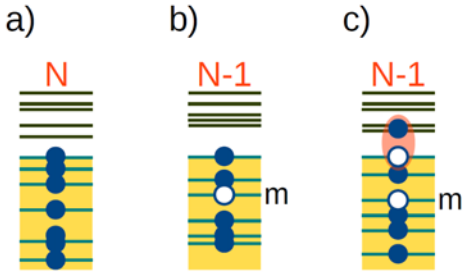

Figure 1.5.: Possible excitations due to photoionization: A N-particle system in its ground state (a) is excited by the ejection of an electron in state m. The subgroup $\Psi^{N-1}_{f,m,0}$ of excitations which corresponds to the pure ionization of orbitals m and the subsequent adiabatic relaxation of the energy levels is depicted in (b). Such a group corresponds to a quasiparticle peak and is characterized by the fact that the occupation of the remaining levels remains unchanged. For $\Psi^{N-1}_{f,m,s}$ with $s \neq 0$, additional satellite peaks occur, where due to the ionization of the orbital m, diverse neutral excitations such as electron-hole pairs are induced (c). Electrons are depicted in blue, holes in white.

positive. As already pointed out, contributions originate from the pure ionization of orbitals m and the subsequent relaxation of the electronic system. Furthermore, each of these peaks is accompanied by so-called satellite peaks corresponding to the creation of neutral excitations as a consequence of the removal of an electron in state m (see Fig. 1.5). This will be discussed in detail in the subsequent sections.

At this point, it is convenient to introduce the spectral function A, defined as follows:

$$A_m(\omega) \equiv \sum_s \left| \left\langle \Psi^{N-1}_{f,m,s} \right| \Psi^{N-1}_{i,m} \right\rangle \Big|^2 \delta(\hbar\omega - E_b).$$

Here, concerning energy conservation, the limit of excitations with $E_{kin} = 0$ is considered, i.e. the onset of absorption. In second quantization, the matrix element between the initial and the final electronic system can be elegantly formulated by means of the operators $\hat{c}^\dagger_m$ and $\hat{c}_m$, which create/annihilate an electron in state m. This results in:

$$\begin{aligned} A_m(\omega) &= \textstyle\sum_s |\langle N-1, m, s| \hat{c}_m |N, 0\rangle|^2 \, \delta(\hbar\omega - E_b) \\ &= \textstyle\sum_s \langle N, 0| \hat{c}^\dagger_m |N-1, m, s\rangle \langle N-1, m, s| \hat{c}_m |N, 0\rangle \, \delta(\hbar\omega - E_b) \\ &= \textstyle\sum_s g^*_{m,s} g_{m,s} \, \delta(\hbar\omega - |\varepsilon_{m,s}|), \end{aligned} \tag{1.26}$$

where we encounter the Lehmann amplitudes $g_{m,s}$ in an orbital index representation and the Lehmann excitation energies $\varepsilon_{m,s} \equiv E^N_{i,0} - E^{N-1}_{f,m,s}$ corresponding to the negative value of the binding energy.

The spectral function in MBPT The spectral function A denotes a mathematical tool that connects theory and experimental observables. Moreover, its definition involving Lehmann amplitudes and excitation energies illustrates that A is directly related to MBPT through the one-particle Green's function. Provided that A is a real matrix, which is the case for stationary Hamiltonians containing no magnetic fields, it can be shown that it is proportional

to the imaginary part of the Green's function [90]:

$$A(\mathbf{r},\mathbf{r}',\omega) \equiv -\frac{1}{\pi}\,\Im\left[G^T(\mathbf{r},\mathbf{r}',\omega)\right]\,\mathrm{sgn}\left(\omega-\mu\right),$$

where μ represents the chemical potential. The other way around, one can also express the Green's function G in terms of A, yielding its so-called spectral representation:

$$G^T(\mathbf{r},\mathbf{r}',\omega) = \int_{-\infty}^{\infty} d\omega'\,\frac{A(\mathbf{r},\mathbf{r}',\omega')}{\omega-\omega'+i\eta\,\mathrm{sgn}\left(\omega'-\mu\right)}.$$

Here, A is introduced as position resolved function by replacing the creation $\hat{c}_m^\dagger$ and annihilation operators $\hat{c}_m$ in equation (1.26) by field operators $\hat{\Phi}^{(\dagger)}(\mathbf{r})$. However, any basis can be chosen for A and G without loss of generality.

Important properties of the spectral function can be easily deduced by considering the single-particle Green's function G, expressed in a diagonal single-particle Hartree basis (1.24):

$$G_{ii}^T(\omega) = \frac{1}{\omega-\varepsilon_i^0-\Sigma_{ii}\left(\omega\right)}.$$

In the case of non-interacting particles in an effective Hartree potential V_H, one finds:

$$G_{0,ii}^T(\omega) = \frac{1}{\omega-\varepsilon_i^0\pm i\eta}.$$

Using the Dirac identity,

$$\lim_{\eta\to 0^+}\Im\left(\frac{1}{x+i\eta}\right) = \lim_{\eta\to 0^+}\left(-\frac{\eta}{x^2+\eta^2}\right) = -\pi\delta(x)$$

for $x\in\mathbb{R}$, we find for the spectral function:

$$A_{0,ii}(\omega) = \delta\left(\omega-\varepsilon_i^0\right).$$

In the non-interacting case, the spectral function thus consists of δ-peaks at the Hartree energies ε_i^0. Since we used the time-ordered Green's function for the derivation, A is generalized compared to equation (1.26) and accounts both for the ejection ($\varepsilon_i^0<\mu$) and the insertion ($\varepsilon_i^0>\mu$) of an electron to the system. For the interacting case, A becomes more difficult to evaluate due to the non-local, non-Hermitian and frequency dependent nature of the self-energy Σ:

$$A_{ii}(\omega) = \frac{1}{\pi}\frac{\Im\left\{\Sigma_{ii}\left(\omega\right)\right\}}{\left[\omega-\varepsilon_i^0-\Re\left\{\Sigma_{ii}\left(\omega\right)\right\}\right]^2+\left[\Im\left\{\Sigma_{ii}\left(\omega\right)\right\}\right]^2}.$$

Due to the frequency-dependent self-energy, it is difficult to make predictions of photoemission spectra from the above formula. However, in general, one can distinguish between at least two kinds of excitations. When slowly turning on interactions in the system, the former δ-peaks in A are shifted from $\left(\omega=\varepsilon_i^0\right)$ to $\left(\omega=\varepsilon_i^0+\Re\left\{\Sigma_{ii}\left(\omega\right)\right\}\right)$. Moreover, they broaden to

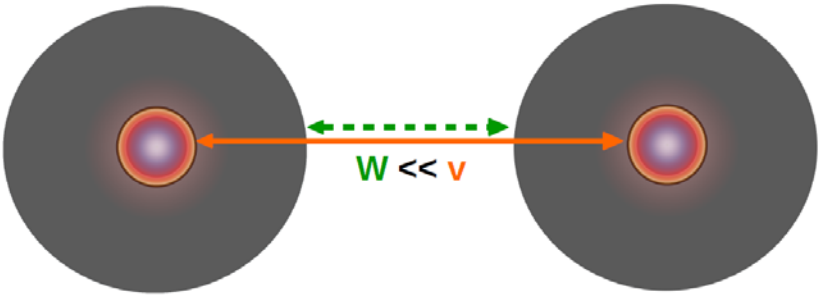

Figure 1.6.: The quasiparticle picture: the many-body system is approximated by replacing the bare Coulomb interaction v between electrons by quasiparticles that interact through the weaker screened Coulomb potential W. The quasiparticles represent bare particles (purple) surrounded by an inversely charged cloud (grayish), accounting for all kinds of many-body interactions.

Lorentzian functions, whose full width at half maximum (FWHM) is proportional to $\Im\{\Sigma_{ii}\}$. These peaks, which are in close correspondence to the original non-interacting peaks, are attributed to so-called quasiparticle excitations, whose lifetime is inversely proportional to the peak width. This point will be discussed in detail below. In addition, satellite peaks occur in the spectrum. The latter are caused by excitations, where due to the creation of a photohole different kinds of neutral excitations such as plasmons, spin waves, phonons or electron-hole pairs are provoked. These elementary excitations related to bosons are usually termed collective excitations. In the following, we treat collective excitations only sketchily and focus on the former case, the quasiparticle excitations.

The quasiparticle picture Quasiparticles are approximate low-lying elementary excitations of macroscopic systems [97]. They are not real particles, but mathematical tools which offer the possibility to describe the motion of particles in an interacting many-body system. Many kinds of different quasiparticles exist, in the following we focus on electron/hole quasiparticles. In this limit, a quasiparticle can be thought of as an electron/hole injected into the system and a surrounding positively/negatively charged cloud, see Fig. (1.6). The latter is formed due to repulsive interactions with the remaining electrons/holes through Coulomb interactions and the Pauli exclusion principle. The many-body problem consequently reduces to a single particle picture, where not a bare electron/hole, but a particle encircled by a screening cloud moves through the system. As a result, two quasiparticles are not interacting via the bare, but via the much weaker screened Coulomb interaction W. Screening is thus supposed to be the main physical effect when adding a particle to a system. It is governed by the inverse of the material specific dielectric function ε:

$$W\left(\mathbf{r},\mathbf{r}',\omega\right) = \int d^3\mathbf{r}''\, v\left(\mathbf{r}''-\mathbf{r}'\right)\varepsilon^{-1}\left(\mathbf{r},\mathbf{r}'',\omega\right) = \int d^3\mathbf{r}''\,\frac{\varepsilon^{-1}\left(\mathbf{r},\mathbf{r}'',\omega\right)}{|\mathbf{r}''-\mathbf{r}'|}.$$

Due to the supposed weak interaction, we assume a one-to-one correspondence of the interacting and the non-interacting system and label quasiparticles by the same quantum numbers $\mathbf{k}$ or σ as their non-interacting counterparts. However, these dressed particles possess a renor-

malized energy ε_{qp} and mass, and a finite life-time τ_k, since they are not eigenstates of the system. In this context, we want to point out that quasiparticle energies, and the quasiparticle picture in general, are mathematical tools, introduced to make the description of the many-body system feasible. The corresponding observables are the already presented excitation energies $\varepsilon_m = E_m^{N+1} - E_0^N$ and $\varepsilon_l = E_0^N - E_l^{N-1}$, as occurring in the Lehmann representation of the Green's function. The connection between quasiparticle and excitation energies is depicted in Fig. (1.7).

Reducing the motion of bare electrons interacting with each other through the bare Coulomb potential v to the picture of weakly interacting quasiparticles denotes an effective way to simplify the many-body problem. However, this approach is not generally valid and it breaks down in strongly correlated materials, where the elementary excitations significantly depend on each other.

The spectral function within the quasiparticle picture Within the quasiparticle picture, the Green's function and hence the spectral function are strongly simplified by supposing weak correlations and thus excitations with a long lifetime τ, i.e. $\Im\{\Sigma_{ii}(\omega)\} \to 0$. Moreover, one is interested in the position of poles at:

$$\omega - \varepsilon_i^0 - \Re\{\Sigma_{ii}(\omega)\} = 0,$$

where ε_i^0 is the mean-field Hartree solution. The energies fulfilling the above relation are labeled quasiparticle (qp) energies:

$$\varepsilon_{qp,i} \equiv \varepsilon_i^0 + \Re\{\Sigma_{ii}(\varepsilon_{qp,i})\}.$$

Instead of accounting for the complete frequency dependence of the self-energy, we limit our considerations on frequencies near the quasiparticle poles and expand the real part of the self-energy around these poles in a Taylor series:

$$\Re\{\Sigma_{ii}(\omega)\} = \Re\{\Sigma_{ii}(\varepsilon_{qp,i})\} + \left.\frac{\partial \Re\{\Sigma_{ii}(\omega)\}}{\partial \omega}\right|_{\omega=\varepsilon_{qp,i}} (\omega - \varepsilon_{qp,i}) + \dots .$$

As it will be detailed in the following and corresponding to Fig. (1.7), this can be interpreted as a "scan" of the spectral function in a narrow frequency window around ε_i^0, where δ-function like excitation peaks are grouped together to a single quasiparticle peak at $\varepsilon_{qp,i}$. That way, broad satellite peak structures, which are farther apart from ε_i^0, are not included. As demonstrated below, the quasiparticle peak has a Lorentzian shape associated with a finite peak width. Inserting the above expansion of the self-energy in the one-particle Green's function G_{ii} yields:

$$\begin{aligned} G_{ii}(\omega) &= Z_{qp} \tfrac{1}{\omega - \varepsilon_i^0 - \Re\{\Sigma_{ii}(\varepsilon_{qp,i})\}} + (1 - Z_{qp})\, G_{inc} \\ &= G_{coh} + (1 - Z_{qp})\, G_{inc}, \end{aligned}$$

where the expansion terms up to linear order are grouped together in the coherent and higher order terms in the incoherent part of the Green's function (see Appendix A.4). The coherent part yields for non-interacting particles ($\Re\{\Sigma_{ii}(\varepsilon_{qp,i})\} \to 0$) poles at the Hartree energies ε_i^0. Therefore, this part can be associated with the creation of a quasiparticle. The introduced factor Z_{qp} is called quasiparticle weight and defined as:

$$Z_{qp} \equiv \left(1 - \left.\frac{\partial \Re\{\Sigma_{ii}(\omega)\}}{\partial \omega}\right|_{\omega=\varepsilon_{qp,i}}\right)^{-1}.$$

For the spectral function, we consequently retrieve a similar decomposition:

$$A_{ii}(\omega) = \frac{1}{\pi} Z_{qp} \frac{\Im\{\Sigma_{ii}(\varepsilon_{qp,i})\}}{\left[\omega - \varepsilon_i^0 - \Re\{\Sigma_{ii}(\varepsilon_{qp,i})\}\right]^2 + \left[\Im\{\Sigma_{ii}(\varepsilon_{qp,i})\}\right]^2} + (1 - Z_{qp}) A_{inc},$$

providing an intuitive physical interpretation of A. In the non-interacting case, the coherent part of A reduces to a δ-function centered at ε_i^0, but for interacting particles it represents a Lorentzian curve centered at the renormalized energy $\varepsilon_{qp} = \varepsilon_i^0 - \Re\{\Sigma_{ii}(\varepsilon_{qp,i})\}$ with a width related to $\Im\{\Sigma_{ii}(\varepsilon_{qp,i})\}$. This can be associated with the creation of a quasiparticle, whose lifetime τ is inversely proportional to the peak width. Thus, the broadening of the curve with respect to the non-interacting particle picture contains information about many-particle interactions. The incoherent part A_{inc} covers satellite excitations, i.e. all kinds of excitations which can not be described within a weakly correlated quasiparticle picture. Since the spectral function has to fulfill the following sum rule [90]:

$$\frac{1}{2\pi} \int d\omega\, A(\omega) = 1,$$

the renormalization factor or quasiparticle weight Z_{qp} is a measure of correlations in the system. Z_{qp} is obtained by integrating the coherent (quasiparticle) part of the spectral function, whereas the weight of the incoherent part is $(1 - Z_{qp})$. Consequently, for non-interacting problems Z_{qp} equals 1. However, in systems, where correlations become important it is diminished and the quasiparticle picture becomes questionable (see Fig. 1.7). Indeed, the quasiparticle concept is only applicable to systems, where quasiparticles have a sufficiently long lifetime, i.e. where little scattering occurs. Fermion systems in which the picture of almost non-interacting quasiparticles holds are called Fermi liquids [90, 97]. Quasiparticles are *approximate* excitations of these systems, only making sense for timescales shorter than the quasiparticle lifetime. Contrary, the incoherent part of A accounts for all interactions which are not describable by a particle and its screening cloud, such as the already mentioned collective excitations. In cases, where the quasiparticle picture breaks down and incoherent contributions become dominant, one has to consider other levels of theory than Fermi liquid theory. Due to the Peierls divergence and charge-spin separation, this is for example the case for $1D$ systems, where one has to pass on to Luttinger liquid theory [90].

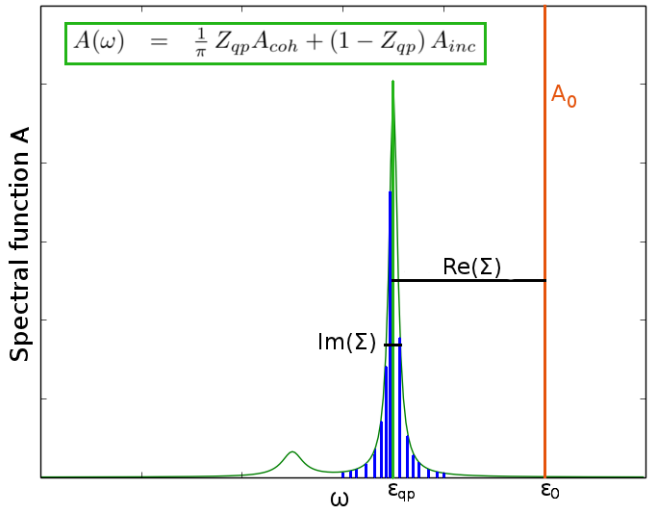

Figure 1.7.: Schematic representation of the spectral function $A(\omega)$: For infinite systems (thermodynamic limit) and finite systems with unresolved energy levels, the real excitation energies (blue) as defined in the Lehmann representation of the Green's function form a continuum and consequently $A(\omega)$ becomes a continuous function (green). Introducing the quasiparticle concept, the spectral function is separated into a coherent and incoherent part. The coherent contribution has Lorentzian shape and is centered at energy ε_{qp} with a FWHM proportional to the imaginary part of the self-energy. It represents a quasiparticle with energy ε_{qp}, whose lifetime is inversely proportional to the peak width. The quasiparticle peak is found shifted (by the real part of the self-energy) from a δ-peak located at the Hartree energy ε_0, which corresponds to the case of non-interacting electrons (orange). Moreover, as a signature of collective excitations, also a satellite peak occurs farther apart from ε_0, which is governed by the incoherent part of the spectral function.

The quasiparticle equation In the following, we restrict our considerations to the quasiparticle case and neglect the incoherent part of A. Instead of directly calculating the poles of A_{coh} or G_{coh} to access quasiparticle energies, it is more convenient to pass by the so-called quasiparticle equation. The latter is obtained by inserting the biorthonormal representation of the Green's function [98] in the equation of motion (EOM) in frequency space (see Appendix A.4). The quasiparticle equation represents one of the central equations of the Green's function approach, since it is the mathematical foundation of the above introduced quasiparticle concept:

$$H_0(\mathbf{r})\,\psi_\nu^{qp}(\mathbf{r}) + \int d\mathbf{r}''\,\Sigma\left(\mathbf{r},\mathbf{r}'',\varepsilon_{qp}\right)\psi_\nu^{qp}\left(\mathbf{r}''\right) = \varepsilon_{qp}\psi_\nu^{qp}(\mathbf{r})\,. \tag{1.27}$$

Equation (1.27) determines the quasiparticle energies ε_{qp} and the quasiparticle wave functions ψ_ν^{qp}. Contrary to the real excitation energies occurring in the Lehmann representation of the Green's function, the quasiparticle energies ε_{qp} are complex, demonstrating the finite lifetime of the excitations. At first sight, equation (1.27) strongly resembles the Hartree, Hartree-Fock or DFT-KS eigenvalue equations. However, instead of local mean-field and instantaneous potentials, all interactions beyond Hartree are governed by the non-local and energy-dependent self-energy. Since the equations depend, through the self-energy, on the

state on which they are applied, the eigenvalue problem is non-linear. Nevertheless, important conclusions can be drawn with respect to the introduced mean-field equations. Comparing the latter to the quasiparticle equation strictly derived within a Green's functions approach, the effective fields in Hartree, HF and $DFT\text{-}KS$ can be interpreted as approximate self-energies of different level of theory. By way of example, the $DFT\text{-}KS$ exchange-correlation functional can be regarded as a (semi)local and energy-independent self-energy neglecting life-time effects. In this spirit, the often good quantitative agreement of $DFT\text{-}KS$ band structures with experimental dispersion relations seems plausible.

In order to find a practical solution to the quasiparticle equation, further approximations are inevitable. The main difference between the introduced mean-field approaches and the quasiparticle formalism is supposed to manifest in differing eigenenergies, whereas the effect on the wave functions is said to be small [55]. Therefore, as a starting point, one assumes that HF or $DFT\text{-}KS$ wave functions are almost identical to the unknown quasiparticle wave functions $\psi_\nu^{qp} \approx \psi_\nu^{HF} \approx \psi_\nu^{KS}$ and one diagonalizes equation (1.27) for example in a Kohn-Sham basis:

$$\varepsilon_{qp,\nu} = \left\langle \psi_\nu^{KS} \right| \hat{H}_0 \left| \psi_\nu^{KS} \right\rangle + \left\langle \psi_\nu^{KS} \right| \Sigma\left(\varepsilon_{qp,\nu}\right) \left| \psi_\nu^{KS} \right\rangle .$$

In this case, H_0 is chosen to be the Kohn-Sham Hamiltonian,

$$\hat{H}_0 \equiv \hat{H}^{KS} = -\frac{1}{2}\nabla^2 + \hat{V}_{ext} + \hat{V}_H + \hat{V}_{xc}.$$

Consequently, the already covered effects in the exchange-correlation functional have to be removed from the self-energy in order to avoid a double counting:

$$\varepsilon_{qp,\nu} = \left\langle \psi_\nu^{KS} \right| \hat{H}^{KS} \left| \psi_\nu^{KS} \right\rangle + \left\langle \psi_\nu^{KS} \right| \Sigma\left(\varepsilon_{qp,\nu}\right) - \hat{V}_{xc} \left| \psi_\nu^{KS} \right\rangle .$$

The quasiparticle energy ε_{qp} is thus obtained in first-order perturbation theory from Kohn-Sham eigenvalues and wave functions following:

$$\varepsilon_{qp,\nu} = \varepsilon_\nu^{KS} + \left\langle \psi_\nu^{KS} \right| \Sigma\left(\varepsilon_{qp,\nu}\right) - V_{xc} \left| \psi_\nu^{KS} \right\rangle . \tag{1.28}$$

In order to circumvent the state-dependence of the above equation, the self-energy can be expanded up to linear order in a Taylor series around the known Kohn-Sham eigenvalues (see Appendix A.4). This yields:

$$\varepsilon_{qp,\nu} \approx \varepsilon_\nu^{KS} + Z_\nu^{KS} \left\langle \psi_\nu^{KS} \right| \Sigma\left(\varepsilon_\nu^{KS}\right) - V_{xc} \left| \psi_\nu^{KS} \right\rangle , \tag{1.29}$$

where Z_ν^{KS} is a renormalization factor:

$$Z_\nu^{KS} = \left[1 - \left. \frac{\partial \Sigma_{\nu\nu}\left(\omega\right)}{\partial \omega} \right|_{\omega = \varepsilon_\nu^{KS}} \right]^{-1} \text{ with } \Sigma_{\nu\nu}\left(\omega\right) = \left\langle \psi_\nu^{KS} \left| \Sigma\left(\omega\right) \right| \psi_\nu^{KS} \right\rangle .$$

Provided that the chosen linear approximation is valid, Z^{KS} should be very similar to the introduced quasiparticle weight Z_{qp}, i.e. the first derivatives $(\partial\Sigma_{\nu\nu}/\partial\omega)$ at ε_ν^{KS} and ε_ν^{qp} are

assumed to be of the same order. As a result, equation (1.28) no longer depends on the quasiparticle energy, but on the known *DFT-KS* energies. One has to keep in mind that the demonstrated approach is only valid if the *DFT-KS* wave functions are close to the true quasiparticle wave functions. The validity of this assumption will be discussed in detail in subsequent chapters. Finally, the last missing ingredient in equation (1.29) is the self-energy $\Sigma\left(\varepsilon_\nu^{KS}\right)$. Containing all many-body effects beyond Hartree, the latter is a highly complex quantity still to be determined.

1.4. Hedin's equations

Linear response theory In principle, the self-energy can be obtained by self-consistently solving a cycle of integro-differential equations. Before going into that, it is necessary to introduce several auxiliary quantities. In order to connect experiment and theory, it is very interesting to study the system's reaction in equilibrium to a small external disturbance $\hat{H}'$ applied at a certain time t_0. In terms of the Hamiltonian, the system is governed by an equilibrium and a perturbation part:

$$\hat{H} = \hat{H}_0 + \hat{H}'.$$

Provided that the applied external potential is weak, the response of the system linearly depends on it. Within this so-called linear response regime, the system's reaction in terms of the expectation value of any operator $\hat{O}$ is governed by response/correlation functions C:

$$\left\langle \hat{O}\left(t\right)\right\rangle = \left\langle \hat{O}\right\rangle_0 - i\int_{t_0}^{\infty} dt'\, C\left(t-t'\right), \tag{1.30}$$

with

$$C\left(t-t'\right) = -i\left\langle \left[\hat{O}\left(t\right), \hat{H}'\left(t'\right)\right]\right\rangle_0 \Theta\left(t-t'\right).$$

Equation (1.30) is known as the general Kubo formula [90]. It denotes an important relation, since it connects out-of-equilibrium quantities $\left\langle \hat{O}\left(t\right)\right\rangle$ to equilibrium averages represented by $\langle \ldots \rangle_0$. The step function ensures that C is a retarded quantity, i.e. respects causality. Strictly speaking, only retarded response functions are physically meaningful and can be compared to experiment, however, for mathematical reasons, we are going to work with time-ordered quantities only in the following.

In the case of PES or optical absorption experiments, the incoming light represents an external electromagnetic perturbation causing charge redistributions and thus a polarization of the system. In addition to the applied perturbative potential $\hat{U}_{ext}$, one also has to take into account the potential created by the induced charge density n_{ind}. Therefore, the total field sums up to:

$$\hat{V}_{tot} = \hat{U}_{ext} + \hat{V}_{ind},$$

where the induced potential denotes an induced Hartree potential [90]:

$$V_{ind}\left(\mathbf{r}\right)=\int d\mathbf{r}'\,v\left(\mathbf{r}-\mathbf{r}'\right)n_{ind}\left(\mathbf{r}'\right). \tag{1.31}$$

It is important not to confound the applied time-dependent potential $\hat{U}_{ext}$ with the static potential $\hat{V}_{ext}$, accounting for the core ion potential. The relation between the total and the external potential defines the inverse of the dielectric function ε^{-1}, which is a measure for the polarizability of the system:

$$V_{tot}\left(1\right)=\int d2\,\varepsilon^{-1}\left(1,2\right)U_{ext}\left(2\right).$$

We already encountered ε^{-1} for the definition of the screened Coulomb potential W:

$$W\left(1,2\right)=\int d3\,\epsilon^{-1}(13)\,v(32),$$

which characterizes how strongly a bare charge is screened. Assuming linear response theory and a perturbation of $\hat{H}'=\int d\mathbf{r}\,\hat{n}\left(\mathbf{r}\right)U_{ext}\left(\mathbf{r},t\right)$, the induced charge density, $\langle\hat{n}\left(1\right)\rangle\equiv n_{ind}\left(1\right)$, can be readily determined from the Kubo formula:

$$n_{ind}\left(1\right)=\int d3\,\chi(1,3)U_{ext}(3). \tag{1.32}$$

Here, we assumed that the equilibrium system is charge neutral, i.e. $\langle\hat{n}\left(1\right)\rangle_0=0$. This introduces the corresponding response function, the reducible polarizability χ:

$$\chi^{R}\left(\mathbf{r}t,\mathbf{r}'t'\right)=-i\left\langle N,0\right|\left[\hat{n}\left(\mathbf{r}t\right),\hat{n}\left(\mathbf{r}'t'\right)\right]\left|N,0\right\rangle\Theta\left(t-t'\right).$$

The latter is a retarded quantity and represents a density-density correlation function. Its time-ordered analogue, which is used in the following, reads:

$$\chi^{T}\left(\mathbf{r}t,\mathbf{r}'t'\right)=-i\left\langle N,0\right|T\left[\hat{n}\left(\mathbf{r}t\right),\hat{n}\left(\mathbf{r}'t'\right)\right]\left|N,0\right\rangle.$$

χ can also be expressed as derivative of the induced density with respect to the external perturbing potential $\hat{U}_{ext}$:

$$\frac{\partial n_{ind}\left(1\right)}{\partial U_{ext}(2)}=\int d3\,\underbrace{\frac{\partial\chi(1,3)}{\partial U_{ext}(2)}}_{0}U_{ext}(3)+\int d3\,\chi(1,3)\underbrace{\frac{\partial U_{ext}(3)}{\partial U_{ext}(2)}}_{\delta(2,3)}$$

$$\rightarrow\chi(1,2)\equiv\frac{\partial n_{ind}\left(1\right)}{\partial U_{ext}(2)}. \tag{1.33}$$

It is a non-local quantity, since in an interacting system a perturbation at (1) can induce modifications at (2). A related response function is the irreducible polarizability P which

gives the change in the density with respect to the total potential V_{tot}:

$$P(1,2) \equiv \frac{\partial n_{ind}(1)}{\partial V_{tot}(2)}. \tag{1.34}$$

P accounts for the fact that the application of an external field not only affects the electron density, but consequently also induces an additional Hartree potential. It is closely related to the reducible polarizability through a Dyson-like equation:

$$\chi(1,2) = P(1,2) + \int d34\, P(1,3) v(3,4)\, \chi(4,2) \tag{1.35}$$

and represents the irreducible part with respect to the bare Coulomb potential v, singled out from χ.

Hedin's equations As already discussed before, screening is supposed to be the main physical effect of the system's reaction to an additional charge. Hedin's approach consists of expanding the self-energy in terms of the screened Coulomb potential W, while supposing that Σ is a functional of the single-particle Green's function G. That way, the problem is assumed to converge much faster as compared to expansions in the bare Coulomb potential v and eventually only very few expansion terms have to be considered. The expansion in W can be derived following Schwinger's functional derivative approach [99, 100], where a small time-varying external perturbation U_{ext} is first introduced as mathematical tool and then set to zero, as soon as the self-energy is obtained. In the course of the derivation, one last quantity is needed in addition to the ones introduced above, the so-called irreducible vertex function Γ:

$$\Gamma(1,2;3) \equiv -\frac{\partial G^{-1}(1,2)}{\partial V_{tot}(3)}.$$

As detailed in Appendix A.3, the outcome of the derivation is that the self-energy Σ, the single-particle Green's function G, the irreducible vertex function Γ, the irreducible polarizability P and the screened Coulomb potential W are closely related to each other. They form Hedin's equations, an exact closed set of five integro-differential equations [1]:

$$\begin{aligned}
\Sigma(1,2) &= i \int d34\, G(1,3)\, \Gamma(3,2;4)\, W(1,4) \\
G(1,2) &= G_0(1,2) + \int d34\, G_0(1,3)\, \Sigma(3,4)\, G(4,2) \\
\Gamma(1,2;3) &= \delta(1,2)\, \delta(2,3) + \int d4567\, \frac{\delta\Sigma(1,2)}{\delta G(4,5)}\, G(4,6)\, \Gamma(6,7;3)\, G(7,5) \\
P(1,2) &= -i \int d34\, G(1,3)\, \Gamma(3,4;2)\, G(4,1) \\
W(1,2) &= v(1,2) + \int d34\, v(1,3)\, P(3,4)\, W(4,2).
\end{aligned}$$

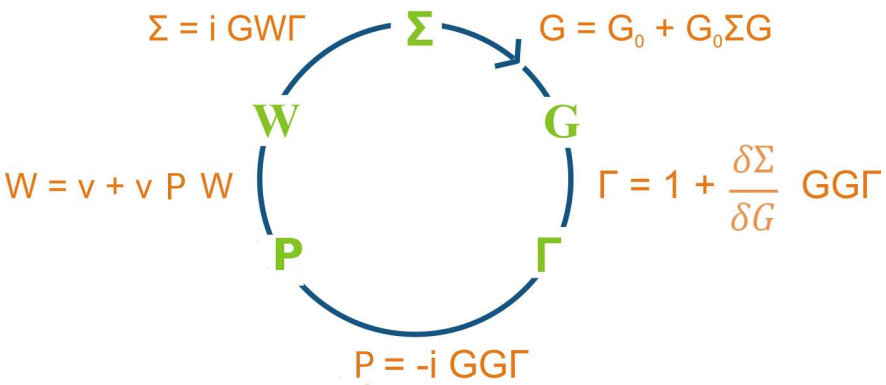

Figure 1.8.: Hedin's self-consistent calculation scheme of the self-energy Σ: Starting with an initial guess for the single-particle Green's function, the irreducible vertex correction Γ can be calculated. Γ is in turn used to obtain the irreducible polarizability P. The latter leads to an expression for W and finally to the self-energy Σ. This cycle has to be repeated until convergency is reached. For the sake of simplicity, a short notation is used neglecting the explicit notation of integrals.

These equations generate a perturbation series in the screened Coulomb potential W for the self-energy, following:

$$\Sigma = GW + GWGWG + \dots ,$$

where a symbolical notation is used. They can be related to important physical processes. As already discussed in detail, the single-particle Green's function G describes the propagation of a quasiparticle, whereas the screened Coulomb potential W is a measure for the weak interaction between quasiparticles. W can also be expressed in terms of the reducible polarizability χ as follows:

$$W(1,2) = v(1,2) + \int d34\, v(1,3)\, \chi(3,4)\, v(4,2).$$

The irreducible polarizability P contains the system's response to an added charge in terms of charge accumulations or depletions in certain regions and finally the irreducible vertex function Γ introduces information how electrons (charge accumulations) and holes (charge depletions) interact. In principle, the self-energy can be determined exactly from these equations through a self-consistent cycle with respect to G as depicted in Fig. (1.8). However, Hedin's equations denote a set of demanding integro-differential equations and truncations of the series are inevitable to make the problem computationally feasible.

1.5. The GW approximation

For real systems, an exact self-consistent determination of the self-energy Σ is not in reach and suited approximations have to be made. Unfortunately, a controlled and convergent perturbative treatment based on a small parameter has not been developed yet. Therefore, it is indispensable to exigently test the chosen simplifications to the Hedin's equations.

The simplest approximation is to neglect the second term in Γ, a three-body contribution,

and to suppose that the vertex function is diagonal in space and time:

$$\Gamma^{GW}(1,2;3) \equiv \delta(1,2)\,\delta(2,3)\,.$$

This assumption significantly simplifies Hedin's equations (see Fig. 1.9):

$$\begin{aligned}
\Sigma^{GW}(1,2) &= i\,G(1,2)\,W(1,2) \\
G(1,2) &= G_0(1,2) + \int d34\,G_0(1,3)\,\Sigma^{GW}(3,4)\,G(4,2) \\
\Gamma^{GW}(1,2;3) &= \delta(1,2)\,\delta(2,3) \\
P^{GW}(1,2) &= -i\,G(1,2)\,G(2,1) \\
W(1,2) &= v(1,2) + \int d34\,v(1,3)\,P^{GW}(3,4)\,W(4,2),
\end{aligned}$$

where the self-energy is taken to first order in the perturbation W. Both the self-energy Σ and the irreducible polarizability P reduce to convolution products when Fourier transformed into frequency space:

$$\begin{aligned}
P^{GW}(\mathbf{r},\mathbf{r}',\omega) &= -\tfrac{i}{2\pi}\int_{-\infty}^{\infty} d\omega'\,G(\mathbf{r},\mathbf{r}',\omega+\omega')\,G(\mathbf{r},\mathbf{r}',\omega'), \\
\Sigma^{GW}(\mathbf{r},\mathbf{r}',\omega) &= \tfrac{i}{2\pi}\int_{-\infty}^{\infty} d\omega'\,e^{i\omega'\eta}G(\mathbf{r},\mathbf{r}',\omega-\omega')\,W(\mathbf{r},\mathbf{r}',\omega').
\end{aligned}$$

Since the screened Coulomb potential is a symmetric function of the frequency ω' (see equation 1.36), the self-energy can equivalently be expressed as:

$$\Sigma^{GW}(\mathbf{r},\mathbf{r}',\omega) = \frac{i}{2\pi}\int_{-\infty}^{\infty} d\omega'\,e^{i\omega'\eta}G(\mathbf{r},\mathbf{r}',\omega+\omega')\,W(\mathbf{r},\mathbf{r}',\omega').$$

The factor $e^{i\eta\omega'}$ with $\eta \to 0^+$ enters to ensure convergency. The GW approximation [4, 5, 9, 91] is not a "rigorous" approach in terms of perturbation theory, but its validity range is much larger than one could expect. That will be pointed out in subsequent chapters, where we will see that GW gives significantly improved results for excitation energies compared to Hartree-Fock or DFT-KS, yielding a good agreement with experiment. As a hand wave justification, it seems physically sound to express Σ in terms of the dynamically screened potential W. That way, energy-dependent correlations are included, which are not present in simple one-particle approaches based on mean-fields of the bare (static) Coulomb potential. One thus relies on the assumption that interactions are covered to a large amount by W. However, due to their screened nature, the system almost behaves like a non-interacting system and W is assumed to be small, justifying the use of the lowest order approximation $\Sigma = iGW$. From a practical point of view, the GW approximation opens the way to calculate quasiparticle energies from first principles for real-size systems.

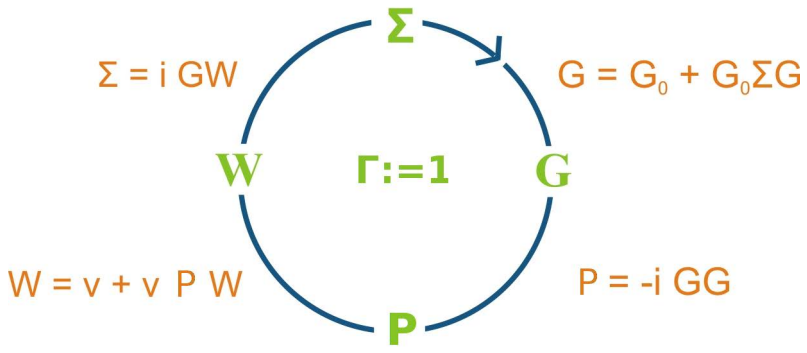

Figure 1.9.: Self-consistent calculation scheme of the self-energy Σ within the GW approximation: due to the neglect of vertex corrections, both the self-energy Σ and the irreducible polarizability P reduce to simple convolution products. Analogue to Hedin's equations, a self-consistent scheme with respect to G can be carried out to calculate Σ, however, with significantly simplified equations. For the sake of simplicity, a short notation is used neglecting the explicit notation of integrals.

1.6. Separation of the GW self-energy

The GW approximation allows to recast the self-energy in a form, where physical conclusions can be easily drawn and where it becomes clear which approximations are meaningful [5, 55]. First, we shortly demonstrate the separation of the self-energy into an energy-dependent correlation and a bare exchange part. Later in this section, we present the COHSEX formulation, where the self-energy is separated into a so-called Coulomb-hole (COH) and a screened exchange (SEX) contribution.

1.6.1. Separation of the self-energy in Fock exchange and correlation

The self-energy Σ, taken within the GW approach, can be split into a static non-local Fock exchange operator Σ^x and an energy-dependent correlation term Σ^c accounting for screening effects:

$$\Sigma^{GW}\left(\mathbf{r},\mathbf{r}',\omega\right) = \frac{i}{2\pi}\int d\omega'\, e^{i\eta\omega'} G(\mathbf{r},\mathbf{r}',\omega')\, W(\mathbf{r},\mathbf{r}',\omega-\omega') \equiv \Sigma^x + \Sigma^c.$$

In order to arrive at this separation, the screened Coulomb potential is, analogue to the Green's function, expressed in its Lehmann representation, i.e. in terms of fluctuation potentials V_m [9]:

$$\begin{aligned} W\left(\mathbf{r},\mathbf{r}',\omega\right) &= \int d^3\mathbf{r}''\, v\left(\mathbf{r}'',\mathbf{r}'\right)\varepsilon^{-1}\left(\mathbf{r},\mathbf{r}'',\omega\right) = v\left(\mathbf{r},\mathbf{r}'\right) + \textstyle\sum_m \frac{2\omega_m V_m(\mathbf{r}) V_m^*(\mathbf{r}')}{\omega^2-\omega_m^2}, \\ V_m\left(\mathbf{r}\right) &= \int d^3\mathbf{r}'\, v\left(\mathbf{r},\mathbf{r}'\right)\langle N,m|\,\hat{n}\left(\mathbf{r}'\right)|N,0\rangle\,. \end{aligned} \tag{1.36}$$

The poles of the screened Coulomb potential are introduced as $(\omega_m = E_{N,m} - E_{N,0} - i\eta)$, where E_N denote total energies of the N-particle system. The latter correspond to neutral excitation energies, such as plasmon or electron-hole pair excitations induced by some external

perturbation. For the self-energy, this leads to:

$$\Sigma^{GW}\left(\mathbf{r},\mathbf{r}',\omega\right)=\frac{i}{2\pi}v\left(\mathbf{r},\mathbf{r}'\right)\int d\omega'\,e^{i\eta\omega'}G(\mathbf{r},\mathbf{r}',\omega')+\frac{i}{2\pi}\int d\omega'\,e^{i\eta\omega'}G(\mathbf{r},\mathbf{r}',\omega')\tilde{W}\left(\mathbf{r},\mathbf{r}',\omega-\omega'\right),$$

where we defined $\tilde{W}\equiv\left[W\left(1,2\right)-v\left(1,2\right)\right]$. As it is demonstrated in Appendix A.6, assuming a non-interacting Green's function G_0, the first part, i.e. the exchange operator Σ^x, reduces to the Fock exchange:

$$\left\langle\phi_{k,0}\right|\Sigma^{x}\left|\phi_{k,0}\right\rangle=-\sum_{n}^{occ}\int d\mathbf{r}d\mathbf{r}'\,\frac{\phi_{k,0}\left(\mathbf{r}\right)\phi_{n,0}\left(\mathbf{r}'\right)\phi_{k,0}^{*}\left(\mathbf{r}'\right)\phi_{n,0}^{*}\left(\mathbf{r}\right)}{\left|\mathbf{r}-\mathbf{r}'\right|}. \tag{1.37}$$

Using again the non-interacting Green's function G_0, the second part of the self-energy can be analytically integrated by means of contour deformation techniques, yielding:

$$\Sigma^{c}\left(\mathbf{r},\mathbf{r}',\omega\right)=\sum_{i}\sum_{m\neq0}\frac{V_m\left(\mathbf{r}\right)V_m^{*}\left(\mathbf{r}'\right)\phi_{i,0}\left(\mathbf{r}\right)\phi_{i,0}^{*}\left(\mathbf{r}'\right)}{\omega+\omega_m-\varepsilon_{i,0}}+\sum_{j}\sum_{m\neq0}\frac{V_m\left(\mathbf{r}\right)V_m^{*}\left(\mathbf{r}'\right)\phi_{j,0}\left(\mathbf{r}\right)\phi_{j,0}^{*}\left(\mathbf{r}'\right)}{\omega-\omega_m-\varepsilon_{j,0}},$$

where the index i labels occupied and j unoccupied states. Taking the expectation value of Σ^c with respect to the same one-particle basis and considering diagonal elements only results in:

$$\left\langle k\right|\Sigma^{c}\left(\omega\right)\left|k\right\rangle=\sum_{i}\sum_{m\neq0}\frac{\left|\left\langle k\right|V_m\left|i\right\rangle\right|^{2}}{\omega+\omega_m-\varepsilon_{i,0}}+\sum_{j}\sum_{m\neq0}\frac{\left|\left\langle k\right|V_m\left|i\right\rangle\right|^{2}}{\omega-\omega_m-\varepsilon_{j,0}}. \tag{1.38}$$

Finally, the quasiparticle energy can be evaluated within a Hartree-Fock basis ($\{\phi_{i,0}\}\equiv\{\phi_{i,HF}\}$, $\varepsilon_{i,0}\equiv\varepsilon_{i,HF}$) analogue to equation (1.29) as follows:

$$\begin{aligned}\varepsilon_{qp,k} &\approx \left\langle\psi_k^{HF}\right|h_0+V_H+\Sigma^{x}\left|\psi_k^{HF}\right\rangle+Z_k^{HF}\,\left\langle\psi_k^{HF}\right|\Sigma^{c}\left(\varepsilon_{k,HF}\right)\left|\psi_k^{HF}\right\rangle\\ &= \varepsilon_k^{HF}+Z_k^{HF}\,\left\langle\psi_k^{HF}\right|\Sigma^{c}\left(\varepsilon_{k,HF}\right)\left|\psi_k^{HF}\right\rangle.\end{aligned}$$

From the above equation and equation (1.38), the effect of interactions beyond Hartree-Fock on the quasiparticle energy is obvious. Calculating the expectation value for an electron in the highest valence band, $\left\langle vb\right|\Sigma^{c}\left(\varepsilon_{vb,HF}\right)\left|vb\right\rangle$, the sum over unoccupied states provides only a small contribution, whereas the major part stems from the sum over occupied states. In the case of small intra-spacings between occupied/unoccupied states, the neutral excitation energy ω_m, which is on the scale of the Hartree-Fock gap, is much larger than the difference $\left|\varepsilon_{vb,HF}-\varepsilon_{i,HF}\right|$. Consequently, we obtain a positive contribution to the quasiparticle energy, i.e. the highest valence band is shifted upwards in energy with respect to the Hartree-Fock value. Analyzing the expectation value for the lowest conduction band, $\left\langle cb\right|\Sigma^{c}\left(\varepsilon_{cb,HF}\right)\left|cb\right\rangle$, we find that a large negative contribution originates from the sum over unoccupied states, shifting the lowest conduction band down in energy. This explains the systematic overestimation of the gap within Hartree-Fock and elucidates that energy-dependent correlations within *GW* tend to close the bare exchange gap.

1.6.2. The COHSEX reformulation of the self-energy

Another way of reformulating the self-energy Σ within the GW approximation is the COHSEX formulation, i.e. the separation of Σ^{GW} into two terms, the Coulomb-hole (COH) and screened exchange (SEX) contribution: $\Sigma^{GW} = \Sigma^{COH} + \Sigma^{SEX}$. Since COHSEX calculations on molecules will be discussed later in this chapter, we briefly introduce the relevant terminology. In order to arrive at the COHSEX formulation, the frequency integral of the self-energy,

$$\Sigma(\mathbf{r}, \mathbf{r}', E) = \frac{i}{2\pi} \int_{-\infty}^{\infty} d\omega \, e^{i\eta\omega} G(\mathbf{r}, \mathbf{r}', E+\omega) W\left(\mathbf{r}, \mathbf{r}', \omega\right), \tag{1.39}$$

is evaluated in terms of contour deformation techniques. The derivation is tedious and can be found in the Appendix A.5. It can be obtained upon inserting the time-ordered single-particle Green's function G in its Lehmann representation and the screened Coulomb potential in terms of fluctuation potentials V_m in equation (1.39):

$$\begin{aligned} G^T(\mathbf{r}, \mathbf{r}', \omega) &= \textstyle\sum_l \frac{\phi_l^*(\mathbf{r})\phi_l(\mathbf{r}')}{\omega - \varepsilon_l + i\eta \,\mathrm{sgn}(\mu - \varepsilon_l)}, \\ W\left(\mathbf{r}, \mathbf{r}', \omega\right) &= v\left(\mathbf{r}, \mathbf{r}'\right) + \textstyle\sum_m \frac{2\omega_m V_m(\mathbf{r}) V_m^*(\mathbf{r}')}{\omega^2 - \omega_m^2}, \end{aligned}$$

where $(\omega_m = E_{N,m} - E_{N,0} - i\eta)$ are neutral excitation energies. ϕ_l and ε_l should be actually Lehmann amplitudes and excitation energies, however, without loss of generality in the COHSEX derivation, single-particle wave functions and eigenvalues as obtained from HF or DFT can be equally used. The outcome of the derivation is that the GW self-energy can be split into two terms, where the screened exchange contribution reads:

$$\Sigma^{SEX}\left(\mathbf{r}, \mathbf{r}', \omega\right) = -\sum_{l}^{occ} \phi_l^*\left(\mathbf{r}'\right) \phi_l\left(\mathbf{r}\right) \, W\left(\mathbf{r}, \mathbf{r}', \omega - \varepsilon_l\right). \tag{1.40}$$

Its main ingredient is the screened Coulomb potential W, shifted by the poles of the Green's function for occupied states ε_l. Comparing Σ^{SEX} to the bare exchange operator Σ^x in equation (1.37) illustrates that Σ^{SEX} represents a screened exchange interaction depending on the energy of the particular state. The Coulomb hole contribution reads:

$$\Sigma^{COH}\left(\mathbf{r}, \mathbf{r}', \omega\right) = \textstyle\sum_{m,l} \phi_l^*\left(\mathbf{r}\right) \phi_l\left(\mathbf{r}'\right) \frac{V_m(\mathbf{r}) V_m^*(\mathbf{r}')}{\omega - \varepsilon_l + \omega_m}. \tag{1.41}$$

1.6.3. The *static* COHSEX approximation

In general, the separation of the self-energy in Σ^{COH} and Σ^{SEX} is exact, representing an ideal starting point for approximations. Within the so-called static COHSEX approximation, one assumes that the interaction via the screened exchange interaction W is constant. Instead of a frequency dependent screened Coulomb potential, we consider W for $(\omega - \varepsilon_l) = 0$ only. This corresponds to the response of a system to a weak *static* external potential, where the ground state density is reorganized due to the modified total potential, however, where the

system is not excited. This seems a plausible approximation for both the low-frequency and the high-frequency limit, where the system density can not follow the rapid perturbation. Within the static limit, the screened exchange contribution reads:

$$\Sigma^{\mathrm{SEX}}_{static}\left(\mathbf{r},\mathbf{r}',0\right)=-\sum_{l}^{occ}\phi_l\left(\mathbf{r}\right)\phi_l^*\left(\mathbf{r}'\right)W\left(\mathbf{r},\mathbf{r}',0\right),$$

while the Coulomb hole term becomes:

$$\Sigma^{\mathrm{COH}}_{static}\left(\mathbf{r},\mathbf{r}',0\right)=\frac{1}{2}\delta\left(\mathbf{r}-\mathbf{r}'\right)\left[W\left(\mathbf{r},\mathbf{r}',0\right)-v\left(\mathbf{r}-\mathbf{r}'\right)\right].$$

Here, we used that $\sum_l \phi_l^*\left(\mathbf{r}\right)\phi_l\left(\mathbf{r}'\right)=\delta\left(\mathbf{r}-\mathbf{r}'\right)$ and $W\left(\mathbf{r},\mathbf{r}',0\right)=v\left(\mathbf{r}-\mathbf{r}'\right)+2\sum_m \frac{V_m(\mathbf{r})V_m^*(\mathbf{r}')}{\omega_m}$.

The static COHSEX approximation provides an intuitive understanding of the self-energy. It differs from directly setting W to its static limit in the original Σ^{GW} expression, which would only yield the $\Sigma^{\mathrm{SEX}}_{static}$ term. The $\Sigma^{\mathrm{SEX}}_{static}$ contribution resembles the bare exchange Σ^x, however, static screening effects due to the system's polarizability are considered. These weaken the effect of the bare exchange. Therefore, in polarizable materials, $\Sigma^{\mathrm{SEX}}_{static}$ is expected to improve excitation energies with respect to the Hartree-Fock approach. Compared to a full evaluation of Σ^{SEX}, computational costs are reduced tremendously, since W has only to be evaluated once instead of calculating it as a function of the frequency.

The Coulomb hole contribution not only becomes static, but also local. It corresponds to the interaction energy of a classical point charge with an induced charge distribution. The latter can be calculated within linear response theory, assuming an external potential $U_{ext}\left(\mathbf{r},\mathbf{r}_0\right)=\int d\mathbf{r}'\,v\left(\mathbf{r},\mathbf{r}'\right)\left(\pm\delta\left(\mathbf{r}',\mathbf{r}_0\right)\right)$ created by a $(\pm)$point charge adiabatically added at $\mathbf{r}_0$. U_{ext} causes an induced potential, which in turn acts on the point charge. Following equations (1.31) and (1.32), it is given by:

$$V_{ind}\left(\mathbf{r},\mathbf{r}_0\right)=\int d\mathbf{r}'d\mathbf{r}''d\mathbf{r}'''\,v\left(\mathbf{r},\mathbf{r}''\right)\chi\left(\mathbf{r}'',\mathbf{r}'\right)v\left(\mathbf{r}',\mathbf{r}'''\right)\delta\left(\mathbf{r}''',\mathbf{r}_0\right).$$

The above expression can be rewritten in terms of the screened Coulomb potential,

$$\tilde{W}\left(\mathbf{r},\mathbf{r}'\right)=W-v=\int d\mathbf{r}''d\mathbf{r}'''\,v\left(\mathbf{r},\mathbf{r}''\right)\chi\left(\mathbf{r}'',\mathbf{r}'''\right)v\left(\mathbf{r}''',\mathbf{r}'\right),$$

resulting in:

$$V_{ind}\left(\mathbf{r},\mathbf{r}_0\right)=\tilde{W}\left(\mathbf{r},\mathbf{r}_0\right).$$

The energy needed to insert a point charge into a polarizable medium is then given by:

$$E_{ind}=\frac{1}{2}\int d\mathbf{r}\,\left(\pm\delta\left(\mathbf{r},\mathbf{r}_0\right)\right)V_{ind}\left(\mathbf{r},\mathbf{r}_0\right)=\frac{1}{2}\tilde{W}\left(\mathbf{r}_0,\mathbf{r}_0\right),$$

where the factor $\frac{1}{2}$ enters, because the charge is added adiabatically to the system [9]. Includ-

ing also the probability to find a charge i at $\mathbf{r}_0$, we arrive at:

$$E_{ind}^{ii} = \frac{1}{2} \int d\mathbf{r}_0 \, \tilde{W}(\mathbf{r}_0, \mathbf{r}_0) \, |\phi_i(\mathbf{r}_0)|^2 ,$$

which is nothing else than the static Coulomb hole self-energy, $\langle i| \Sigma_{static}^{\mathrm{COH}} |i\rangle$, for the state i.

Neglecting dynamical effects, the static COHSEX approximation denotes a rather strong approximation. However, in cases where the added charge can be considered as a classical point charge, e.g. in the case of core level ionization, it is expected to work rather well. Moreover, it represents a very interesting approximation to the GW self-energy from the computational point of view. A detailed discussion about its accuracy and limitations is provided in subsequent chapters.

1.7. Optical absorption spectroscopy

As already pointed out in the introductory chapter, two physical properties are of main interest for our study on organic solar cells. First, we focus on an accurate calculation of the electronic structure. The latter determines for instance band offsets which are crucial for organic solar cell efficiencies. As discussed in detail in the preceding sections, it can be obtained from first principles by a Green's function formalism, where PES excitation energies are calculated within the many-body perturbation theory framework of GW. Second, we are interested in optical absorption quantities, such as electron-hole binding energies, since they are decisive for the optimization of the photoabsorption process with respect to the amount of sunlight absorbed by the solar cell. In the present section, a many-body perturbation theory approach based on the Bethe-Salpeter equations (BSE) is presented, where electron-hole interactions are explicitly included in order to accurately determine absorption spectra.

Optical absorption experiments When exposing a material to electromagnetic radiation, the latter is partially absorbed on its way through the medium. This is attributed to neutral excitations which occur if the photon energy $\hbar\omega$ matches the neutral excitation energies ($\epsilon_m = E_{N,m} - E_{N,0}$). The latter are the difference between the total energy of the equilibrium system $E_{N,0}$ and the excited one $E_{N,m}$. This implies that we need to properly describe the excited states of the N particle system. Depending on the energy range, different kinds of neutral excitations exist. Within the microwave regime, rotational excitations are most likely for molecules. Changes in the vibrational state (phonons) often occur in the infrared, whereas electronic excitations such as electron-hole pairs or plasmonic oscillations are typical for the optical range. In addition, mixtures of different types of excitations with a combined excitation energy are also possible. In the following, we focus on the optical regime, i.e. we consider excitations of the electronic system only.

In a typical optical absorption spectroscopy experiment, a probe is exposed to visible radiation with intensity I from one side, while a detector on the facing side measures the amount of radiation passing through. Since absorption depends on a manifold of material specific quantities, absorption spectroscopy provides important information about the medium under

study. It is a widely applied tool and, e.g. in analytical chemistry, used to distinguish between different kinds of substances present in a sample. Measuring the absorption with respect to $\hbar\omega$ and subtracting the reference spectrum of the light source provides the material specific absorption spectrum. The related observable is the absorption coefficient $\sigma(\hbar\omega)$, which is defined as the ratio of the absorbed energy and the incoming intensity I:

$$\sigma(\hbar\omega) \equiv \frac{\hbar\omega \cdot U(\hbar\omega)}{I},$$

where $U(\hbar\omega)$ represents the number of absorbed photons per unit volume and time. The absorption coefficient is closely related to the macroscopic dielectric function $\bar{\varepsilon}_M$. The latter determines the linear response of a system with respect to a small external electromagnetic perturbation and describes its optical properties. It is a complex quantity,

$$\bar{\varepsilon}_M(\hbar\omega) = \varepsilon_1(\hbar\omega) + i\varepsilon_2(\hbar\omega), \tag{1.42}$$

where real and imaginary part can be deduced from each other through the Kramers-Kronig relations:

$$\begin{aligned} \varepsilon_1(\hbar\omega) - 1 &= \tfrac{2}{\pi}\mathcal{P}\int_0^\infty d\omega' \tfrac{\omega'\varepsilon_2(\hbar\omega')}{(\omega')^2-\omega^2}, \\ \varepsilon_2(\hbar\omega) &= -\tfrac{2\omega}{\pi}\mathcal{P}\int_0^\infty d\omega' \tfrac{\varepsilon_1(\hbar\omega')}{(\omega')^2-\omega^2}. \end{aligned}$$

In the above equations, $\mathcal{P}$ represents the Cauchy principle value. The imaginary part $\varepsilon_2(\hbar\omega)$ is directly accessible through experiment through its relation to the absorption coefficient:

$$\varepsilon_2(\hbar\omega) = \frac{n_r c_0}{\omega}\sigma(\hbar\omega),$$

where c_0 is the speed of light in vacuum and where we assume a constant refraction index n_r.

The dielectric function within a single-particle picture Neutral excitations can be treated on different levels of sophistication. In order to get a rough overview of the most important features, we only consider interband electron-hole excitations where an electron is promoted from an occupied (v) to an unoccupied (c) state leaving behind its corresponding hole. In semiconductors and isolators, these type of excitations are lowest in energy. In addition, plasmons can be excited, i.e. collective oscillations relative to the positive background of the ion cores. In semiconductors, the plasmon excitation energies are usually higher than the lowest electron-hole excitations and meanwhile they are not included in our considerations.

On the simplest level of theory, we work in a single-particle picture, i.e. we decouple the excited electron from the remaining electronic system and approximate the neutral excitation energy by single-particle energies:

$$\epsilon_m = E_{N,m} - E_{N,0} \approx \varepsilon_c - \varepsilon_v.$$

The number of absorbed photons per unit volume and time, $U(\hbar\omega)$, is obtained by summing

up the probabilities Ω of all possible transitions from occupied to unoccupied states:

$$U(\hbar\omega) \propto \sum_{vc} \Omega_{v\to c}(\hbar\omega).$$

Within first-order time-dependent perturbation theory, Ω is given by Fermi's golden rule:

$$\Omega_{v\to c}(\hbar\omega) \propto |\langle v|\,\mathbf{A}\hat{p}\,|c\rangle|^2\,\delta(\varepsilon_c - \varepsilon_v - \hbar\omega), \tag{1.43}$$

where $\mathbf{A}$ denotes the vector potential of the radiation and $\hat{p} = -i\hbar\nabla$ the electronic momentum operator. Equation (1.43) is analogue to the transition rate introduced for PES experiments, but here one is interested in a neutral final state, i.e. the electron is not supposed to leave the system. Moreover, only vertical transitions are considered, where the photon momentum is not explicitly taken into account, since it is small as compared to electronic momenta in solids. Again, the initial and final state of the decoupled remaining electronic system are taken to be equal, i.e. we assume a frozen-orbital (Koopmans) picture. In order to arrive at an expression for ε_2, the matrix element in equation (1.43) has to be evaluated. The derivation is somewhat lengthy[6]and therefore only the final result is presented. For non-degenerate parabolic bands and excitations at the direct gap, ε_2 can be derived to [104]:

$$\varepsilon_2(\hbar\omega) \propto \frac{1}{\hbar^2\omega^2}\sqrt{\hbar\omega - E_g}\;\Theta(\hbar\omega - E_g), \tag{1.44}$$

where E_g represents the fundamental electronic energy gap. The latter is defined by charged excitations, namely as the energy difference between the first ionization energy, i.e. the energy needed to eject an electron from the system, and the first electron affinity, which is the necessary energy to insert an electron. The above equation is valid for singlet transitions without spin flips. For photon energies smaller than E_g, there is no absorption and the material is transparent. For photon energies greater than E_g, the function $\left(\hbar^2\omega^2\cdot\varepsilon_2\right)$ increases like the square root of $(\hbar\omega - E_g)$ with increasing ω (see Fig. 1.11). Equation (1.44) provides a first intuitive picture of the absorption process. However, comparing the model to experimental absorption spectra reveals large quantitative and qualitative discrepancies (see Fig. 1.10). This suggests that the single-particle approximation seems to miss important physical effects.

The dielectric function including excitonic effects One crucial effect that has to be included in the independent particle model is the electron-hole interaction. Indeed, the promoted electron and the created hole are not uncorrelated, but they influence each other through an attractive Coulomb potential. We rather have to consider a quasiparticle in the form of a bound electron-hole pair instead of two independent particles. Due to the attractive potential, the energy needed to excite this so-called exciton is smaller than the excitation energy needed to create two bare particles. Therefore, in contrast to equation (1.44), optical absorption is

[6]Based on equation (1.43), ε_2 can be evaluated in the vicinity of critical points of the band structure, the so-called van Hove singularities. Its spectral characteristics depend on the type and the dimension of the singularity. Equation (1.44) has been derived for a $3D$-M_0 singularity in a periodic semiconductor with parabolic bands. See Refs. [101, 102, 103] for more details.

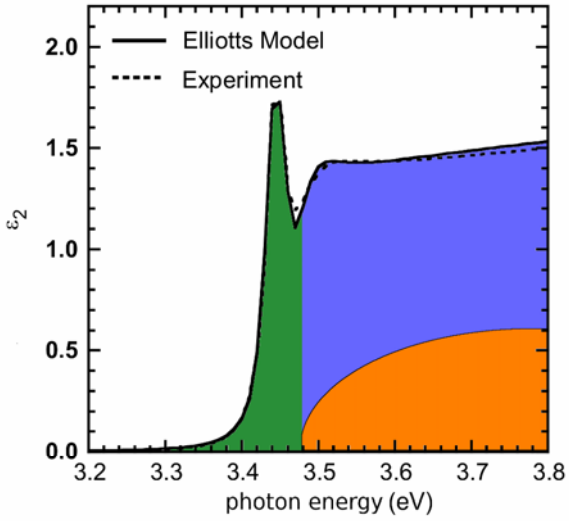

Figure 1.10.: Imaginary part of the dielectric function ε_2 of gallium nitride (GaN) as measured at room temperature in ellipsometry experiments and as calculated using the Elliott model: Comparing the experimental result to a simple one-particle approach, one observes large discrepancies. Corresponding to equation (1.44), $(\hbar^2\omega^2\varepsilon_2)$ is plotted as a guide for the eye (area highlighted in orange). Accordingly, absorption should start at the fundamental electronic gap E_g. Instead, an absorption peak is observed for $(\hbar\omega < E_g)$ in experiment. As it will be discussed in detail later in this chapter, this is due to excitonic effects, i.e. interactions between the excited electron and the created hole, which are not taken into account in the simple one-particle approach. As a result, absorption already starts at the optical gap E_{opt}, which differs from the fundamental gap by the first bound electron-hole pair binding energy E_B^{e-h}. Elliott's theory accounts both for bound excitonic states (area highlighted in green) and the exciton continuum (area highlighted in blue), resulting in an excellent agreement with experiment. This demonstrates the importance of accounting for electron-hole interactions. Figure taken from Ref. [103] and modified.

expected to start at energies lower than the fundamental electronic gap. The absorption onset is called optical gap E_{opt} and it differs from the fundamental gap by the binding energy E_B^{e-h} of the lowest excited dipole-allowed electron-hole pair.

For further considerations, it is convenient to distinguish two limiting cases of excitons. The first one are so-called Frenkel excitons [105], which represent very tightly bound electron-hole pairs. They preferentially occur in ionic crystals or organic molecules/polymers and are characterized by a very strong electron-hole interaction of the order of several eV due to rather poor screening effects in these systems. As a consequence, the spatial extent of the exciton is of the order of one nanometer, i.e. the electron and the hole are confined within the same unit cell or on the same molecule. The second type are Wannier-Mott excitons [106], which occur in most standard semiconductors. They are distinguished by their weak binding energy of the order of a few meV. Efficient screening mechanisms lead to a weak Coulomb interaction and as a consequence, the electron and the hole are correlated, but of the order of

some nanometer apart from each other.

For the sake of pedagogy, we focus on the description of Wannier-Mott excitons in the following. Here, due to efficient screening, we can straightforwardly treat the electron and the corresponding hole within the quasiparticle picture. The latter is also called effective-mass approximation, since the electron and the hole are regarded as bare particles, however, they are assigned a renormalized energy and mass m^*. Within this approximation, the exciton is governed by the excitonic wave function Φ^{exc},

$$\Phi^{exc}\left(\mathbf{r}_h, \mathbf{r}_e\right) = \sum_{vc} a_{vc} \phi_v\left(\mathbf{r}_h\right) \phi_c\left(\mathbf{r}_e\right).$$

It is a linear combination of products from quasielectron $\phi_c\left(\mathbf{r}_e\right)$ and quasihole $\phi_v\left(\mathbf{r}_h\right)$ wave functions with the coefficients a_{vc}. That implies that one needs to go beyond a single-particle picture and instead considers a two-particle problem. The corresponding Schrödinger equation reads [102, 107]:

$$\left(-\frac{\hbar^2}{2m_e^*}\nabla_{\mathbf{r}_e}^2 - \frac{\hbar^2}{2m_h^*}\nabla_{\mathbf{r}_h}^2 - \frac{e^2}{4\pi\varepsilon_0\varepsilon_r\left|\mathbf{r}_e - \mathbf{r}_h\right|} + E_g\right)\Phi^{exc}\left(\mathbf{r}_h, \mathbf{r}_e\right) = E^{exc}\Phi^{exc}\left(\mathbf{r}_h, \mathbf{r}_e\right).$$

It models the absorption process by a quasielectron and a quasihole in a potential equal to the gap energy E_g. They have effective masses m^* and are coupled to each other via a screened Coulomb potential expressed in terms of the permittivity of the vacuum $4\pi\varepsilon_0$ and the relative permittivity ε_r. The above equation can be solved in terms of a separation ansatz, where the motion of the center of gravity and the relative motion of the electron and the hole are decoupled. The latter can be treated analogously to the hydrogen problem or the positronium atom (for details see Ref. [101, 102, 107, 108]). As a result, one obtains bound excitonic states for exciton energies ($E^{exc} < 0$) and continuum states for ($E^{exc} > 0$). The exciton energy of bound states at the Γ-point of the band structure is given by:

$$E_n^{exc} = E_g - \frac{Ry^*}{n^2},$$

where

$$Ry^* = \frac{m_r^* e^4}{2\left(4\pi\varepsilon_0\varepsilon_r\hbar\right)^2} = \frac{m_r^*}{m_e}\frac{1}{\varepsilon_r^2}Ry$$

is an effective Rydberg energy accounting for screening effects in the medium. The latter is determined by the ratio of the reduced effective mass $m_r^* = m_e^* m_h^* / \left(m_e^* + m_h^*\right)$ and the free electron mass, the relative permittivity ε_r and the Rydberg constant $Ry = 13.6$ eV. By way of example, in indium nitride (InN), with $m_e^* \approx 0.06 m_e$ [109, 110] and $m_h^* \approx 0.5 m_e$ [111], and a relative permittivity of $\varepsilon_r = 9.5$ [112], one obtains for the first bound exciton ($n = 1$) an effective Rydberg energy of $Ry^* \approx 8$ meV. This is one order of magnitude smaller than the Rydberg constant Ry, which elucidates the importance of screening. Moreover, room temperature, which corresponds to a thermal energy of around 25 meV, is sufficient to dissociate the bound electron-hole pair, whose binding energy can be calculated following ($E_{b,n}^{e-h} = Ry^*/n^2$). Contrary, the binding energy of organic semiconductors is usually one

order of magnitude larger, as it will be explicitly shown for the coumarin family later in this work.

The consideration of electron-hole interactions significantly modifies the imaginary part of the dielectric function compared to the already discussed single-particle picture, yielding a hydrogen-like Rydberg series [101, 102, 103, 113]:

$$\varepsilon_2^{exc,b}(\hbar\omega) \propto \frac{1}{\hbar^2\omega^2}\sum_n \frac{Ry^*}{n^3}\delta\left(\hbar\omega - E_n^{exc}\right). \tag{1.45}$$

Due to the creation of bound excitonic states, sharp absorption peaks occur at energies ($E_n^{exc} = E_g - Ry^*/n^2$) below the gap. The first peak in the spectrum is at ($E_1^{exc} = E_g - Ry^*$), the second at ($E_2^{exc} = E_g - \frac{Ry^*}{4}$), etc. , i.e. for ($n \to \infty$) peaks are getting closer and closer to each other. Since the function value is diminishing at the same time with ($1/n^3$), they sum up to a finite value close to ($\hbar\omega = E_g$), see Fig. (1.11). For excitation frequencies higher than E_g, the electron and the hole are not bound anymore, but still somewhat correlated by the interaction with the medium. The imaginary part of the dielectric function ε_2 for the exciton continuum is given by [101, 102, 113]:

$$\varepsilon_2^{exc,f}(\hbar\omega) \propto \frac{1}{\hbar^2\omega^2}\Theta\left(\hbar\omega - E_g\right)\frac{1}{1-\exp\left(-\sqrt{Ry^*/\left|\hbar\omega - E_g\right|}\right)}. \tag{1.46}$$

The latter is expected to coincide with equation (1.44) of the single-particle approximation. However, even though the curves are very similar for high energies $\hbar\omega$, they strongly differ close to ($\hbar\omega = E_g$). In contrast to equation (1.44), $\varepsilon_2^{exc,f}$ is non-zero and has a peak at ($\hbar\omega = E_g$), see Fig. (1.11). This is due to the fact that the limit of both $\varepsilon_2^{exc,b}$ and $\varepsilon_2^{exc,f}$ for ($\hbar\omega \xrightarrow{0^-} E_g$) and ($\hbar\omega \xrightarrow{0^+} E_g$) are identical and finite. Moreover, one observes a significant enhancement of absorption above E_g with respect to equation (1.44), which is described by the so-called Sommerfeld enhancement factor. Combining the results for bound and continuum states and considering in addition broadening effects through a temperature dependent parameter Γ, one finally arrives at the so-called Elliott's model for the imaginary part of the dielectric function [107, 113]:

$$\varepsilon_2^{exc}(\hbar\omega) \propto \frac{1}{\hbar^2\omega^2}\sum_n \frac{Ry^*}{\Gamma n^3}\exp\left[-\frac{\left(\hbar\omega - E_g + Ry^*/n^2\right)^2}{\Gamma^2}\right] + \frac{1}{\hbar^2\omega^2}\frac{1+\operatorname{erf}\left[\left(\hbar\omega - E_g\right)/\Gamma\right]}{1-\exp\left(-\sqrt{Ry^*/\left|\hbar\omega - E_g\right|}\right)}.$$

One thus obtains an equation to model optical absorption spectra, which contains three fitting input parameters: the fundamental gap E_g, the broadening parameter Γ and the effective Rydberg constant Ry^*.

Including excitonic effects, using even simple models such as the presented effective-mass approximation, drastically changes the characteristics of ε_2. The agreement with respect to experimental absorption spectra can be significantly improved (see Fig. 1.10). We therefore conclude that electron-hole interactions play an important role in absorption experiments. In the following, we transfer the gained insights to the already presented many-body perturbation theory formalism. That means we go beyond the single-quasiparticle description

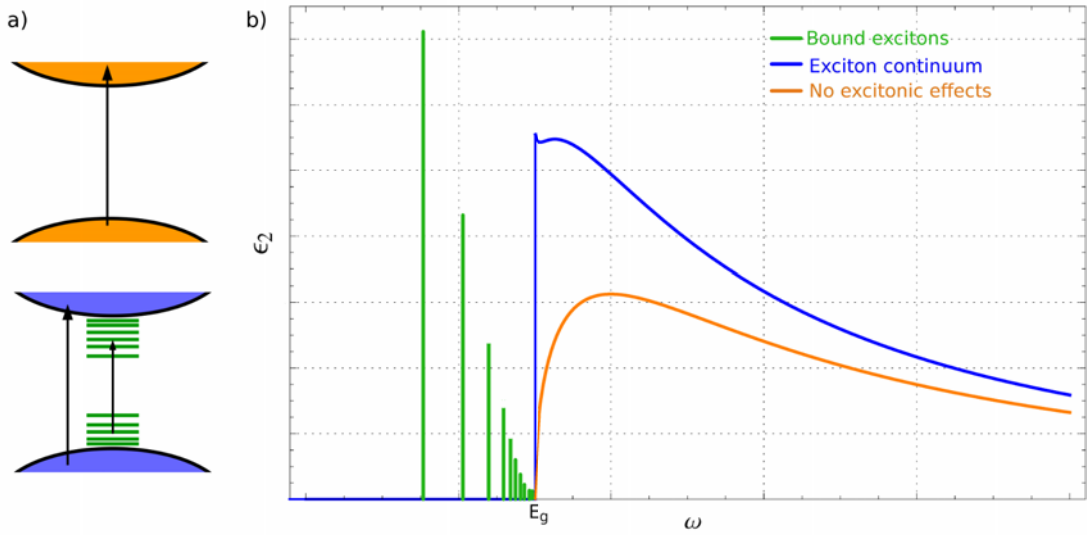

Figure 1.11.: Schematic view of the absorption process within a single-particle and a two-particle picture, respectively: the single-particle picture (a, top) corresponds to the promotion of an electron from an occupied state into an unoccupied one, while neglecting the remaining electronic system. The resulting imaginary part of the dielectric function ε_2 (b, orange) is zero for $(\hbar\omega \leq E_g)$ and grows like $\left[\left(\hbar^2\omega^2\right)^{-1}\sqrt{\hbar\omega - E_g}\right]$ for $(\hbar\omega > E_g)$, see equation (1.44). The curve is significantly modified within a two-particle model (a, bottom). According to equation (1.45), as a signature of bound excitonic states, absorption peaks occur for $(\hbar\omega < E_g)$. The latter converge to a finite value for $(\hbar\omega \to E_g)$. Moreover, for $(\hbar\omega \to E_g)$, the curves for bound and unbound (b, green/blue) excitons coincide, resulting in a finite absorption value at $(\hbar\omega = E_g)$.

within the *GW* method towards a quasielectron-quasihole picture governed by the so-called Bethe-Salpeter equations.

1.8. Optical absorption within the framework of MBPT

1.8.1. Preliminary considerations

The microscopic dielectric function As demonstrated in the preceding chapter, the single-particle Green's function is the many-body quantity of interest for the description of PES experiments, since its poles correspond to the measured excitation energies. However, for absorption experiments, where neutral electron-hole excitations occur, it is not sufficient. Instead, the quantity of choice is the already introduced dielectric function ε, defined as follows:

$$V_{tot} = \int d2\, \varepsilon^{-1}(1,2)\, U_{ext}(2)\,. \tag{1.47}$$

It describes the electronic response of the system to a small time-dependent perturbation in form of charge redistributions. Compared to the ground state density, charge accumulations and depletions are created, which can be interpreted as the excitation of electron-hole pairs. The dielectric function can be expressed in terms of the reducible polarizability χ and its

irreducible analogue P through:

$$\varepsilon(1,2) = \delta(1,2) - \int d3\, v(1,3)\, P(3,2)$$

and

$$\varepsilon^{-1}(1,2) = \delta(1,2) + \int d3\, v(1,3)\, \chi(3,2).$$

If the system is not polarizable, χ is zero and consequently the total potential V_{tot} equals the external potential U_{ext}. However, for polarizable media, induced internal fields are created. In this case, χ is in average usually negative, thus it weakens the effect of the external potential. As already introduced in preceding chapters, χ is a density-density correlation function following:

$$\chi\left(\mathbf{r}t, \mathbf{r}'t'\right) \equiv \frac{\partial n_{ind}(\mathbf{r}t)}{\partial U_{ext}(\mathbf{r}'t')} = -i \left\langle N,0\right| T\left[\hat{n}(\mathbf{r}t), \hat{n}\left(\mathbf{r}'t'\right)\right] \left|N,0\right\rangle.$$

Analogue to the single-particle Green's function, it reads in the Lehmann representation [2]:

$$\begin{aligned} \chi(\mathbf{r},\mathbf{r}',\omega) &= \textstyle\sum_{m\neq 0} \frac{\rho_m(\mathbf{r})\rho_m^*(\mathbf{r}')}{\omega+\left(E_{N,m}-E_{N,0}\right)-i\eta} - \frac{\rho_m^*(\mathbf{r})\rho_m(\mathbf{r}')}{\omega-\left(E_{N,m}-E_{N,0}\right)+i\eta}, \\ \rho_m(\mathbf{r}) &= \left\langle N,m\right| \hat{n}(\mathbf{r}) \left|N,0\right\rangle, \end{aligned}$$

where ρ_m are charge fluctuations. The reducible polarizability thus has poles at the neutral excitation energies ($\epsilon_m = E_{N,m} - E_{N,0}$) of the created electron-hole pair like excitations.

From microscopic to macroscopic Up to now, two different kinds of dielectric functions have been presented. The microscopic dielectric function ε (1.47) as introduced within linear response theory and its macroscopic counterpart ε_M (1.42), which is accessible through optical experiments. However, no relation between these two quantities has been established so far. Following Refs. [114, 115, 116], the macroscopic dielectric function can be expressed in terms of the microscopic dielectric function for periodic structures through:

$$\varepsilon_M(\omega) \equiv \lim_{\mathbf{k}\to 0} \frac{1}{\varepsilon^{-1}_{G=0,G'=0}(\mathbf{k},\omega)}.$$

Here, $\varepsilon_{GG'}(\mathbf{k},\omega) \equiv \varepsilon(\mathbf{k}+\mathbf{G}, \mathbf{k}+\mathbf{G}', \omega)$ is the Fourier transform of $\varepsilon(\mathbf{r},\mathbf{r}',\omega)$, where $\mathbf{G}$ is the reciprocal lattice vector and where the electronic wave vector $\mathbf{k}$ is limited to the first Brillouin zone. The dielectric constant ε_0 corresponds to the static limit of the macroscopic dielectric function: $\varepsilon_0 \equiv \varepsilon_M(\omega = 0)$. For crystals, the absorption spectrum, i.e. the imaginary part of the macroscopic dielectric function ε_2, is thus obtained by calculating the microscopic dielectric function in reciprocal space followed by an inversion. In general, $\varepsilon(\mathbf{r},\mathbf{r}',\omega)$ is non-local, i.e. it depends on $(\mathbf{r},\mathbf{r}')$ and not on the difference $(\mathbf{r}-\mathbf{r}')$. As a consequence, in reciprocal space $\varepsilon_{GG'}(\mathbf{k},\omega)$ is a non-diagonal matrix and thus an inversion couples the matrix elements with each other. This is known as local field effects, arising in systems with microscopic inhomogeneities.

In finite systems, the photoabsorption cross section η can directly be accessed through the

imaginary part of the dynamical polarizability $\alpha(\omega)$:

$$\eta(\omega) \equiv \frac{4\pi\omega}{c} \Im\{\alpha(\omega)\}.$$

The dynamical polarizability in turn depends solely on the applied external field and the reducible polarizability χ [42]:

$$\alpha_{ij}(\omega) = -\int d\mathbf{r}d\mathbf{r}' U_{ext,i}(\mathbf{r},\omega)\,\chi\left(\mathbf{r},\mathbf{r}',\omega\right) U_{ext,j}\left(\mathbf{r}',\omega\right).$$

By way of example, for dipolar external fields along the x and z direction, respectively, one obtains the non-diagonal α_{xz} polarizability [42]:

$$\alpha_{xz}(\omega) = -\int d\mathbf{r}d\mathbf{r}'\, x\,\chi\left(\mathbf{r},\mathbf{r}',\omega\right)\, z'.$$

Consequently, absorption is directly accessible through the introduced Green's function techniques. Nevertheless, it is important to note that the previously considered quantities, such as the Green's function G or the polarizability χ, are time-ordered objects. This implies that they include the knowledge of future interactions and hence they are no observables. Instead, their retarded analogues only refer to bygone interactions and are thus measured in experiments. Contrary to the introduced time-ordered quantities, it is, however, not possible to establish a set of coupled integral equations for their calculation, since certain identities in the derivation do not hold. One has to pass by the time-ordered functions instead, which afterwards are transformed into their retarded counterparts. For the reducible polarizability, and correlation functions in general, simple transformation rules exist [2, 117], e.g.:

$$\begin{aligned}
\Re\left[\chi^R(\mathbf{r},\mathbf{r}',\omega)\right] &= \Re\left[\chi^T(\mathbf{r},\mathbf{r}',\omega)\right] \\
\Im\left[\chi^R(\mathbf{r},\mathbf{r}',\omega)\right] &= \operatorname{sign}(\omega)\,\Im\left[\chi^T(\mathbf{r},\mathbf{r}',\omega)\right]
\end{aligned}$$

For frequencies $\omega > 0$, the retarded polarizability χ^R equals thus the time-ordered polarizability. In subsequent sections, only time-ordered quantities are considered. Therefore, the superscript T will be dropped.

Common approximations to the polarizability Analogue to the one-particle Green's function, applying the equation of motion (EOM) technique to the polarizability yields a Dyson-like equation for χ in terms of the irreducible polarizability P and the bare Coulomb potential v:

$$\chi(1,2) = P(1,2) + \int d34\, P(1,3) v(3,4)\,\chi(4,2).$$

However, the building blocks P from which χ is constructed are complicated objects themselves, given by Hedin's equation:

$$P(12) = -i \int d34\, G(1,3)\,\Gamma(3,4;2)\,G(4,1). \tag{1.48}$$

This is in contrast to the Dyson equation for the single particle Green's function,

$$G(11') = G_0(11') + \int d2 \int d3\, G_0(12)\Sigma(23)G(3'1), \tag{1.49}$$

where the non-interacting Green's function G_0 represents known building blocks and where the complexity of the problem is fully governed by the self-energy Σ.

The simplest approximation to P consists of considering non-interacting particles, yielding the independent irreducible polarizability P_{IP}:

$$P_{IP}\,(12) \equiv -iG_0\,(12)\,G_0\,(21)\,.$$

The latter describes the absorption process as the uncorrelated motion of an excited bare electron and the created hole. These are completely decoupled from each other and the remaining electronic system. In the Lehmann representation (see Appendix A.7), it reads:

$$P_{IP}\,(\mathbf{r}_1,\mathbf{r}_2;\omega) = \sum_{m,l} \frac{\phi_l\,(\mathbf{r}_1)\,\phi_l^*\,(\mathbf{r}_2)\,\phi_m\,(\mathbf{r}_2)\,\phi_m^*\,(\mathbf{r}_1)}{\omega - \left(\varepsilon_l^0 - \varepsilon_m^0\right) + i\eta} - \frac{\phi_m\,(\mathbf{r}_1)\,\phi_m^*\,(\mathbf{r}_2)\,\phi_l\,(\mathbf{r}_2)\,\phi_l^*\,(\mathbf{r}_1)}{\omega + \left(\varepsilon_l^0 - \varepsilon_m^0\right) - i\eta}, \tag{1.50}$$

i.e. it is constructed from single-particle wave functions ϕ. Its poles correspond to the transition of an electron from an occupied single-particle state with energy ε_m^0 to an unoccupied state with energy ε_l^0. This approximation is known as the random-phase approximation (RPA). Within the RPA, χ and ε read:

$$\begin{aligned} \chi^{RPA}\,(1,2) &= P_{IP}(1,2) + \textstyle\int d34\, P_{IP}(1,3)v\,(3,4)\,\chi^{RPA}(4,2) \\ \varepsilon^{RPA}\,(1,2) &= \delta\,(1,2) - \textstyle\int d3\, v\,(1,3)\,P_{IP}\,(3,2)\,. \end{aligned} \tag{1.51}$$

In order to go beyond the RPA, one considers quasiparticles instead of bare electrons and holes:

$$P_{QIP} \equiv -iG\,(12)\,G\,(21)\,. \tag{1.52}$$

The subscript "QIP" refers to *quasi-independent particles*. This highlights the fact that the two particles propagate without interacting with each other, however, both are quasiparticles and interact with the surrounding medium. Analogue to equation (1.50), the Lehmann representation is obtained by:

$$P_{QIP}\,(\mathbf{r}_1,\mathbf{r}_2;\omega) = \sum_{m,l} \frac{f_l\,(\mathbf{r}_1)\,f_l^*\,(\mathbf{r}_2)\,f_m\,(\mathbf{r}_2)\,f_m^*\,(\mathbf{r}_1)}{\omega - (\varepsilon_l - \varepsilon_m) + i\eta} - \frac{f_m\,(\mathbf{r}_1)\,f_m^*\,(\mathbf{r}_2)\,f_l\,(\mathbf{r}_2)\,f_l^*\,(\mathbf{r}_1)}{\omega + (\varepsilon_l - \varepsilon_m) - i\eta}.$$

Contrary to the independent-particle polarizability, Lehmann amplitudes $f_{l,m}$ and quasiparticle energies $\varepsilon_{l,m}$ enter instead of single-particle quantities. P_{QIP} corresponds to the irreducible polarizability calculated within the GW approximation, therefore this approach is called GW-RPA in the following. It represents the independent motion of a quasielectron and a quasihole. This is an important extension to P_{IP}, however, as pointed out in the preceding section, it is crucial to explicitly include the interaction between the excited electron

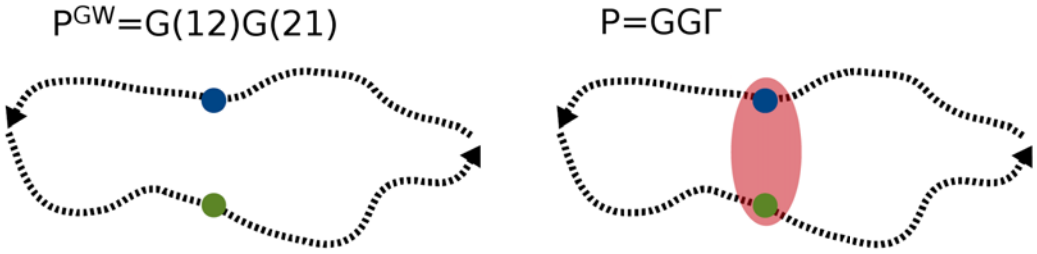

Figure 1.12.: The irreducible polarizability P: Within the GW approach ($\Gamma \equiv 1$), P describes the uncorrelated motion of a quasielectron (green) and a quasihole (blue). Therefore, bound excitonic states are not accessible. The vertex function Γ correlates the motion of the two particles, hence it is crucial to go beyond its first order approximation in order to include electron-hole interactions.

and the hole in order to reproduce signatures of bound electron-hole pairs in the spectrum.

As a consequence, one can not restrict oneself to the lowest order vertex function,

$$\Gamma^{GW}(1,2;3) = \delta(1,2)\,\delta(2,3),$$

but one has to consider the exact P, given in equation (1.48). That way, all interactions are included through the higher-order terms of Γ (see Fig. 1.12). Difficulties arise from the irreducible vertex function Γ, which is a complicated quantity:

$$\Gamma(1,2;3) = \delta(1,2)\,\delta(2,3) + \int d4567\, \frac{\delta\Sigma(1,2)}{\delta G(4,5)}\, G(4,6)\,\Gamma(6,7;3)\,G(7,5).$$

Multiplying the above equation by $[-iG(1,3)G(4,1)]$ and integrating over $\left(\int d34\right)$ results in:

$$\begin{aligned} P(12) &= -i \int d34\, G(1,3)\,\Gamma(3,4;2)\,G(4,1) \\ &= -i \int d34\, G(1,3)G(4,1)\delta(3,4)\,\delta(4,2) \\ &\quad -i \int d345678 G(1,3)G(4,1)\,\tfrac{\delta\Sigma(3,4)}{\delta G(5,6)}\, G(5,7)\,\Gamma(7,8;2)\,G(8,6) \qquad (1.53) \\ &= -i\,G(1,2)G(2,1) - i \int d3456 G(1,3)G(4,1)\,\tfrac{\delta\Sigma(3,4)}{\delta G(5,6)}\, P(5,2,6). \end{aligned}$$

This points out the fact that the two-point polarizability $P(1,2)$ is given by the three-point polarizability $P(5,2,6)$. Since the latter can not be contracted to a two-point function, equation (1.53) is not closed and therefore not a well suited starting point for further considerations.

1.8.2. The Bethe-Salpeter method for optical excitations

The Bethe-Salpeter equation As illustrated in the preceding section, a closed Dyson-like equation for the two-point polarizability $P(12)$ can not be obtained within the Green's function formalism, see equation (1.53). An alternative is to generalize the approach to four-point quantities. Since the considered process describes the creation of two-particles, four-point quantities such as the two-particle Green's function G_2 seem suited for an intuitive description. Indeed, the two-particle Green's function is used to define a two-particle correlation

function L following:

$$L(1,\mathbf{r}'t;2,\mathbf{r}t^{+}) = -G_2(1,\mathbf{r}'t;2,\mathbf{r}t^{+}) + G_1(1,2)G_1(\mathbf{r}'t,\mathbf{r}t^{+}).$$

The latter contains both the independent propagation of two particles through the one-particle Green's functions G_1 and their coupled motion through the two-particle Green's function G_2. Comparing the identities for the two-point polarizability χ,

$$\chi(1,2) \equiv \frac{-iG_1(11^{+})}{U_{ext}(2)} = i\left[G_2(1,2;1^{+},2^{+}) - G_1(1,1^{+})G_1(2,2^{+})\right],$$

and the two-particle correlation function L, we realize that χ is nothing else than a degenerate form of L obtained from:

$$\chi(1,2) = -iL(1,2;1^{+},2^{+}). \tag{1.54}$$

From the following relation (see Appendix A.1),

$$G_2\left(1,\mathbf{r}'t;2,\mathbf{r}t^{+}\right) = G_1(1,2)\,G_1\left(\mathbf{r}'t,\mathbf{r}t^{+}\right) - \frac{\partial G_1(1,2)}{\partial U_{ext}(\mathbf{r},\mathbf{r}',t)},$$

we directly find:

$$L(1,\mathbf{r}'t;2,\mathbf{r}t^{+}) = \frac{\partial G_1(1,2)}{\partial U_{ext}(\mathbf{r},\mathbf{r}',t)}.$$

Using the relation:

$$\frac{\partial G_1(12)}{\partial U_{ext}(34)} = -\iint d5d6\, G_1(15)\frac{\partial G_1^{-1}(56)}{\partial U_{ext}(34)}G_1(62),$$

L is transformed into:

$$L(1,\mathbf{r}'t;2,\mathbf{r}t^{+}) \;=\; -\int d3d4\, G_1(1,3)\,\tfrac{\partial G_1^{-1}(3,4)}{\partial U_{ext}(\mathbf{r},\mathbf{r}',t)}G_1(4,2). \tag{1.55}$$

The inverse of the one-particle Green's function is determined through the following Dyson equation:

$$G_1^{-1} = \left(G_1^{0}\right)^{-1} - (M + U_{ext}),$$

where M is the mass operator (1.20) containing all possible interactions and where G_1^0 is the one-particle Green's function for a system of non-interacting particles. As it is demonstrated in Appendix A.8, inserting the above relation for G_1^{-1} into equation (1.55) yields a closed Dyson-like equation:

$$L(1,2;1',2') = G_1\left(1,2'\right)G_1\left(2,1'\right) + \int d3456\, G_1(1,3)\,G_1\left(4,1'\right)\,K(3,5;4,6)\,L(6,2;5,2'). \tag{1.56}$$

The latter is known as *Bethe-Salpeter equation for L* [2, 42, 43, 117, 118, 119]. It describes the propagation of an electron and a hole through two terms. The first one represents the propagation of two independent quasiparticles, whereas the second one describes their coupled

motion through an effective two-particle interaction, the so-called kernel K:

$$K \equiv \frac{\partial M\left(3,4\right)}{\partial G_1\left(5,6\right)}.$$

For the uncorrelated motion term, it is convenient to introduce a quasi-independent two-particle correlation function L_{QIP} analogue to equation 1.52:

$$L_{QIP}(1,2;1',2') = G_1\left(1,2'\right) G_1\left(2,1'\right).$$

Expressing the Bethe-Salpeter equation (1.56) in terms of L_{QIP} yields:

$$L(1,2;1',2') = L_{QIP}(1,2;1',2') + \int d3456\, L_{QIP}(1,4;1',3)\, K\left(3,5;4,6\right) L(6,2;5,2').$$

One thus obtains an equation, where the quasi-independent quantity L_{QIP} is connected to the full four-point polarizability L through the kernel K. This is completely analogue to the Dyson equation for the single-particle Green's function (1.49), where the self-energy Σ links the non-interacting to the interacting Green's function. To describe absorption experiments, the two-point quantities P and χ are in principle sufficient, however, no closed equations can be set up for them within the Green's function approach. Therefore, one passes by the four-point quantity L. The latter contains more information than actually needed to describe absorption. Once the Bethe-Salpeter equation is solved, L is hence contracted to χ following equation (1.54). This yields:

$$\begin{aligned} -iL(1,2;1,2) &= -iG_1\left(1,2\right) G_1\left(2,1\right) \\ &\quad + \int d3456\, \left[-iG_1\left(1,4\right) G_1\left(4,1\right)\right] iK\left(3,5;4,6\right) \left[-iL(6,2;6,2)\right] \\ \chi\left(1,2\right) &= P^{GW}\left(1,2\right) + \int d3456\, P^{GW}\left(1,4\right)\, iK\left(3,5;4,6\right)\, \chi\left(6,2\right), \end{aligned} \tag{1.57}$$

where $P^{GW}\left(1,2\right) = -iG_1\left(1,2\right) G_1\left(2,1\right)$.

Reducible and irreducible quantities In order to single out the Hartree term from the effective two-particle interaction K, we split the mass operator into the Hartree contribution and the self-energy Σ:

$$M = V_H + \Sigma,$$

with $V_H\left(1,2\right) = \delta\left(1,2\right)\left[-i\int d3\, v\left(1,3\right) G_1\left(3,3^+\right)\right]$. The latter follows from: $n\left(1\right) = -iG\left(11^+\right)$. The kernel is consequently separated into:

$$\begin{aligned} K &= \tfrac{\partial V_H(3,4)}{\partial G_1(5,6)} + \tfrac{\partial \Sigma(3,4)}{\partial G_1(5,6)} \\ &= -i\delta\left(3,4\right)\delta\left(5,6\right) v\left(3,5\right) + \tfrac{\partial \Sigma(3,4)}{\partial G_1(5,6)}, \end{aligned} \tag{1.58}$$

i.e. a Hartree term $K_H = -i\delta\left(3,4\right)\delta\left(5,6\right) v\left(3,5\right)$ and the remainder $K_R = \frac{\partial \Sigma(3,4)}{\partial G_1(5,6)}$. The remaining part K_R including all interactions beyond Hartree defines the irreducible four-point

polarizability $\tilde{L}$ through:

$$\tilde{L}(1,2;1',2') = G_1\left(1,2'\right) G_1\left(2,1'\right) + \int d3456\, G_1\left(1,3\right) G_1\left(4,1'\right)\, K_R\left(3,5;4,6\right)\, \tilde{L}(6,2;5,2').$$

From that, the reducible analogue L is obtained via:

$$L(1,2;1',2') = \tilde{L}(1,2;1',2') + \int d3456\, \tilde{L}(1,4;1',3)\, K_H\left(3,5;4,6\right)\, L(6,2;5,2').$$

The choice of the kernel The kernel K accounts for all interactions and is hence a complicated many-body object. It can be strongly simplified depending on the chosen approximation for the self-energy Σ in equation (1.58). The roughest approximation consists of completely neglecting the self-energy ($\Sigma \equiv 0$). As a result, the Bethe-Salpeter equation reduces to a time-dependent Hartree approach:

$$\begin{aligned} L^{TDH}(1,2;1',2') &= G_1\left(1,2'\right) G_1\left(2,1'\right) \\ &\quad + \int d46\, G_1\left(1,4\right) G_1\left(4,1'\right)\, \left[-iv\left(4,6\right)\right] L(6,2;6,2'). \end{aligned} \tag{1.59}$$

Equation (1.59) can be contracted to χ following equation (1.57). This results in a closed equation for χ:

$$\chi^{TDH}(1,2) = P^{GW}\left(1,2\right) + \int d46\, P^{GW}\left(1,4\right)\, v\left(4,6\right) \chi^{TDH}(6,2),$$

with $P^{GW}\left(1,2\right) \equiv -iG_1\left(1,2\right) G_1\left(2,1\right)$. The latter is nothing else than the already introduced *GW-RPA* for χ.

In order to go beyond *GW-RPA*, a possibility is to use the bare exchange part Σ^x of the self-energy to construct the kernel K:

$$\Sigma \approx \Sigma^x = iG_1\left(1,2,\tau\right) v\left(1,2\right).$$

This results in a Hartree-Fock like kernel following:

$$K^{HF}\left(3,5;4,6\right) = -i\delta\left(3,4\right)\delta\left(5,6\right) v\left(3,5\right) + i\,\delta(3,5)\delta\left(4,6\right) v\left(3,4\right).$$

As it is demonstrated in Appendix A.8, one obtains for the Bethe-Salpeter equation:

$$\begin{aligned} L^{TDHF}(1,2;1',2') &= G_1\left(1,2'\right) G_1\left(2,1'\right) \\ &\quad + \int d46\, G_1\left(1,4\right) G_1\left(4,1'\right)\, \left[-iv\left(4,6\right)\right] L^{TDHF}(6,2;6,2') \\ &\quad + \int d56\, G_1\left(1,5\right) G_1\left(6,1'\right)\, \left[iv\left(5,6\right)\right]\, L^{TDHF}(6,2;5,2'), \end{aligned} \tag{1.60}$$

which represents a time-dependent Hartree-Fock approach ($TDHF$). The independent motion of an electron and a hole is governed by the first term in the above equation, whereas the second term includes the classical Hartree contribution and the third term the Fock exchange. The excited electron and the hole thus interact through exchange interactions, however, correlation is not taken into account. It is important to note that in contrast to equation (1.59), the terms

can not be readily contracted to two-point quantities following ($1' \to 1$, $2' \to 2$). Indeed, the exchange term remains a true four-point quantity. That implies that one is obliged to solve the Bethe-Salpeter equation for L, instead of a closed equation for χ as it is the case in the TDH approach. In general, including interactions beyond Hartree enforces a detour over four-point equations.

In order to go beyond the $TDHF$ approach, one can include correlations by using Σ within the GW approximation. This yields for the kernel:

$$\begin{aligned} K^{GW}(3,5;4,6) &= -i\delta(3,4)\,\delta(5,6)\,v(3,5) + \tfrac{\partial iG(3,4)W(3,4)}{\partial G_1(5,6)} \\ &= -i\delta(3,4)\,\delta(5,6)\,v(3,5) + i\delta(3,5)\,\delta(4,6)\,W(3,4), \end{aligned}$$

where we imposed ($\partial W/\partial G \equiv 0$), i.e. the change in the screening due to the excitation is neglected. This effect is usually supposed to be small, even though systematic studies on this approximation are scarce. As shown in Appendix A.8, the Bethe-Salpeter equation for the GW kernel reads:

$$\begin{aligned} L^{TDSHF}(1,2;1',2') &= G_1(1,2')\,G_1(2,1') \\ &\quad + \int d46\, G_1(1,4)\,G_1(4,1')\,[-iv(4,6)]\,L^{TDSHF}(6,2;6,2') \\ &\quad + \int d56\, G_1(1,5)\,G_1(6,1')\,[iW(5,6)]\,L^{TDSHF}(6,2;5,2'). \end{aligned} \tag{1.61}$$

The comparison to expression (1.60) points out that one obtains a time-dependent *screened* Hartree-Fock approach ($TDSHF$), where the time-dependent screened Coulomb potential W replaces the static bare Coulomb potential v in the third term. Consequently, the independent motion of two particles is not only correlated by the Hartree contribution of the second term, but also by a screened dynamical exchange contribution. In the following, a solution scheme for the time-dependent screened HFA is worked out.

Fourier transformation to frequency space and the static approximation Since L is a four-point quantity, it depends, in principle, on four different time arguments. However, the Coulomb potential v is instantaneous,

$$v(1,2) = v(\mathbf{x}_1\mathbf{x}_2)\,\delta(t_1 - t_2),$$

and also the one-particle Green's functions in equation (1.61) only depend on time differences. This suggests that the time arguments can be contracted to a single one in order to permit a straightforward Fourier transformation to frequency space. However, as it is demonstrated in the Appendix, this is not possible without further ado and approximations are implied. First, one assumes translational time invariance and an isochronous propagation of the electron and the hole.[7] In addition, the dynamically screened interaction W is approximated within its static limit:

$$W(1,2) \approx W_{stat}(\mathbf{x}_1\mathbf{x}_2)\,\delta(t_1 - t_2),$$

[7] For $L = L(1234)$, i.e. $L = L(t_1 - t_4; t_2 - t_3)$, we set $t_1 = t_3; t_2 = t_4$.

an approximation we already encountered for the static COHSEX approach. This is a drastic assumption, however, as it is shown in detail in Appendix A.8, it greatly simplifies equation (1.61) and one obtains:

$$\begin{aligned} L(\tau) &= L_{QIP}(\tau) \\ &\quad -i\int d\tau' L_{QIP}(\tau') L(\tau-\tau') v(\mathbf{x}_3\mathbf{x}_4) \\ &\quad +i\int d\tau' L_{QIP}(\tau') L(\tau-\tau') W_{stat}(\mathbf{x}_3\mathbf{x}_4), \end{aligned}$$

where $\tau = t_1 - t_2'$ and $\tau' = t_4 - t_1$. In order to simplify the notation, space coordinates are omitted. As a result, a straightforward Fourier transformation using the convolution theorem can be performed, yielding:

$$L(\omega) = L_{QIP}(\omega) - iL_{QIP}(\omega) L(\omega) v(\mathbf{x}_3\mathbf{x}_4) + iL_{QIP}(\omega) L(\omega) W_{stat}(\mathbf{x}_3\mathbf{x}_4).$$

Reintroducing space coordinates, $L(\omega)$ reads:

$$\begin{aligned} &L\left(\mathbf{x}_1\mathbf{x}_2;\mathbf{x}_1'\mathbf{x}_2';\omega\right) = \\ &L_{QIP}\left(\mathbf{x}_1\mathbf{x}_2;\mathbf{x}_1'\mathbf{x}_2';\omega\right) \\ &+\int d\mathbf{x}_3\mathbf{x}_4\mathbf{x}_5\mathbf{x}_6\, L_{QIP}\left(\mathbf{x}_1\mathbf{x}_4;\mathbf{x}_1'\mathbf{x}_3;\omega\right) K(\mathbf{x}_3\mathbf{x}_4;\mathbf{x}_5\mathbf{x}_6) L\left(\mathbf{x}_6\mathbf{x}_2;\mathbf{x}_5\mathbf{x}_2';\omega\right), \end{aligned} \tag{1.62}$$

with

$$L_{QIP}\left(\mathbf{x}_1\mathbf{x}_2;\mathbf{x}_1'\mathbf{x}_2';\omega\right) = \frac{1}{2\pi}\int d\omega' G_1\left(\mathbf{x}_1\mathbf{x}_2';\omega+\omega'\right) G_1\left(\mathbf{x}_2\mathbf{x}_1';\omega'\right)$$

being the Fourier transform of the already introduced quasi-independent two-particle correlation function L_{QIP}. K is the many-body perturbation theory kernel within the GW approximation, following:

$$K(\mathbf{x}_3\mathbf{x}_4;\mathbf{x}_5\mathbf{x}_6) = i\delta(\mathbf{x}_5,\mathbf{x}_3)\delta(\mathbf{x}_6,\mathbf{x}_4) W_{stat}(\mathbf{x}_3\mathbf{x}_4) - i\delta(\mathbf{x}_3,\mathbf{x}_4)\delta(\mathbf{x}_5,\mathbf{x}_6) v(\mathbf{x}_3\mathbf{x}_5).$$

It is important to keep in mind that we used a static, i.e. strongly approximated, screened Coulomb potential W in order to straightforwardly carry out the Fourier transformation.

The effective two-particle problem In principle, equation (1.62) can be solved by inversion for every frequency ω. However, it seems more handy to reformulate the problem in terms of an effective eigenvalue equation. This is analogue to the already introduced one-particle effective equations, such as the HF, DFT-KS or quasiparticle equation. However, in the case of absorption, an effective two-particle equation is needed. This equation then serves e.g. to determine neutral excitation energies efficiently.

Using the Lehmann representation of the Green's function in Fourier space, an explicit expression for the quasi-independent two-particle correlation function L_{QIP} within the RPA

or *GW-RPA* is obtained (see Appendix A.7):

$$\begin{aligned} &-iL_{QIP}^{RPA}\left(\mathbf{x}_1\mathbf{x}_2;\mathbf{x}_1^{'}\mathbf{x}_2^{'};\omega\right) = \\ &\sum_{m,l}\frac{\phi_l(\mathbf{x}_1)\phi_m(\mathbf{x}_2)\phi_m^*\left(\mathbf{x}_1^{'}\right)\phi_l^*\left(\mathbf{x}_2^{'}\right)}{\omega-(\varepsilon_l-\varepsilon_m)+i\eta} - \frac{\phi_m^*\left(\mathbf{x}_2^{'}\right)\phi_l(\mathbf{x}_2)\phi_l^*\left(\mathbf{x}_1^{'}\right)\phi_m(\mathbf{x}_1)}{\omega+(\varepsilon_l-\varepsilon_m)-i\eta}, \end{aligned} \tag{1.63}$$

where $\phi_{l,m}$ are single-particle wave functions and $\varepsilon_{l,m}$ are single- or quasiparticle energies. Occupied states are labeled by the index m, unoccupied ones by l. Equation (1.63) suggests to work in transition space, i.e. to define a two-particle excitonic basis $\{\psi^{exc}\}$,

$$\psi_i^{exc}\left(\mathbf{x}_1,\mathbf{x}_2\right) \equiv \sum_{n_1n_2} c_{i,n_1n_2}\phi_{n_1}\left(\mathbf{x}_1\right)\phi_{n_2}^*\left(\mathbf{x}_2\right),$$

where one sums over all single-particle basis functions $\phi_{m,l}$ appearing in G_0 and L_{QIP}^{RPA}. The transformation of any four-point quantity $F\left(\mathbf{x}_1\mathbf{x}_2\mathbf{x}_3\mathbf{x}_4\right)$ to this basis follows:

$$F\left(\mathbf{x}_1\mathbf{x}_2;\mathbf{x}_3\mathbf{x}_4\right) = \sum_{n_1n_2n_3n_4}\phi_{n_1}\left(\mathbf{x}_1\right)\phi_{n_2}^*\left(\mathbf{x}_2\right)F^{n_1n_2n_3n_4}\phi_{n_3}\left(\mathbf{x}_3\right)\phi_{n_4}^*\left(\mathbf{x}_4\right)$$

with

$$F^{n_1n_2n_3n_4} = \int d\mathbf{x}_1\mathbf{x}_2\mathbf{x}_3\mathbf{x}_4\phi_{n_1}\left(\mathbf{x}_1\right)\phi_{n_2}^*\left(\mathbf{x}_2\right)F\left(\mathbf{x}_1\mathbf{x}_2;\mathbf{x}_3\mathbf{x}_4;\omega\right)\phi_{n_3}\left(\mathbf{x}_3\right)\phi_{n_4}^*\left(\mathbf{x}_4\right).$$

Transferred to the Bethe-Salpeter equation (1.62), this yields the following matrix elements:

$$L^{n_1n_2n_3n_4}\left(\omega\right) = L_{QIP}^{n_1n_2n_3n_4}\left(\omega\right) + L_{QIP}^{n_1n_2n_5n_6}\left(\omega\right)\,K^{n_5n_6n_7n_8}\,L^{n_7n_8n_3n_4}\left(\omega\right),$$

or, represented in matrix notation:

$$\left[L\left(\omega\right)\right] = \left[L_{QIP}\left(\omega\right)\right] + \left[L_{QIP}\left(\omega\right)\right]\left[K\right]\left[L\left(\omega\right)\right]. \tag{1.64}$$

At this point it is useful to multiply the Bethe-Salpeter equation with a factor $(-i)$ following equation (1.57), since in the end of the calculation one is interested in contracting L to χ:

$$\chi\left(1,2\right) = -iL(1,2;1^+,2^+).$$

One thus finds for the matrix equation:

$$\left[-iL\left(\omega\right)\right] = \left[-iL_{QIP}\left(\omega\right)\right] + \left[-iL_{QIP}\left(\omega\right)\right]\left[iK\right]\left[-iL\left(\omega\right)\right].$$

Evaluating the quasi-independent polarizability L_{QIP}^{RPA} within the single-particle basis starting

from equation (1.63), results in (see Appendix A.8):

$$\begin{aligned} -iL_{QIP}^{n_1n_2n_3n_4}(\omega) &= -i\int d\mathbf{x}_1\mathbf{x}_1'\mathbf{x}_2\mathbf{x}_2'\phi_{n_1}\left(\mathbf{x}_1'\right)\phi_{n_2}^*(\mathbf{x}_1)\, L_{QIP}\left(\mathbf{x}_1\mathbf{x}_2;\mathbf{x}_1'\mathbf{x}_2';\omega\right)\phi_{n_3}^*(\mathbf{x}_2)\,\phi_{n_4}\left(\mathbf{x}_2'\right) \\ &= \sum_{m,l}\frac{\delta(n_1,m)\delta(n_2,l)\delta(n_3,m)\delta(n_4,l)}{\omega-\left(\varepsilon_{n_2}-\varepsilon_{n_1}\right)+i\eta}-\frac{\delta(n_1,l)\delta(n_2,m)\delta(n_3,l)\delta(n_4,m)}{\omega+\left(\varepsilon_{n_1}-\varepsilon_{n_2}\right)-i\eta}, \end{aligned}$$

which points out that the matrix $\left[-iL_{QIP}^{RPA}\right]$ is diagonal in the transition basis ($n_1 = n_3$, $n_2 = n_4$). Moreover, only (occupied $\rightarrow$ unoccupied) or (unoccupied $\rightarrow$ occupied) transitions contribute, whereas (occupied $\rightarrow$ occupied) or (unoccupied $\rightarrow$ unoccupied) do not occur. This can be depicted in form of a (n_1n_2, n_3n_4) matrix:

$$[-iL_{QIP}(\omega)] = \begin{array}{c|cccc} (n_1n_2)(n_3n_4) & mm & ll & ml & lm \\ \hline mm & 0 & 0 & 0 & 0 \\ ll & 0 & 0 & 0 & 0 \\ ml & 0 & 0 & \frac{-1}{\Delta\varepsilon_{n_2n_1}-\omega} & 0 \\ lm & 0 & 0 & 0 & \frac{1}{\Delta\varepsilon_{n_2n_1}-\omega} \end{array} \tag{1.65}$$

where $\Delta\varepsilon_{n_2n_1} = (\varepsilon_{n_2} - \varepsilon_{n_1})$. Consequently, the quasi-independent polarizability L_{QIP}^{RPA} can be compactly written in terms of occupation factors f_i ($f_m = 1$, $f_l = 0$):

$$-iL_{QIP}^{n_1n_2n_3n_4}(\omega) = \frac{(f_{n_2}-f_{n_1})\,\delta(n_1,n_3)\,\delta(n_2,n_4)}{\Delta\varepsilon_{n_2n_1}-\omega},$$

where zeros on the diagonal appear for $f_{n_2} = f_{n_1}$. From now on, we restrict ourselves to the physical meaningful (ml, lm) subspace, where $[-iL_{QIP}]$ has only non-zero diagonal elements and thus is invertible. Moreover, we introduce an occupation matrix $[F]$,

$$F^{n_1n_2n_3n_4} = (f_{n_2}-f_{n_1})\,\delta(n_1,n_3)\,\delta(n_2,n_4),$$

which also has only non-zero elements in the chosen subspace. It follows:

$$[-iL_{QIP}(\omega)] = \left[-i\breve{L}_{QIP}(\omega)\right][F]$$

with

$$\left[-i\breve{L}_{QIP}(\omega)\right][F] = \begin{pmatrix} \frac{1}{\Delta\varepsilon_{n_2n_1}-\omega} & 0 \\ 0 & \frac{1}{\Delta\varepsilon_{n_2n_1}-\omega} \end{pmatrix}\begin{pmatrix} \underbrace{f(n_2-n_1)}_{-1} & 0 \\ 0 & \underbrace{f(n_2-n_1)}_{1} \end{pmatrix}. \tag{1.66}$$

The Bethe-Salpeter matrix equation within the (ml, lm) subspace then reads:

$$[-iL(\omega)] = \left(\left[-i\breve{L}_{QIP}(\omega)\right]^{-1}-[F][iK]\right)^{-1}[F]. \tag{1.67}$$

Since $[-iL_{QIP}]$ is a diagonal matrix, its inverse is readily calculated from equation (1.66) to:

$$\left[-i\breve{L}_{QIP}(\omega)\right]^{-1} = \begin{pmatrix} \Delta\varepsilon_{n_2n_1} & 0 \\ 0 & \Delta\varepsilon_{n_2n_1} \end{pmatrix} - \omega \begin{pmatrix} 1 & 0 \\ 0 & 1 \end{pmatrix},$$

where the frequency dependence has been singled out. This permits to introduce a frequency-independent two-particle effective Hamiltonian H^{2p}, following:

$$[-iL(\omega)] = \left(\left[H^{2p}\right] - \bar{1}\omega\right)^{-1}[F]. \tag{1.68}$$

with

$$\left[H^{2p}\right] = \begin{pmatrix} \Delta\varepsilon_{lm} & 0 \\ 0 & \Delta\varepsilon_{ml} \end{pmatrix} + i \begin{pmatrix} K_{ml,ml} & K_{ml,lm} \\ -K_{lm,ml} & -K_{lm,lm} \end{pmatrix}.$$

In general, the two-particle effective Hamiltonian H^{2p} is a non-Hermitian block matrix, reading in a shorthand notation:

$$\left[H^{2p}\right] = \begin{pmatrix} H^{res} & K^{coupl} \\ -\left(K^{coupl}\right)^* & -\left(H^{res}\right)^* \end{pmatrix}. \tag{1.69}$$

H^{res} is called resonant part, i.e. transitions between (occupied $\rightarrow$ unoccupied) states are treated. On the contrary, $-\left(H^{res}\right)^*$ is an anti-resonant part, where transitions between (unoccupied $\rightarrow$ occupied) states and thus negative frequency transitions are considered. The K^{coupl} and $-\left(K^{coupl}\right)^*$ blocks couple the resonant to the anti-resonant part and include both (occupied $\rightarrow$ unoccupied) and (unoccupied $\rightarrow$ occupied) transitions. Within the the so-called Tamm-Dankoff approximation (TDA), these off-diagonal coupling terms in $\left[H^{2p}\right]$ are neglected. As a result, $\left[H^{2p}\right]$ becomes a block-diagonal, Hermitian matrix, whose eigenvalues are obtained by diagonalizing the Hermitian block matrix $[H^{res}]$, while the eigenvalues of $[-H^{res}]$ are just opposite in sign. The qualities and limitations of the TDA are discussed later in this work.

For the sake of convenience, we focus on the resonant part of the two-particle effective Hamiltonian in the following and search for suited solution schemes. The polarizability L for the resonant part can be obtained within the TDA analogue to equation (1.68) by:

$$[-iL(\omega)] = \left([H^{res}] - \bar{1}\omega\right)^{-1}[F].$$

This implies that, in principle, a matrix with elements stemming from four-point quantities has to be inverted for every frequency ω. As demonstrated in the following, this laborious approach can be circumvented by making use of some mathematical transformations. In the so-called spectral representation, any Hermitian matrix $[M]$ can be expressed in terms of their eigenvalues ε_λ and eigenvectors $|\lambda\rangle$, following:

$$[M] = \sum_\lambda \varepsilon_\lambda |\lambda\rangle \langle\lambda|.$$

If $[M]$ is invertible, its inverse $[M]^{-1}$ is given by:

$$[M]^{-1} = \sum_{\lambda} \frac{1}{\varepsilon_\lambda} |\lambda\rangle \langle\lambda| .$$

For our actual problem, we thus obtain:

$$\begin{aligned} [-iL(\omega)] &= ([H^{res}] - \omega)^{-1} \\ &= \textstyle\sum_\lambda \frac{|\lambda\rangle\langle\lambda|}{\varepsilon_\lambda - \omega}, \end{aligned}$$

where $|\lambda\rangle$ and ε_λ are the eigenvectors and eigenvalues of $[H^{res}]$. The problem of inverting a four-point equation for every frequency ω is thus reduced to an eigenvalue problem for the effective two-particle Hamiltonian:

$$[H^{res}] |\lambda\rangle = \varepsilon_\lambda |\lambda\rangle .$$

This implies that H^{res} has to be diagonalized once in order to obtain its eigenvectors and eigenvalues, the latter corresponding to neutral excitation energies. The presented solution scheme is equivalently valid for the full two-particle Hamiltonian $\left[H^{2p}\right]$, however, due to its non-Hermitian nature, a *generalized* eigenvalue equation distinguishing between left and right eigenvectors has to be solved.

As it is detailed in Appendix A.8, the matrix elements $H^{res}_{ml,m'l'}$ of the resonant part read:

$$H^{res}_{ml,m'l'} = H^{diag}_{ml,ml} + H^{exch}_{ml,m'l'} + H^{scr}_{ml,m'l'},$$

i.e. it is split into a diagonal, an electron-hole exchange and a screened electron-hole interaction part with:

$$\begin{aligned} H^{diag}_{ml,ml} &= \Delta\varepsilon_{lm}\delta_{mm'}\delta_{ll'}, \\ H^{exch}_{ml,m'l'} &= 2\eta \int d\mathbf{x}_1\mathbf{x}_2 \phi_m(\mathbf{x}_1)\, \phi^*_l(\mathbf{x}_1)\; v(\mathbf{x}_1\mathbf{x}_2)\; \phi^*_{m'}(\mathbf{x}_2)\, \phi_{l'}(\mathbf{x}_2), \\ H^{scr}_{ml,m'l'} &= -\int d\mathbf{x}_1\mathbf{x}_2 \phi_m(\mathbf{x}_1)\, \phi^*_l(\mathbf{x}_2)\; W_{stat}(\mathbf{x}_2\mathbf{x}_1)\; \phi^*_{m'}(\mathbf{x}_1)\, \phi_{l'}(\mathbf{x}_2). \end{aligned}$$

This implies that the neutral excitation energies which are obtained by diagonalizing $[H^{res}]$ consist of three contributions. The first one stems from the diagonal part $H^{diag}_{ml,ml}$ and is simply the energy difference between an occupied and an unoccupied single- or quasiparticle level. Further, electron-hole interactions are taken into account through the exchange and the static screened exchange term. The spin is not explicitly included in the derivation, however, the factor 2η in the second term implicitly accounts for it. For singlet excitations, where the promoted electron and the corresponding hole have the same spin, one has $(\eta = 1)$, whereas for triplet excitations one sets $(\eta = 0)$. Note that the standard notation 'exchange' is misleading, since $H^{exch}_{ml,m'l'}$ is clearly a Hartree and not a Hartree-Fock contribution.

In conclusion, the many-body perturbation theory BSE formalism offers the possibility

to access optical absorption properties from first principles. Usually, it is applied in its time-dependent screened Hartree-Fock approximation, see equation (1.60). In practice, it goes along with an underlying GW calculation, from which electronic excitation energies $\varepsilon_{l,m}$ are drawn out to construct the quasi-independent polarizability L_{QIP}^{RPA}. In addition, also the bare Coulomb potential v and the static screened Coulomb potential W_{stat} needed for the (screened) exchange term of the two-particle Hamiltonian H^{2p} can be directly reused from the GW calculation. Once the GW electronic structure is calculated, electron-hole interactions can thus be included in a relatively inexpensive fashion. The BSE approach enjoys great popularity and its reliability has been shown for diverse systems, such as clusters [120], surfaces [121] and solids [122, 123]. In subsequent chapters, its applicability to molecular systems will be discussed in detail.

1.8.3. Excursus: time-dependent DFT

A widely used alternative to the GW/BSE formalism to calculate optical excitation properties for finite systems is time-dependent density functional theory (TDDFT) [35, 36, 124, 125], where one obtains the entire excitation spectrum of relatively large systems at reasonable costs. Analogue to DFT, the time-dependent many-body Schrödinger equation is mapped onto an effective one-particle time-dependent Kohn-Sham equation in TDDFT, through a one-to-one correspondence of the time-dependent one-body external potential $U_{ext}(\mathbf{r},t)$ and the time-dependent one-body density $n(\mathbf{r},t)$ [35, 36]:

$$\hat{H}(t)\,\Psi(\mathbf{r}_1\ldots\mathbf{r}_N,t) = i\frac{d\Psi(\mathbf{r}_1\ldots\mathbf{r}_N,t)}{dt} \longrightarrow \left[-\frac{\nabla^2}{2} + V_{eff}[n](\mathbf{r},t)\right]\phi_i(\mathbf{r},t) = i\frac{d\phi_i(\mathbf{r},t)}{dt}.$$

The fictitious Kohn-Sham system with density $n(\mathbf{r},t) = \sum_i^N |\phi_i(\mathbf{r},t)|^2$ yields by construction the density of the real system and is governed by a time-dependent one-particle effective Kohn-Sham potential $V_{eff}(\mathbf{r},t)$, consisting of a time-dependent external $U_{ext}(\mathbf{r},t)$, a time-dependent Hartree,

$$V_H(\mathbf{r},t) = \int d^3\mathbf{r}'\,\frac{n(\mathbf{r}',t)}{|\mathbf{r}-\mathbf{r}'|},$$

and a time-dependent exchange-correlation contribution $V_{xc}(\mathbf{r},t)$. This is completely similar to the time-independent DFT formalism, however, the exchange-correlation potential is now much more complex, since it is a functional of the entire history of the density $n(\mathbf{r},t)$, involving the solution of all time-dependent Coulomb-interacting problems [36]. One therefore not only has to make assumptions on its spatial, but also on its temporal form. In practice, the adiabatic approach is most common, where $V_{xc}(\mathbf{r},t)$ is assumed to not depend on the history of the density, but only on its present form [82]. In principle, the TDDFT framework can be useful, whenever time-dependent electrons are involved. In practice, TDDFT is widely applied within the linear response regime in order to access the system's response to a weak time-dependent external perturbation. Within this regime, one only has to consider the effective potential for densities close to the ground state density $n_{GS}(\mathbf{r},t)$, i.e. $n(\mathbf{r},t) = n_{GS}(\mathbf{r},t) + n_{ind}(\mathbf{r},t)$, instead of densities strongly varying in time. Different TDDFT methods

to calculate excitation energies within the linear response regime exist, such as the real-time-evolution scheme, and the reader is referred to Ref. [36] for a comprehensive overview. Here, we focus on one of the most popular approaches to access excitation energies for finite systems, namely the eigenvalue problem approach in transition space proposed by Casida [124].

In general, assuming that the time-dependent external perturbation is a weak electric field, the response of the ground state charge density $n_{GS}(\mathbf{r},t)$ is to induce small changes $n_{ind}(\mathbf{r},t)$ via the already introduced reducible polarizability χ [42, 126]:

$$n_{ind}(\mathbf{r},t) = \int dt' \int d^3\mathbf{r}'\, \chi\left[n_{GS}\right](\mathbf{r},\mathbf{r}',t)\, U_{ext}(\mathbf{r}',t').$$

As a remainder, χ denotes in its Lehmann representation in frequency space:

$$\begin{aligned} \chi(\mathbf{r},\mathbf{r}',\omega) &= \textstyle\sum_{k\neq 0} \frac{\rho_k(\mathbf{r})\rho_k^*(\mathbf{r}')}{\omega+\epsilon_k-i\eta} - \frac{\rho_k^*(\mathbf{r})\rho_k(\mathbf{r}')}{\omega-\epsilon_k+i\eta}, \\ \rho_k(\mathbf{r}) &= \langle N,k|\,\hat{n}(\mathbf{r})\,|N,0\rangle, \end{aligned}$$

where ρ_k are charge fluctuations and $(\epsilon_k = E_{N,k} - E_{N,0})$ neutral excitation energies which one wants to calculate [2, 126]. Within the *DFT* framework, the *exact* reducible polarizability χ can be expressed in terms of a closed Dyson-like equation following [36]:

$$\chi(\mathbf{r},\mathbf{r}',\omega) = \chi_0(\mathbf{r},\mathbf{r}',\omega) + \int d\mathbf{r}_1\mathbf{r}_2\, \chi_0(\mathbf{r},\mathbf{r}_1,\omega)\left[v(\mathbf{r}_1,\mathbf{r}_2) + f_{xc}(\mathbf{r}_1,\mathbf{r}_2,\omega)\right]\chi(\mathbf{r}_2,\mathbf{r}',\omega). \quad (1.70)$$

This is the central equation of TDDFT linear response in frequency space, where all quantities are functionals of the ground state density. Whereas time-independent *DFT-KS* eigenvalues can not be mapped straightforwardly on physical quantities, i.e. quasiparticle excitation energies, TDDFT directly provides optical excitation energies and oscillator strengths from the poles of χ [82]. One needed ingredient is χ_0, the non-interacting Kohn-Sham polarizability defined as:

$$\chi_0(\mathbf{r}t,\mathbf{r}'t') \equiv \frac{\partial n_{ind}(\mathbf{r},t)}{\partial V_{tot}(\mathbf{r}',t')}.$$

Here, the total potential V_{tot} consists of the applied external potential, the induced Hartree and the induced exchange-correlation potential. The non-interacting Kohn-Sham polarizability χ_0 can be readily obtained from a standard time-independent *DFT-KS* calculation, where one uses the time-independent *DFT-KS* eigenstates $\phi_{v,c}$ and eigenvalues $\varepsilon_{v,c}$ to construct it:

$$\chi_0(\mathbf{r},\mathbf{r}',\omega) = \sum_{m,l} \frac{\phi_l(\mathbf{r})\,\phi_l^*(\mathbf{r}')\,\phi_m(\mathbf{r}')\,\phi_m^*(\mathbf{r})}{\omega-\left(\varepsilon_l^0-\varepsilon_m^0\right)+i\eta} - \frac{\phi_m(\mathbf{r})\,\phi_m^*(\mathbf{r}')\,\phi_l(\mathbf{r}')\,\phi_l^*(\mathbf{r})}{\omega+\left(\varepsilon_l^0-\varepsilon_m^0\right)-i\eta}.$$

Here, l stands for unoccupied and m for occupied states. It thus corresponds to a special type of a non-interacting polarizability P_{IP}, see equation (1.50). However, its physical interpretation is difficult due to the missing correspondence of Kohn-Sham eigenvalues and single-particle excitation energies. Expression (1.70) is very similar to the presented Dyson equation for χ within the Green's functions approach (see below), however, important differences have to be noted. First, the TDDFT framework allows to find a closed Dyson-like

equation for the exact χ. Within the Green's function approach, this is only achieved within the random-phase approximation for χ, see equation (1.51). Instead, for the exact χ, the irreducible polarizability P enters the Dyson equation:

$$\chi(1,2) = P(1,2) + \int d34\, P(1,3) v(3,4)\, \chi(4,2).$$

The definition of P (1.34) is analogue to that of χ_0, however, it does not include the induced exchange-correlation potential, but solely the external and the induced Hartree potential. It is a complex object itself, resulting in a highly non-trivial equation for χ, see equation (1.53). On the contrary, by utilizing χ_0, it is possible to shift the complexity of the problem into the time-dependent exchange correlation kernel f_{xc}. As a result, one has a closed equation for the two-point polarizability χ and avoids the detour by the four-point polarizability L. However, the exact kernel, defined as

$$f_{xc}\left(\mathbf{r}t, \mathbf{r}'t'\right) = \left.\frac{\partial V_{xc}\left[n\left(\mathbf{r},t\right)\right]}{\partial n\left(\mathbf{r}',t'\right)}\right|_{n=n_{GS}},$$

is unknown and one has to find appropriate approximations to it. The most common approach is the adiabatic local-density approximation (TDLDA), where f_{xc} is approximated by the derivative of the static and local LDA exchange-correlation functional [42]:

$$f_{xc}^{LDA}\left(\mathbf{r},\mathbf{r}'\right) = \delta\left(\mathbf{r}-\mathbf{r}'\right)\frac{\partial V_{xc}^{LDA}\left[n\left(\mathbf{r}\right)\right]}{\partial n\left(\mathbf{r}\right)}.$$

This is a drastic approximation, but its simplicity is nevertheless tempting.

In the case of frequency-independent exchange-correlation kernels and systems with a discrete excitation energy spectrum, such as e.g. finite systems, it is convenient to reformulate the response equation (1.70) in terms of an eigenvalue problem. By rewriting the equations in terms of a transition basis $\psi^{exc}\left(\mathbf{r},\mathbf{r}'\right)$ consisting of products of Kohn-Sham occupied $\phi_m\left(\mathbf{r}\right)$ and empty $\phi_l\left(\mathbf{r}'\right)$ states, one obtains, analogously to the BSE approach, an effective two-particle Hamiltonian H^{2p}. The latter is composed of (anti-)resonant H^{res} and coupling K^{coupl} blocks and is non-Hermitian. For real wave functions and in the case of TDDFT, Casida demonstrated that one can simplify the problem to the following eigenvalue equation [36, 42, 124, 126]:

$$\left[H^{diag}\right]^{\frac{1}{2}}\left(\left[H^{diag}\right] + 4\left\{\left[H^{exch}\right] + \left[H^{xc}\right]\right\}\right)\left[H^{diag}\right]^{\frac{1}{2}}\left[X\right] = \varepsilon_m^2\left[X\right],$$

for which efficient algorithms, such as Haydock's recursion method [127], can be applied [36, 42]. The eigenvalues are the square of the excitation energies and the eigenvectors are related to oscillator strengths. $\left[H^{diag}\right]$, $\left[H^{exch}\right]$ and $\left[H^{xc}\right]$ represent matrix operators, whose

elements read:

$$
\begin{aligned}
H^{diag}_{ml,m'l'} &= \delta_{mm'}\delta_{ll'}\left(\varepsilon^0_l - \varepsilon^0_m\right), \\
H^{exch}_{ml,m'l'} &= \int d\mathbf{r}d\mathbf{r}'\phi_m(\mathbf{r})\,\phi^*_l(\mathbf{r})\; v(\mathbf{r},\mathbf{r}')\;\phi^*_{m'}(\mathbf{r}')\,\phi_{l'}(\mathbf{r}'), \\
H^{xc}_{ml,m'l'} &= \int d\mathbf{r}d\mathbf{r}'\phi_m(\mathbf{r})\,\phi^*_l(\mathbf{r})\; f_{xc}(\mathbf{r},\mathbf{r}')\;\phi^*_{m'}(\mathbf{r}')\,\phi_{l'}(\mathbf{r}').
\end{aligned}
$$

A direct comparison of the resonant part H^{res} of the BSE and the TDDFT formalism,

$$
H^{res} = H^{diag} + H^{exch} + H^{scr/xc},
$$

reveals that in TDDFT one also starts from a single-particle excitation spectrum (the diagonal H^{diag} term) and then includes electron-hole interactions through the two remaining contributions. The diagonal terms within BSE and TDDFT are similar, however, in one case Kohn-Sham eigenvalues are taken as a starting point and in the other case quasiparticle excitation energies. The "exchange" terms are totally equal, whereas the screening is included through the static and non-local exchange-correlation kernel $f_{xc}(\mathbf{r},\mathbf{r}')$ within TDDFT and through the static and non-local screened Coulomb potential $W_{stat}(\mathbf{r},\mathbf{r}')$ within BSE, respectively. In the case of TDLDA, the exchange-correlation kernel becomes the static and local LDA functional, i.e. the screened exchange contribution simplifies to:

$$
H^{xc,LDA}_{ml,m'l'} = \int d\mathbf{r}\;\phi_m(\mathbf{r})\,\phi^*_l(\mathbf{r})\;\frac{\partial V^{LDA}_{xc}[n]}{\partial n(\mathbf{r})}\,\phi^*_{m'}(\mathbf{r})\,\phi_{l'}(\mathbf{r}).
$$

Important differences between TDDFT with (semi)local kernels and BSE in the electron and hole space integration variables will be highlighted later in the course of the discussion of charge-transfer optical excitations.

By expressing the response equation in transition space, one has to solve, similar to the BSE approach, a four-point problem. Whereas this is inevitable in BSE, one can choose between a representation in the transition space basis consisting of pairs of occupied and unoccupied states and a two-point problem in TDDFT, since χ is governed by a closed Dyson-like two-point response equation. The advantage of the transition space representation is that a direct comparison with BSE is possible. Moreover, one can directly access the character of a transition, i.e. the mainly contributing occupied and unoccupied orbitals, associated with a specific excitation energy. This information is not provided by the solution of the two-point equation, where one only obtains excitation energies and the corresponding oscillator strengths. However, from a computational point of view, the four-point representation is only convenient if the diagonalization of the effective eigenvalue problem is less demanding than the inversion of the response equation for several frequencies, which automatically implies frequency-independent kernels [36]. Moreover, the quadratic basis of contributing occupied and unoccupied states must be smaller than the real-space (reciprocal-space) basis for the corresponding two-point problem. In TDDFT, this is only the case for small finite systems with well separated energy levels, where only a small part of the optical spectrum is of

interest [36]. For these systems, Casida's TDDFT approach to calculate optical excitation spectra is most popular. Later in this work, a detailed comparison of the seemingly so similar, but nevertheless conceptually different TDDFT linear response and GW/BSE approach is presented for organic molecules in the gas phase.

2 | Details on the Implementation

Many-body perturbation theory GW/BSE calculations, as presented later in this work, have been carried out using the FIESTA package [6, 8, 7]. The latter is a recent Gaussian-basis implementation of the GW/BSE formalisms, suited for calculations on finite systems. Computationally demanding non-local quantities, such as the irreducible polarizability or the screened Coulomb potential, are expressed within an auxiliary basis instead of a full product basis. Both the resolution of the identity technique (RI-SVS) and the resolution of the identity Coulomb metric technique (RI-V) are available to express the auxiliary basis. The self-energy is obtained by explicitly evaluating the frequency integral over the one-particle Green's function and the screened Coulomb potential using contour deformation techniques, i.e. one goes beyond any plasmon pole approximation. Details on the mentioned aspects are given in the following.

2.1. Ab initio calculations using a Gaussian basis

The equations derived in the last chapter, ranging from Hartree-Fock to TDDFT, provide mathematical formalisms to describe matter at a quantum level. Although approximations and simplifications have already been carried out in their derivation, one ends up with computationally demanding integro-differential equations, depending on a multitude of arguments. Due to their complexity, it is not evident that an analytic solution exists.

2.1.1. The Linear Combination of Atomic orbitals (LCAO) approach

Numerically, different approaches to tackle these complicated equations have been developed. One approach consists of expressing these problems in terms of basis sets. The advantage is that the resulting equations can be readily transformed into matrix equations. This reduces the original problem to a system of linear equations, a task for which computers are more than suited and for which efficient algorithms have been developed [128]. This will be demonstrated for eigenvalue problems of the type [69]:

$$\hat{O} \left| f \right\rangle = w \left| f \right\rangle . \tag{2.1}$$

Here, $|f\rangle$ is an eigenvector to the operator $\hat{O}$ with eigenvalue w. In the following, we are working in the real space representation, i.e. $f(\mathbf{r}) = \langle \mathbf{r} | f \rangle$ and $\hat{O}(\mathbf{r}) = \langle \mathbf{r} | \hat{O} | \mathbf{r} \rangle$. Several equations already encountered in preceding chapters represent eigenvalue problems, such as

the Hartree-Fock, the Kohn-Sham or the quasiparticle equation.

The basis set is introduced by expanding the eigenfunctions $f(\mathbf{r})$ in a complete set of basis functions $\{\alpha_\mu\}$ with weighting coefficients c_μ:

$$f(\mathbf{r}) = \sum_{\mu=1}^{\infty} c_\mu \alpha_\mu(\mathbf{r}). \tag{2.2}$$

We assume the general case of non-orthogonal basis sets, for which the matrix elements of the overlap matrix $[S]$ are given by:

$$S_{\mu\nu} = \int d^3\mathbf{r}\, \alpha_\mu^*(\mathbf{r})\, \alpha_\nu(\mathbf{r}).$$

Inserting (2.2) into equation (2.1) leads to:

$$\sum_{\mu=1}^{\infty} \hat{O}(\mathbf{r})\; c_\mu \alpha_\mu(\mathbf{r}) = \sum_{\mu=1}^{\infty} w\, c_\mu \alpha_\mu(\mathbf{r}).$$

Multiplication by an arbitrary basis function $\alpha_\nu(\mathbf{r})$ from the left and integration over $d^3\mathbf{r}$ results in:

$$\sum_{\mu=1}^{\infty} c_\mu \int d^3\mathbf{r}\, \alpha_\nu(\mathbf{r})\, \hat{O}(\mathbf{r})\, \alpha_\mu(\mathbf{r}) = \sum_{\mu=1}^{\infty} w\, c_\mu \int d^3\mathbf{r}\, \alpha_\nu(\mathbf{r})\, \alpha_\mu(\mathbf{r}) = \sum_{\mu=1}^{\infty} w\, c_\mu S_{\mu\nu},$$

i.e. the introduction of a basis $\{\alpha_\mu\}$ transforms equation (2.1) into a generalized eigenvalue matrix equation:

$$[O]\,[c] = w\,[c]\,[S], \tag{2.3}$$

where the vector $[c]$ contains the weighting coefficients $[c]_\mu = c_\mu$ and where the matrix elements of $[O]$ denote $O_{\mu\nu} = \int d\mathbf{r}\, \alpha_\mu^*(\mathbf{r})\; \hat{O}(\mathbf{r})\; \alpha_\nu(\mathbf{r})$. Once the matrix elements are calculated, efficient linear algebra routines exist to solve equation (2.3). In the case of orthogonal basis sets, the overlap matrix $[S]$ simply reduces to the unitary matrix.

In principle, the $\{\alpha_\mu\}$ form a complete basis set, i.e. on the one hand any $f(\mathbf{r})$ is reproduced exactly, but on the other hand $\bar{O}$ becomes an infinite matrix. In practice, a certain cut-off N is chosen limiting the amount of available basis functions:

$$f(\mathbf{r}) \approx \sum_{\mu=1}^{N} c_\mu \alpha_\mu(\mathbf{r}).$$

In that way, the eigenvalue problem is reduced to a $N \times N$ problem, where the calculated N eigenvalues approximate the true eigenvalues. This implies that the basis set has to be selected very carefully, since it has a strong impact on the quality of the results within the chosen level of theory (HF, $DFT\text{-}KS$, GW). In the case of orthogonal basis sets, the inclusion of more and more basis functions always improves the completeness, i.e. these basis sets are systematic. However, as it will be detailed later in this section, this is not the case for non-orthogonal basis sets, where therefore special care must be taken.

Within the Linear Combination of Atomic Orbitals ($LCAO$) approach, molecular wave functions are expanded in atom-centered basis functions, such as Gaussian functions. These atom-centered functions consist of single-electron functions localized at the nuclei of the specific atoms, which very efficiently describe the critical region near the nuclei. It tends to produce, in particular for finite size systems, much more compact basis sets than plane wave or real-space basis sets, even though convergency is a more difficult issue. A detailed review of state-of-the-art atom-centered basis sets is provided by Ref. [129].

2.1.2. From a product to an auxiliary basis

Introducing a basis $\{\alpha\}$ consisting of N basis functions leads for matrix elements of non-local operators such as the screened Coulomb potential W, the irreducible susceptibility P and the Fock operator V_F to four-center-two-electron integrals of the type:

$$\int d^3\mathbf{r}\, d^3\mathbf{r}'\, \alpha_\mu^*(\mathbf{r})\, \alpha_{\kappa'}^*(\mathbf{r}')\, \hat{O}(\mathbf{r},\mathbf{r}')\, \alpha_\kappa(\mathbf{r})\, \alpha_\nu(\mathbf{r}')\,. \tag{2.4}$$

Evaluating these matrix elements is equivalent to working in a so-called product basis:

$$P_{\mu\kappa}(\mathbf{r}) = \alpha_\mu^*(\mathbf{r})\, \alpha_\kappa(\mathbf{r})\,,$$

containing $\frac{N^2}{2}$ different elements. This implies rather large basis sets compared to the original $\{\alpha(\mathbf{r})\}$ basis and consequently high computational costs. Moreover, assuming a Gaussian function basis set for $\{\alpha(\mathbf{r})\}$, their product is not further centered on single atoms, but on barycentric points $\mathbf{P}$. By way of example, for two unnormalized primitive s-type Gaussian functions $G_1 = e^{-\gamma_1(\mathbf{r}-\mathbf{A})^2}$ and $G_2 = e^{-\gamma_2(\mathbf{r}-\mathbf{B})^2}$ centered at atoms $\mathbf{A}$ and $\mathbf{B}$ one finds (see Appendix A.10):

$$G_1 G_2 = C\, e^{-\eta(\mathbf{r}-\mathbf{P})^2},$$

with $(\eta = \gamma_1 + \gamma_2)$, $\mathbf{P} = \frac{\gamma_1\mathbf{A}+\gamma_2\mathbf{B}}{\eta}$ and $C = e^{-\frac{\gamma_1\gamma_2(\mathbf{A}-\mathbf{B})^2}{\gamma_1+\gamma_2}}$. The mentioned points suggest not to work in the full product basis, but in a smaller basis consisting of L elements which approximately reproduces the product basis. Such a basis is called an *auxiliary basis* $\{\beta(\mathbf{r})\}$:

$$P_{\mu\kappa}(\mathbf{r}) \simeq \sum_{\lambda}^{L} c_{\mu\kappa\lambda}\beta_\lambda(\mathbf{r})\,,$$

where $c_{\mu\kappa\lambda}$ are weighting coefficients. The equality can become exact for $L \to \infty$. Concerning the character of the auxiliary basis $\{\beta(\mathbf{r})\}$, no general form is specified. For $\{\alpha(\mathbf{r})\}$ consisting of Gaussian functions of the type $e^{-\mu(\mathbf{r}-\mathbf{A})^2}$, it seems convenient to choose an auxiliary basis with Gaussian functions centered on specific atoms. The number of considered auxiliary basis functions per atom and the best exponential coefficients μ represent a crucial point which requires extensive accuracy tests. Even though representing a strong approximation to the full product basis, auxiliary basis sets strongly reduce computational costs and make the evaluation of matrix elements for large systems technically feasible.

Supposing for the moment that $\{\beta(\mathbf{r})\}$ is complete, one can define two different closure

relations, namely:

$$\sum_{\lambda\lambda'} |\beta_\lambda\rangle\, S^{-1}_{\lambda\lambda'}\, \langle\beta_{\lambda'}| = \bar{1} \tag{2.5}$$

and

$$\sum_{\lambda\lambda'} |\hat{v}\beta_\lambda\rangle\, [\hat{v}]^{-1}_{\lambda\lambda'}\, \langle\beta_{\lambda'}| = \bar{1}, \tag{2.6}$$

with $[\hat{v}]_{\lambda\lambda'} = \langle\beta_\lambda(\mathbf{r})|\, \hat{v}(\mathbf{r},\mathbf{r}')\, |\beta_{\lambda'}(\mathbf{r}')\rangle$ and $S_{\lambda\lambda'} = \langle\beta_\lambda|\, \beta_{\lambda'}\rangle$. Based on these closure relations, matrix elements for non-local operators can be formulated in two ways.

The *resolution of the identity technique* (RI-SVS) is based on equation (2.5) and yields:

$$\langle\alpha_\mu(\mathbf{r})\,\alpha_\nu(\mathbf{r})|\, \hat{O}(\mathbf{r},\mathbf{r}')\, |\alpha_\tau(\mathbf{r}')\,\alpha_\sigma(\mathbf{r}')\rangle = \textstyle\sum_{\lambda\lambda'}\; c_{\mu\nu\lambda} c^*_{\tau\sigma\lambda'} \left\langle \hat{O} \right\rangle_{\lambda\lambda'},$$

where the coefficients are given by:

$$\begin{aligned} c_{\mu\nu\lambda} &= \langle\alpha_\mu(\mathbf{r})\,\alpha_\nu(\mathbf{r})|\, \beta_\lambda(\mathbf{r})\rangle \\ c^*_{\tau\sigma\lambda'} &= \langle\beta_{\lambda'}(\mathbf{r}')|\, \alpha_\tau(\mathbf{r}')\,\alpha_\sigma(\mathbf{r}')\rangle\,. \end{aligned}$$

The matrix elements read:

$$\begin{aligned} \left\langle \hat{O} \right\rangle_{\lambda\lambda'} &= S^{-1}_{\lambda\lambda'} \left[\hat{O}\right]_{\lambda\lambda'} S^{-1}_{\lambda\lambda'}, \\ \left[\hat{O}\right]_{\lambda\lambda'} &= \langle\beta_\lambda(\mathbf{r})|\, \hat{O}(\mathbf{r},\mathbf{r}')\, |\beta_{\lambda'}(\mathbf{r}')\rangle\,. \end{aligned} \tag{2.7}$$

Consequently, only three ingredients are necessary in the RI-SVS representation: the inverse overlap between auxiliary basis functions S^{-1}, the overlap $\langle\alpha_\mu\alpha_\nu|\, \beta_\lambda\rangle$ between the original basis $\{\alpha\}$ and the auxiliary basis $\{\beta\}$, and the matrix elements $\langle\beta_\lambda|\, \hat{O}\, |\beta_{\lambda'}\rangle$, whose number is significantly reduced due to the limited number of used auxiliary basis functions. For Dyson-like equations, such as $W = v + vPW$, one thus obtains within the RI-SVS equations of the type:

$$\langle W\rangle = \langle v\rangle + \langle v\rangle\, [P]\, \langle W\rangle\,, \tag{2.8}$$

as it can be easily verified by inserting (2.5). These equations are solved by inversion, following:

$$\langle W\rangle = \langle v\rangle\, (\bar{1} - \langle v\rangle\, [P])^{-1}\,.$$

Within the *resolution of the identity Coulomb metric technique* (RI-V), matrix elements are expressed according to equation (2.6):

$$\begin{aligned} &\langle\alpha_\mu(\mathbf{r})\,\alpha_\nu(\mathbf{r})|\, \hat{O}(\mathbf{r},\mathbf{r}')\, |\alpha_\tau(\mathbf{r}')\,\alpha_\sigma(\mathbf{r}')\rangle = \\ &\textstyle\sum_{\lambda\lambda'}\; \langle\alpha_\mu(\mathbf{r})\,\alpha_\nu(\mathbf{r})|\, \hat{v}\beta_\lambda(\mathbf{r})\rangle\;\; [\hat{v}]^{-1}_{\lambda\lambda'}\;\; \left\langle \beta_{\lambda'}(\mathbf{r}')\, \hat{O} \right| \alpha_\tau(\mathbf{r}')\,\alpha_\sigma(\mathbf{r}') \Big\rangle. \end{aligned}$$

To conclude, within the resolution of the identity framework, four-center-two-electron integrals are transformed to expressions containing only two- and three-center integrals. The latter can be efficiently computed in a Gaussian basis, which will be demonstrated later in this

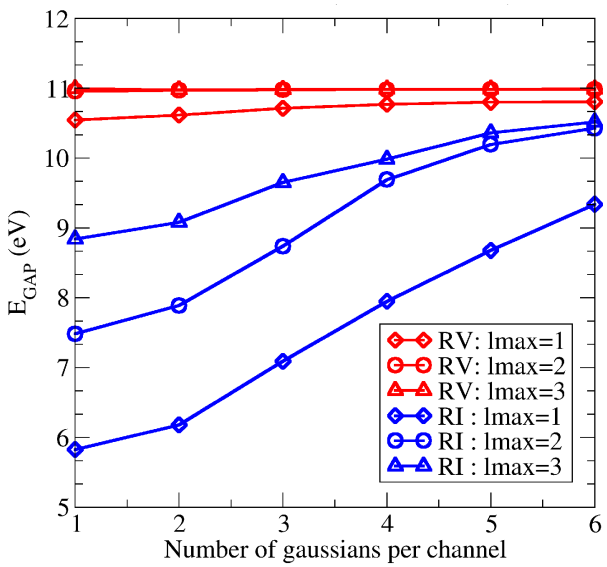

Figure 2.1.: Convergence plot of the *GW* gap energy of the benzene molecule with respect to the number N of Gaussian functions per angular channel of the auxiliary basis within the RI-SVS and the RI-V approach, respectively. The calculations have been carried out using a TZ2P Kohn-Sham basis and a Gaussian function auxiliary basis ($e^{-\alpha r^2}$) with an even-tempered distribution of the localization coefficients α ranging from $\alpha_{min} = 0.10$ Bohr^{-2} to $\alpha_{max} = 3.2$ Bohr^{-2} and N Gaussian functions per l-channel, with $l_{max} = 1 \ldots 3$. Clearly, the gap converges significantly faster with respect to N and l_{max} within the RI-V approach, allowing thus for the utilization of smaller basis sets within this method. Figure reproduced by courtesy of P. Boulanger.

chapter. The RI-SVS method bears the advantage of producing sparse matrices, reducing significantly computational costs. This is not the case for the RI-V approach, which is therefore more expensive (by way of example see Table 2.1). Reducing the number of auxiliary basis functions to L, an error on the matrix elements is introduced. Provided that the operator $\hat{O}$ in the above equations corresponds to the Coulomb operator $\hat{v}$, i.e. for Coulomb integrals, it can be shown that the error cancels to first order in the RI-V approach [130]. On the contrary, within RI-SVS non-zero first order terms arise. Consequently, errors in the Coulomb integrals due to the incompleteness of the auxiliary basis are minimized using the RI-V rather than the RI-SVS technique (see Fig. 2.1).

2.1.3. Common atom-centered basis sets

Slater-type orbitals Slater introduced so-called *Slater-type orbitals* (*STO*), which resemble the wave functions of the hydrogen atom. They consist of a radial and angular part, following:

$$\alpha^{STO} = \alpha_n^{STO}(|\mathbf{r}|)\, Y_{lm}(\phi, \varphi),$$

with

$$\alpha_n^{STO}(|\mathbf{r}|) = |\mathbf{r}|^{n-1} e^{-\gamma|\mathbf{r}|}.$$

Y_{lm} are spherical harmonics describing the angular part of the wave function and γ is a constant accounting for the screening of the nuclear charge by the surrounding electrons. The main quantum number is presented by n, the angular momentum quantum number by l and the magnetic quantum number by m. The radial part of the wave function is represented by $\alpha_{nl}^{STO}(|\mathbf{r}|)$. This basis is very suited for atomic calculations, since the cusp condition at the origin and the exponential decay known from the hydrogen atom are well satisfied. However, matrix elements become computationally very demanding, because simple analytic relations valid for e.g. Gaussian functions do not exist.

Gaussian-type functions To circumvent this problem, Boys introduced Gaussian-type orbitals (GTO) in 1950 [65, 131]. The angular part is still described by spherical harmonics, however, for the radial part Gaussian functions are introduced:

$$\alpha^{GTO}(\mathbf{r}) = e^{-\gamma \mathbf{r}^2}.$$

As it will be shown later in this chapter, matrix elements are tremendously simplified in this basis, counterbalancing their improper behavior both for $\mathbf{r}$ at the nucleus and at infinity. Indeed, they show neither a cusp at the origin nor the right $e^{-|\mathbf{r}|}$ decay for $\mathbf{r} \to \infty$.

Combining both numerical efficiency and a reasonable physical behavior is achieved by introducing *contracted Gaussian functions* (CGF). They are based on the fact that a Slater-type function can already be well reproduced using a linear combination of only a few different Gaussian-type functions [132]:

$$\alpha^{CGF} = \sum_n d_n \alpha_n^{GTO}.$$

Typically, ($n = 2$-6) Gaussian-type functions are sufficient to fit a Slater-type orbital. The simplest basis set using these contracted Gaussian functions is the STO-nG basis set. By way of example, in the case of the STO-3G basis set, one attempts to fit a Slater-type function by a linear combination of three different GTOs.

Minimal basis sets STO-nG belong to the so-called group of minimal basis sets. The latter include only one CGF per occupied orbital in the neutral atom. For the hydrogen atom, only a single $1s$ CGF, while for the carbon atom five CGF for the $1s$, $2s$, and three $2p$ orbitals are considered. The CGF, in turn, are obtained by linear combinations of Gaussian-type functions. Calculations performed with these basis sets are very fast, however, they provide only qualitative results suited as a starting point for more precise calculations.

Split-valence basis sets An expansion to minimal basis sets are so-called split-valence basis sets. They are taking into account that valence electrons are much more involved in chemical processes compared to the nearly chemically inert core electrons. Therefore, instead of a single CGF, a linear combination of several CGF is used to describe a valence orbital. Corresponding to the number of CGF included, these basis sets are called split-valence (double-, triple-, quadruple-)zeta basis sets. The group of Pople [133] introduced the following notation

for split-valence basis sets:

$$X - YZg,$$

where X represents the number of Gaussian-type functions g comprised in the fit of each core orbital. Y and Z denote that valence orbitals are a linear combination of two CGF, each of them composed of Y and Z Gaussian-type functions. Split-valence triple- or quadruple-zeta basis sets are denoted $X - YZWg$ and $X - YZWVg$, respectively.

Only increasing the number of CGF per atomic orbital does not automatically improve the quality of the basis. In addition, one should also include CGFs whose character significantly differs from the ones already considered. One possibility is to add polarization functions, i.e. functions with higher angular channels. They increase the flexibility of the atom to form chemical bonds in every direction and thus improve the calculated molecular structures. In the notation of Pople, an asterisk denotes additional polarization orbitals:

$$X - YZg*.$$

Two asterisks signify that polarization orbitals are also added to light atoms. For the hydrogen atom, this means adding a p-like function to the basis. Another possibility is to include diffuse functions, i.e. very shallow Gaussian-type functions:

$$X - YZ + g.$$

In Pople's notation, they are represented by one/two plus sign(s). They are used to describe more accurately the tail of molecular orbitals. For the sake of illustration, a 6-31+g* basis set contracts six GTO to one CGT for each core orbital, whereas the valence orbitals are described by linear combinations of two CGT – one of them consisting of three GTO, the other one of a single GTO. Moreover, except for light atoms, polarization and diffusive functions are added.

2.1.4. Gaussian function basis sets and analytic properties

Basis sets using Gaussian functions [65, 129, 131] are commonly used in quantum chemistry calculations on molecules. First, physical meaningful STO can be reproduced by contracting only a few GTO, i.e. the size of the basis is not significantly augmented compared to a STO basis. Moreover, Gaussian functions provide mathematical properties which transform complicated matrix elements in simple analytic expressions making calculations extremely efficient. These mathematical properties are presented in detail in this subsection.

2.1.4.1. General definitions

Before presenting in detail mathematical advantages, the common nomenclature is shortly reviewed in order to avoid confusion. Gaussian functions are called *primitive,* if they consist of a single Gaussian function. They have to be distinguished from *contracted* Gaussian functions which are a linear combination of several primitive Gaussian functions located at the same center. Moreover, one distinguishes between Cartesian and spherical Gaussian functions. An

unnormalized primitive Cartesian Gaussian function centered at $\mathbf{A}$ reads:

$$\alpha^{GTO}(\mathbf{r}) = (r_x - A_x)^h (r_y - A_y)^i (r_z - A_z)^j \; e^{-\gamma(\mathbf{r}-\mathbf{A})^2},$$

where (h, i, j) are natural numbers and γ the exponential coefficient. Similar to the wave functions of the hydrogen atom, we can define the angular momentum quantum number using the exponents like $(l = h + i + j)$. For $(l = 0)$, we obtain a s-orbital-like Gaussian function, $(\alpha_s^{GTO}(\mathbf{r}) = e^{-\gamma\mathbf{r}^2})$, for $(l = 1)$ p-like functions, $(\alpha_p^{GTO}(\mathbf{r}) = r_x e^{-\gamma\mathbf{r}^2},\ r_y e^{-\gamma\mathbf{r}^2},\ r_z e^{-\gamma\mathbf{r}^2})$, et cetera. Besides Cartesian Gaussian functions, so-called Spherical Gaussian functions are widely used:

$$\alpha^{GTO} = |\mathbf{r} - \mathbf{A}|^l \; e^{-\gamma(\mathbf{r}-\mathbf{A})^2} Y_{lm}(\phi, \varphi),$$

where m is the magnetic quantum number and $Y_{lm}(\phi, \varphi)$ spherical harmonics. Cartesian and Spherical Gaussian function basis sets are only equivalent up to $(l = 1)$, so one has to be careful which type of Gaussian functions is actually implemented. Nevertheless, unitary transformations allow one to easily switch between one representation and the other.

2.1.4.2. Advantages and subtleties of Gaussian basis sets

Using Gaussian function basis sets results in important computational advantages. Demanding parts of the calculation, which are otherwise only solvable with much computational effort, can be treated analytically. However, some subtleties have to be considered in order to produce accurate results. Once these points are respected, the ratio between efficiency and accuracy is impressive.

Calculating matrix elements in a Gaussian basis Calculating matrix elements denotes the main step in most ab initio calculations and, once this is done, efficient linear algebra routines exist to solve systems of linear equations. Basis sets with Gaussian functions bare the advantage that a lot of matrix elements can be transformed in analytic expressions using for example the Gaussian product theorem or the Gaussian integral properties (see Appendix A.10). In turn, these analytic expressions can be evaluated efficiently on computers. For the sake of illustration, this is demonstrated for two examples. The first one is the three-center integral

$$M_{\mu\nu\lambda} = \langle \alpha_\mu \alpha_\nu | \, \beta_\lambda \rangle,$$

which has been already encountered previously within the RI-SVS formalism and which is frequently needed in calculations dealing with non-local operators. For the sake of clarity, we choose α_μ, α_ν and β_κ to be unnormalized primitive s-like Gaussian functions centered at atoms $\mathbf{R}_\mu, \mathbf{R}_\nu$ and $\mathbf{R}_\lambda$, respectively. Following the Gaussian product theorem, the product of three Gaussians yields a Gaussian function, multiplied by a constant C and centered at the barycentric point $\mathbf{P} = \frac{\mu\mathbf{R}_\mu + \lambda\mathbf{R}_\lambda + \nu\mathbf{R}_\nu}{\eta}$ with an exponential coefficient $(\eta = \mu + \lambda + \nu)$:

$$\begin{aligned} M_{\mu\nu\lambda} &= \int d^3\mathbf{r} \; e^{-\mu(\mathbf{r}-\mathbf{R}_\mu)^2} \, e^{-\lambda(\mathbf{r}-\mathbf{R}_\lambda)^2} \, e^{-\nu(\mathbf{r}-\mathbf{R}_\nu)^2} \\ &= C_{\mu\nu\lambda} \int d^3\mathbf{r} \, e^{-\eta(\mathbf{r}-\mathbf{P})^2}. \end{aligned}$$

This Gaussian integral can be straightforwardly solved by separation and gives:

$$\begin{aligned} M_{\mu\nu\lambda} &= C_{\mu\nu\lambda} \int d^3r_x \, e^{-\eta(r_x-P_x)^2} \int d^3r_y \, e^{-\eta(r_y-P_y)^2} \int d^3r_z \, e^{-\eta(r_z-P_z)^2} \\ &= C_{\mu\nu\lambda} \left(\tfrac{\pi}{\eta}\right)^{\frac{3}{2}}, \end{aligned}$$

an analytic expression easily computed. Moreover, taking for illustration the derivative of $M_{\mu\nu\lambda}$ with respect to P_x, leads to the product of a primitive s-like and p_x-like Gaussian function, initiating by successive derivations efficient recursion relations.

We now come to the central Coulomb integrals, which, in an auxiliary basis $\{\beta\}$ within the RI-SVS representation, read:

$$[V_C]_{\lambda\lambda'} = \iint d^3\mathbf{r} d^3\mathbf{r}' \, \frac{\beta^*_\lambda(\mathbf{r}) \; \beta_{\lambda'}(\mathbf{r}')}{|\mathbf{r}\text{-}\mathbf{r}'|}.$$

In a Gaussian function auxiliary basis, this demanding non-local integral reduces to a simple analytic expression. This is demonstrated in detail in Appendix A.10 for two unnormalized, primitive s-like Gaussian functions centered at $\mathbf{A}$ and $\mathbf{B}$ and results in:

$$\begin{aligned} [V_C]_{s,s'} &= \int\int d^3\mathbf{r} \, d^3\mathbf{r}' \, \frac{e^{-\kappa|\mathbf{r}-\mathbf{A}|^2} e^{-\lambda|\mathbf{r}'-\mathbf{B}|^2}}{|\mathbf{r}-\mathbf{r}'|} \\ &= \left(\tfrac{\pi}{\kappa}\right)^{\frac{3}{2}} \left(\tfrac{\pi}{\lambda}\right)^{\frac{3}{2}} \tfrac{1}{\mathbf{R}} \mathrm{erf}\left(\sqrt{\tfrac{\mathbf{R}^2}{4\gamma}}\right), \end{aligned}$$

where we defined $(\mathbf{R} = \mathbf{A} - \mathbf{B})$ and $\left(\gamma = \frac{1}{4\kappa} + \frac{1}{4\lambda}\right)$. We also introduced the error function $\left[\mathrm{erf}(y) = \frac{2}{\sqrt{\pi}} \int_0^y du \, e^{-u^2}\right]$. The latter is directly related to the so-called Boys function F_n of order n [65, 131], obeying:

$$\begin{aligned} F_n(x) &= \int_0^1 dt \; t^{2n} e^{-xt^2} \\ F_0(x) &= \tfrac{\sqrt{\pi}}{2\sqrt{x}} \, \mathrm{erf}(\sqrt{x}), \; x > 0. \end{aligned}$$

The Boys function plays a key role in one- or two-electron Coulomb integral evaluation, since efficient evaluation methods based on upward/downward recursion exist [134]:

$$\begin{aligned} F_n(x) &= \tfrac{1}{2x} \left[(2n-1) \, F_{n-1}(x) - e^{-x}\right], \\ F_n(x) &= \tfrac{1}{2n+1} \left[2x \, F_{n+1}(x) - e^{-x}\right]. \end{aligned}$$

Rewriting the Coulomb matrix elements for two s-like Gaussian functions in terms of the Boys function gives:

$$[V_C]_{s,s'} = \frac{1}{\sqrt{\pi}\sqrt{\gamma}} \left(\frac{\pi}{\kappa}\right)^{\frac{3}{2}} \left(\frac{\pi}{\lambda}\right)^{\frac{3}{2}} F_0\left(\frac{\mathbf{R}^2}{4\gamma}\right).$$

$[V_C]_{s,s'}$ can not only be efficiently calculated, moreover it serves as a starting point for the calculation of the Coulomb integrals between higher l-number orbitals, such as $[V_C]_{s,p_x}$. A derivation from scratch is not necessary, but solutions can be obtained using the analytical expression obtained for $[V_C]_{s,s'}$. This is shown for the s-like and p_x-like Gaussian interaction

in Appendix A.10, resulting in:

$$[V_C]_{s,p_x} = -\frac{1}{\kappa}\frac{1}{\sqrt{\pi}}\gamma^{-\frac{3}{2}}\left(\frac{\pi}{\kappa}\right)^{\frac{3}{2}}\left(\frac{\pi}{\lambda}\right)^{\frac{3}{2}} R_x \; F_1\left(\frac{\mathbf{R}^2}{4\gamma}\right).$$

Following the same procedure and taking $[V_C]_{s,p_x}$ as a starting point, we can derive an analytical expression for a p_x-like and p_y-like Gaussian interaction:

$$[V_C]_{p_x,p_y} = -\frac{1}{8\kappa^2\lambda}\frac{1}{\sqrt{\pi}}\gamma^{-\frac{5}{2}}\left(\frac{\pi}{\kappa}\right)^{\frac{3}{2}}\left(\frac{\pi}{\lambda}\right)^{\frac{3}{2}} R_x R_y \; F_2\left(\frac{\mathbf{R}^2}{4\gamma}\right).$$

Step by step, expressions for the different Coulomb matrix elements can be derived, using the previous analytic solutions. As a result, we obtain analytical expressions for the two-electron bare exchange interaction containing Boys functions of different order. As already mentioned, these can be efficiently evaluated applying recursion. This clearly demonstrates the computational advantages of Gaussian basis sets.

Non-Orthogonality Despite the advantages a Gaussian basis offers, one has to bear in mind that these basis sets are not orthogonal. As a consequence, basis sets have to be chosen carefully in order to minimize linear dependencies and generalized eigenvalue problem routines have to be used, removing overlap matrix eigenvectors which yield too small eigenvalues for numerical stability (see below).

Another subtlety arising from non-orthogonality is the non-systematic extension of the basis set. For orthogonal basis sets, a complete basis set (CBS), i.e. the inclusion of $N \to \infty$ basis functions, reproduces wave functions exactly. Since this is technically impossible to realize, introducing a finite basis set represents a major approximation. The calculated wave functions and observables are only solutions in the function space of the basis within the chosen level of theory. The introduced error is called basis set superposition error (BSSE), which can be diminished by including more basis functions. For non-orthogonal basis sets, however, the inclusion of more basis functions does not automatically improve the result, i.e. the problem does not converge systematically like it is the case for orthogonal basis sets. Adding a basis function does not necessarily add supplemental information, but the added function can be very similar to a function already contained in the basis set. That leads to an unphysical weighting of directions and consequently unpredictable changes in the overlap and other observables. Therefore, convergence tests are of crucial importance for non-orthogonal basis sets. In the case of Gaussian functions, special basis sets, such as the correlation-consistent bases of Dunning [135], have been specifically designed to smoothly converge to the complete basis set limit. The basic idea of these basis sets is to compare the incremental change in correlation energy calculated at the configuration interaction to second order (CISD) level upon addition of higher angular momentum functions. The important outcome is that added functions separate in groups defined by the amount of correlation energy they cover. Each added group after the first one has less and less contributions to the correlation energy. By way of example, for the oxygen atom, adding a $3d$-function has the largest effect in terms of correlation energy, this function is part of the first group. Contrary,

Figure 2.2.: The FIESTA project was initiated in 2009, having in mind a computational framework that would allow to efficiently treat electronic and optical properties of molecular systems at a many-body perturbation theory level.

adding a second $3d$-functions nearly gives the same results as adding a single $4f$-function, thus the two belong to a second group. The third group consists of a third $3d$-function, a second $4f$-function and a $5g$-function. In general, every function belongs to a specific group and according to this adds a more or less consistent amount of correlation energy. Combining the idea of function grouping with the split-valence concept results in the widely used correlation-consistent polarized valence n zeta, cc-pVnZ, basis sets. With increasing cardinal number n, energies and several other properties smoothly converge for the shown case studies to the CBS limit. However, one has to keep in mind that they are in general not systematic due to their non-orthogonality. These basis sets have been developed for study cases on the CISD level, nevertheless they can give a good indication how to converge on the DFT level to the CBS limit.

2.1.5. Basis set specifications of the FIESTA code

GW/BSE calculations, as presented later in this work, have been carried out using the FIESTA package (see Fig. 2.2). A comprehensive overview of technical specifications and first results of GW calculations on organic molecules can be found in Ref. [6]. In Table (2.1), we give details on the computational costs related to the molecular systems presented later in this work, namely a model dipeptide, the coumarin molecule NKX-2677 and the Buckminster fullerene $C60$.

As a single-particle starting point, DFT-LDA eigenvalues and eigenfunctions are used, e.g. to construct the starting RPA polarizability P_{IP}. For the systems studied in this thesis, DFT calculations are performed with the SIESTA package [136], applying standard norm-conserving pseudopotentials. Since the SIESTA package is based on numerical basis sets, the radial part of the numerical basis functions is first fitted by up to eight spherical contracted Gaussian functions in order to exploit the discussed advantages a Gaussian basis offers. The cutoff radius used by the SIESTA package is chosen large enough so that the "normalization spilling" induced by truncating the Gaussian tails amounts to less than 10^{-10} [6]. This fitted Gaussian basis set is then applied both for the underlying DFT calculation and the subsequent GW/BSE step. The difference between the fitted Gaussian basis and the original numerical basis is usually of the order of 10 meV on the DFT level. For the presented calculations, both a triple-zeta plus polarization (TZP) and a triple-zeta plus double polarization ($TZDP$) have

	Dipeptide		C60	NKX-2677
Kohn-Sham basis	TZ2P	TZ2P	TZP	TZ2P
Auxiliary basis	6G, RI-SVS	6G, RI-V	4G, RI-SVS	6G, RI-SVS
# atoms	19	19	60	57
# valence bands	26	26	120	99
# Kohn-Sham basis functions	288	288	1020	1110
# Auxiliary basis functions	1006	963	2160	3426
# GW corrected bands	20	20	28	20
# Processors	4	4	576	256
Wall time 1 GW cycle	276 s	627 s	215 s	1450 s

Table 2.1.: Compilation of technical specifications for three molecular systems, namely a model dipeptide, the Buckminster fullerene $C60$ and the coumarin molecule NKX-2677, in order to give a rough estimate of the computational costs for GW calculations using the FIESTA package. The label 6G in the auxiliary basis specification stands for a basis containing 6 Gaussian functions per angular momentum channel with an even-tempered distribution of the exponential coefficients between 0.1 and 3.2. Similar, 4G represents an auxiliary basis with 4 Gaussian functions per angular momentum channel with an even-tempered distribution of the exponential coefficients between 0.2 and 3.2. The number of auxiliary basis functions corresponds to the number after the basis refinement, where linear dependencies have been removed. The given wall time, i.e. the real elapsed time per processor, corresponds to a G_0W_0 calculation, where the GW correction has been explicitly calculated for several bands around the gap (see chapter "GW/BSE in practice").

been applied. By way of example, in the case of the $TZDP$ basis, the first basis orbitals of the valence s,p-channels are taken to be the $2s$ and $2p$ eigenfunctions of isolated atoms in the corresponding pseudopotential approximation. This is analogue to strategies developed for post-Hartree-Fock correlated calculations, along the line of natural atomic orbitals (NAO). The additional valence channels are taken to be two primitive Gaussian functions, which are optimized in order to minimize the total energy at the $DFT\text{-}LDA$ level. For carbon, the resulting most diffuse Gaussian functions present a decay coefficient α =0.1 Bohr^{-2}, very close to the values optimized by Dunning at the cc-pVQZ level [135]. Following Ref. [136], the first d-channel orbital is taken to be the polarization orbital of the atomic p-orbital, namely the d-component of the perturbation induced by a uniform electric field, complemented by a primitive Gaussian with decay constant α =0.3 Bohr^{-2} for carbon. Following Dunning, we finally add a single primitive Gaussian for the f-channel with e.g. α =0.76 Bohr^{-2} for carbon. See Table (2.2) for a typical convergency test with respect to the used correlation-consistent Kohn-Sham basis.

The used auxiliary basis is composed of atomic-like orbitals centered at the atoms A, with real spherical harmonics for the angular part and a radial dependence composed of Gaussian functions:

$$\beta\left(\mathbf{r},\phi,\varphi\right)=\left|\mathbf{r}-\mathbf{A}\right|^{l}\ e^{-\alpha\left(\mathbf{r}-\mathbf{A}\right)^{2}}R_{lm}\left(\phi,\varphi\right).$$

Real spherical harmonics are used instead of complex spherical harmonics Y_{lm}, since this is

	Excitation energy		Oscillator strength	
	cc-pVXZ	aug-cc-pVXZ	cc-pVXZ	aug-cc-pVXZ
X=D	5.17	4.92	0.53	0.49
X=T	4.96	4.82	0.49	0.48
X=Q	4.87	4.81	0.49	0.47

Table 2.2.: Convergency test of the first Bethe-Salpeter singlet excitation energy (in eV) and oscillator strength with respect to the used standard correlation-consistent Kohn-Sham basis set of Dunning [135] for the cyanine $CN5$ molecule (see Ref. [141] and Fig. 2.3). It is important to note that the augmentation by diffuse orbitals is very important in order to obtain highly converged excitation energies. The oscillator strengths are less affected, except for the smallest cc-pvdz basis.

computationally more efficient [6]. The choice of the optimal decay coefficients α for the radial part, i.e. the specific extent of the basis functions, is crucial for the quality of the result. For the presented calculations, even-tempered auxiliary basis sets have been employed [6, 137, 138]. The latter come from the assumption that it is advantageous to generate a series of α coefficients with $(\alpha_i + 1)/\alpha_i$ = constant, rather than taking uniformly spread values between α_{min} and α_{max}. This goes back to the observation that the overlap of two Gaussian functions depends on the ratio of their α coefficients. Imposing a constant overlap between joining Gaussian functions with α_i and $\alpha_{i\pm1}$ allows to better span the corresponding Hilbert space [6, 138]. Consequently, α_{min}, α_{max} and the number of Gaussian functions per l-channel given, the remaining decay coefficients can be readily generated. Fig. (2.3) provides a typical plot of convergence concerning the number of used primitive Gaussian functions per angular momentum channel.

An important point to mention are numerical difficulties arising from the non-orthogonality and the possible over-completeness of Gaussian function basis sets. Calculating the overlap between auxiliary basis functions, one observes that it tends to be rather large for diffuse auxiliary functions on neighboring atoms. While auxiliary functions belonging to the same atom can be easily orthogonalized using e.g. a Gram-Schmidt procedure, a different scheme is necessary to avoid singularities in the overlap matrix stemming from neighboring basis functions [6]. Referring to a method conceived for full product basis sets [139, 140], the problem is transformed to the eigenvector space of the overlap matrix S, where eigenvectors yielding eigenvalues smaller than 10^{-8} are typically removed [6]. This does not significantly reduce the number of basis functions, however, prevents from possible numerical instabilities associated with the inversion of a quasi-singular S matrix and the amplification of errors due to the transformations $\left\langle \hat{O} \right\rangle = S^{-1}_{\lambda\lambda'} \left[\hat{O} \right] S^{-1}_{\lambda\lambda'}$.

Apart from computational advantages a Gaussian basis offers by providing analytic expressions for demanding matrix elements, another convenient factor is that these basis sets are widely applied in the quantum chemistry community. That way, one can resort to a large experience, which is crucial when converging non-orthogonal basis sets. Moreover, there is also the possibility of using eigenvalues and eigenstates generated by DFT quantum chemistry codes, where all-electron calculations and the use of hybrid functionals are standard. This

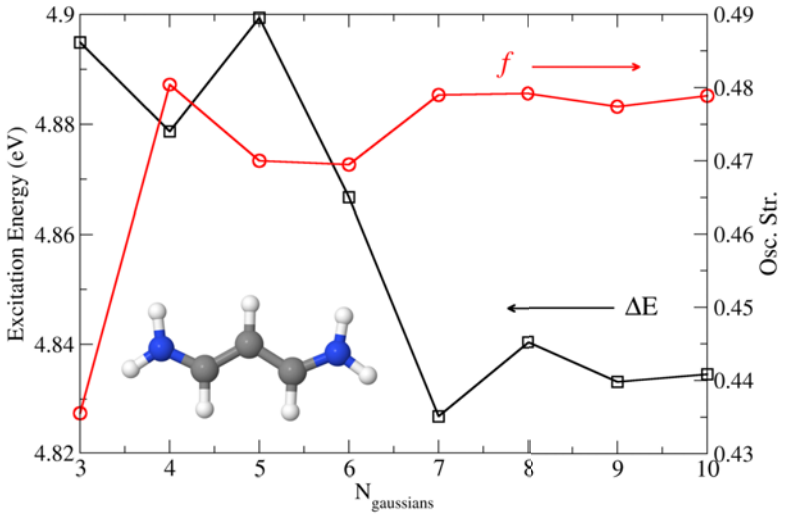

Figure 2.3.: Convergence plot of the lowest singlet excitation energy and the oscillator strength with increasing number N of primitive Gaussian functions per angular momentum channel for the cyanine $CN5$ molecule (see inlet). Note the energy scale, which is 40 meV between four and ten Gaussian functions. Figure taken from Ref. [141] and modified.

allows to go beyond the pseudopotential approximation and purely local exchange-correlation functionals. As it will be discussed later in this work, this can provide better starting points for finite systems. A recent extension to the FIESTA package allows to branch FIESTA to the NWCHEM package [142], an open-source quantum chemistry code developed to handle large computational chemistry problems.

2.2. Calculation of the dynamical screened exchange using contour deformation techniques

As discussed in Section (1.6), the self-energy Σ can be separated into a bare exchange Σ^x and a correlation part Σ^c:

$$\Sigma = iGW = \Sigma^x + \Sigma^c = iGv + iG(W - v).$$

In the preceding section, it has been shown that the non-local expectation value of the bare exchange Σ^x simplifies to an analytic expression in a Gaussian basis and thus can be efficiently evaluated. This is not the case for the correlation part Σ^c, implying computationally demanding calculations. As a reminder, the following integral in frequency space has to be explicitly evaluated:

$$\Sigma^c\left(\mathbf{r}, \mathbf{r}', E\right) = \frac{i}{2\pi} \int_{-\infty}^{\infty} d\omega \, e^{i\eta\omega} \, G\left(\mathbf{r}, \mathbf{r}', E + \omega\right) \widetilde{W}\left(\mathbf{r}, \mathbf{r}', \omega\right), \tag{2.9}$$

where $\eta \to 0^+$ and $\widetilde{W} = W - v$. The main difficulty stems from the evaluation of the non-local and frequency dependent screened Coulomb potential $\widetilde{W}$, whose calculation implies the construction of the irreducible polarizability P. Imagine the first iteration of a GW cycle, P is based on single-particle wave functions and eigenvalues, following:

$$P_{IP}\left(\mathbf{r}_1, \mathbf{r}_2; \omega\right) = \sum_{m,l} \frac{\phi_l\left(\mathbf{r}_1\right)\phi_l^*\left(\mathbf{r}_2\right)\phi_m\left(\mathbf{r}_2\right)\phi_m^*\left(\mathbf{r}_1\right)}{\omega - \left(\varepsilon_l^0 - \varepsilon_m^0\right) + i\eta} - \frac{\phi_m\left(\mathbf{r}_1\right)\phi_m^*\left(\mathbf{r}_2\right)\phi_l\left(\mathbf{r}_2\right)\phi_l^*\left(\mathbf{r}_1\right)}{\omega + \left(\varepsilon_l^0 - \varepsilon_m^0\right) - i\eta}.$$

Due to its more complex form – as compared to the Green's function G – involving the summation over four wave functions, the polarizability represents, even within the presented RPA expression, a computationally demanding object. The screened Coulomb potential is then obtained through a Dyson-like equation, which reads in matrix notation following equation (2.8):

$$\left\langle W^{RPA}\right\rangle = \langle v\rangle + \langle v\rangle\left[P_{IP}\right]\left\langle W^{RPA}\right\rangle.$$

Here, W is expressed in terms of the auxiliary basis within the $RI\text{-}SVS$ representation. The above equation is solved by inversion following:

$$\left\langle W^{RPA}\right\rangle = \left(\bar{1} - \langle v\rangle\left[P_{IP}\right]\right)^{-1}\langle v\rangle.$$

Dealing with frequency dependent quantities, the above procedure has to be performed on a frequency grid in order to obtain the frequency dependence of W. Since $G\left(\omega\right)$ and $W\left(\omega\right)$ represent strongly varying functions along the real frequency axis, the latter have to be evaluated on rather closely spaced grid points. The calculation of W presents one of the crucial steps in a GW calculation and improvements in terms of efficiency have a large impact on the necessary computational requirements.

The plasmon pole approximation One way to facilitate the calculation of the correlation contribution to the self-energy Σ^c is the so-called plasmon pole approximation (PPA). Here, the frequency dependence of the screened Coulomb potential is not explicitly calculated, but a simpler and physically meaningful form of $\widetilde{W}$ is constructed, yielding an approximate correlation contribution to the self-energy. The screened Coulomb potential $\widetilde{W}$ is composed of the bare Coulomb potential v and the inverse of the dielectric function ε^{-1}, following: $W\left(12\right) = \int d3\ \epsilon^{-1}(13)\, v(32)$. Different approaches to model $W\left(\omega\right)$ exist [3, 143, 144, 145, 146, 147, 148]. They are based on the observation that the imaginary part of $\epsilon^{-1}\left(\omega\right)$ is a function with peaks at the neutral excitation energies. It is supposed that one main peak is dominating the spectrum, originating from plasmon excitations. In the most straightforward approach, $\Im\left[\epsilon^{-1}\left(\omega\right)\right]$ is simply approximated by a single narrow Lorentzian peak. The resulting dielectric function ϵ^{-1} then also has a simple peaked form, where the peak position $\tilde{\omega}_k$ and the peak strength A_k have to be fitted for the particular system and must obey certain limits or constraints. The advantage of the PPA is that the convolution of G and W simplifies to an analytic expression, superseding the demanding integration in equation (2.9). However, one can not access the imaginary part of the self-energy, i.e. quasi-

particle lifetimes, since $Im\Sigma^c$ is zero everywhere except at $\tilde{\omega}_k$. Further, molecular systems do usually not possess a simple peaked structure for ϵ^{-1}.

Exact calculation of Σ^c using contour deformation techniques The Fiesta package [6, 7, 8] does not make use of plasmon pole models, instead, a reformulation of equation (2.9) using contour deformation techniques is applied. The latter opens the way to an exact and, in addition, efficient evaluation of the correlation energy integral as compared to the direct integration along the real frequency axis.

In order to find a suited reformulation of equation (2.9), one tries to replace the integral along the real frequency axis by an equivalent, but computationally less demanding expression [149, 150]. For convenience and without loss of generality, the non-interacting Green's function G_0 and $\widetilde{W}$ in the Lehmann representation are used for the demonstration:

$$G_0\left(\mathbf{r},\mathbf{r}',\omega+E\right)=\sum_{m}^{occ}\frac{\phi_m^*\left(\mathbf{r}\right)\phi_m\left(\mathbf{r}'\right)}{E+\omega-\varepsilon_m-i\eta}+\sum_{l}^{unocc}\frac{\phi_l^*\left(\mathbf{r}'\right)\phi_l\left(\mathbf{r}\right)}{E+\omega-\varepsilon_l+i\eta}$$

$$\widetilde{W}\left(\mathbf{r},\mathbf{r}',\omega\right)=\sum_{k}\frac{2\,\omega_k\,V_k\left(\mathbf{r}\right)V_k^*\left(\mathbf{r}'\right)}{\left(\omega+\omega_k-i\delta\right)\left(\omega-\omega_k+i\delta\right)},$$

with $V_k\left(\mathbf{r}\right)=\int d^3\mathbf{r}'\,v\left(\mathbf{r},\mathbf{r}'\right)\left\langle N,k\right|\hat{n}\left(\mathbf{r}'\right)\left|N,0\right\rangle$. The indices m and l label occupied and unoccupied states, respectively. $\phi_{m,l}$ and $\varepsilon_{m,l}$ are single-particle wave functions and energies. Neutral excitation energies are represented by ω_k. Applying analytic continuation, equation (2.9) is transferred from real space to the complex plane ($\omega\rightarrow\bar{\omega}$).[1] The resulting complex integral is evaluated along the closed contour depicted in Fig. (2.4) using contour deformation techniques:

$$\begin{aligned}
\oint d\bar{\omega}\,f\left(\bar{\omega}\right) &= \oint_C d\bar{\omega}\,f\left(\bar{\omega}\right)+\oint_D d\bar{\omega}\,f\left(\bar{\omega}\right)\\
\oint_C d\bar{\omega}\,f\left(\bar{\omega}\right) &= \int_0^{\infty}d\omega'\,f\left(\omega'\right)+\int_0^{\frac{\pi}{2}}d\varphi\,iRe^{i\rho}f\left(Re^{i\rho}\right)-\int_0^{\infty}d\omega''\,f\left(\omega''\right)\\
\oint_D d\bar{\omega}\,f\left(\bar{\omega}\right) &= \int_{-\infty}^{0}d\omega'\,f\left(\omega'\right)+\int_{\frac{3\pi}{2}}^{\pi}d\Theta\,iRe^{i\Theta}f\left(Re^{i\Theta}\right)-\int_{-\infty}^{0}d\omega''\,f\left(\omega''\right),
\end{aligned}$$

where $\left[f\left(\bar{\omega}\right)=\frac{i}{2\pi}e^{i\eta\bar{\omega}}\,G_0\left(\mathbf{r},\mathbf{r}',\bar{\omega}+E\right)\widetilde{W}\left(\mathbf{r},\mathbf{r}',\bar{\omega}\right)\right]$ with $\eta\rightarrow 0^+$. One thus deals with integrals of the form:

$$\oint d\bar{\omega}\,f\left(\bar{\omega}\right)=\oint_C d\bar{\omega}\,\frac{g\left(\bar{\omega}\right)e^{i\eta\bar{\omega}}}{\left(\bar{\omega}-\bar{\omega}_i\right)^n},\tag{2.10}$$

where n is the order of the poles $\bar{\omega}_i$ originating from the Green's function and the screened Coulomb potential.

A short overview of the theorems used in the following is provided in Appendix A.9. Corresponding to the residue theorem, a closed path integral over a function $f(z)$ with $z\in\mathbb{C}$ yields:

[1] $\bar{\omega}=\omega'+i\omega"=R\,e^{i\varphi}$ with $R=\sqrt{\left(\omega'\right)^2+\left(\omega''\right)^2}$ and $\varphi=\arctan\left(\frac{\omega''}{\omega'}\right)$.

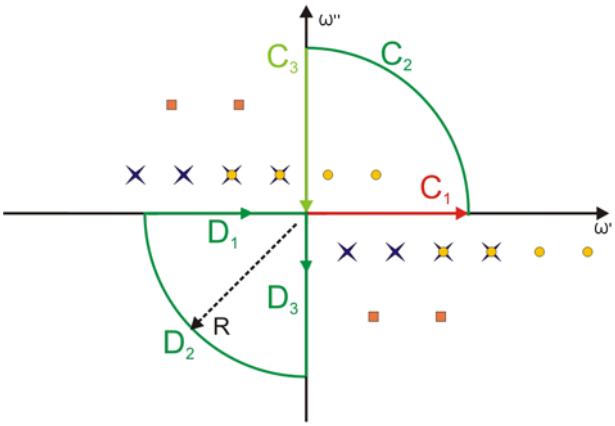

Figure 2.4.: The chosen closed contour consists of contours C and D as illustrated. The poles of $\widetilde{W}$ at the neutral excitation energies are represented by orange squares. The poles of the non-interacting single-particle Green's function $G_0(\mathbf{r}, \mathbf{r}', \omega)$ are in the upper-half plane for occupied states and in the lower-half complex plane for unoccupied states (blue crosses), while the poles of $G_0(\mathbf{r}, \mathbf{r}', \omega + E)$ are shifted by E with respect to them (yellow dots). Consequently, part of these poles are within the closed contour C.

$$\oint dz\, f(z) = \begin{cases} 0, & \text{if no poles are enclosed} \\ 2\pi i \sum_i \mathrm{Res}(f, z_i), & \text{if poles at } z_i \text{ are enclosed.} \end{cases}$$

$\mathrm{Res}(f, z_i)$ denotes the so-called residue of the function f at the enclosed pole z_i of order n. It is the coefficient of the $(z - z_i)^{-1}$ summand in a Laurent expansion and is evaluated following:

$$\mathrm{Res}(f, z_i) = \frac{1}{(n-1)!} \frac{d^{n-1}}{dz^{n-1}} \left[(z - z_i)^n f(z) \right]_{z=z_i}. \tag{2.11}$$

The poles of the screened Coulomb potential are not enclosed by the chosen contour, thus they do not require further discussion. However, for the poles of the Green's function, a case-by-case study is necessary. As depicted in Fig. (2.4), the energy zero is chosen to be in the center of the energy gap between occupied and unoccupied states. The contour C thus contains poles, if $(\omega = \varepsilon_i - E > 0)$. These poles stem from the poles of the Green's function for occupied states, i.e. $\varepsilon_i < 0$ and consequently $E < 0$. In this case, the contour D encloses no poles and one thus deduces from the residue theorem:

$$\oint d\bar{\omega}\, f(\bar{\omega}) = \oint_C d\bar{\omega}\, f(\bar{\omega}) = 2\pi i\, \Theta(-\varepsilon_i)\, \Theta(\varepsilon_i - E) \sum_i Res(f, \bar{\omega}_i).$$

For the case $(\omega = \varepsilon_i - E < 0)$, the contour integral along C vanishes. On the contrary, contour D now encloses poles of the Green's function for unoccupied states, i.e. $\varepsilon_i > 0$ and thus $E > 0$:

$$\oint d\bar{\omega}\, f(\bar{\omega}) = \oint_D d\bar{\omega}\, f(\bar{\omega}) = 2\pi i\, \Theta(\varepsilon_i)\, \Theta(E - \varepsilon_i) \sum_i Res(f, \bar{\omega}_i).$$

A detailed discussion of the two presented cases follows. In the first one, the fact that contour D vanishes can be used to deduce an expression for the integral along the positive real frequency axis:

$$\begin{aligned} \oint_D d\bar{\omega}\, f(\bar{\omega}) &= \int_{-\infty}^{0} d\omega'\, f(\omega') + \int_{\frac{3\pi}{2}}^{\pi} d\Theta\, iRe^{i\Theta} f\left(Re^{i\Theta}\right) - \int_{-\infty}^{0} d\omega''\, f(\omega'') &= 0, \\ \int_{-\infty}^{0} d\omega'\, f(\omega') &= -\int_{\frac{3\pi}{2}}^{\pi} d\Theta\, iRe^{i\Theta} f\left(Re^{i\Theta}\right) + \int_{-\infty}^{0} d\omega''\, f(\omega''). \end{aligned}$$

The integral in the lower half plane from $\left[\Theta = \frac{3\pi}{2} \ldots \pi\right]$ can be expressed in terms of $\left[\varphi = 0 \ldots \frac{\pi}{2}\right]$, following:

$$\begin{aligned} \Theta &= - (\varphi + \pi) \\ d\Theta &= -d\varphi \\ Re^{i\Theta} &= -R\cos(\varphi+\pi) - iR\sin(\varphi+\pi) = R\cos\varphi + iR\sin\varphi = Re^{i\varphi}, \end{aligned}$$

where we applied the addition theorem for sine and cosine. For the integral it follows with $\bar{\omega} = Re^{i\varphi}$:

$$\int_{\frac{3\pi}{2}}^{\pi} d\Theta\, iRe^{i\Theta} f\left(Re^{i\Theta}\right) = -\int_{0}^{\pi} d\varphi\, iRe^{i\varphi} \frac{g\left(Re^{i\varphi}\right)}{\left(Re^{i\varphi} - \bar{\omega}_i\right)^n} e^{i\eta R\cos\varphi} e^{-\eta R\sin\varphi}$$

and for the limit $R \to \infty$, respectively:

$$\lim_{R\to\infty} \int_{0}^{\pi} d\varphi \ldots \frac{e^{-\eta R\sin\rho}}{R^{n-1}}.$$

Corresponding to Jordan's lemma, the circular integral vanishes and one thus obtains:

$$\int_{-\infty}^{0} d\omega'\, f\left(\omega'\right) = \int_{-\infty}^{0} d\omega''\, f\left(\omega''\right),$$

i.e. the integral along the negative real axis can be replaced by an integral along the negative imaginary axis. Concerning the positive real axis, the contour integral along C has to be evaluated. In this case, it directly follows from Jordan's lemma that the circular integral vanishes, resulting in:

$$\int_{0}^{\infty} d\omega'\, f\left(\omega'\right) = \int_{0}^{\infty} d\omega''\, f\left(\omega''\right) + 2\pi i\, \Theta(-\varepsilon_i)\, \Theta(\varepsilon_i - E) \sum_i Res\left(f, \bar{\omega}_i\right).$$

Following equation (2.11), the residues are calculated to:

$$2\pi i \sum_i Res\left(\bar{\omega}_i\right) = -\sum_i \phi_i^*(\mathbf{r})\, \phi_i\left(\mathbf{r}'\right) \widetilde{W}\left(\mathbf{r}, \mathbf{r}', \varepsilon_i - E\right),$$

where η has been set to zero. Combining the obtained results, the correlation part of the

self-energy Σ^c along the entire real axis can be evaluated through:

$$\begin{aligned} \Sigma^c(\mathbf{r},\mathbf{r}',E) &= \int_{-\infty}^{\infty} d\omega'\, f(\omega') \\ &= \int_{-\infty}^{\infty} d\omega''\, f(\omega'') - \Theta(-\varepsilon_i)\,\Theta(\varepsilon_i - E)\,\sum_i \phi_i^*(\mathbf{r})\,\phi_i(\mathbf{r}')\,\widetilde{W}(\mathbf{r},\mathbf{r}',\varepsilon_i - E)\,. \end{aligned} \tag{2.12}$$

For the second case, i.e. $(\omega = \varepsilon_i - E < 0)$, an analogue expression is obtained. Again, the circular integrals vanish, resulting in:

$$\begin{aligned} \int_0^{\infty} d\omega'\, f(\omega') &= \int_0^{\infty} d\omega''\, f(\omega'') \\ \int_{-\infty}^{0} d\omega'\, f(\omega') &= \int_{-\infty}^{0} d\omega''\, f(\omega'') + 2\pi i\,\Theta(\varepsilon_i)\,\Theta(E-\varepsilon_i)\,\sum_i Res(f,\bar{\omega}_i)\,, \end{aligned}$$

where the residues are:

$$2\pi i \sum_i Res(\bar{\omega}_i) = -\sum_i \phi_i^*(\mathbf{r})\,\phi_i(\mathbf{r}')\,\widetilde{W}(\mathbf{r},\mathbf{r}',\varepsilon_i - E)\,.$$

Combining the two cases leads for Σ^c to:

$$\begin{aligned} \Sigma^c(\mathbf{r},\mathbf{r}',E) &= \int_{-\infty}^{\infty} d\omega''\, f(\omega'') \\ &\quad - \left[\Theta(-\varepsilon_i)\,\Theta(\varepsilon_i - E) + \Theta(\varepsilon_i)\,\Theta(E-\varepsilon_i)\right]\,\sum_i \phi_i^*(\mathbf{r})\,\phi_i(\mathbf{r}')\,\widetilde{W}(\mathbf{r},\mathbf{r}',\varepsilon_i - E)\,. \end{aligned}$$

The residues in equation (2.12) can be efficiently calculated, since $\widetilde{W}$ has only to be evaluated at the poles ε_i of the Green's function, which fall within contour C or D. Replacing the integration along the real axis by an integration along the imaginary axis has the advantage that one avoids the strong pole structure along the real axis, since G_0 and $\widetilde{W}$ are well behaved along the imaginary frequency axis [149, 150]. Consequently, the frequency grid on which the integral is numerically evaluated can be much rougher compared to a grid on the real axis. As implemented in the FIESTA package, the smooth function $\widetilde{W}(\omega'')$ can be fold onto the finite $[0,1]$ interval by a change of variable, which allows to perform a Gaussian quadrature procedure for the integral,

$$\int dx\, f(x) \approx \sum_{i=1}^{N} w_i\, f(x_i),$$

with as little as $N = 12$ points [6]. The efficiency and accuracy of the presented contour deformation techniques method has been recently successfully tested for molecular systems [6, 7, 12, 126, 151]. Furthermore, the results presented later in this work clearly show that contour deformation techniques offer an accurate and fairly efficient way to evaluate the correlation contributions to the self-energy.

3 | The GW/BSE method in practice

3.1. Preliminary considerations and motivation

3.1.1. The band gap problem

In order to predict suited material combinations for organic solar cells and to study in detail the underlying fundamental processes from first principles, one needs an universal *ab initio* formalism. By universal, we mean a parameter-free approach likely to be reliable for diverse systems, such as bulk systems, surfaces, molecules, metals, semiconductors or insulators. Since gap energies, band offsets and optical excitation energies are the experimental quantities of interest and since usually the experimentally aspired accuracy is of the order of 0.1-0.2 eV, our computational results are only interesting, if they meet the same error range. In addition, since typical molecular building blocks of interest for the targeted photovoltaic applications may contain hundreds of atoms, such as functionalized polythiophene chains, the chosen computational approach must be tractable on available computers.

Due to its favorable scaling, *DFT-KS* is the method of choice concerning ab initio calculations on ground state properties. *DFT* within the Kohn-Sham formulation allows one to access ground state total energies and densities. By way of example, related quantities such as bond lengths, bulk moduli or phonon frequencies usually come in excellent agreement ($< 1\%$) with experiments [152, 153]. The available codes scale with N^3 or even linearly [136, 154, 155]. However, serious discrepancies are observed, when the *DFT-KS* approach is used to predict excited state properties. In principle, the ground state density contains all information to set up the many-body Hamiltonian. However, up to now, no solution schemes are available to extract information about excited states. Difficulties are especially encountered, when *DFT-KS* eigenvalues are directly compared to one-particle excitation energies measured in photoemission experiments. In principle, as already discussed in detail in preceding chapters, *DFT-KS* eigenvalues are pure mathematical tools entering the formalism as Lagrange multipliers in order to ensure orthogonality for the wave functions. Referring to the ionization potential theorem, only the eigenvalue of the highest occupied level can be associated with the negative value of the ionization energy, $IE \equiv E_{ho}^{N-1} - E_0^N$, provided that the *exact* exchange-correlation functional is used. Nevertheless, it is common practice to associate the complete Kohn-Sham eigenvalue spectrum with experimental band structures, where in addition approximate exchange-correlation functionals are applied. This is motivated by the apparent similarities between the Kohn-Sham and the Hartree-Fock equations.

For the latter, Koopmans theorem directly connects the HF eigenvalues to excitation energies within the frozen orbital approximation. Following this approach on the DFT level, in some cases the obtained band structures agree surprisingly well with experiment – at least from a qualitative point of view [156]. Concerning quantitative results, systematic studies on the band gap have been carried out [3, 4, 152, 156, 157, 158, 159]. In these studies, the true fundamental gap, defined as the difference between the ionization energy IE and the electron affinity ($EA = E_0^N - E_{lu}^{N+1}$),

$$E_g = IE - EA = E_{lu}^{N+1} + E_{ho}^{N-1} - 2E^N, \tag{3.1}$$

is compared to the standard DFT-KS gap:

$$E_g^{KS} = \varepsilon_{lu}^{DFT} - \varepsilon_{ho}^{DFT},$$

where ε_{ho}^{DFT} represents the eigenvalue of the highest occupied (ho) level and ε_{lu}^{DFT} the eigenvalue of the lowest unoccupied (lu) Kohn-Sham level in a N particle system. These studies demonstrated that standard DFT-KS calculations applying (semi)local exchange-correlation functionals, such as LDA, severely underestimate the band gap by up to several eV [3, 4, 152, 156, 157, 158, 159]. This is known as the band gap problem and is depicted in Fig. (3.1) for selected semiconductors and insulators.

3.1.2. Excited states within DFT-KS

The calculation and interpretation of excited state properties takes a prominent place within the DFT community. The reason is that the determination of excitation energies from Kohn-Sham eigenvalues is not straightforward and associated with certain subtleties. Since the quality of the obtained excitation energies can strongly depend both on the system itself and on the used approximate functional, much care is needed. This problem also affects our many-body perturbation theory GW/BSE results, since DFT-KS eigenvalues and eigenstates serve as a starting point. As it will be pointed out later, especially for the "single-shot" G_0W_0 approach, a reliable DFT-KS starting point is indispensable.

In order to get to the heart of the band gap problem and to estimate the errors introduced both by the use of approximate exchange-correlation functionals and the association of DFT eigenvalues with single-particle excitation energies, two limiting cases are discussed in the following – the homogeneous electron gas and the free atom. These are thought as a guideline to assess the reliability of DFT-KS calculations. For the electron gas, the exact exchange-correlation functional V_{xc} is by construction the LDA one. This offers the possibility to carry out an *exact* DFT calculation and to compare the obtained eigenvalues to many-body perturbation theory quasiparticle energies [145]. Concerning the highest occupied eigenvalue, the two methods perfectly agree. This underlines the validity of the ionization potential theorem. However, for the remaining spectrum, discrepancies occur, which simply arise from the association of DFT-KS eigenvalues with excitation energies. Differences are small for (un)occupied states close to the Fermi energy E_F, however, increase for states farther from

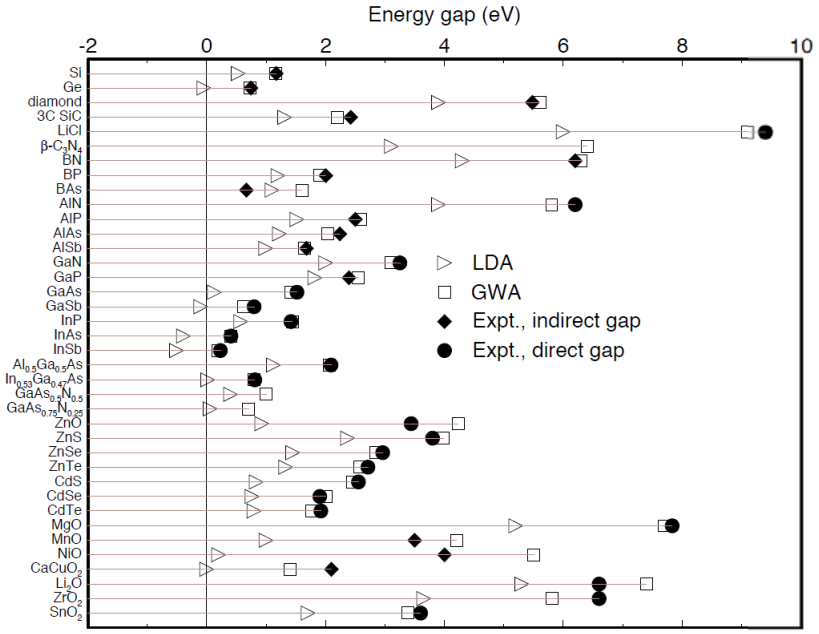

Figure 3.1.: Band gaps as calculated within *DFT-LDA* (triangles) and *GW* (squares) are compared to experimental data measured in ARPES experiments (diamonds, filled circles): Apparently, *DFT-LDA* underestimates the band gap by up to several eV. The discrepancies are one order of magnitude larger than the desired accuracy of around 0.1-0.2 eV. Green's functions based methods, namely the *GW* approach, significantly improve the situation and reproduce experimental gaps within some tenth of meV. Figure taken from Ref. [5], which also provides a detailed listing of the corresponding references.

E_F. This implies that special care has to be taken when comparing to measurements probing these states.

In the limit of the free atom, the charge density strongly varies. Comparing *exact DFT*,[1] *DFT-LDA* and *HF* calculations for the beryllium atom to quasiparticle excitation energies [87, 160], one again observes that exact *DFT* perfectly reproduces the ionization energy, whereas discrepancies arise for the other states. Concerning *HF* and *DFT-LDA* calculations, the ionization energy is strongly defective, in particular in the case of *DFT-LDA* [87]. The poor performance of *DFT-LDA* can be attributed to the fact that *LDA* is not the functional of choice to mimic strong charge fluctuations, in particular due to self-interaction effects. The latter are caused by the spurious interaction of an electron with itself, which is inherent in the Hartree term and only completely canceled by the Fock exchange term in *HF* theory. Thus, applying hybrid functionals containing a certain percentage of exact exchange usually improves the situation, however, self-interaction errors are only partly removed.

The $\triangle$SCF scheme for finite systems For finite systems, a practical approach to obtain *DFT-KS* ionization energies and electronic affinities in good agreement with experiment is

[1] By exact *DFT*, it is meant a Kohn-Sham equation including an exchange-correlation potential built from an exact charge density as calculated using advanced correlated techniques.

the $\triangle SCF$ method [87, 161, 162, 163]. The procedure consists of performing three different DFT-KS ground state calculations, namely for the N-electron and for the corresponding $(N \pm 1)$ system. Subtracting the resulting ground state energies provides the ionization energy IE, the electron affinity EA and consequently also the gap E_g following equation (3.1). Since ground state energies calculated within DFT are usually in very good agreement with experiment, one obtains reliable binding energies and gaps at reasonable computational costs. It is important to note, however, that $\triangle SCF$ only provides the ionization energy and the electron affinity, whereas the remaining excitation energies can not be accessed. This is due to the fact that the charged system is relaxed in its ground state and consequently total energies other than $E_{s=0}^{N\pm1}$ are not accessible. Another drawback is that this method can only be applied for finite systems. Usually, periodic boundary conditions are used in solids, leading to a "Coulomb explosion", i.e. an unphysical charging of the system by adding an electron (hole) to each of the unit cells. Even though techniques exist, where a positive background charge is introduced as compensation, it is not clear how to straightforwardly deduce the fundamental gap from the obtained total energies [83, 164, 165].

The DFT-KS derivative discontinuity As an alternative approach to obtain within DFT-KS the ionization energy, the electron affinity and thus the band gap, the ionization potential theorem suggests to calculate the derivative of the total energy for a N_0 and (N_0+1) system with respect to the fractional occupation number $\tilde{n}_i \in [0,1]$:

$$-IE\left(N_0\right) = \varepsilon_{ho=N_0}^{DFT} = \left.\frac{\partial E^{N_0}}{\partial \tilde{n}_{ho}}\right|_{\tilde{n}_{ho}=1-\eta},$$

$$-EA\left(N_0\right) = \varepsilon_{ho=N_0+1}^{DFT} = \left.\frac{\partial E^{N_0+1}}{\partial \tilde{n}_{ho}}\right|_{\tilde{n}_{ho}=1-\eta}, \tag{3.2}$$

where $\eta = 0^+$. Since charged configurations are disadvantageous for infinite systems, one makes use of the fact that the total energy is a piecewise function with respect to the fractional particle number N (see Fig. 1.4a). This allows to evaluate the electron affinity by analyzing the right limit $\varepsilon_{ho}^{DFT}\left(N_0+\delta\right)$ of the neutral system instead of working with the left limit of the charged system $\varepsilon_{ho}^{DFT}\left(N_0+1-\delta\right)$ as suggested by equation (3.2):

$$E_g = IE - EA = \varepsilon_{ho}^{N_0+\delta} - \varepsilon_{ho}^{N_0-\delta}. \tag{3.3}$$

As shown in Fig. (1.4b), when infinitesimally crossing the integer value N_0 from $(N_0-\delta)$ to $(N_0+\delta)$, the Kohn-Sham eigenvalue ε_{ho} is subject to an abrupt change. In this context, it is important to mention that the Kohn-Sham eigenvalues, as calculated in a single DFT-KS calculation on N_0 particles, correspond to the left limit, i.e. $(N_0-\delta)$ [82]. Since the external and the Hartree potential are continuous with respect to the density, within the DFT-KS formalism, the discontinuity can stem either from the kinetic energy of the non-interacting electrons or the exchange-correlation energy contribution [82]. First, the abrupt slope change in the kinetic energy is due to a change in the leading orbital, i.e. the fact that the state labeled *ho* at the left is not identical to the *ho* state on the right, since one already starts to in-

finitesimally occupy the next available state. The *ho* state on the right thus corresponds to the lowest unoccupied state (*lu*) on the left. Second, the change in the exchange-correlation energy is due to a spatially constant discontinuity in the exchange-correlation potential, usually termed derivative discontinuity Δ_{xc} [82]. The *ho* state on the left can therefore be expressed in terms of the *lu* state on the left and the derivative discontinuity [82, 83]:

$$\varepsilon_{ho}^{N_0+\delta} = \varepsilon_{lu}^{N_0-\delta} + \Delta_{xc}.$$

Consequently, one obtains for the band gap:

$$E_g = IE - EA = \varepsilon_{lu}^{N_0-\delta} - \varepsilon_{ho}^{N_0-\delta} + \Delta_{xc}. \tag{3.4}$$

This is an important outcome, since it shows that even for the exact exchange-correlation functional, the Kohn-Sham gap ($E_g^{KS} = \varepsilon_{lu}^{N_0-\delta} - \varepsilon_{ho}^{N_0-\delta}$) obtained from a single calculation on a N-body system does not exactly yield the fundamental gap E_g. Instead, the derivative discontinuity has to be taken into account. Depending on the system, the magnitude of the latter can vary from negligible amounts, i.e. the jump is too a large amount described by the kinetic energy term, to values of the order of E_g^{KS} [82, 87]. For approximate exchange-correlation functionals, the degree by which equation (3.4) is fulfilled differs [83]. In these cases, discrepancies between E_g^{KS} and the true gap can thus arise both from the discontinuity and from the approximate nature of the functional. Determining the discontinuity is a highly non-trivial task and the reader is referred to Ref. [83] for a comprehensive overview of current approaches.

An alternative to the standard Kohn-Sham scheme is the so-called generalized Kohn-Sham (GKS) approach, where non-local potentials are introduced. The idea is that discontinuity effects, which are not already covered by the kinetic energy, are not solely shouldered by the unknown local KS exchange-correlation potential. Instead, they are supposed to automatically come in through non-local potentials, such as e.g. the Fock term [82]. The GKS equations take the following form:

$$\left(\hat{O}\left[\{\phi_i\}\right] + V_{ext}\left(\mathbf{r}\right) + V_r\left[n\right]\left(\mathbf{r}\right)\right)\phi_i\left(\mathbf{r}\right) = \varepsilon_i\phi_i\left(\mathbf{r}\right),$$

where $\hat{O}\left[\{\phi_i\}\right]$ is a non-local, orbital-dependent operator and V_r the local "remainder" potential determined by the derivative of the remainder energy with respect to the density. In the case where $\hat{O}\left[\{\phi_i\}\right]$ is chosen to be the single-particle kinetic operator, one retrieves the standard Kohn-Sham equations, where the remainder contains the Hartree and the usual exchange-correlation contribution. If instead $\hat{O}\left[\{\phi_i\}\right]$ is the kinetic energy operator and the Hartree-Fock operator, one obtains a Hartree-Fock-Kohn-Sham scheme, which is in principle exact and where the remainder accounts for correlation only. Unfortunately, only very little is known about the correct form of the remainder in this case, making this scheme difficult to apply in practice [82]. Apart from these two limiting cases, the most common applications of the GKS are hybrid exchange-correlation functionals. The latter contain a certain amount α of Fock exchange $\hat{V}_F$, a complementary amount $(1-\alpha)$ of the standard approximate (semi)local

exchange V_x^{sl} and correlation V_c^{sl} contributions [82]:

$$\left(-\frac{\nabla^2}{2} + V_{ext}(\mathbf{r}) + V_H[n](\mathbf{r}) + \alpha\hat{V}_F + (1-\alpha)V_x^{sl}[n](\mathbf{r}) + V_c^{sl}[n](\mathbf{r})\right)\phi_i(\mathbf{r}) = \varepsilon_i\phi_i(\mathbf{r}).$$

These functionals are a special case of the GKS scheme, where $\hat{O}[\{\phi_i\}]$ consists of the kinetic energy operator and a fraction of the Hartree-Fock operator [82]. As a consequence, one obtains the kinetic energy and a fraction of the Hartree and of the Fock contribution, whereas one chooses the remainder to contain the rest of the Hartree term and the (semi)local exchange-correlation contributions. By way of example, the *LDA* and *PBE* [74] functionals correspond to $(\alpha = 0)$, while Hartree-Fock is characterized by $(\alpha = 1)$ and $\left(V_x^{sl} = V_c^{sl} = 0\right)$. One of the most popular hybrid functionals, the already introduced B3LYP functional [75], is determined by $(\alpha = 0.2)$, the similar PBE0 functional [166] by $(\alpha = 0.25)$ [48]. The choice of α crucially influences the accuracy of the methods. Usually, α is either obtained by semi-empirical fitting on a set of study case systems or formal considerations. However, there is no transferability from one system to another, so describing semi-conducting, metallic, finite or extended systems on the same footing is questionable [82]. Nevertheless, as already discussed for the limiting case of a free atom and as depicted in Fig. (3.2) for three organic molecules, hybrid functionals usually significantly improve over (semi)local functionals such as *LDA* or *GGA*. However, since self-interaction errors are only partly removed, non-negligible discrepancies with correlated theories and experiment and thus the band gap problem still persist.

A promising extension of hybrid functionals are so-called range-separated hybrid (RSH) functionals. Based on the work of Savin and coworkers [168, 169, 170], range-separated hybrid (RSH) functionals have been specifically designed to tackle the band gap problem. The idea is to separate the exchange energy functional into a short-range (SR) and a long-range (LR) part. This is achieved by a decomposition of the Coulomb potential, following e.g.:

$$\frac{1}{|\mathbf{r}-\mathbf{r}'|} = \frac{1-\mathrm{erf}(\kappa, |\mathbf{r}-\mathbf{r}'|)}{|\mathbf{r}-\mathbf{r}'|} + \frac{\mathrm{erf}(\kappa, |\mathbf{r}-\mathbf{r}'|)}{|\mathbf{r}-\mathbf{r}'|}, \tag{3.5}$$

where erf is the error function and κ a parameter characterizing the range-separation, i.e. the spatial extent of the short-range interaction [171]. At a characteristic distance of around $\sim 2/\kappa$, short-range contributions become negligible. Bearing an important influence on the accuracy of the obtained results, the range-separation parameter κ has to be carefully chosen, either through fitting or physical considerations. The first term in equation (3.5), i.e. the short-range contribution $V_x^{sr,\kappa}$, is not evaluated directly, but replaced by a standard (semi)local *DFT* exchange functional, whereas the long-range is governed by a Hartree-Fock like operator $\hat{V}_F^{lr,\kappa}$ [82]:

$$\left(-\frac{\nabla^2}{2} + V_{ext}(\mathbf{r}) + V_H[n](\mathbf{r}) + \hat{V}_F^{lr,\kappa} + V_x^{sr,\kappa}[n](\mathbf{r}) + V_c^{sl}[n](\mathbf{r})\right)\phi_i(\mathbf{r}) = \varepsilon_i\phi_i(\mathbf{r}).$$

This offers the possibility to include the full exact exchange in the long range regime, yielding

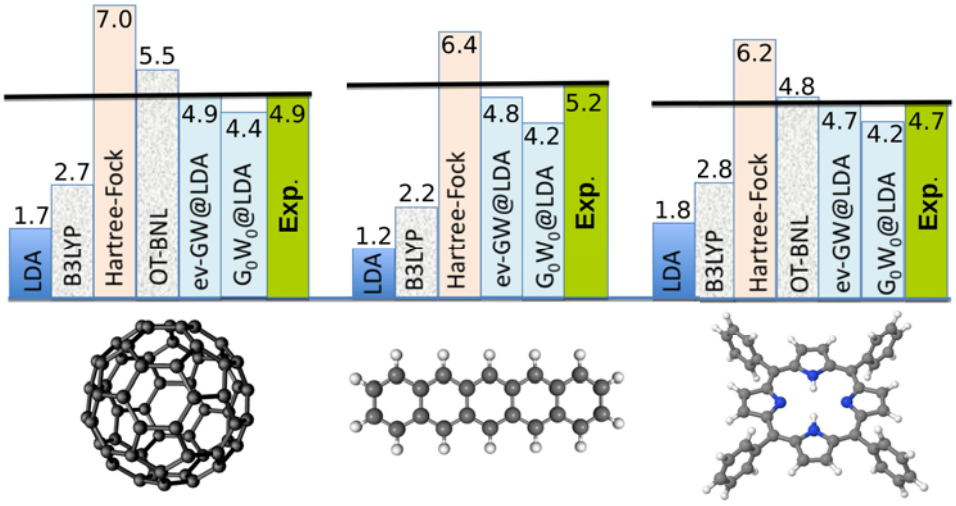

Figure 3.2.: Synthetic representation of the HOMO-LUMO fundamental gaps for the Buckminster fullerene C60, pentacene and H_2TPP as obtained within DFT-KS with various approximations to the exchange-correlation functional, Hartree–Fock and many-body perturbation theory $G_0W_0@LDA$, $G_0W_0@HF$ and partially self-consistent $evGW@LDA$ with self-consistency on the eigenvalues (see next section). The experimental values are taken from the NIST chemistry webbook (http://webbook.nist.gov/chemistry/) and indicated both below the charts and by a black horizontal line. DFT-LDA, DFT-$B3LYP$ and HF calculations have been performed at the all-electron cc-pVTZ level with the NWCHEM package [142], GW results are taken from Ref. [6]. Whereas HF clearly overestimates the experimental gap due to the lack of correlations, DFT-LDA gives gaps, which are several eV too small. Standard hybrid functionals, such as B3LYP, ameliorate the situation, however, for an agreement of the order of a few tenths of an eV, one has to resort to e.g. range-separated hybrid functionals, such as the optimally-tuned (OT) BNL functional [167]. As discussed in the subsequent section, many-body perturbation theory approaches come in very close agreement with experiment, in particular the partially self-consistent $evGW$ scheme. The difference between $G_0W_0@LDA$ and $G_0W_0@HF$ calculations clearly points out the importance of the starting point.

the correct asymptotic image charge potential, while maintaining the appropriate (crucial) balance of short-range exchange and correlation [50]. These functionals correspond to the specific GKS case, where $\hat{O}[\{\phi_i\}]$ consists of the kinetic energy operator and a fraction of the *long-range* Coulomb operator. The corresponding remainder then contains the short-range Hartree term, the short-range exchange and the correlation contribution. The hope is that in such a scheme the role of the derivative discontinuity $\triangle_{xc}$ can be significantly reduced compared to the standard Kohn-Sham scheme, enabling the identification of the Kohn-Sham gap with the fundamental gap.

A special class of RSH functionals are so-called Coulomb-attenuating method (CAM) functionals, where the decomposition of the Coulomb potential in short- and long-range contribu-

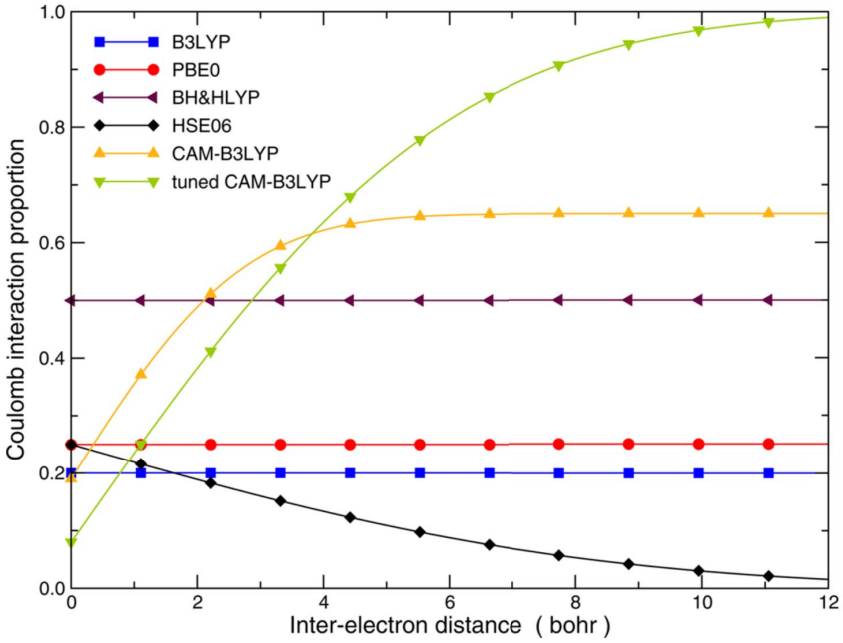

Figure 3.3.: Exact exchange proportion $[\alpha + \beta \operatorname{erf}(\kappa, |\mathbf{r} - \mathbf{r}'|)]$ applied by diverse RSH functionals (see text) with respect to the inter-electron distance $|\mathbf{r} - \mathbf{r}'|$. (Semi)local functionals such as LDA or PBE would be a horizontal line at 0.0 ($\alpha = \beta = 0$), Hartree-Fock at 1.0 ($V_x^{sl} = V_c^{sl} = 0$, $\alpha = 1$, $\beta = 0$). In between these extremes, one finds the diverse hybrid functionals. The tuned CAM-B3LYP functional [172] has been optimized to reproduce the correct long-range behavior of $(-1/|\mathbf{r} - \mathbf{r}'|)$. Figure taken from Ref. [48].

tions is further generalized, following [49]:

$$\frac{1}{|\mathbf{r} - \mathbf{r}'|} = \frac{1 - [\alpha + \beta \operatorname{erf}(\kappa, |\mathbf{r} - \mathbf{r}'|)]}{|\mathbf{r} - \mathbf{r}'|} + \frac{\alpha + \beta \operatorname{erf}(\kappa, |\mathbf{r} - \mathbf{r}'|)}{|\mathbf{r} - \mathbf{r}'|}. \tag{3.6}$$

Here, the parameters α and β, for which $(0 \leq \alpha \leq 1)$, $(0 \leq \beta \leq 1)$ and $(0 \leq \alpha + \beta \leq 1)$, provide an additional flexibility to control the strength of the respective contributions. Analyzing the two summands of equation (3.6), it is clear that the first term and the second term contribute over the whole range. This is contrary to the original decomposition of equation (3.5), where either the first or the second summand, i.e. the local DFT or the long-range exact exchange contribution, vanishes at $|\mathbf{r} - \mathbf{r}'| = \infty$ or $|\mathbf{r} - \mathbf{r}'| = 0$, respectively. Again, the first term is replaced by standard (semi)local DFT exchange functionals, whereas the second term is governed by an orbital-dependent Fock operator. Representing the second term following:

$$\frac{\alpha}{|\mathbf{r} - \mathbf{r}'|} + \frac{\beta \operatorname{erf}(\kappa, |\mathbf{r} - \mathbf{r}'|)}{|\mathbf{r} - \mathbf{r}'|},$$

it is obvious that one obtains for the limit $|\mathbf{r} - \mathbf{r}'| = 0$, in addition to the (semi)local DFT exchange (first term), a fixed portion α of non-local exact exchange. This corresponds to the case of standard hybrid functionals. Concerning the long-range limit $|\mathbf{r} - \mathbf{r}'| = \infty$, the first term in equation (3.6) contributes with a factor of $[1 - (\alpha + \beta)]$, whereas the second term provides the

remaining contribution of $(\alpha + \beta)$. As a consequence, for (semi)local DFT exchange functionals which vanish in this limit, the exchange interaction is solely governed by the second term and thus reduces from the correct physical limit of 1 to $(\alpha + \beta)$. Later in this chapter, consequences of this reduction will be discussed in detail in the context of optical charge-transfer excitations. A popular representative of the CAM functionals, which will be important in the following, is the CAM-B3LYP functional [49] with $\alpha = 0.19$, $\beta = 0.46$ and $\kappa = 0.33$. Apart from CAM functionals, a variety of RSH functionals has been developed, yielding very satisfying results for gap energies (see Fig. 3.2). Important representatives are among others HSE06 [173], long-range corrected (LRC or LC) RSH functionals reproducing the physical long-range limit, such as LC-BLYP [174, 175], or the Baer, Neuhauser and Livshits (BNL) RSH functional [176, 177]. The exact exchange contribution $[\alpha + \beta \text{ erf}(\kappa, |\mathbf{r} - \mathbf{r}'|)]$ with respect to the inter-electron distance $|\mathbf{r} - \mathbf{r}'|$ is provided by Fig. (3.3) for diverse functionals.

In the following, the band gap problem is revisited from the viewpoint of many-body perturbation theory. Here, the calculated quasiparticle energies can be directly connected to excitation energies. Even though usually more expensive in terms of necessary computing power than $DFT\text{-}KS$, the universality and accuracy of the GW/BSE approach are striking.

3.1.3. The many-body perturbation theory GW formalism in practice

The first full GW calculation of the self-energy goes back to the 1960s, where Hedin studied the electron gas and demonstrated a systematic way to expand the electron-electron self-energy in terms of the screened Coulomb potential [1]. However, due to computational difficulties, GW calculations on real systems have not been carried out until the 1980s [3, 149, 178, 179]. The latter provided promising results, yielding significantly improved excitation energies compared to $DFT\text{-}KS$. A compelling example is the case of lanthanum hydride LaH_3, where $DFT\text{-}LDA$ predicts a semi-metal (see Fig. 3.4), whereas experiments document a semiconducting behavior. The latter is well reproduced within GW [180]. It is interesting to note that for this system, $DFT\text{-}LDA$ already gives good qualitative characteristics and that GW then corrects the quantitative values by an opening of the band gap. This is a typical outcome and therefore GW is often equated with a scissor operator, which cuts the band structure within the gap and shifts occupied and unoccupied states apart from each other. Up to now, systematic studies on a variety of systems demonstrated the reliability and the accuracy of the GW method for the qualitative and quantitative prediction of band structures [4, 157], with the exception of strongly-correlated materials, such as e.g. Mott insulators. A compilation is provided by Fig. (3.1).

3.1.3.1. GW for finite systems

Originating from the solid state community, most of the popular GW implementations are conceived for periodic systems [181, 182, 183]. Finite systems, such as molecules or clusters, can in principle be treated within the same framework by introducing an artificial periodicity. This implies that one constructs periodically repeated supercells containing the finite electronic system under study. In order to avoid an unphysical interaction between the cells,

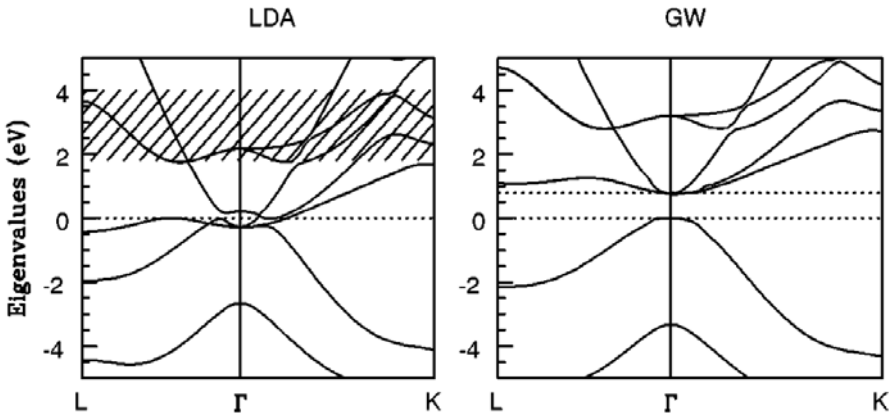

Figure 3.4.: From semi-metallic to semi-conducting: in the case of lanthanum hydride LaH_3, *DFT-LDA* band structure calculations predict a semi-metal (left), whereas experiment yields a semi-conducting system. Within *GW*, the band gap is opened and the correct semi-conducting behavior is reproduced (right). Figure taken from Ref. [180].

either large cells are needed or special techniques to attenuate Coulomb interactions at the cell borders have to be introduced. An additional difficulty arises from the fact that most of the standard *GW* implementations use plane wave basis sets, where the number of included basis functions increases with the volume of the unit cell. Therefore, for finite systems with satisfactorily large unit cells, a non-negligible amount of plane waves is required. This significantly enhances the computational effort and explains the relatively small number of available *GW* studies on molecules in gas phase. After the pioneering work of Shirley in 1993 [184], only very recently, *GW* has been applied to atomic and molecular systems and implementations have been designed to specifically account for the requirements which come along with localized systems [6, 48, 126, 151, 185, 186, 187, 188, 189, 190, 191, 192, 193, 194, 195, 196, 197, 198, 199, 200, 201, 202, 203, 204]. This meets the demand of upcoming fields, such as organic electronics or organic photovoltaics, which definitely seek for accurate single-particle excitation energies. Nevertheless, contrary to the case of periodic systems, systematic studies on the performance of the *GW* formalism for molecular systems remain scarce. Hence, the present work focuses on exploring the merits and limitations of *GW* for molecules.

3.1.3.2. From G_0W_0 to self-consistency

The G_0W_0 approach As already detailed in preceding chapters, in order to obtain one-particle excitation energies within the many-body Green's function framework, one has to solve the quasiparticle eigenvalue equation:

$$H_0\left(\mathbf{r}\right)\psi_\nu^{qp}\left(\mathbf{r}\right)+\int d\mathbf{r}''\,\Sigma\left(\mathbf{r},\mathbf{r}'',\varepsilon_{qp}\right)\psi_\nu^{qp}\left(\mathbf{r}''\right)=\varepsilon_{qp}\psi_\nu^{qp}\left(\mathbf{r}\right), \tag{3.7}$$

where H_0 contains contributions from the kinetic energy, the external potential and the Hartree potential. All interactions beyond Hartree are governed by the self-energy Σ, which is non-local, non-Hermitian and energy-dependent. As a consequence, the resulting quasiparticle

wave functions ψ_ν^{qp} are not orthogonal and quasiparticle energies are complex.

In most *GW* applications, a perturbative approach is used to solve equation (3.7). Based on the similarity of the quasiparticle and the Kohn-Sham equations, one usually supposes that the Kohn-Sham wave functions are in close agreement with the quasiparticle wave functions and that the perturbation $(\Sigma - V_{xc})$ is small with respect to the complete Hamiltonian [55]. It has been demonstrated early, in the case of silicon, that the self-energy is indeed diagonal in the *DFT-LDA* basis [3]. To first order in the perturbation, one can then approximate the quasiparticle energy by:

$$\varepsilon_{qp,\nu} = \varepsilon_\nu^{KS} + \left\langle \psi_\nu^{KS} \right| \Sigma\left(\varepsilon_{qp,\nu}\right) - V_{xc} \left| \psi_\nu^{KS} \right\rangle . \tag{3.8}$$

Linearizing the above equation in the vicinity of the Kohn-Sham eigenvalues ε_ν^{KS} removes the dependence of Σ on the solution $\varepsilon_{qp,\nu}$ and leads to:

$$\varepsilon_{qp,\nu} \approx \varepsilon_\nu^{KS} + Z_\nu^{KS} \left\langle \psi_\nu^{KS} \right| \Sigma\left(\varepsilon_\nu^{KS}\right) - V_{xc} \left| \psi_\nu^{KS} \right\rangle , \tag{3.9}$$

where the renormalization factor,

$$Z_\nu^{KS} = \left[1 - \left. \frac{\partial \Sigma_{\nu\nu}(\omega)}{\partial \omega} \right|_{\omega=\varepsilon_\nu^{KS}} \right]^{-1} \text{ with } \Sigma_{\nu\nu}(\omega) = \left\langle \psi_\nu^{KS} \left| \Sigma(\omega) \right| \psi_\nu^{KS} \right\rangle ,$$

accounts for dynamical effects of the self-energy. In the standard procedure, quasiparticle energies are obtained within a single-shot *GW* approach from equation (3.9), usually referred to as G_0W_0 method [3]. Single-particle Kohn-Sham eigenvalues are used to construct the non-interacting (mean-field) Green's function G_0, from which in turn the non-interacting irreducible polarizability, the zero-order screened Coulomb potential and the single-shot self-energy are obtained:

$$\begin{array}{l} \varepsilon_{KS}, \psi_{KS} \\ \Downarrow \\ G_0 = \sum_\nu \frac{\psi^*_{KS,\nu}(\mathbf{r})\psi_{KS,\nu}(\mathbf{r}')}{\omega - \varepsilon_\nu^{KS} \pm i\eta} \Longrightarrow P_0 = -iG_0G_0 \Longrightarrow W_0 = v + vP_0W_0 \Longrightarrow \Sigma = iG_0W_0. \end{array}$$

Here, the laborious calculation of self-consistent *GW* quantities is avoided, thus providing a computationally feasible and consequently a very popular *GW* scheme. However, since input single-particle energies are corrected within one cycle only, a dependence of the *GW* result on the underlying single-particle calculation is induced. This has been recently demonstrated for several molecular systems, where both Hartree-Fock and *DFT* calculations applying diverse (semi)local and hybrid functionals have been evaluated as a starting point [6, 7, 48, 130, 196, 201]. Discrepancies concerning the quasiparticle energies amount to 1 eV for very small molecules. Further, it was shown that standard G_0W_0 calculations based on *DFT-LDA* obviously underestimate fundamental gaps (see Fig. 3.2), due to an overscreening when building the screened Coulomb potential with too small *DFT-LDA* gaps. *DFT-KS* with hybrid functionals seems to be a more suited starting point compared to (semi)local functionals

such as LDA or PBE [48]. However, it is indicated that none of the approaches can be considered as generally reliable and that the amount of exact exchange needed to be included in the hybrid functional is not clear at first sight. This points out the need to improve on the standard G_0W_0 scheme. By way of example, there are approaches searching for a unique and consistent $DFT\text{-}KS$ starting point by determining the appropriate amount of exact exchange in the hybrid functional for each system under study [201]. In this work, we rather focus on self-consistency in the GW scheme as a mean to overcome the starting point dependence.

Self-consistent schemes In order to bypass the starting point dependency of the perturbative G_0W_0 approach, it would be desirable to have a self-consistent scheme starting from input single-particle eigenstates and eigenvalues, which are iteratively updated and converged. The most intuitive way is to start from a non-interacting Green's function G_0, which is used to obtain the corresponding self-energy through Hedin's cycle. The latter in turn serves to calculate an updated Green's function through the inversion of Dyson's equation. One thus repeats the following cycle until the Green's function obtained from the Dyson equation equals the G used to calculate Σ:

$$
\begin{array}{lcl}
\varepsilon_{KS}, \psi_{KS} & & \\
\Downarrow & & \\
G_0,\ G & \Longrightarrow & P = -iGG \\
\Uparrow & & \Downarrow \\
\Sigma = iGW & \Longleftarrow & W = v + vPW
\end{array}
$$

Such a fully-self-consistent scheme guarantees that the obtained results are independent of the starting point. It allows to obtain self-consistent Green's functions, from which converged spectral functions or total energies, e.g. through the Galitskii-Migdal equation [92], can be directly deduced. If one is interested in the excitation energy spectrum, a similar scheme involving the self-consistent solution of the quasiparticle equation can be applied. This is computationally very demanding, since, due to the non-Hermitian nature of the self-energy, left and right eigenvectors of the Hamiltonian $(H_0 + \Sigma)$ have to be considered and its energy-dependence implies a matrix eigenvalue problem for each energy grid point. Due to the enormous workload fully self-consistent schemes imply, only few works have been carried out so far. For solids, the quality of fully self-consistent schemes is strongly debated [150, 205, 206, 207, 208]. By way of example, for the homogeneous electron gas, a worsening of the spectral function with a strong underestimation of the quasiparticle weight as compared to the incoherent part has been observed, whereas the total energy shows an excellent agreement with Monte Carlo calculations [205]. On the contrary, in the case of Si and Ge an improvement of the band gaps compared to perturbative single-shot calculations has been demonstrated [206]. Concerning finite systems, such as atoms or molecules, full self-consistency seems to perform better than G_0W_0 starting from (semi)local functionals, however, G_0W_0 calculations based on hybrid functionals yield an equivalent quality. Again, owing to the complexity of the problem, only few studies are available [189, 193, 202].

As an alternative to fully self-consistent schemes, different less demanding self-consistent

	self-consistency on:	
	wave functions	eigenvalues
evCOHSEX	–	√
scCOHSEX	√	√
G_0W_0	–	–
evGW	–	√

Table 3.1.: Short overview of the different many-body perturbation theory *GW* and COHSEX schemes available in the FIESTA code [6].

GW approaches have been recently introduced. Faleev and coworkers [208] developed the so-called quasiparticle self-consistent GW scheme ($QPscGW$), where the true self-energy is first approximated by a Hermitian self-energy, following:

$$\langle i|\,\Sigma^{QPscGW}\,|j\rangle = \frac{1}{2}\Re\left[\langle i|\,\Sigma\left(\varepsilon_{qp,j}\right)|j\rangle + \langle j|\,\Sigma\left(\varepsilon_{qp,i}\right)|i\rangle\right].$$

This greatly simplifies the fully self-consistent solution. After convergency is reached, equation (3.8) is evaluated at the obtained quasiparticle energies. This approach has been shown to yield accurate quasiparticle energies in solids [208, 209]. However, even though much less demanding than a standard fully self-consistent scheme, its computational costs are not negligible [151]. In this work, we want to access the reliability of two self-consistent schemes, which are less expensive and thus promising for calculations on large molecular systems. One is a simple partially self-consistent approach, where only the eigenvalues are updated in each cycle, whereas the $DFT\text{-}KS$ input eigenstates are unchanged [6, 7, 10, 210]. This approach will be labeled *evGW* in the following. The other one consists of a self-consistent COHSEX calculation to improve the $DFT\text{-}KS$ starting point, followed by a partially self-consistent *GW* calculation to obtain converged quasiparticle energies. Self-consistency at the COHSEX level can be partial, i.e. on the eigenvalues only ($evGW@evCOHSEX$), or both on the eigenvalues and eigenfunctions ($evGW@scCOHSEX$) [10, 209]. See Table (3.1) for an overview of the different approaches.

3.2. The GW formalism applied

3.2.1. The studied system: the model dipeptide

The present *GW* study [10] comprises a small - even though delicate - system, namely a model dipeptide based on the N-methylacetamide C_3H_7NO molecule (see Fig. 3.5). It represents a model system which was initially chosen by Serrano-Andrès and Fülscher [47] to mimic the essential optical properties of polypeptides, i.e. small proteins consisting of amino acides. The latter are biologically important organic compounds possessing at least one amine ($-NH2$) and one carboxylic acid ($-COOH$) functional group. In peptides and proteins, they are covalently bound to each other through peptide bonds [$-C(=O)NH-$] and form long molecular chains. Due to the large amount of atoms present in polypeptides, ab initio studies on their optical properties are very demanding. However, since optical spectra are supposed to be

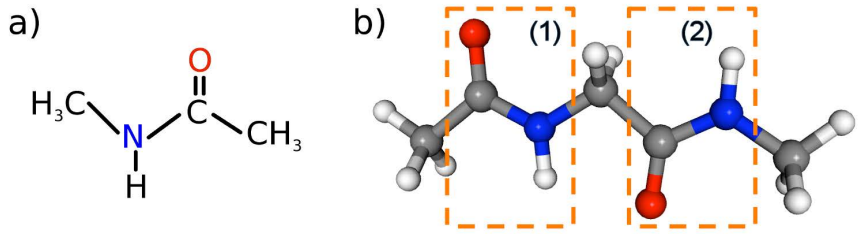

Figure 3.5.: Symbolic representation of the studied model dipeptide based on the N-methylacetamide C_3H_7NO molecule (a). The model dipeptide (b) is chosen in its planar geometry (see Ref. [47], structure 1a). The active peptide bonds $[-C(=O)NH-]$ are singled out in orange boxes. Carbon atoms are represented in gray, oxygen in red, nitrogen in blue and hydrogen in white, respectively.

a superposition of the spectra of the corresponding small building blocks, studies on simple model fragments can help to understand the characteristic absorption features of polypeptides. The combined GW/BSE study performed on the electronic and optical properties of the model dipeptide is presented in detail in the following. In this section, we focus on the GW part with emphasis on self-consistency within the GW formalism. This is followed by an in-depth discussion of the optical properties of the dipeptide as calculated within BSE in the subsequent section. Our attention is turned to charge-transfer excitations, a physically highly important, but theoretically tricky class of electron-hole pair excitations.

3.2.2. Technical details

The studied molecular structure as represented in Fig. (3.5) compares to structure (1a) of Ref. [47], where results for different rotational structures of the dipeptide are presented. We relaxed the used structure at a DFT-$B3LYP$ level with a 6-311G** basis using the Gaussian09 package [75, 211].

The starting single-particle input eigenstates/energies for our GW calculation are taken from DFT Kohn-Sham calculations using the SIESTA code [136] within the local density approximation (LDA) combined with standard norm-conserving pseudopotentials [212]. A large triple-zeta plus double polarization basis ($TZDP$) is used to converge the correlation contribution to the self-energy [135]. The Kohn-Sham wave functions for states around the energy gap are depicted in Fig. (3.6). It is primarily these states which contribute to the lowest-lying optical transitions. The listed states possess either σ- or π-character and are mainly localized on one side of the molecule or the other (denoted with a subscript $i = 1, 2$). The asterisk stands for unoccupied states.

Our GW calculations are performed with the FIESTA package [6, 7, 8]. Dynamical screening and correlations are explicitly treated using contour deformation techniques without any plasmon-pole approximation [6, 213]. All unoccupied states, as appearing in the Green's function G and the irreducible polarizability P, are included in the summation over empty states. Non-local operators, such as P, the bare and screened Coulomb potentials v and W, and the self-energy Σ, are expressed in terms of a large auxiliary atom-centered Gaussian

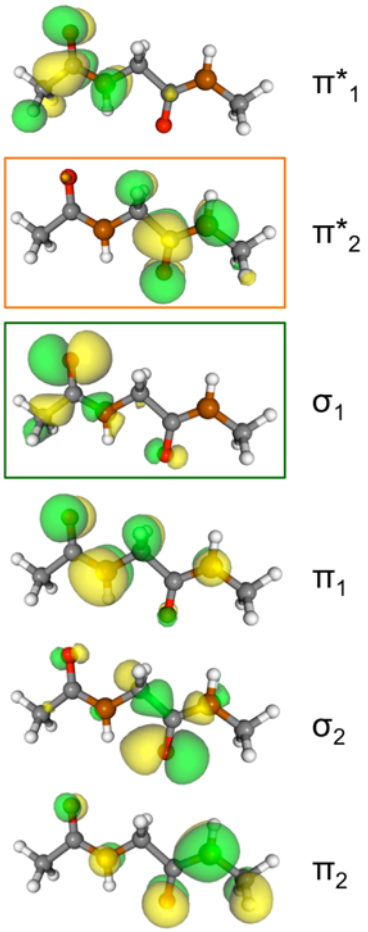

Figure 3.6: Isocontour representation of the Kohn-Sham wave functions around the gap classified by their σ- or π-character. The highest occupied molecular orbital (HOMO) and the lowest unoccupied molecular orbital (LUMO) are singled out in a green and orange box, respectively. The asterisk denotes unoccupied orbitals, the subscripts (1, 2) the peptide unit on which the orbital is localized. The ordering corresponds to the *DFT-LDA* ordering. Carbon atoms are represented in gray, oxygen in red, nitrogen in orange and hydrogen in white, respectively.

basis combined with standard RI-V techniques [130, 214, 215]. The used auxiliary basis is composed of six primitive Gaussian functions ($e^{-\alpha r^2}$) per l-channel, up to $l = 2$ orbitals for first row elements. The localization coefficients α possess an even-tempered distribution [138] ranging from $\alpha_{min} = 0.10$ Bohr^{-2} to $\alpha_{max} = 3.2$ Bohr^{-2}, except for hydrogen, where the coefficient goes from $\alpha_{min} = 0.10$ Bohr^{-2} to $\alpha_{max} = 1.5$ Bohr^{-2}.

3.2.3. Beyond the scissor operator: level crossings

Following the results of previous G_0W_0@*LDA* studies, showing that this approach leads to too small ionization energies, gaps and optical excitation energies [6, 7, 8], we test the partial self-consistency *evGW* scheme for the dipeptide with an update of the eigenvalues [10]. It is important to note that we explicitly calculate the quasiparticle correction for several occupied and unoccupied energy levels around the gap, while the remaining eigenvalues are correspondingly shifted.[2] This is an extension to standard G_0W_0 approaches, in the following denoted *GW* Scissor, where usually only a quasiparticle correction to the HOMO and LUMO is calculated. The partially self-consistent cycle is repeated until convergency is reached for the quasiparticle energies. Implying a threshold of about 0.01 eV, the quasiparticle energies

[2] We performed a convergency test with a *GW* correction on the 10/15/20 highest occupied and lowest unoccupied states. The resulting excitation energies for the *W*1, *W*2, *CTa* and the *CTb* exciton converge within 0.05 eV with respect to the number of self-consistently corrected (un)occupied states.

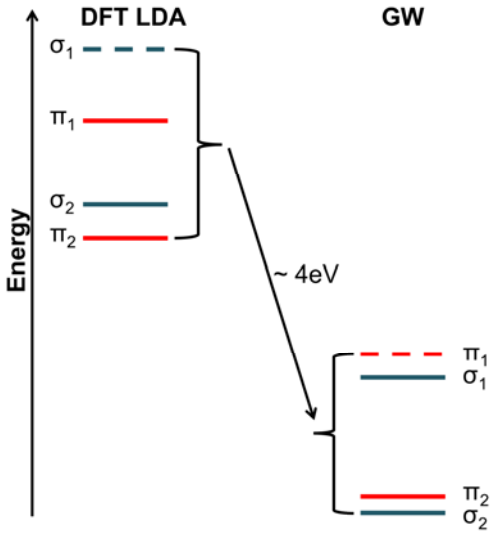

Figure 3.7.: Qualitative representation of the highest occupied molecular orbitals level ordering within *DFT-LDA* and *GW*. States with σ-character are depicted in blue, states with π-character in red. The HOMO is highlighted with a dashed line. The occupied energy levels are not only shifted to lower energies by the self-energy correction, but also reordered with significantly changed inter-level spacings.

usually converge within 5 *evGW* cycles.

The resulting *DFT-LDA* and *evGW* energy levels are compiled in Table (3.2) and Fig. (3.7). As expected, the gap is significantly opened from 4.6 eV in *DFT-LDA* to 11.9 eV within *evGW*. Beyond this known scissor operator effect, important σ- and π-level crossings appear for the highest occupied levels (see Fig. 3.7). In addition, the spacing between the levels changes strongly compared to *DFT-LDA*. In particular, a *GW* correction of around 0.5 eV larger for the two σ- than for the two π-levels is observed. An important consequence of the reordering is that the highest occupied molecular level (HOMO) changes its character from σ within *DFT-LDA* to π within *evGW*. Bearing in mind that the frontier orbitals are the most important ones for chemical reactions, the correct determination of their symmetry is crucial. Further, the wrong ordering of the states leads to erroneous optical spectra, difficult to reconcile with higher level calculations (see next section). A similar effect has been noticed in our recent *evGW* study on the DNA/RNA nucleobases [7, 216], where it has been shown that the present *evGW@LDA* scheme leads to quasiparticle energies in excellent agreement with correlated quantum chemistry EOM-IP-CCSD or CASSCF/CASPT2 calculations (for details see Ref. [7]). For the same reasons than in the nucleobases, one can speculate that the stronger localization of the σ-orbital leads to a larger self-interaction error as compared to π-orbitals, pushing them at too high energies at the *DFT-LDA* level.

3.2.4. Improving the starting point: scCOHSEX

The COHSEX approximation to the *GW* self-energy has already been introduced in preceding chapters, where it has been shown that the demanding *GW* self-energy becomes static and

state	DFT-LDA	scCOHSEX		
HOMO	-6.20	-10.63		
HOMO-1	-5.79	-10.88		
HOMO-2	-6.89	-11.37		
HOMO-3	-6.68	-11.62		
	evGW@LDA	evGW@scCOHSEX	G_0W_0@LDA	G_0W_0@scCOHSEX
HOMO	-9.47	-9.31	-8.71	-9.46
HOMO-1	-9.60	-9.57	-8.44	-9.75
HOMO-2	-10.28	-10.06	-9.46	-10.21
HOMO-3	-10.34	-10.28	-9.23	-10.46

Table 3.2.: Compilation of the four highest occupied energy level eigenvalues as obtained within the different approaches discussed in the text. Notice that the given *DFT-LDA* and G_0W_0@LDA eigenvalues are switched, in order to match them to the correct ev*GW* ordering. The presented *GW* results correspond to a quasiparticle correction explicitly calculated for 20 states around the gap. *DFT-LDA* eigenvalues strongly differ from ev*GW*, whereas a self-consistent scCOHSEX already gives the right ordering and level spacing. Even though the occupied levels are shifted by about 1 eV to too low energies, the scCOHSEX approach is a valuable starting point for ev*GW* and even G_0W_0 calculations (see column evGW@scCOHSEX and G_0W_0@scCOHSEX). Concerning the G_0W_0@LDA approach, even though several states around the gap are corrected, the right ordering can not be restored within a single-shot G_0W_0 calculation. Consequently, the reliability of the G_0W_0 *Scissor* approach as commonly applied seems questionable in this case.

Hermitian within this approach. This opens the door to efficient fully self-consistent quasiparticle calculations, since the eigenvectors are orthogonal and solutions to the same static and Hermitian operator.

The approach studied in this work [10] consists of fully self-consistent scCOHSEX calculations with an update of both eigenvalues and eigenfunctions. These serve as an input for subsequent G_0W_0 or *evGW* calculations [209]. The obtained results are compiled in Table (3.2). In the case of transparent conductive oxides and quaternary thin films for photovoltaics [217, 218] or for bulk gold [219], the G_0W_0@scCOHSEX approach has been shown to yield excellent results in semiconductors combining extended and localized states [209, 220]. Very recently, Korbel and coworkers confirmed this observation for small transition metal clusters using the FIESTA package [221].

In this section, we are interested in assessing the quality of the self-consistent scCOHSEX scheme as a starting point for *evGW* calculations on molecules. It is important to have in mind that in the present contour deformation implementation, calculating repeatedly the *GW* correction to several states away from the gap turns out to be expensive due to the poles contribution. In addition, we want to test one of the common approximations in the *GW* community, namely the assumption that the Kohn-Sham and quasiparticle eigenfunctions strongly overlap, even though the energy gap may differ significantly. By way of example, in the case of simple bulk systems, an agreement of 99.9% has been claimed [3], which justifies the presented perturbative *GW* approach. However, a well-known example, where such an

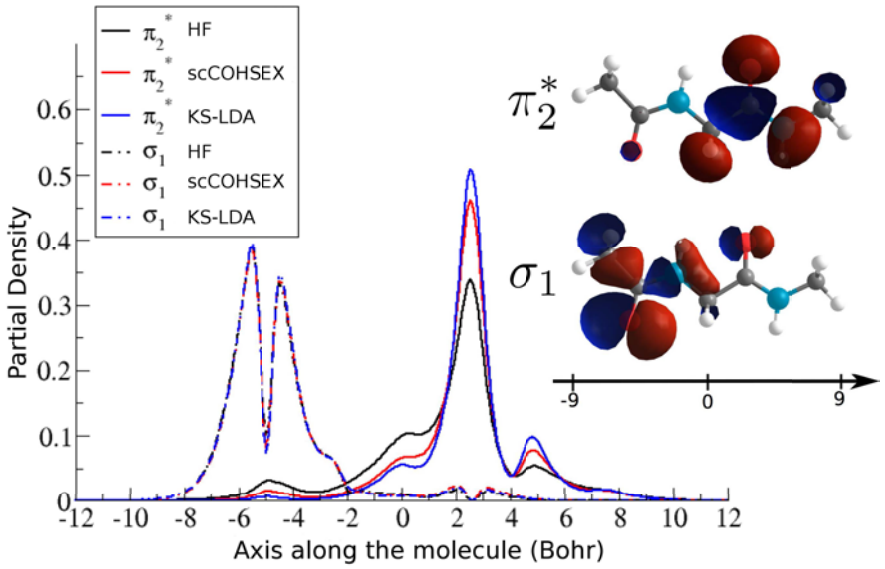

Figure 3.8.: Comparison between the *DFT-LDA* (blue), scCOHSEX (red) and *HF* (black) wave functions for the σ_1 (dotted lines) and π_2^* (full lines) wave functions. We represent the modulus squared of the wave function averaged over planes perpendicular to the molecular "axis" represented as an inset (average charge in electron/Bohr). This partial density averages to one for each state when integrated along the axis.

approximation fails and where self-consistent schemes are indispensable, is the case of systems combining delocalized (*s*,*p*)-orbitals and tight 3*d*-levels, such as transition metal oxides [208, 210].

Our findings concerning scCOHSEX are consistent with previous observations on extended semiconductors [3], namely that the COHSEX approximation overcorrects the energy gap. Our scCOHSEX gap for the dipeptide, i.e. the difference between the highest occupied (HOMO) and the lowest unoccupied molecular level (LUMO), is found to be 12.9 eV, instead of 4.62 eV within *DFT-LDA* and 11.8 eV for *evGW*@scCOHSEX. Providing a first indication that updating the wave functions does not affect very significantly the quasiparticle energy spectrum, we see that the 11.8 eV *evGW*@scCOHSEX energy gap is in good agreement with the 11.9 eV *evGW*@LDA value previously found. For the sake of comparison, the Hartree-Fock HOMO-LUMO gap[3] is found to be 13.85 eV. Clearly, the scCOHSEX gap is much closer to the final *evGW* value than the starting *DFT-LDA* gap. As compared to *GW* calculations, the slightly too large scCOHSEX gap originates mainly from the HOMO which is located nearly 1 eV too low in energy (overbinding), while the LUMO is found to agree within 0.1-0.2 eV with the final *GW* value.[4]

Besides the improved value of the energy gap, an important finding is that the scCOHSEX approach yields the correct ordering of states (see Table 3.2). In particular, the HOMO level

[3]The all-electron cc-pVTZ Hartree-Fock calculations have been performed with the Gaussian09 package [211].
[4]The scCOHSEX, *evGW@LDA* and *evGW*@scCOHSEX LUMO energies are found to be 2.32 eV, 2.42 eV and 2.47 eV, respectively. This can be compared to the *DFT-LDA* starting Kohn-Sham value of −1.17 eV and to the all-electron *DFT-B3LYP* ΔSCF value (2.13 eV) obtained with the Gaussian09 code and a 6-311G(d,p) basis set.

is a π_1 state, located $(0.25, 0.74, 0.99)$ eV above the σ_1, π_2 and σ_2 states, respectively. This can be compared to spacings of $(0.26, 0.75, 0.97)$ eV within the *evGW*@scCOHSEX value. Such an excellent agreement in level ordering and energy spacing, together with a better HOMO-LUMO gap, indicates that the scCOHSEX eigenvalue spectrum is certainly a better starting point for *evGW* calculations as compared to the *DFT-LDA* approach. In particular, a simple G_0W_0@scCOHSEX *Scissor* approach, correcting only the HOMO and LUMO, yields already very similar results as compared to a full *evGW*@scCOHSEX calculation correcting a large number of states around the fundamental gap.

Inferring a better quality of the scCOHSEX eigenfunctions from the strongly ameliorated energy spectrum, as compared to Kohn-Sham *DFT-LDA* calculations, remains a difficult issue. However, the analysis of the scCOHSEX σ_1 and π_2^* states indicates that they project within 99.8% and 98.9%, respectively, onto the corresponding *DFT-LDA* eigenstates. This demonstrates that the Kohn-Sham and scCOHSEX eigenstates do not differ significantly, in contrast to the very large discrepancy for the eigenvalue spectra. For the sake of illustration, in Fig. (3.8), we plot the *DFT-LDA*, scCOHSEX and Hartree-Fock σ_1 and π_2^* wave functions, where the charge is averaged within planes perpendicular to the molecular "axis". For the occupied σ_1 state, the *DFT-LDA*, scCOHSEX and Hartree-Fock wave functions (dotted lines) are nearly indistinguishable. However, for the π_2^* state (full lines), differences start to appear in particular at the Hartree-Fock level. Clearly, the scCOHSEX wave function is closer to the *DFT-LDA* one, even though the scCOHSEX (and *evGW*) quasiparticle spectrum is closer to the Hartree-Fock one.

3.2.5. Conclusion

In conclusion, the presented *GW* results on the model dipeptide aimed at studying the performance of two computationally efficient self-consistent *GW* schemes. We now summarize the main conclusions of the present study:

- The G_0W_0@*LDA Scissor* approach, where only HOMO and LUMO are explicitly corrected, fails as the HOMO-LUMO gap is underestimated and, importantly, the ordering of occupied states close to the gap is wrong. This subsequently leads to optical spectra difficult to compare to experiment.

- While *DFT* calculations with hybrid functionals may possibly be a better starting point, we explored inexpensive partially self-consistency *GW* schemes in order to come up with an approach that does not depend on the starting guess. Moreover, this approach is supposed to work equally well for extended solids of various kind (sp- or spd-systems) and molecular systems.

- The *evGW*@*LDA* scheme, namely an approach where only the eigenstates are updated, has been shown to yield very accurate quasiparticle energies for the present π-conjugated molecules without transition metal atoms. This was demonstrated for example during our diploma thesis in the case of DNA/RNA nucleobases (for details see Ref. [7]),

showing similar important level crossings from *DFT-LDA* to *GW*. However, the problem of level crossings requires that *GW* calculations are performed several times for a large number of corrected states, implying important computational costs related to the present contour deformation techniques (contribution from the poles).

- The inexpensive self-consistent scCOHSEX scheme leads to a much better starting point for *GW* calculation. Not only the gap is closer to the quasiparticle value, but the ordering and spacing of the occupied state is found to be accurate. Consequently, an *evGW* correction calculated for the HOMO and LUMO only, or even a G_0W_0@scCOHSEX calculation, leads to results of the same quality than performing *evGW* on a large set of levels. Therefore, this is becoming our preferred option for large molecular systems.

- For the model dipeptide, despite the presence of localized σ-states suffering from significant self-interaction problems, the scCOHSEX wave functions were not found to differ very significantly from the *DFT-LDA* ones, just as usually assumed in extended solids with delocalized (s,p) electrons.

We finally conclude this section by admitting that, contrary to the DNA/RNA nucleobases, our *evGW* calculations could not be compared to higher level theory or experimental data. Since the "proof of the pudding is in the eating", we now turn to the absorption spectrum for which comparisons can be directly drawn.

3.3. The BSE formalism applied: charge-transfer excitations

3.3.1. Charge-transfer excitations

In the presented *BSE* calculations, we study the optical properties of two systems, one is the already introduced dipeptide, the other one is a family of organic dyes, namely coumarin molecules of interest for dye-sensitized solar cells. They have in common that their lowest-lying optical excitations are so-called charge-transfer (*CT*) excitations. The latter are a special class of electron-hole excitations, where the excited electron and the created hole are spatially separated from each other. These non-local excitations are very interesting both from a fundamental and an applied point of view. Apart from the fact that they are often the principal excitations in organic molecules composed of functional groups with different electro-negativity (push-pull systems), they are believed to represent the intermediate state between bound electron-hole pairs and dissociated free carriers in organic solar cells [39, 40, 41]. However, the exact mechanisms leading to charge separation remain rather controversial [21, 37, 38], urging for computational quantum mechanical studies which allow an accurate exploration of local and CT excitations at various energies. Moreover, since it is also believed that they allow an efficient charge separation, molecules characterized by low-lying *CT* excitations are promising candidates for organic photovoltaics [50, 28, 29, 222, 223, 224]. Recently, we already demonstrated that our *GW/BSE* approach works well for *intermolecular CT* excitations, where the excited electron and hole are located on two different molecules

[8, 44]. We now want to tackle a situation which often occurs in nature, namely the problem of *intramolecular CT* excitations, where donor and acceptor are situated on the same molecule.

Treating CT excitations theoretically using ab initio methods remains difficult. Wave function-based quantum chemistry methods such as complete active space second order perturbation theory (CASPT2) or multi-reference configuration interaction (MRCI) methods [225] yield accurate results, however, they are computationally too demanding to treat systems with more than a few tens of atoms. At the density functional theory level, constrained DFT formalisms [226, 227] have proven to be extremely efficient in providing a good description of the lowest-lying CT excitations in rather large systems, but generalizing such techniques to higher excited states remains a difficult issue. Further, excited states wave functions, needed to calculate e.g. transfer rates, are not available. Another candidate is time-dependent density functional theory (TDDFT) [35, 36, 125], where one obtains optical excitations properties of systems significantly larger than that amenable to e.g. CASPT2 or MRCI approaches. While describing very well local optical excitations, applied with standard (semi-)local functionals, it fails in reproducing CT excitations in most instances and can not be considered reliable. The reason is that long-range interactions between electrons and holes which are distant to each other and which are (almost) not overlapping can not be treated properly with these local functionals [228, 229, 230]. This can be made clear by considering the TDLDA case, where one finds within Casida's effective eigenvalue formulation [124] that the resonant matrix elements read (see preceding chapters):

$$\begin{aligned} H^{diag}_{vc,v'c'} &= \delta_{vv'}\delta_{cc'}\left(\varepsilon^0_c - \varepsilon^0_v\right), \\ H^{exch}_{vc,v'c'} &= \int d\mathbf{r}d\mathbf{r}'\phi_v\left(\mathbf{r}\right)\phi^*_c\left(\mathbf{r}\right)\, v\left(\mathbf{r},\mathbf{r}'\right)\, \phi^*_{v'}\left(\mathbf{r}'\right)\phi_{c'}\left(\mathbf{r}'\right), \\ H^{LDA}_{vc,v'c'} &= \int d\mathbf{r}\phi_v\left(\mathbf{r}\right)\phi^*_c\left(\mathbf{r}\right)\, \frac{\partial V^{LDA}_{xc}}{\partial n(\mathbf{r})}\, \phi^*_{v'}\left(\mathbf{r}\right)\phi_{c'}\left(\mathbf{r}\right). \end{aligned}$$

Clearly, the product of $\phi_v\left(\mathbf{r}\right)$ and $\phi_c\left(\mathbf{r}\right)$, and consequently the two electron-hole interaction terms, go to zero for excitations, where the electron ϕ_c and the hole ϕ_v do not overlap, since the wave functions depend on the same space variable. As a consequence, one ends up with the diagonal part, i.e. with the time-independent Kohn-Sham eigenvalue differences $\left(\varepsilon^0_c - \varepsilon^0_v\right)$, and electron-hole interactions are neglected. More specifically, for long-range CT excitations, where an electron is promoted from a donor to a distant acceptor,[5] Mulliken's rule should be satisfied. The latter states that the lowest charge-transfer excitation energy E^{exc}_{CT} equals [82, 231]:

$$E^{exc}_{CT} = IE_D - EA_A - \frac{1}{R},$$

where IE_D is the ionization energy of the donor, EA_A the electron affinity of the acceptor and $R = |\langle\mathbf{r}_e\rangle - \langle\mathbf{r}_h\rangle|$ the donor-acceptor distance, given by the average position of the excited electron $\langle\mathbf{r}_e\rangle$ and hole $\langle\mathbf{r}_h\rangle$. This implies that the charge-transfer excitation energy is determined by the fundamental energy gap of the entire complex $(IE_D - EA_A)$ and the

[5] It is assumed that the chemical interaction between the donor and the acceptor is negligible.

electron-hole binding energy ($1/R$). Within TDLDA, this limit is not correctly reproduced and the $1/R$ term is completely neglected [50]. Further, $(IE_D - EA_A)$ reduces to the too small *DFT-LDA* gap. Within the *BSE* approach, the exchange contribution H^{exch} also vanishes for *CT* excitations. However, the screened part H^{scr} does not necessarily go to zero, since the electron wave function ϕ_c and the hole wave function ϕ_v depend on different space coordinates. Instead, ϕ_v (ϕ_c) and $\phi_{v'}$ ($\phi_{c'}$) depend on the same space coordinate, which yields non-zero densities for $v = v'$ and $c = c'$ weighted by the non-local screened Coulomb potential W:

$$H^{scr}_{vc,v'c'} = -\int d\mathbf{r}\mathbf{r}' \phi_v(\mathbf{r})\, \phi^*_c(\mathbf{r}')\; W_{stat}(\mathbf{r}', \mathbf{r})\; \phi^*_{c'}(\mathbf{r}')\, \phi_{v'}(\mathbf{r}).$$

Clearly, the correct $1/R$ Mulliken limit is automatically obtained within *BSE*, which can be made clear setting $v = v'$, $c = c'$, $|\phi_v(\mathbf{r})|^2 = \delta(\mathbf{r} - \langle \mathbf{r}_h \rangle)$ and $|\phi_c(\mathbf{r})|^2 = \delta(\mathbf{r} - \langle \mathbf{r}_e \rangle)$. This yields for the screened exchange term:

$$H^{scr}_{LR} = -\frac{1}{\varepsilon_M R},$$

which is the long-range limit of W_{stat}. For donor-acceptor systems in vacuum, the macroscopic dielectric function equals $\varepsilon_M = 1$. Since the diagonal part of the Bethe-Salpeter resonant Hamiltonian yields the quasiparticle energy differences $\left(\varepsilon^{GW}_c - \varepsilon^{GW}_v\right)$ and since the exchange term goes to zero for charge-transfer excitations, one directly arrives within the long-range limit of the screened exchange contribution H^{scr}_{LR} in vacuum at the Mulliken limit:

$$E^{exc}_{CT} = IE^{GW}_D - EA^{GW}_A - \frac{1}{R}.$$

This has been recently shown for the case of intermolecular *CT* excitations in the zinc-bacteriochlorin/bacteriochlorin complex [44], as depicted in Fig. (3.9).

The encountered difficulties within TDLDA paved the way for the success of non-local hybrid functionals [49, 82, 174, 175, 176]. Analogue to the time-independent case, one can also set up a *generalized* TDDFT scheme with Fock-like non-local potentials. In this case, an additional term appears in the $H^{xc}_{vc,v'c'}$ contribution:

$$\begin{aligned} H^{xc}_{vc,v'c'} \;=\; & \int d\mathbf{r} \phi_v(\mathbf{r})\, \phi^*_c(\mathbf{r})\; f^{sl,\gamma}_{xc}(\mathbf{r})\; \phi^*_{v'}(\mathbf{r})\, \phi_{c'}(\mathbf{r}) \\ & + \int d\mathbf{r} d\mathbf{r}' \phi_v(\mathbf{r})\, \phi^*_{v'}(\mathbf{r})\; u_\kappa(\mathbf{r}, \mathbf{r}')\; \phi^*_c(\mathbf{r}')\, \phi_{c'}(\mathbf{r}'). \end{aligned} \tag{3.10}$$

The short-range exchange and correlation are governed by the (semi)local exchange-correlation kernel $f^{sl,\gamma}_{xc}$, whereas long-range is included through $u_\kappa(\mathbf{r}, \mathbf{r}') = \frac{\mathrm{erf}(\kappa|\mathbf{r},\mathbf{r}')}{|\mathbf{r}-\mathbf{r}'|}$. This is the most general form, also applicable for range-separated hybrid functionals. Concerning limiting cases, provided that u_κ is zero and $f^{sl,\gamma}_{xc}$ the standard *LDA* exchange-correlation functional, one retrieves the TDLDA scheme. The case of TDDFT with hybrid functionals is obtained by setting u_κ to $(\alpha/|\mathbf{r} - \mathbf{r}'|)$, i.e. by introducing a fixed amount of exact exchange [82]. Concerning charge-transfer optical excitations, from equation (3.10), it becomes immediately clear that similar to (semi)local functionals, also standard hybrid functionals do not correctly

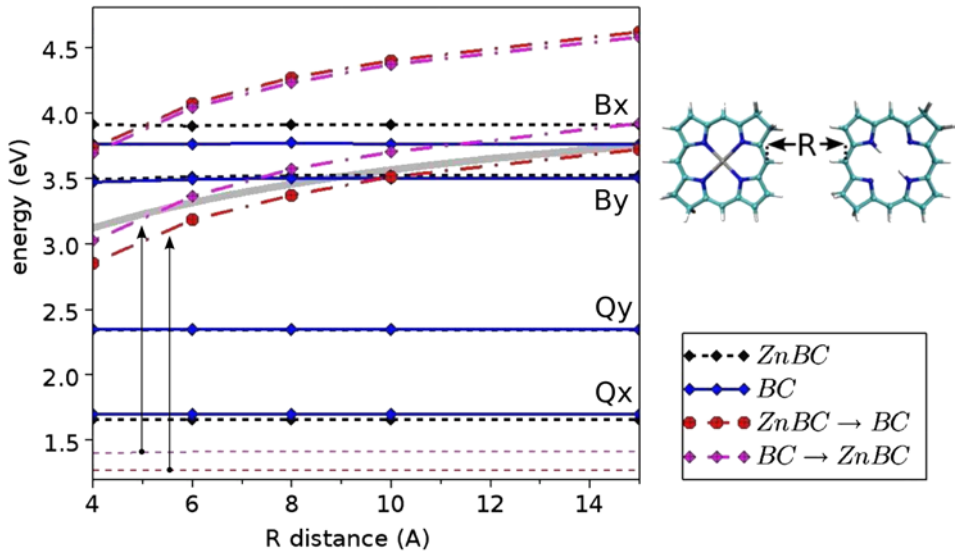

Figure 3.9.: *GW/BSE* optical excitation energies as a function of the zinc-bacteriochlorin (ZnBC) to bacteriochlorin (BC) distance R. The small box on the right indicates the represented *GW/BSE* intramolecular (Q-band and higher lying Soret B transitions) or charge-transfer transitions between the two molecules. The lowest lying ZnBC→BC charge-transfer excitation energy is compared to the $(E_g^{GW} - e^2/D)$ Mulliken limit (thick gray line), where E_g^{GW} is the *GW* quasiparticle gap of the dimer in the large D limit, where D is the distance between the two molecule centers. For the sake of comparison, the TDLDA values for the two lowest lying *CT* excitations are indicated by the two non-dispersive dotted lines below 1.5 eV. The two vertical arrows indicate the difference between the TDLDA and *GW/BSE* values. Figure and caption (both modified) taken from Ref. [44].

reproduce the long-range Mulliken limit. Since H^{exch} and the *local* exchange-correlation term in H^{xc} vanish for a small overlap of the excited electron and the hole, the lowest excitation energy is given by:

$$E_{CT}^{exc} = IE_D - EA_A - \int d\mathbf{r}d\mathbf{r}' \phi_v(\mathbf{r}) \phi_{v'}^*(\mathbf{r}) \; u_\kappa(\mathbf{r}, \mathbf{r}') \; \phi_c^*(\mathbf{r}') \phi_{c'}(\mathbf{r}') \, .$$

As it is depicted in Fig. (3.3), only certain, specifically designed range-separated hybrid functionals show the right $1/R$ dependence in the long-range and correctly describe charge-transfer excitations. However, for standard hybrid functionals, the lowest *CT* excitation energy reduces to:

$$E_{CT}^{exc} = IE_D - EA_A - \frac{\alpha}{R},$$

i.e. one finds a reduced electron-hole binding energy of e.g. 20% in the case of B3LYP.

Range-separated hybrids give precise results both for local and *CT* excitations [49, 82, 174, 175, 176]. However, they contain adjustable parameters, which are not known a priori. They have to be determined either semi-empirically by fitting ground state properties of a given set of molecules or by taking into account physical criteria applying to the specific system

[50]. The transferability from one system to another remains difficult, since it has been shown that the optimal value for these parameters can be strongly system-dependent and even state-dependent [223, 232, 233]. Within GW/BSE, on the contrary, the screening is determined by the system itself instead of being fixed at the beginning. This makes this approach universal and systems ranging from metals with a very effective screening to molecules with poor screening properties should be equally accessible. The strength of the screening is automatically adjusted and thus both local and CT excitations are reproduced. In the following, this will be discussed first for the model dipeptide and second for the coumarin family, both showing intramolecular CT excitations. High-quality quantum chemistry and TDDFT calculations serve as a valuable reference.

3.3.2. Charge-transfer excitations in the model dipeptide

3.3.2.1. Background and Notation

The studied model dipeptide was originally introduced in Ref. [47] to rationalize the origin of the 7.3-7.5 eV absorption structure common to many polypeptides in gas phase. This work revealed the importance of intramolecular CT excitations between neighboring peptide units and subsequently, the dipeptide served as a test case for intramolecular CT excitations. It is one of the first examples, where large errors have been observed at the TDDFT level. This triggered its study by a large variety of approaches, including CASPT2 [47], TDDFT with various (semi)local, hybrid or range-separated hybrid functionals [49, 234, 235] and also a Bethe-Salpeter study based on an empirical scissor approach [236]. Difficulties were encountered to reproduce the CASPT2 results [47] with unusual discrepancies between the mentioned state-of-the-art techniques. Moreover, a very large sensitivity of CT excitation energies on the chosen functional parameters within e.g. the same CAM-B3LYP TDDFT framework was observed [49, 234].

In this work, we focus on two different kinds of optical excitations. On the one hand, we are interested in valence transitions between states localized on the same peptide unit. These are labeled $W1$ and $W2$ and the electron is promoted from an occupied σ_i-state to an unoccupied π_i^*-state. On the other hand, we study CT excitations between states localized on different peptide groups, namely the CTa exciton, a $\sigma_1 \rightarrow \pi_2^*$ transition, and the CTb exciton, a $\pi_1 \rightarrow \pi_2^*$ transition. As a reminder, the corresponding Kohn-Sham wave functions are depicted in Fig. (3.6). Anticipating on our BSE results, Fig. (3.10) illustrates the studied excitations by providing an isocontour representation of the hole-averaged electron distribution (transparent green) as obtained from the expectation value of the electron density operator $\delta(\mathbf{r} - \mathbf{r}_e)$ on the corresponding two-body $\psi(\mathbf{r}_e, \mathbf{r}_h)$ BSE eigenstate. Similarly, the electron-averaged hole distribution is represented (gray wireframe). The clear CT character of the CTa transition and the partial CT character of the CTb excitation can be readily verified.

Concerning the technical details of the BSE calculations presented in the following, we go beyond the already introduced Tamm-Dancoff approximation (TDA). This implies that the coupling between resonant (R) and anti-resonant (R^*) transitions is explicitly treated, i.e.

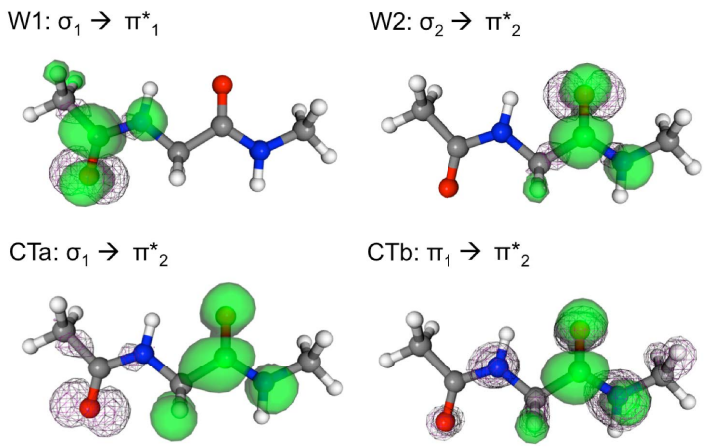

Figure 3.10.: Isocontour representation in green (wireframe) of the averaged electron (hole) distribution for the valence transitions W_i ($\sigma_i \rightarrow \pi_i$), the CTa ($\sigma_1 \rightarrow \pi_2^*$) and the CTb ($\pi_1 \rightarrow \pi_2^*$) excitations. Carbon atoms are represented in gray, oxygen in red, nitrogen in blue and hydrogen in white, respectively.

the coupling terms C and C^* are not neglected. As recently shown in several BSE studies [44, 236, 237, 238], it is important to go beyond the TDA in nanosized systems, where it can lead to a blue-shift of the order of 0.3 eV. Due to the quick increase in size of the $(\phi_v\phi_c)$ transition space product basis, we include all occupied states, but restrict the contributing transitions to the lowest-lying 160 unoccupied states.[6]

3.3.2.2. Comparison to multi-reference quantum chemistry perturbation theory and TDDFT methods

In Table (3.3) and Fig. (3.11), we provide the excitation energies as obtained by our GW/BSE calculations for the local $W1$ and $W2$ and the charge-transfer CTa and CTb transitions. Our GW/BSE values are compared to standard TDLDA calculations performed both with the FIESTA code, using the same basis than for our GW/BSE calculations, and the QuantumEspresso package [239] using a plane wave basis [236]. Further, the results of previous TDDFT calculations using B3LYP, the long-range corrected LC-BLYP and the CAM-B3LYP functional with two different sets of parameters [49, 234] are presented, together with an early quantum chemistry CASPT2 calculation [47].

Our TDLDA calculations come in very good agreement with the previous TDLDA plane wave based calculations performed with the QuantumEspresso package [236]. Both calculations predict CT states in nearly perfect agreement, with a negligible 0.02 eV discrepancy. The local $W1$ and $W2$ transitions agree within 0.1 eV. Such an agreement certainly comes as a good confirmation of the quality of the Kohn-Sham and auxiliary Gaussian basis sets used in the present study. Very similar results were also obtained at the TDDFT-PBE level in Ref. [234] with a maximum discrepancy of 0.05 eV as compared to our TDLDA calculations.

[6] We carefully tested the influence of the number of involved conduction bands on the resulting excitation energies and oscillator strengths. Between 120 and 160 conduction bands, the excitation energies varied by less then 10 meV.

	TDDFT					
	LDA		B3LYP	LC-LYP	CAM-B3LYP	
	Ref. [236]	FIESTA	Refs. [49, 234]	Ref. [49]	$(0.65)^a$	$(0.8)^b$
$W1$	5.30	5.40	5.49/5.55	5.56 (0.001)	5.65/5.68 (0.001)	5.72 (0.001)
$W2$	5.66	5.73	5.73/5.77	5.80 (0.000)	5.88/5.92 (0.000)	5.95 (0.000)
CTb	5.15	5.13	6.06/6.15	7.02 (0.043)	6.94/7.00 (0.018)	7.24 (0.040)
CTa	4.61	4.63	6.24/6.31	8.38 (0.000)	7.88/7.84 (0.000)	8.58 (0.000)

	GW/BSE		CASPT2[c]
	@LDA	*@COHSEX*	
$W1$	5.55 (0.001)	5.58 (0.001)	5.62 (0.001)
$W2$	5.79 (0.000)	5.80 (0.000)	5.79 (0.001)
CTb	7.20 (0.095)	7.13 (0.063)	7.18 (0.134)
CTa	8.36 (0.000)	8.58 (0.000)	8.07 (0.000)

Table 3.3.: Singlet excitation energies for the model dipeptide as obtained within various TDDFT, many-body perturbation theory and CASPT2 approaches. Energies are in eV. For the CAM-B3LYP columns, the (0.65) and (0.8) numbers indicate the $(\alpha + \beta)$ parameter that controls in particular the percentage of long-range exchange. The *@LDA* and *@COHSEX* columns indicate *evGW* calculations with either *DFT-LDA* or self-consistent COHSEX eigenstates as a starting point. Numbers in parenthesis are the oscillator strengths. Oscillator strengths in the $(\alpha + \beta = 0.65)$ CAM-B3LYP column are taken from Ref. [49].
[a] Refs. [49, 234]
[b] Ref. [49]
[c] Ref. [47] (Table II, structure 1a)

The main outcome of the TDLDA or TDDFT-PBE calculations is that CT excitation energies are much too small. The CT excitations are located below the lowest intramonomer $W1$ or $W2$ transitions. This is in great contrast to the CASPT2 results, where the CT excitations are found to lie about 1.4 eV to 2.4 eV above the $W1$ and $W2$ excitations. Our TDLDA value (4.63 eV) for the CTa transition, which consists nearly entirely of a transition between the Kohn-Sham HOMO and LUMO, can be compared to the HOMO-LUMO Kohn-Sham gap of 4.62 eV. This confirms that within TDDFT using local exchange-correlation functionals, the electron-hole interaction term vanishes for spatially separated electron and hole states and one is left with the energy difference between Kohn-Sham states. On the other hand, the local $W1$ and $W2$ transitions, with a strong overlap between final and initial states, are much better described, even though showing a $0.2-0.3$ eV red shift for the $W1$ transition as compared to CASPT2.

Introducing some amount of exact exchange to the TDDFT kernel allows even spatially separated electrons and holes to partially interact. Previous TDDFT-B3LYP calculations (see Table 3.3) indeed show some improvement as compared to TDLDA by locating the CT states above the $W1$ and $W2$ transitions. However, compared to CASPT2 calculations, the CT excitations energies are still about 1 eV to 1.8 eV too small, as a reminder that the B3LYP functional captures only 20% of exact exchange. This problem can be cured using range-separated functionals such as LC-BLYP or CAM-B3LYP, where the CT excitations come in much better agreement [49, 234] with the quantum-chemistry reference as indicated

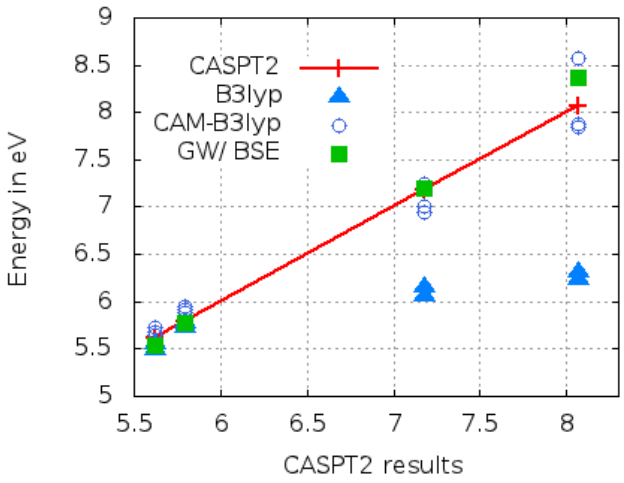

Figure 3.11.: Excitation energies as provided within several theoretical frameworks plotted against the CASPT2 results (first diagonal in red). The TDDFT values with the B3LYP (blue up triangles) and the CAM-B3LYP (open circles) functionals, and the present $GW/BSE@LDA$ calculations (green squares) are depicted. Several CAM-B3LYP values are found for each excitation, showing in particular the spread of values as a function of the $(\alpha+\beta)$ parameter. Energies are given in eV.

in Table (3.3). Nevertheless, within the CAM-B3LYP method itself, one observes energy differences of the order of 0.7 eV for the CTa exciton, leading to the standard question of the proper choice of the parameters ($\alpha+\beta=0.65$ or $\alpha+\beta=0.8$ in the present case).

Comparing our GW/BSE calculations ($@LDA$ column in Table 3.3) to CASPT2 values, we find an excellent agreement for the $W1$, $W2$ and the CTb excitation. The maximum discrepancy is 0.07 eV for the $W1$ transition, while remarkably both the local $W2$ and charge-transfer CTb excitation agree within 0.02 eV.[7] Clearly, tuning the (α,β) and range-separation parameters may bring the CAM-B3LYP calculations in better agreement with CASPT2 values, but we emphasize that the present GW/BSE scheme does not contain any adjustable parameters. Concerning the oscillator strengths of the respective transitions (see numbers in parenthesis in Table 3.3), the GW/BSE values are in reasonable agreement with the CASPT2 reference. The LC-BLYP and CAM-B3LYP values also agree for the transitions with vanishing oscillator strength, whereas they significantly underestimate the value of the oscillator strength for the CTb exciton, where the GW/BSE oscillator strength is closer to the CASPT2 value. Obtaining an excellent agreement between the various formalisms proves more difficult for the oscillator strengths than for the corresponding excitation energies.

The largest discrepancy between the present $GW/BSE@LDA$ and available CASPT2 calculations is of 0.3 eV for the CTa excitation. For such a transition, our GW/BSE value is

[7] The use of the Tamm-Dancoff approximation at the GW/BSE level leads to increased excitation energies and a deteriorated spectrum as compared to CASPT2. In agreement with the 0.15 eV blue shift reported by Rocca and coworkers [236], the largest TDA induced shift concerns the CTb excitation energy, which is blue-shifted by 0.17 eV in our calculations. The TDA further induces a small blue-shift of 0.03 eV for the $W1$ and $W2$ transitions, in perfect agreement with Ref. [236]. The CTa charge-transfer state is marginally affected by a 0.01 eV blue-shift.

in nearly perfect agreement with the LC-BLYP prediction, lying in between the two CAM-B3LYP values. As evidenced in Table (3.3) and Fig. (3.11), observing the rather large ~ 0.7 eV variation between the two CAM-B3LYP values, such a transition is clearly very sensitive to the details of the exchange and correlation potential. Before commenting on such a deviation, we will test the impact of using frozen Kohn-Sham LDA eigenstates in the present GW and Bethe-Salpeter approach here below.

3.3.2.3. GW/BSE calculations starting from self-consistent COHSEX eigenstates

The results of our GW/BSE study starting from self-consistent COHSEX eigenstates and eigenvalues is presented in the column "@$COHSEX$" of Table (3.3). As compared to GW/BSE calculations where the Kohn-Sham eigenstates are kept frozen ("@LDA" column), the $W1$ and $W2$ excitation energies hardly change by a maximum of 0.03 eV for the $W1$ transition. The largest variation is again related to the CTa transition, with an increase of 0.22 eV. This worsens the agreement with the CASPT2 value, but brings our GW/BSE calculations in excellent agreement with the CAM-B3LYP ($\alpha + \beta = 0.8$) results. Such an evolution can be traced back to a ~ 0.2 eV blue-shift of the π_2^* energy level within $GW@COHSEX$ as compared to $GW@LDA$. The oscillator strength associated with this transition is also seen to adopt a smaller value, worsening the agreement with the CASPT2 value, but improving the agreement with the CAM-B3LYP result.

It is interesting to observe that what we may consider to be our most accurate values, namely our $evGW/BSE$ calculations based on scCOHSEX eigenstates, come in excellent agreement with the CAM-B3LYP value with enhanced long-range exchange, namely setting $(\alpha + \beta)$ to 0.8 instead of the original 0.65 value. In the case of CT excitations, the correct long-range Mulliken limit can only be reproduced with a long-range ($\alpha + \beta = 1$) parametrization of the CAM-B3LYP functional (see Fig. 3.3). As such, the ($\alpha + \beta = 0.8$) functional provides in principle a better description of the long-range CT electron-hole interaction. Very consistently, the LC-BLYP functional, with a proper asymptotic scaling, locates the CTa transition at 8.38 eV [49], in much better agreement with our GW/BSE values than the CASPT2 prediction. However, the analysis of the contributing wave functions in Fig. (3.10) shows that the CTa transition in the dipeptide is far from the ideal case of the long-range well-separated electron-hole CT limit. Overall, our GW/BSE@COHSEX results show a mean absolute error of 0.1 eV and 0.08 eV as compared to CAM-B3LYP ($\alpha + \beta = 0.8$) and LC-BLYP, respectively.

Regarding previous studies on CT excitations within the present GW/BSE formalism, with typical errors of the order of 0.1 eV as compared to experiment, TDDFT with optimized range-separated functionals or CASPT2 calculations [8, 44, 240], the present 0.3 eV to 0.5 eV discrepancies for the CTa transition are somehow unusual, even though dramatically smaller than the typical errors induced by TDDFT calculation with (semi)local kernels or even B3LYP. The 0.7 eV difference obtained between CAM-B3LYP calculations with various parametrizations [49] indicates that such variations cannot be explained by differences in running parameters (basis sizes and type, pseudopotential, etc.), but really hinge on the sensitivity of this transition onto the balance between short- and long-range exchange and

correlation.

While we cannot comment on the accuracy and limitations of the available CASPT2 calculations, we certainly can emphasize in particular the lack of double-excitations in the present GW/BSE formalism and in TDDFT calculations, a possible explanation that would require more sophisticated treatments such as the inclusion of dynamical effects in the screened Coulomb potential matrix elements at the BSE level [241]. While this is certainly beyond the scope of the present work, we can conclude that as it stands, the present parameter-free GW/BSE approach offers an accuracy comparable to TDDFT calculations performed with the best available parametrized range-separated functionals.

3.3.2.4. Conclusion

We studied within the many-body Green's function GW/BSE approach the excitation energies of a paradigmatic dipeptide. The latter served as a benchmark for describing intramolecular CT excitations in organic systems within various theoretical frameworks, including TDDFT with local, classical hybrid and range-separated hybrid functionals, CASPT2 calculations and a previous Bethe-Salpeter study based on an empirical GW Scissor approach. Based on $evGW$ calculations, our calculated optical excitation energies are found to agree with CASPT2 calculations within 0.07 eV for the local $W1$, $W2$ and the charge-transfer CTb excitation and a maximum discrepancy of 0.3 eV for the CTa transition. The effect of further updating self-consistently the quasiparticle wave functions within the static COHSEX approximation leads to rather marginal variations for the $W1$, $W2$ and CTb excitations, but shifts the discrepancy to 0.5 eV as compared to CASPT2 for the ubiquitous CTa transition. Our BSE calculations based on the GW@COHSEX eigenvalues and eigenfunctions agree very well with both CAM-B3LYP calculations with enhanced long-range exchange ($\alpha + \beta = 0.8$) and the original LC-BLYP formulation, with a maximum mean absolute error of 0.1 eV. The present results confirm the reliability of the parameter-free GW/BSE formalism in describing local and charge-transfer excitations in organic systems of interest e.g. for photovoltaics, photosynthesis or photocatalysis.

3.3.3. Charge-transfer excitations in the coumarin family

3.3.3.1. The studied system: the coumarin molecules

Promising to become a low-cost alternative to standard silicon-based photovoltaics, dye-sensitized solar cells (DSSCs) have been intensively studied over the past 20 years [27, 242]. The most prominent modern DSSCs, also known as Grätzel cells, consist of porous layers of titanium dioxide (TiO_2) nanoparticles covered by a monolayer of an organic dye absorbing the sun light. The working principle is schematically illustrated in Fig. (3.12). While the most efficient sensitizers are composed of ruthenium dye complexes, intense research is conducted so as to find molecular alternatives which are cheaper, easier to synthesize and free from the resource limitations related to the noble metal ruthenium. As a promising direction, Hara and coworkers demonstrated that coumarin-based dyes, such as the so-called NKX-2xxx fam-

ily (see Fig. 3.13), could lead to conversion efficiencies approaching that of ruthenium-based DSSCs [28, 29, 30, 31].

Coumarins show very good photoelectric properties [28, 30] and they are an impressive example of chemical molecular design. Starting from the originally tested C343 coumarin [243], the introduction of (-C=C-) methine fragments between the coumarin unit and the terminal (-COOH) carboxyl group (see Fig. 3.14) induces a red shift of the absorption spectrum [28]. This improves the light harvesting in the visible range, since the absorption edge is shifted to lower energies (see Fig. 3.16). The resulting molecular structures of the NKX-2xxx family are represented in Fig. (3.13) showing the so-called (cis) conformations, with a (trans) structural isomer represented in Fig. (3.14) for one of them. Further, inclusion of the cyano (-C=N) group enhances the acceptor character of the combined (-COOH) and (-C=N) cyanoacrylic acid group, increasing the charge-transfer character of the internal excitations. This is believed to favor the injection of the photoelectron into the TiO_2 conduction band through the anchoring (-COOH) carboxylic unit [28]. Finally, the replacement of the methine spacer by thiophene chains reduces the adverse aggregation of dyes onto the TiO_2 surface, leading to the NKX-2677 dye with a solar-energy-to-electricity conversion efficiency of 7.7% [29].

Due to its internal donor-acceptor structure, this family of molecules became also a bench-

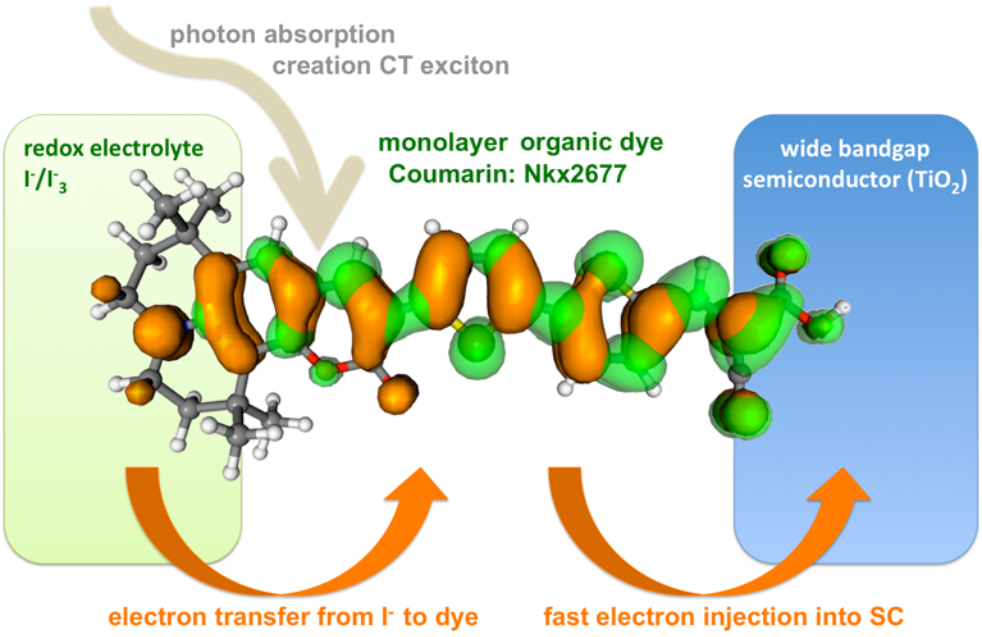

Figure 3.12.: Functional principle of an exemplary DSSC with the NKX-2677 coumarin dye: light is absorbed in the monolayer of the NKX-2677 dye, creating as lowest-lying excitation a CT state (averaged electron/ hole distribution in green/ orange). The excited electron then goes from the conduction band of the dye into the conduction band of TiO_2 (lower in energy) and finally in the anode (not shown). The circuit is closed, as the redox system I^-/I_3^- transports electrons from the cathode (not shown) to the dye, which in turn recovers charge neutrality.

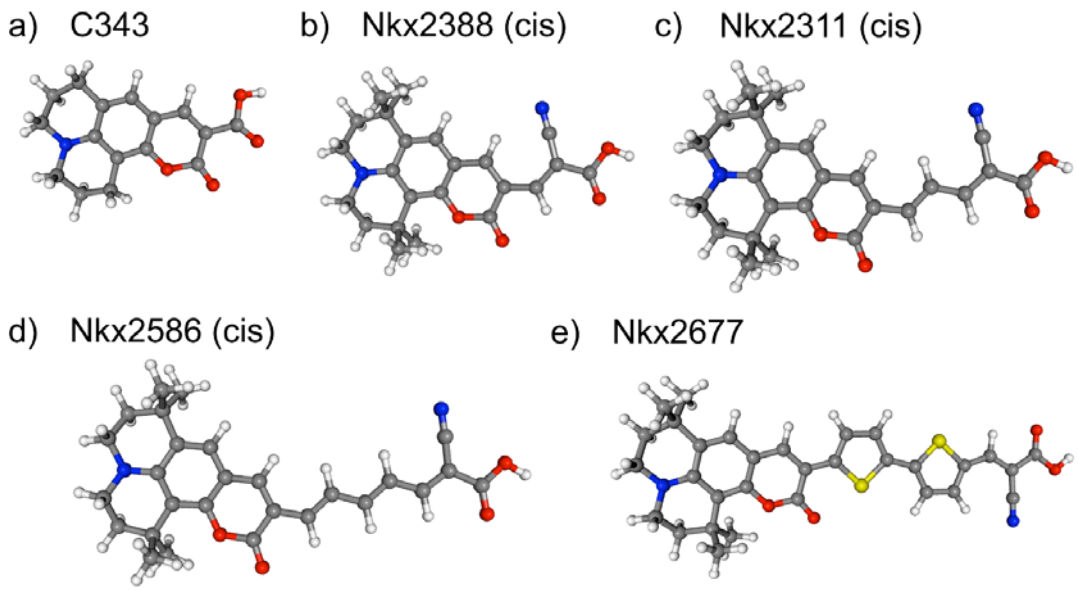

Figure 3.13.: Symbolic representation of the studied coumarins: (a) parent C343, (b) NKX-2388 (cis), (c) NKX-2311 (cis), (d) NKX-2586 (cis) and (e) NKX-2677. The difference with the corresponding (trans) structures is represented in Fig. (3.14) for the NKX-2311 case. Black, white, red, blue and yellow atoms represent carbon, hydrogen, oxygen, nitrogen and sulfur, respectively.

mark for theoretical studies aiming at solving the already mentioned problem of describing *CT* excitations within time-dependent density functional theory (TDDFT) [228, 230]. In particular, TDDFT calculations with (semi)local [224] and hybrid [50, 222, 223] kernels were conducted and compared to reference quantum chemistry coupled-cluster CC2 calculations [222] in order to assess the accuracy of the various approaches. This offers us a broad spectrum of ab initio reference data. In the present work, we analyze the (singlet) excitation energies of various coumarin-based molecules such as the parent C343 dye and the related NKX-2388, NKX-2311, NKX-2586 and NKX-2677 structures.

3.3.3.2. Technical details

The used molecular structures have been relaxed at the all-electron DFT-B3LYP 6-311G(d,p) level using the Gaussian09 package [211]. As a single-particle starting point for the *GW/BSE* calculations, *DFT-LDA* eigenstates and eigenvalues as provided by the SIESTA package [136] with a large triple-zeta plus double polarization basis (TZDP) are used.

The *GW* correction is explicitly calculated for the 10 highest occupied and lowest unoccupied levels, whereas the remaining levels are rigidly shifted. We performed iterative *GW* calculations with a simple self-consistency on the eigenvalues as presented in the preceding section. Our auxiliary basis contains six $e^{-\alpha r^2}$ Gaussian functions for the radial part of each (s, p, d) channel, with an even-tempered distribution of the localization coefficients α ranging from 0.1 to 3.2, except for hydrogen, where the range is set to 0.1 to 1.5. As such, our auxiliary basis contains typically 54 orbitals per atom. Using these running parameters, the

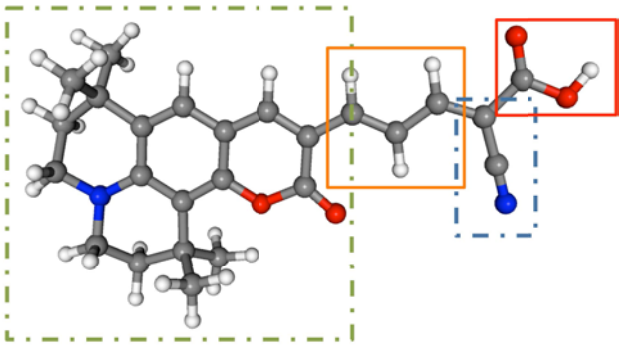

Figure 3.14.: Symbolic representation of the NKX-2311 (trans) coumarin dye. This structure can be compared to the NKX-2311 (cis) structure in Fig. (3.13), which differs from the orientation of the π-conjugated polymethine (-HC=CH-) bridge (orange frame), the cyano (-C=N) (blue dot-dashed box) and the carboxylic (-COOH) (full red box) groups. The donor coumarin parent is highlighted in a green dot-dashed frame. The anchoring group to the semiconducting TiO_2 surface is the carboxylic unit.

comparison to GW/BSE results calculated with a reference plane wave code [183] showed excellent agreement in the case of acene-tetracyanoethylene (TCNE) donor-acceptor complexes [8], demonstrating the accuracy of the present Gaussian-based formalism.

While in the GW calculation all empty states are included in the construction of the irreducible susceptibility P and the Green's function G, the number of empty states included in the BSE Hamiltonian has been set to 160. Convergency tests for the largest NKX-2677 molecule indicate that increasing this number to 200 decreases the excitation energy by less than 10 meV. In what follows, we go beyond the Tamm-Dancoff approximation (TDA) by mixing resonant and antiresonant contributions. As shown in recent studies [237, 238], the TDA tends to overestimate the excitations energies by a few tenths of an eV in small size systems, where single-particle and collective excitations can strongly mix. This is what we observe here with the low-lying excitation energies, which are blue shifted by up to 0.25 eV for the C343 dye and 0.18 eV in the NKX-2677 case, when the off-diagonal coupling blocks are neglected.

3.3.3.3. Comparison to quantum chemistry CC2 and TDDFT reference data

Our results are compiled in Table (3.4) and in Fig. (3.15) with a comparison to previously published TDDFT and CC2 calculations. As expected, the TDLDA and TD-PBE values from Ref. [224] display an underestimation of the transition energies related to the CT character of the excitations. The mean absolute error (MAE) averaged over the available data points amounts to 0.47 and 0.44 eV as compared to CC2 within TDLDA and TD-PBE, respectively. Further, the oscillator strength seems to be significantly underestimated, in particular, for the C343 parent molecule expected to show the smallest CT character.

Due to its 20% of exact exchange, the B3LYP results of Ref. [222] (filled black circles in Fig. 3.15) show a reduced MAE of 0.2 eV. However, the discrepancy can still be as large as

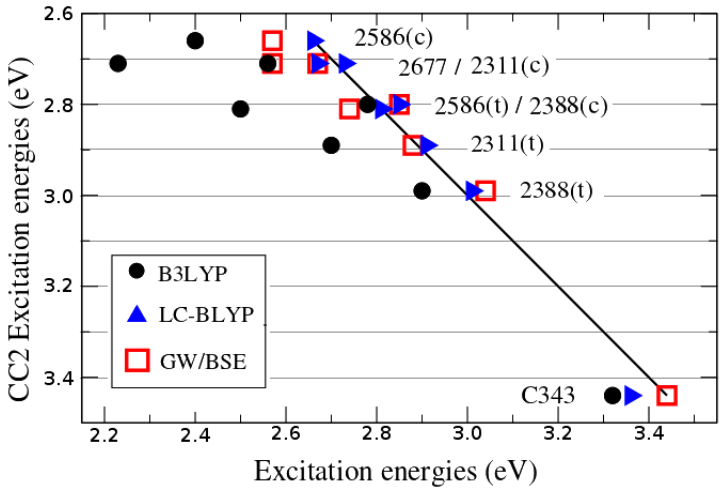

Figure 3.15.: Calculated lowest optical excitation energies (in eV) as a function of the coupled-cluster CC2 reference values. Results in perfect agreement with the CC2 calculations should fall on the diagonal (black line). The present *GW/BSE* calculations (empty red squares) are compared to the TD-B3LYP results of Refs. [222] and [223] (filled black circles) and the TD-LC-BLYP data from Ref. [223] (blue triangles up). The coumarins are indicated by their number (removing the NKX prefix) with (c) standing for (cis) and (t) for (trans). The axes' physical length is scaled according to their respective energy range.

0.48 eV for the NKX-2677 structure. This is certainly the signature that in the long-range charge-separation limit, the restricted amount of exact exchange in the B3LYP functional [75] is not enough to account for the correct electron-hole interaction. To illustrate that point, we plot in Fig. (3.16) the Kohn-Sham HOMO (a, d) and LUMO (b, e) eigenstates associated with the C343 and NKX-2677 structures. While the HOMO states are found to be rather delocalized, the LUMO in the NKX-2677 dye is clearly much more localized close to the electron-acceptor cyanoacrylic group. This results in an enhanced *CT* character as compared to the C343 parent molecule.

The nature of the transitions can be better quantified by studying the electron and hole spatial localization in the excited states. This can be achieved by taking the expectation value of the electron position operator $\delta(\mathbf{r}-\mathbf{r}_e)$ over the two-body $\psi(\mathbf{r}_e,\mathbf{r}_h)$ BSE excitonic wave function, leading to an electron probability of presence averaged over the hole position. A similar quantity can be defined for the hole spatial distribution. The resulting densities are provided in Fig. (3.16) with an isocontour representation for the C343 and NKX-2677 molecules. These densities allow to obtain the mean electron or hole positions (see red arrows in Fig. 3.16) and the related average electron-hole separation distance which amounts to 3.2 Å in C343. This clear *CT* character is certainly at the origin of the difficulties met by TDLDA or TD-PBE to describe such an excitation. In the NKX-2677 case, this average distance increases to 4.6 Å as a signature of the enhanced *CT* character, explaining that the B3LYP results significantly worsen from C343 to NKX-2677.

We now come to the central results of the present study, namely the many-body pertur-

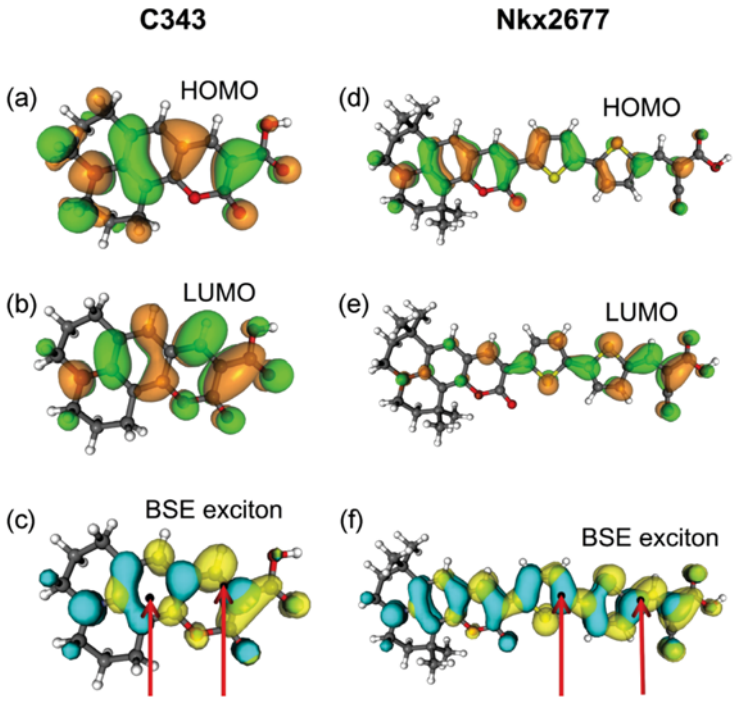

Figure 3.16.: Isocontour representation of the C343 HOMO (a) and LUMO (b) Kohn-Sham eigenstates. Different colors indicate different signs of the wave function. In panels (d) and (e), similar plots for NKX-2677. In panels (c) and (f), isocontour representation of the electron (yellow) and hole (light blue) probability distribution for the lowest C343 and NKX-2677 optical excited states, respectively, as obtained within BSE. The red arrows indicate the average hole (left arrow) and electron (right arrow) positions. The C343 and NKX-2677 molecules are not represented on the same scale.

bation theory data. In contrast to the TDLDA, TD-PBE or even TD-B3LYP results, our GW/BSE values (empty red squares in Fig. 3.15) are in much better agreement with the CC2 data points, with a mean absolute error of 0.06 eV. Such an agreement is remarkable accounting for the fact that the present GW/BSE approach does not contain any adjustable parameter. Concerning the longest NKX-2677 dye, which shows the largest discrepancy with CC2 calculations, we observe that our result falls within the values provided by the range-separated hybrid BNL functional study of Ref. [50], where two different strategies to optimize non-empirically the range-separation parameter have been tested.[8] As compared to the RSH-BNL study, our GW/BSE results differ by a MAE ranging from 0.04 to 0.07 eV, which is well within the target maximum error of 0.1 eV. As emphasized in Ref. [50], the CC2 approach is also not free from approximations and differences of the order of 0.1 eV as compared to more accurate e.g. CASPT2 calculations are certainly to be expected.[9]

[8] The range separation parameter is obtained ab initio by minimizing the MAE between the Kohn-Sham HOMO and/or LUMO eigenvalues and the corresponding quantities obtained with a much more accurate ΔSCF approach for the neutral and charged systems. Depending on the chosen criteria, i.e optimization of the HOMO only of the neutral and charged systems ("J_1" scheme) or of the HOMO and LUMO of the neutral system ("J_2" scheme), slightly different values can be obtained. See Ref. [50].

[9] It is to be observed that due to computational costs at the time of publication, the CC2 calculations have

	LDA/PBE[a]	B3LYP[b]	LC-BLYP[c]	BNL[d] J_1/J_2	CC2[b]	*GW-BSE*
C343	2.96/3.0 (0.36/)	3.32 (0.60)	3.36 (0.57)	3.5/3.4 (0.7/0.6)	3.44 (0.74)	3.44 (0.57)
2388 (t)		2.90 (0.94)	3.01 (0.88)	3.1/2.9 (1.0/0.9)	2.99 (1.06)	3.04 (0.88)
2388 (c)		2.78 (0.87)	2.85 (0.80)	2.9/2.8 (0.9/0.9)	2.80 (1.00)	2.85 (0.80)
2311 (t)		2.70 (1.35)	2.91 (1.34)	2.9/2.8 (1.6/1.5)	2.89 (1.51)	2.88 (1.37)
2311 (c)	2.35/2.35 (1.05/)	2.56 (1.19)	2.73 (1.12)	2.7/2.6 (1.3/1.2)	2.71 (1.33)	2.67 (1.13)
2586 (t)		2.50 (1.71)	2.81 (1.83)	2.8/2.6 (2.1/2.0)	2.81 (2.01)	2.74 (1.88)
2586 (c)	2.10/2.15 (1.23/)	2.40 (1.55)	2.66 (1.52)	2.6/2.5 (1.7/1.7)	2.66 (1.74)	2.57 (1.59)
2677		2.23 (1.49)	2.67 (1.76)	2.7/2.5 (2.0/1.8)	2.71 (2.17)	2.56 (1.69)

Table 3.4.: Calculated lowest transition singlet energies (eV). The *GW/BSE* results calculated in the present study are compared to the TDLDA, TD-PBE, TD-B3LYP, TD-LC-BLYP, TD-BNL and CC2 calculations. We provide the TD-B3LYP results from Ref. [222], which are in excellent agreement with the results of Ref. [223]. The numbers in parentheses indicate the associated oscillator strengths. The coumarins are indicated by their number (without the NKX prefix), where (c) stands for (cis) and (t) for (trans).
[a] Ref. [224], [b] Ref. [222], [c] Ref. [223], [d] Ref. [50]

Clearly, as compiled in Table (3.4), TDDFT calculations with the LC-BLYP functional [175] also provide excellent results [223], with a MAE of 0.03 eV as compared to CC2, smaller than our *GW/BSE* MAE of 0.06 eV. However, as emphasized in Ref. [223], the range-separation parameter κ in the LC-BLYP study has been precisely adjusted to minimize the root mean square error compared to CC2 calculations. The best-fit κ value for these systems ($\kappa = 0.17$) is found to be much smaller than the original value ($\kappa = 0.33$) advocated by Iikura and coworkers [175]. The strong dependence of the optical excitation energies as a function of κ indicates that the choice of the originally recommended $\kappa = 0.33$ value would lead to a significant overestimation of the transition energies (by as much as 0.3–0.4 eV; see Fig. 4 of Ref. [223]). This leads to the standard question of the choice and transferability of the range-separation parameter. One observes, however, that with the best-fit κ value, the correlation between LC-BLYP and CC2 results is very remarkable, showing that this class of systems can be described by a unique parameter.

Bearing important consequences on the use of such dyes in DSSCs, our *GW/BSE* calculations show as expected that the onset of absorption is significantly red shifted with increasing size length (see Fig. 3.17). This evolution is in clear contrast with the behavior of *CT* excitations in well-separated gas phase donor-acceptor dyads where the exciton binding energy scales as the inverse distance between the two molecules, leading to an increase of the absorption energy onset. However, contrary to well separated donor or acceptor systems, the quasiparticle HOMO-LUMO gap in donor or acceptor dyads connected by a conducting π-conjugated bridge does not remain constant with varying bridge length. This is clearly exemplified in Table (3.5), where the *GW* gap is found to quickly decrease from the C343 molecule to the longest NKX-2677 dye. Except for the large variation of the electronic affinity (*EA*) from the C343 parent to the NKX-2388 system, analysis of the *GW* HOMO and LUMO quasiparticle energies indicates that this gap reduction stems both from a destabilization of the HOMO

been performed with a limited SV(P) basis. See Ref. [222].

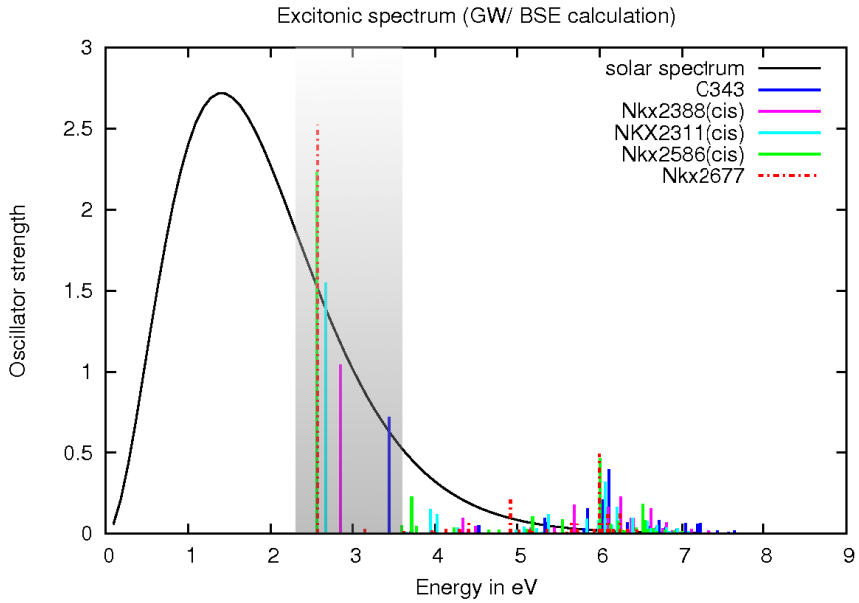

Figure 3.17.: Optical excitation energies versus oscillator strength as calculated within GW/BSE for the coumarin (cis) structures: the lowest-lying excitations for the corresponding molecules, which possess CT character, show in each case the strongest oscillator strength. Through molecular design, the excitation energy of these principal excitations (highlighted in gray) are shifted from 3.44 eV for C343 (blue) to 2.57 eV for NKX-2586(c) (light green) and 2.56 eV for NKX-2677 (red dashed), respectively. As a result, the absorption edge comes closer to the maximum of the solar spectrum (Planck's formula plotted in black as a guide for the eye).

and a stabilization of the LUMO. Subtracting the GW gap from the optical GW/BSE excitation energy, one finds that the electron-hole binding energy decreases with donor-acceptor distance. However, this effect is not strong enough to counterbalance the decrease of the HOMO-LUMO gap. This is an important feature which explains that the longest NKX-2677 dye is most efficient in harvesting photons in the visible range.

We close this study by commenting on the oscillator strength associated with the calculated transitions (see Table 3.4 and Fig. 3.18). Our GW/BSE values lead to an excellent agreement with the parametrized LC-BLYP calculations, with a perfect match for the C343 and NKX-2388 molecules. Such an agreement is remarkable, given the fact that the two approaches are very different. Both GW/BSE and LC-BLYP provide lower values as compared to CC2 calculations, the BNL data yielding somehow intermediate results. The largest discrepancies occur for the NKX-2677 molecule, with a 22% difference between the GW/BSE and CC2 values. For this system, GW/BSE and LC-BLYP agree again extremely well, within 4%, while the two BNL values show their largest spread, indicating that the oscillator strength for this structure is very sensitive to the chosen formalism and related parameters. Further analysis is needed to understand these variations from one type of calculation to another. Beyond the mentioned differences, one should emphasize that all studies agree on the fact that the NKX-2677 dye presents one of the largest oscillator strength, yet another factor

	-IE	-EA	E_g	E_b^{e-h}
C343	7.21	0.60	6.61	3.17
2388 (t)	7.12	1.33	5.79	2.75
2388 (c)	7.11	1.50	5.61	2.76
2311 (t)	6.93	1.55	5.38	2.50
2311 (c)	6.92	1.71	5.21	2.54
2586 (t)	6.76	1.70	5.06	2.32
2586 (c)	6.77	1.85	4.91	2.34
2677	6.52	1.62	4.90	2.33

Table 3.5.: Calculated GW ionization energy (IE), electronic affinity (EA) and HOMO-LUMO gap E_g. The given electron-hole binding energy E_b^{e-h} equals the GW gap minus the first optical excitation energy, $E_b^{e-h} = E_g - E_1^{exc}$. Energies are in eV.

explaining that it leads to one of the largest conversion efficiencies in coumarin based DSSCs.

3.3.3.4. Conclusion

In conclusion, we have studied within the many-body Green's function GW/BSE approach the excitation energies of a family of coumarin dyes recently shown to be very promising candidates for replacing ruthenium-based chromophores in dye-sensitized solar cells (DSSCs). In such donor-bridge-acceptor molecules, the lowest singlet excitations are characterized by a charge-transfer character that varies with the length of the π-conjugated bridge. As a result, TD-B3LYP calculations can lead to an error as large as 0.5 eV as compared to reference quantum chemistry coupled-cluster CC2 calculations, despite the 20% of exact exchange contained in its functional form. We demonstrate that the GW/BSE approach leads to an excellent agreement with CC2 data with a mean absolute error of the order of 0.06 eV for the excitation energies. Such an accuracy is comparable to the best results provided by TDDFT calculations with optimized long-range corrected range-separated hybrids, but with a parameter-free approach that performs equally well for extended insulating or metallic systems and gas phase organic molecules. Such an excellent agreement is also demonstrated for the related oscillator strengths. The ability of the GW/BSE approach to describe both localized and charge-transfer excitations in finite size molecular systems or extended semiconductors originates in particular from the use of the screened Coulomb potential W that automatically adjusts the strength and range of the Coulomb interactions. This flexibility may prove as a significant advantage in the study of DSSCs, where both the organic dye and the extended TiO2 semiconductor must be treated with sufficient accuracy.

After having carefully tested the validity range and accuracy of the presented GW/BSE approach with respect to ab initio quantum chemistry methods, DFT and TDDFT, we go on by studying its quality concerning a property directly related to the quasiparticle energies, namely the electron-phonon coupling (EPC). As discussed in detail in the subsequent section, electron-phonon coupling in molecular systems is at the heart of several important physical phenomena, such as the mobility of charge carriers in organic electronic devices [244, 245, 246, 247]. In the following, we study the electron-phonon coupling in two different systems:

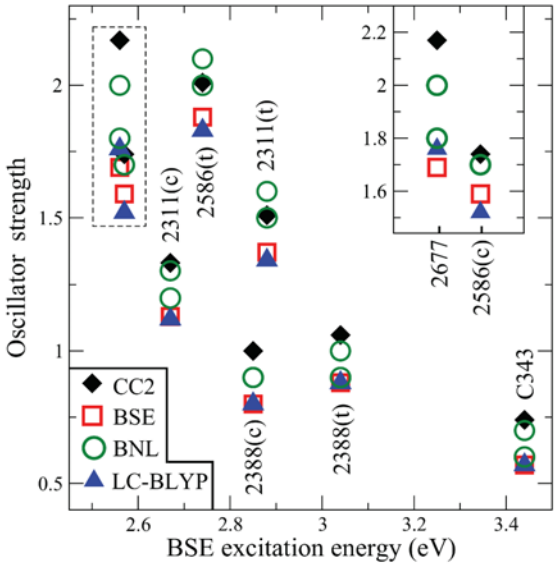

Figure 3.18.: Theoretical oscillator strength as a function of the GW/BSE excitation energies (eV). The GW/BSE values (red empty squares) are compared to the CC2 (black diamond), LC-BLYP (blue triangle up) and the BNL J_1/J_2 (empty green circles) results. Results for the NKX-2677 and NKX-2586 (cis) molecule in the dashed box are reproduced in the upper-right inset.

the molecular Buckminster fullerene C_{60} and the most popular semi-metal graphene.

3.4. Efficient ab initio calculation of electron-phonon coupling matrix elements

Electron-phonon coupling (EPC), i.e. the interplay between electrons and vibrational eigenmodes, takes an important place in diverse fields of research. By way of example, it is believed to play a prominent role for the transport properties of organic semiconductors [244, 245, 246, 247], for the exciton dissociation at the donor-acceptor interface in organic photovoltaics [248], for the life-time of hot electrons in semiconductors [249, 250] and it is also at the heart of the BCS phonon-mediated theory of superconductivity [251, 252, 253, 254]. Concerning organic systems, we recently demonstrated that the inclusion of electron-phonon coupling effects is crucial to obtain accurate band structures in the case of crystalline pentacene [247, 255]. Organic semiconductor crystals are, contrary to standard inorganic semiconductors with strongly covalently bound atoms, composed of molecules which are weakly connected through van der Waals interactions. As such, electronic bands dispersion and electron-phonon coupling strengths may be of the same magnitude. In the case of crystalline pentacene, which is a typical study case for organic semiconductors, accurate GW band structure calculations [256] revealed important discrepancies with experimental ARPES results. Since the GW approach is among the best available ab initio band structure theories, the errors could not be explained on the electronic level. Instead, we demonstrated that it is indispensable to include the interaction of the electrons with the internal vibrations of the molecules. In a

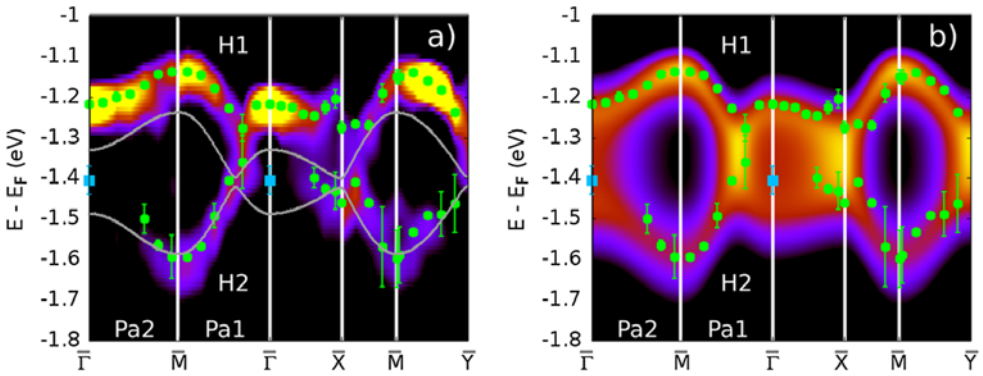

Figure 3.19.: (a) Color density plot of experimental ARPES data for the two highest occupied bands H1 and H2. The (green) dots are the peak positions as derived from Gaussian fits of the individual spectra. The gray line is the ab initio *DFT* band dispersion from Ref. [257], in close agreement with *GW* calculations within this energy window [256]. (b) Calculated spectrum in the presence of EPC interactions and disorder (see text). The dots are the experimental peak positions from panel (a), but now the color density plot originates from the theoretical spectra including electronic lifetimes and thus a broadening through electron-phonon scattering. Figure and caption (modified) taken from Ref. [247].

non-perturbative dynamical mean-field theory (DMFT) approach (S. Ciuchi, S. Fratini), the intramolecular electron-phonon coupling strength (Holstein approximation) calculated for a single pentacene molecule at the *GW* level has been combined with an ab initio band structure of the pentacene crystal [257] in order to describe simultaneously the molecular (vibrational) and crystalline nature (band structure) of these materials. The obtained band structure is in extremely good agreement with the experimental measurements, which is shown in Fig. (3.19) for the two highest occupied bands, important for hole carrier transport. Our combined experimental and theoretical study on pentacene has demonstrated unambiguously that fingerprints of the molecular constituents are clearly visible in the electronic energy spectrum. Since our contribution was "limited" to providing on-site electron-phonon coupling matrix elements within the many-body *GW* formalism, a subject that we describe here below in detail for the Buckminster fullerene case, we do not discuss further this specific example, but directly start analyzing how accurately EPC energies can be calculated.

Concerning ab initio calculations of EPC matrix elements, up to now, mainly *DFT-KS* and its perturbative linear response extension (*DFPT*) [258, 259] have been applied, providing remarkable information at the microscopic level. However, several recent studies questioned the accuracy of the EPC matrix elements calculated within the standard *DFT* approaches using (semi)local exchange-correlation functionals, such as *LDA*. The average electron-phonon coupling of specific phonon modes in graphene [51], the value of the electron-phonon average potential in the electron-doped Buckminster fullerene C_{60} [12, 260], superconducting bismuthates and transition-metal chloronitrides [261], or the renormalization of the photoemission band structure of pentacene [247] and diamond crystals [52], were all shown to be

strongly affected by a significant underestimation of the strength of the EPC matrix elements as calculated within *DFT-KS* and (semi)local exchange-correlation functionals. In the following we comment in detail on three of the mentioned cases, namely C_{60}, graphene and diamond.

The magnitude of the EPC in C_{60} has been subject to numerous theoretical and experimental studies since the early 90ies, offering a variety of reference data. Such a wealth of data can be explained by the observed superconducting transition of alkali-doped (n-doped) fullerides, which has been subject of intense research [252]. On the ab initio level, (semi)local *DFT-LDA* [12] and *DFT*-PBE [260] calculations yield a total EPC strength of 73 meV and 76 meV, respectively, for the coupling of all modes to the LUMO level (see below). This is drastically smaller than available experimental values extracted from PES experiments on C_{60} in the gas phase, which range from 107 meV to 158 meV. A significant increase on the *DFT* level could be achieved by employing the hybrid functional B3LYP, yielding an EPC strength of 94 meV [260]. Moreover, by varying the amount of exact exchange in the hybrid functional from the original 20% value to 30%, the EPC strength could be augmented to up to 111 meV [260], resulting in an excellent agreement with the lower and most recent experimental limit of 107 meV [262, 263]. This demonstrates the sensitivity of the EPC strength on the used amount of exact exchange. Certainly, it would be possible to build a hybrid functional, which yields a perfect match with experiment. However, without comparison to experimental reference data, an estimation of the appropriate amount of exact exchange is difficult and the predictive power of this method thus limited. Moreover, the needed amount of exact exchange may vary from one system to another. Such difficulties do not arise within the *GW* formalism, where the screening is, as already discussed in preceding sections, intrinsically adjusted by the system itself and not artificially fixed at the beginning. That gives this method a large flexibility and systems of different kinds should be accessible on the same footing. Concerning the C_{60} molecule, our recent *evGW* study, as described here below, shows an EPC strength of 101 meV, which is in excellent agreement with the two most recent experimental results and 43% larger than the reference *DFT-LDA* value. This clearly points out the necessity to go beyond the *DFT-LDA* approach for the calculation of the EPC in C_{60}.

A similar result has been recently obtained in the case of graphene [51]. Here, the EPC matrix elements for the coupling of the Γ-E_{2g} and K-A_1' phonon modes with the electronic states at the Fermi level were studied within a non-self-consistent G_0W_0 approach starting from *DFT-LDA*. Within G_0W_0, the square of the corresponding EPC matrix elements (see definition below) were shown to increase by 41% and 114%, respectively, as compared to *DFT-LDA*. This is consistent with the case of C_{60}. Very importantly, this study on graphene also demonstrated that *DFT*-B3LYP yields, contrary to the presented results on C_{60}, significantly too large coupling constants as compared to experiment. This certainly points out the difficulty in obtaining hybrid functionals, which are accurate both for finite and extended systems.

Concerning the case of diamond, very recently, the band-gap renormalization by zero-point motion has been studied by means of *DFT-LDA*, G_0W_0 and *GW* [52]. In this context, the corresponding EPC matrix elements for band edges have been evaluated, since they can be

directly related to the temperature dependent renormalization of the electronic bands. In Ref. [264], it was already shown that standard *DFT* and *DFPT* methods strongly underestimate the zero-point renormalization of the direct gap of diamond compared to experiment. By increasing the zero-point renormalization by more than 40% compared to *DFT-LDA*, the recent G_0W_0/*GW* calculations from Ref. [52] remedied the discrepancies and restored a good agreement between theory and experiment.

To conclude, the hitherto results suggest that the EPC strength is significantly affected by the *GW* correction in both finite and extended systems. It is therefore important to go beyond the *DFT-KS* approach. However, the computational costs of such techniques represent strong limitations to their application. Unfortunately, the kind of theories that are available within *DFT*, and in particular the efficient density functional perturbation theory, are not yet available within the framework of many-body perturbation theory. As detailed later in this section, for *GW* calculations, one has to pass by demanding frozen-phonon techniques. These are only feasible for zone-center or zone-boundary phonon modes, since otherwise large unit cells are needed implying high computational costs. In this work, we explore less demanding many-body perturbation theory approaches to calculate the EPC. Namely, we study the accuracy of the COHSEX approximation, both in its single-shot and its self-consistent version. Further, we also examine the accuracy of a constant screening approximation, namely we neglect the variations of the screened Coulomb potential W upon small changes of the atomic positions along the vibrational eigenmodes. These approximations are evaluated by means of studies on the molecule C_{60} and the popular semi-metal graphene.

3.4.1. The studied systems

3.4.1.1. Electron-phonon coupling in C_{60}

Electronic properties As already mentioned before, electron-doped fullerenes, so-called fullerides, have attracted much attention, since they show phonon-mediated superconducting transitions [251, 252, 253]. Fullerenes are cage-like molecules, where one of the most prominent examples of the fullerene family is the Buckminster fullerene C_{60} (see Fig. 3.20). Under doping, e.g. with alkali atoms such as sodium or potassium, the electronic structure of the neutral C_{60} fullerene is not fundamentally changed. The s-type levels of the alkali atoms appear close to the second lowest-lying unoccupied C_{60} level (denoted LUMO-1 in the following). Moreover, the C_{60} LUMO becomes half-filled by the additional electrons of the dopant, shifting the Fermi level up from the gap center into the LUMO (see Fig. 3.21).

Following second order perturbation theory for electron-phonon scattering in extended solids, one obtains the effective phonon-mediated attractive potential V_{ep}, i.e. a measure of the attractive interaction between electrons in a Cooper pair, via [265]:

$$V_{ep} = \frac{1}{M} \frac{1}{\left[N\left(E_F\right)\right]^2} \sum_{i,j,k} \sum_{\nu,q} \frac{g_{\nu,q}}{\omega_{\nu,q}^2} \left| \langle \psi_{i,k} | \frac{\partial V}{\partial \mathbf{u}_{\nu,q}} | \psi_{j,k+q} \rangle \right|^2 \delta\left(\varepsilon_{i,k}\right) \delta\left(\varepsilon_{j,k+q} - \varepsilon_{i,k} - \hbar\omega_{\nu,q}\right), \tag{3.11}$$

where M is the atomic mass, $N\left(E_F\right)$ the number of states at the Fermi level, $\omega_{\nu,q}$ the eigen-

frequency of the phonon mode and $g_{\nu,q}$ its degeneracy. Here, an electron in state ψ_i with wave vector $\mathbf{k}$ is scattered into an unoccupied state ψ_j with wave vector $(\mathbf{k}+\mathbf{q})$ through a phonon of frequency ω_ν. The phonon gradient represents the variation of the self-consistent potential V felt by the electrons with respect to the distortion along the vibrational eigenmode $\mathbf{u}_{\upsilon,q}$. Energy conservation is ensured by the $\delta-$functions. Since phonon energies are typically rather small, namely only of the order of several meV, only electrons near the Fermi level effectively scatter, where occupied and unoccupied states are close in energy. For molecules, the above equation valid for solids needs to be adapted to discrete energy levels and becomes in the so-called molecular limit [266, 265]:

$$V_{ep} = \frac{1}{9M} \sum_{\nu} \frac{g_\nu}{\omega_\nu^2} \sum_{i,j=1}^{3} \left| \langle \psi_i | \frac{\partial V}{\partial \mathbf{u}_\nu} | \psi_j \rangle \right|^2, \tag{3.12}$$

where i and j run over states near the Fermi level, i.e. in the case of the electron-doped C_{60} over the three degenerate LUMO levels.

Phonon properties Within the harmonic approximation, phonon frequencies ω_ν and displacement patterns $u_{I\alpha}$ for an atom I along Cartesian components α can be obtained by solving the following secular equation:

$$\sum_{J,\beta} \left([D]_{IJ}^{\alpha\beta} - \delta_{IJ}\delta_{\alpha\beta} M_I \omega^2 \right) u_{I,\beta} = 0,$$

where $[D]$ the so-called dynamical or inter-atomic force constant (IFC) matrix:

$$[D]_{IJ} \equiv \frac{\partial^2 E(\mathbf{R})}{\partial R_I^\alpha \partial R_J^\beta}.$$

Here, $E(\mathbf{R})$ is the Born-Oppenheimer energy surface, i.e. the total energy of the electronic system depending parametrically on the ion core positions $\mathbf{R}$. As detailed in Ref. [259], within the framework of *DFT-KS*, density functional perturbation theory (DFPT) has been conceived to efficiently access the second order derivative of the Born-Oppenheimer energy surface with respect to the atomic positions. Going into details of this formalism is clearly

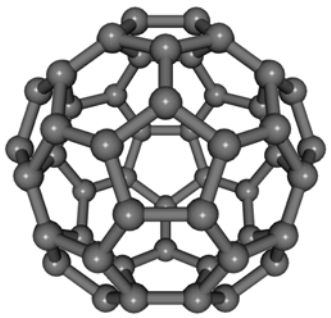

Figure 3.20: Molecular structure of the Buckminster fullerene C_{60}: this fullerene is often compared to a soccer ball, consisting of 12 pentagons and 20 hexagons. Every carbon atom is covalently bound to three neighboring atoms. The valence electrons form three σ-bonds per carbon atom at the molecule's surface, while the fourth electron is part of a delocalized π-system perpendicular to the surface. Due to the curvature of the molecular surface, π-bonds have both a perpendicular and an in-plane component, i.e. C_{60} is partly sp^2- and partly sp^3-hybridized.

beyond the scope of this work and the reader is referred to Refs. [258, 259] for a comprehensive overview. The phonon eigenmodes and eigenfrequencies used in the presented study on the C_{60} molecule are identical to those of Refs. [12, 260] and have been calculated at a *DFT*-B3LYP level with a 6-311G* basis. This was shown to yield excellent phonon eigenfrequencies as compared to Raman experiments [260].

Evaluation of the electron-phonon coupling We now make the connection between EPC matrix elements and *GW* calculations. It can be shown that within the present frozen-phonon approach, the explicit deformation of the molecule diagonalizes the eigenstates with respect to the perturbation, leaving only the intraband transitions [12, 260, 265]. Further, using the Hellman-Feynman theorem [267, 268], the expectation value of $(\partial V/\partial \mathbf{u}_\nu)$ on the $|\psi_i\rangle$ eigenstate can be expressed as the gradient $(\partial \varepsilon_i/\partial \mathbf{u}_\nu)$ of the corresponding energy level, namely:

$$\begin{aligned} V^{ep} &= \frac{1}{9M}\sum_\nu \frac{g_\nu}{\omega_\nu^2}\sum_{i=1}^{3}\left|\langle\psi_i|\,\frac{\partial V}{\partial \mathbf{u}_\nu}\,|\psi_i\rangle\right|^2 \\ &= \frac{1}{9M}\sum_\nu \frac{g_\nu}{\omega_\nu^2}\sum_{i=1}^{3}\left|\frac{\partial \varepsilon_i}{\partial \mathbf{u}_\nu}\right|^2, \end{aligned} \tag{3.13}$$

where ε_i are the LUMO energy eigenvalues as calculated within *DFT-LDA*, *GW* or COHSEX. Clearly, assuming that the $\mathbf{u}_\nu$ vibrational modes are well described within *DFT*, the quality of the V^{ep} is directly related to the that of the ε_i eigenvalues.

For evaluating the matrix element of the electron-phonon coupling, the question arises, which phonon modes can couple to the LUMO states, i.e. for which modes the matrix element $\langle\psi_i|\,\frac{\partial V}{\partial \mathbf{u}_\nu}\,|\psi_i\rangle$ is non-zero. Group theory analysis show that the Kronecker product $t_{1u}\otimes t_{1u}$ of the LUMO states character only projects on the non-degenerate A_g modes and on the five-fold degenerate H_g modes (see Fig. 3.22). This significantly reduces the number of matrix elements to be calculated. In total, ten modes can contribute to the coupling, two of A_g and eight of H_g symmetry. The electron-phonon coupling involving the A_g modes does not lift the degeneracy, i.e. the three LUMO states change their energy by the same amount under distortion. On the contrary, concerning the coupling to the H_g modes, the LUMO levels split

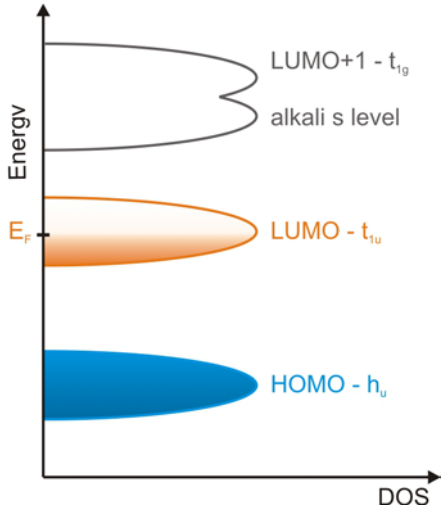

Figure 3.21: Schematic representation of the electronic structure of the alkali-doped C_{60} fulleride: the completely filled HOMO level (blue) is five-fold degenerate and has h_u symmetry. The three-fold degenerate LUMO (orange) has t_{1u} symmetry and is half-filled by the additional electrons of the alkali dopants. Their s-orbitals (black), which are nearly degenerate with the LUMO+1 state (black), are therefore empty. As a guide for the eye, the molecular levels are artificially broadened.

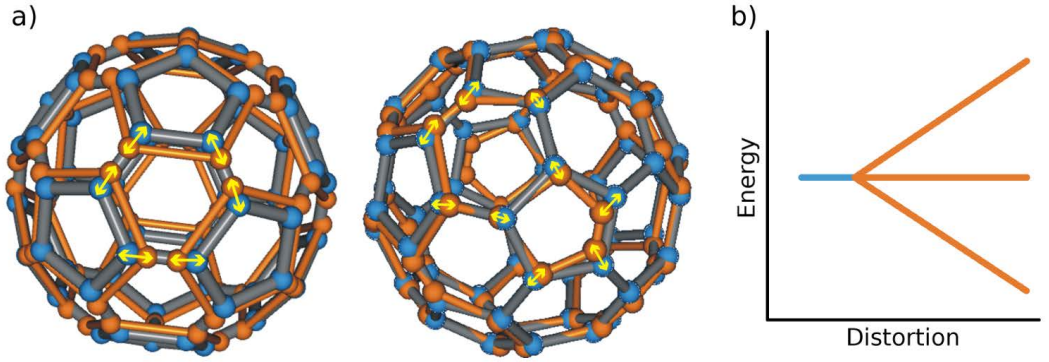

Figure 3.22.: a) Schematic representation of the $A_g(2)$ (left) and $H_g(7)$ (right) phonon modes: the undistorted C_{60} molecule is represented in blue and gray, whereas a frozen distortion along the $A_g(2)$ and $H_g(7)$ phonon modes is given in orange. b) Splitting of the three-fold degenerated LUMO level (blue) under a distortion along a H_g phonon mode (orange). The slopes are directly related to the EPC strengths.

in energy.

The derivatives of the LUMO energy eigenvalues with respect to the phonon eigenmodes in equation (3.13) are evaluated using a frozen-phonon technique. Namely, the molecule is deformed along the phonon mode by typical deformation amplitudes α of $-0.1\,\text{Å} \geq \alpha \leq 0.1\,\text{Å}$ with $\triangle\alpha = 0.05\,\text{Å}$ and the dependence of the LUMO eigenvalue is analyzed. This implies four $evGW$/COHSEX calculations per phonon mode in addition to a calculation on the undistorted C_{60} molecule, i.e. 41 calculations in total, explaining the enormous workload of the frozen phonon scheme. To stay in the linear regime, the deformation amplitude is limited to the above mentioned range and small errors on the regression coefficient within the fitting procedure confirm that linearity (see Fig. 3.27). Another internal accuracy test is based on a condition arising from early group theory considerations [266]:

$$\sum_{i=0}^{2} \frac{\partial \varepsilon_{lumo+i}}{\partial \mathbf{u}_\nu} = 0,$$

i.e. the sum of the slopes has to be zero for the splitting H_g modes. This criterion is well satisfied in our calculations. A schematic representation of the effect of a H_g deformation on the three-fold degenerated LUMO is provided by Fig. (3.22).

Technical details Following Ref. [260], the molecular structure is relaxed at a DFT-B3LYP level with a 6-311G* basis. The many-body GW and COHSEX calculations are performed using the FIESTA package [6, 7, 8]. The starting single-particle eigenstates and eigenvalues are obtained from DFT-LDA calculations using the SIESTA package [136] and a triple-zeta plus polarization (TZP) basis combined with standard norm-conserving pseudopotentials [212]. This triple-zeta plus polarization (TZP) basis consists of 3 shells of s- and p-orbitals, complemented by one polarization d-shell, that is 19 orbitals per carbon atom. This basis is larger than the double-zeta plus polarization (DZP) basis used in Ref. [12], with the inclusion

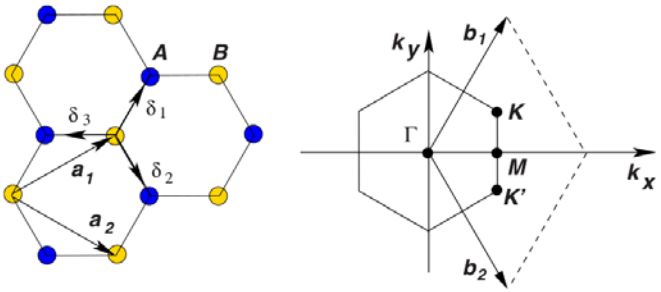

Figure 3.23.: Graphene's honeycomb lattice and its Brillouin zone: Left: lattice structure of graphene, made out of two interpenetrating triangular lattices ($\mathbf{a}_1$ and $\mathbf{a}_2$ are the lattice unit vectors, and δ_i, $i = 1, 2, 3$, are the nearest-neighbor vectors). Right: Corresponding Brillouin zone. The Dirac cones are located at the $\mathbf{K}$ and $\mathbf{K}'$ points. Figure and caption taken from Ref. [277].

in particular of diffuse s- and p-orbitals. The used auxiliary basis consists of four Gaussian functions ($e^{-\alpha r^2}$) per l-channel, up to $l = 3$ orbitals for first row elements. The localization coefficients α possess an even-tempered distribution [138] ranging from $\alpha_{min} = 0.20$ Bohr^{-2} to $\alpha_{max} = 3.2$ Bohr^{-2}. With such a basis, our G_0W_0@LDA ionization potential and HOMO-LUMO gap are found to be 7.33 eV and 4.39 eV, starting from a 1.66 eV DFT-LDA gap. This is in close agreement with the 7.45 eV and 4.40 eV plane wave G_0W_0@LDA values of Ref. [204] (LDA molecular structure). The G_0W_0@LDA gap remains still smaller than the $\sim$ 4.9-5.0 eV experimental value, which can be traced back to the drastically too small DFT-LDA starting point gap. In order to rectify this starting point dependency, we perform partially self-consistent $evGW$@LDA calculations with an update of the eigenvalues, as described in detail at the beginning of this chapter.

3.4.1.2. Electron-phonon coupling in graphene

Graphene, which is a single atomic plane of graphite, has been synthesized only very recently, namely in 2004 by A. Geim and K. Novoselov at the University of Manchester using their "Scotch tape method", a strikingly easy way to produce large-area isolated graphene [269]. This catalyzed the scientific interest in this two-dimensional material and remarkable properties such as a high electrical and thermal conductivity, and a large in-plane strength have been reported [270, 271]. This is only a small excerpt of claimed outstanding properties, which make graphene a promising candidate for potentially disruptive technologies in a variety of fields, ranging from standard electronics with graphene transistors [272] to optoelectronics [273] and energy materials [274]. By way of example, graphene has been recently proposed to efficiently replace expensive platinum counter electrodes in dye-sensitized solar cells, which catalyze the reduction of the electrolyte after electron injection [275]. A complete compendium is clearly beyond the scope of this thesis. The literature about graphene is vast and the reader is referred to e.g. Ref. [276] for a compilation of characterization and fabrication techniques.

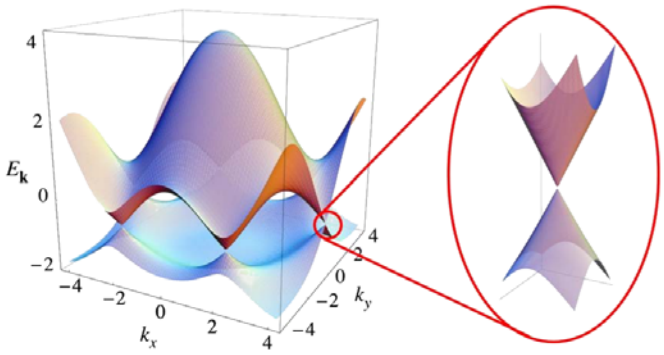

Figure 3.24.: Electronic dispersion of the valence and conduction bands in graphene as calculated within a tight-binding model. The zoom in shows the energy bands close to one of the Dirac points. Figure taken from Ref. [277].

Electronic properties For a subsequent discussion of the electron-phonon coupling, we first want to briefly comment on the electronic properties. Graphene consists of a honeycomb lattice of sp^2-hybridized carbon atoms, i.e. it is characterized by a system of delocalized π-conjugated electrons. As it is depicted in Fig. (3.23), its honeycomb structure can be expressed as a triangular lattice with a basis of two atoms per unit cell. The latter is determined by two lattice vectors $\mathbf{a}_1$ and $\mathbf{a}_2$, with length

$$|\mathbf{a}_1| = |\mathbf{a}_2| = \sqrt{3}a \approx 2.46 \text{ Å},$$

where $a \approx 1.42$ Å is the lattice constant. Its Brillouin zone (BZ) is spanned by two lattice vectors in reciprocal space, $\mathbf{b}_1$ and $\mathbf{b}_2$ [277]. Of particular importance for the physics of graphene are two points of the BZ, namely the so-called Dirac points $\mathbf{K} = \left(\frac{2\pi}{3a}, \frac{2\pi}{3\sqrt{3}a}\right)$ and $\mathbf{K}' = \left(\frac{2\pi}{3a}, -\frac{2\pi}{3\sqrt{3}a}\right)$ [277]. The band structure in the vicinity of these points as obtained in a tight-binding approach is depicted in Fig. (3.24). The Dirac points are the only points in the band structure, where the valence and the conduction band touch each other, i.e. there is no gap between occupied and unoccupied states. Very importantly, in the vicinity of the Dirac points, the energy shows a linear dispersion with respect to $\mathbf{k}$, just as for relativistic particles. Together with the large group velocity, which is the first derivatives of the band energy with respect to $\mathbf{k}$, these properties are amongst others often used to rationalize the excellent conductance of graphene.

Electron-phonon coupling Graphene is a fundamentally important material, since the EPC strength for certain phonon modes can be directly obtained from experiment. This makes graphene a valuable reference for our ab initio EPC calculations. As elaborated in Ref. [278] and depicted in Fig. (3.25), the phonon dispersion of graphene possesses two discontinuities in the frequency derivative for the highest optical-phonon branch (HOB), namely at the zone center ($\mathbf{q} = \mathbf{\Gamma}$) and at the symmetry ($\mathbf{q} = \mathbf{K}$) point. In general, kinks in the phonon dispersion are called Kohn anomalies [279]. They can be observed in metals, where the screening of the atomic vibrations by the conduction electrons can rapidly change for phonons related

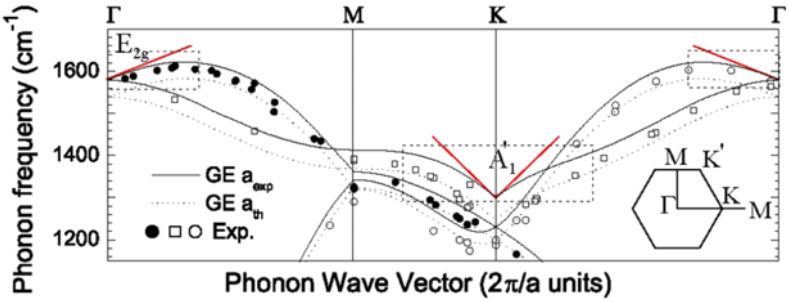

Figure 3.25.: Phonon dispersion of graphene (GE) as calculated (lines) at the experimental and equilibrium lattice spacings (a_{exp} and a_{th}). The points represent experimental data [280]. The red straight lines at $\mathbf{\Gamma}$ and at $\mathbf{K}$ fit the slopes. Figure and caption taken from Ref. [278].

to certain $\mathbf{q}$ points. They are determined by the shape of the electronic Fermi surface and occur when the scattering electronic states $|\psi_{i,k}\rangle$ and $|\psi_{j,k+q}\rangle$ are both at the Fermi level. For graphene, this consequently implies kinks at $(\mathbf{q} = \mathbf{\Gamma})$ and $(\mathbf{q} = \mathbf{K})$. We thus consider processes, where electrons $\psi_{i,K}$ at $(\mathbf{k} = \mathbf{K})$ with Fermi energy are either vertically scattered in unoccupied states $\psi_{i,K+q}$ through phonons with wave vector $\mathbf{q} = \mathbf{\Gamma} = 0$, or horizontally in unoccupied states of the neighboring $\mathbf{k} = \mathbf{K}'$ point through phonons with wave vector $\mathbf{q} = \mathbf{K}$.

In Ref. [278], it has been demonstrated that the slope of the kink is proportional to the square of the EPC matrix element of the respective phonon mode. The phonon modes showing a Kohn anomaly are the so-called E_{2g} and A_1' phonon modes, corresponding to the HOB at $\mathbf{\Gamma}$ and at $\mathbf{K}$, respectively. As a consequence, one can directly deduce the EPC strength of these modes from experimental phonon dispersions [51, 278]. The contribution to the EPC of the other phonon modes at $\mathbf{\Gamma}$ and $\mathbf{K}$ has been shown to be negligible, consistent with their well-behaved continuous dispersion [278].

In the following, it will be discussed how the EPC matrix elements $\mathcal{D}$ are accessed within a frozen-phonon approach. The latter originate from the following expression [51]:

$$\mathcal{D} = \langle \psi_{i,k} | \frac{\partial V}{\partial \mathbf{u}_{\nu,q}} | \psi_{j,k+q} \rangle ,$$

where $\partial V / \partial \mathbf{u}$ is the derivation of the effective potential with respect to the phonon modes. In order to determine the EPC associated with the E_{2g} phonon, the basis atoms are stepwise displaced corresponding to the phonon pattern in Fig. (3.26a). Following Ref. [51], the square of the corresponding EPC matrix element becomes in this frozen-phonon scheme for graphene:

$$\langle \mathcal{D}^2_{\mathbf{\Gamma}} \rangle_F = \lim_{d \to 0} \frac{1}{16} \left(\frac{\Delta E_{\mathbf{\Gamma}}}{d} \right)^2 .$$

Here, each atom is displaced by d and $\langle \ldots \rangle_F$ represents an average over the Fermi surface. $\Delta E_{\mathbf{\Gamma}}$ is the splitting between the doubly degenerate π-states with Fermi energy at $(\mathbf{k} = \mathbf{K})$, namely the opening of the gap induced by the coupling of these π-states with the $\mathbf{\Gamma}$-E_{2g} phonon mode. In a similar way, the square of the EPC matrix element associated with the

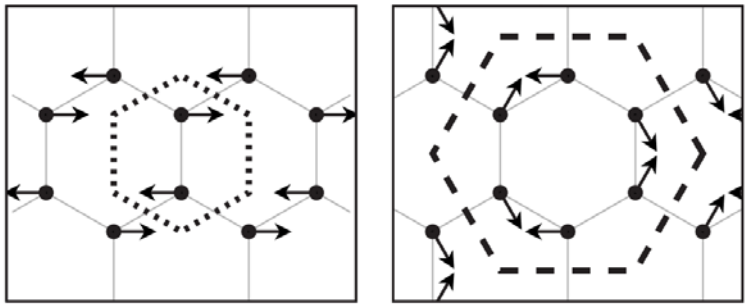

Figure 3.26.: Patterns of the $\mathbf{\Gamma}$-E_{2g} (left) and $\boldsymbol{K}$-$A_1^{'}$ (right) phonons in graphene. Dotted and dashed lines are the Wigner-Seitz cells of the unit cell and of a $\sqrt{3} \times \sqrt{3}$ super cell. Figure and caption taken from Ref. [51].

K-$A_1^{'}$ mode is given by:

$$\left\langle \mathcal{D}^2_{\mathbf{K}} \right\rangle_F = \lim_{d \to 0} \frac{1}{8} \left(\frac{\Delta E_{\mathbf{K}}}{d} \right)^2 ,$$

where the atoms are displaced following the $A_1^{'}$ phonon pattern in Fig. (3.26b). Here, $\Delta E_{\boldsymbol{K}}$ is the splitting between occupied and unoccupied states at ($\mathbf{k} = \mathbf{K}$) induced by the coupling of the doubly degenerate π-states with the **K**-$A_1^{'}$ phonon mode. Again, the accuracy of the EPC matrix elements is related to that of the calculated electronic excitation energies. As in the case of C_{60}, a strong renormalization of the coupling constants has been observed upon replacing the *DFT-LDA* approach by the G_0W_0 formalism [51].

Technical details For the periodic, two-dimensional graphene, we perform G_0W_0 and "single-shot" COHSEX calculations on top of *DFT-LDA* results using the Yambo code, which implements many-body perturbation theory within a plane wave formalism [183]. The starting *DFT-LDA* Kohn-Sham eigenstates are generated by the QuantumEspresso package [239]. The running parameters are identical to those used in a previous *GW* study of the electron-phonon coupling in this material [51]. Namely, we use $|\mathbf{a}| = 2.46$ Å as lattice vector, 20 a.u. distance between the layers, $18 \times 18 \times 1$ **k**-points for the *DFT* and $36 \times 36 \times 1$ **k**-points for the *GW* calculations in the Brillouin zone (BZ) corresponding to the primitive (2-atoms) cell. We adopt the nearest equivalent **k**-grid in the BZ corresponding to the supercell needed to describe zone-boundary ($\mathbf{q} = \mathbf{K}$) phonons in the frozen-phonon approach. The energy cutoff on the plane wave basis was set to 60 Ry. All conduction bands within an energy range of 45 eV above the Fermi level were used to build G and W. The Godby-Needs plasmon pole model was employed for the dynamical dielectric constant entering in W.

3.4.2. Tested approximations

As already emphasized before, the large costs associated with *GW* frozen-phonon calculations for EPC matrix elements call for an exploration of simplified schemes which are less demanding. This is what we will discuss in the following.

COHSEX The already introduced static COHSEX approach represents a drastic approximation to the GW self-energy and was shown to yield too large gaps in the case of semiconductors [3]. By way of example, in the present case of C_{60}, the COHSEX gap is found to be 5.3 eV (B3LYP geometry). This can be compared to the ~ 4.9 eV experimental gap. Even though yielding a too large gap, we note that it is much better than the starting 1.6 eV *DFT-LDA* Kohn-Sham value.

While it cannot be claimed that the static COHSEX approach is a good approximation to absolute quasiparticle energies, we emphasize that we are interested in quasiparticle energy differences upon small (infinitesimal) atomic lattice displacements. The main assumption on which we rely to calculate the electron-phonon coupling within the COHSEX approximation is that the *variations* of the dynamical contribution to the self-energy can be neglected. This can be certainly rationalized by emphasizing that dynamical interactions are driven by the plasmons dynamics, collective excitations much less sensitive to small atomic displacements than single-particle excitation energies and wave functions. In this work, we both test single-shot COHSEX and partially self-consistent COHSEX calculations with an update of the eigenvalues, in the following labeled COHSEX and evCOHSEX, respectively. The obtained data is compared to G_0W_0 and evGW reference values.

Constant screening In addition to the static COHSEX approximation, we want to assess the quality of the so-called constant screening approximation. Namely, the screened Coulomb potential W is calculated once for the undistorted structure, while it is read in for the distorted frozen phonon configurations. Namely, we assume that $(\partial W/\partial \mathbf{u}_\nu)$ is zero. Since the calculation of W denotes one of the most expensive parts, this dramatically reduces computational costs.

Many-body calculations on the C_{60} molecule are carried out using the FIESTA package. The constant screening approximation is tested both within a single-shot COHSEX and an evCOHSEX approach with self-consistency on the eigenvalues. These approaches are labeled COHSEX(W) and evCOHSEX(W), respectively, in the following. We restrict our considerations on the (ev)COHSEX level, since the constant screening approach within *evGW* is computationally not straightforward. This is due to the evaluation of the correlation part of the self-energy using contour deformation techniques with an explicit calculation of the residues. Further, since calculations are performed within a non-orthogonal Gaussian basis, special care must be taken implementing such a constant-screening approximation. As already discussed in preceding chapters, non-local operators such as the bare and screened Coulomb potential are expressed in terms of an atom-centered auxiliary basis $\{\beta\}$ within the RI-SVS technique, following:

$$
\begin{aligned}
[W]_{\beta,\beta'} &= \int\int d\mathbf{r}d\mathbf{r}'\, \beta(\mathbf{r})\, W(\mathbf{r},\mathbf{r}')\, \beta'(\mathbf{r}') \\
W(\mathbf{r},\mathbf{r}') &= \textstyle\sum_{\beta,\beta'} \beta(\mathbf{r})\, \left(S^{-1}[W]S^{-1}\right)_{\beta,\beta'}\, \beta'(\mathbf{r}'),
\end{aligned}
$$

where S is the overlap matrix in the auxiliary basis. Using now the notation: $\underline{W}$ and $\underline{\beta}$ for

the screened Coulomb potential and the auxiliary basis for the slightly distorted system, the assumption: $\underline{W}(\mathbf{r},\mathbf{r}') \simeq W(\mathbf{r},\mathbf{r}')$ leads straightforwardly to the condition:

$$[\underline{W}]_{\underline{\beta},\underline{\beta}'} \simeq S_{\underline{\beta}\beta}[W]_{\beta,\beta'}S_{\beta'\underline{\beta}'},$$

where $S_{\underline{\beta}\beta} =< \underline{\beta}|\beta >$ is an overlap matrix between the auxiliary bases for the perturbed and unperturbed systems, respectively.

Calculations on graphene are performed using the Yambo code [183] within the plasmon pole approximation. We scrutinize the constant-screening approximation within a single-shot COHSEX approach, as in the case of C_{60}, but also at the G_0W_0 level (labeled $G_0W_0\,(W)$ in the following). This is possible due to the use of a fixed plasmon pole frequency, independent of structural deformations. Further, starting from a correct band gap at the *DFT-LDA* level, the effect of self-consistency is not as important as in the case of C_{60} and was shown to have only minor effects.

In order to rationalize the constant screening approach, we briefly discuss similarities to the *BSE* formalism. As discussed in detail in preceding chapters, the latter is based on two main assumptions, which have been shown to be remarkably accurate [122, 123, 281]. The first one is the replacement of the dynamically screened Coulomb potential by its static analogue, which is similar to the static COHSEX approximation. The second one is the neglect of the variation $(\partial W/\partial G)$, assumed to be negligible. In the present constant screening approach, we also neglect variations of W. However, the "perturbation" is not the single-particle Green's function G, but the vibrational distortion of the system in this case.

3.4.3. Results and discussion

The COHSEX approximation Our results are compiled in Table (3.6) for C_{60} and in Table (3.7) for graphene, respectively. For the sake of illustration, the evolution of the lowest unoccupied 3-fold electronic energy level with respect to the phonon displacement along the strongest coupling C_{60} eigenmode $H_g(7)$ is represented in Fig. (3.27).

For C_{60}, the total evGW coupling potential is within 8% of that found by Ref. [12], as a result of the larger basis set we used. For graphene, our *DFT-LDA* and G_0W_0 values are close to those of Ref. [51], namely 197 eV/Å within G_0W_0 for the largest matrix element of the **K**-A_1' phonon in the present study, to be compared to 193 eV/Å in the previous one. The difference can be explained by an increased five point finite-difference formula, instead of only two points, and by shifting the Godby-Needs plasmon model input finite frequency from the (default) 27 eV value in Ref. [51] to 7 eV and thus closer to the π-plasmon resonance in graphene. Such differences are negligible with respect to the more than 100% increase as compared to the *DFT-LDA* value. Further, we emphasize that we are interested in the differences between the *GW* values and the presented COHSEX and constant screening approaches, where all running parameters are the same.

In the case of C_{60}, comparing evGW and evCOHSEX calculations, a global raise of about 7% can be noted, which has to be compared to the 30% increase from *DFT-LDA* to evGW. Besides the $H_g\,(4)$ and $A_g\,(1)$ modes, showing very small couplings, the evCOHSEX approx-

Mode	Theory					Experiment
	LDA	ev*GW*	COHSEX	evCOHSEX	evCOHSEX(W)	
Fullerene						
$H_g(1)$	4.7	5.85	4.99	6.3	6.3	
$H_g(2)$	9.3	10.1	9.99	10.3	11.9	
$H_g(3)$	8.8	12.95	11.96	13.7	15.3	
$H_g(4)$	4.2	5.5	4.9	5.4	5.7	
$H_g(5)$	3.98	4.9	4.5	5.3	5.5	
$H_g(6)$	1.8	1.99	2.05	2.2	2.4	
$H_g(7)$	15.8	25.4	23.3	27.9	26.5	
$H_g(8)$	13.1	18.3	17.1	19.8	19.5	
$A_g(1)$	1.2	1.9	1.85	1.8	1.2	
$A_g(2)$	7.2	13.98	13.2	15.4	12.2	
Total H_g	61.7	84.96	78.8	90.9	93.1	96.2[a], 96.5[b]
Total A_g	8.4	15.9	15.0	17.2	13.4	
Total	70.2	100.9	93.8	108.1	106.6	106.8[a]

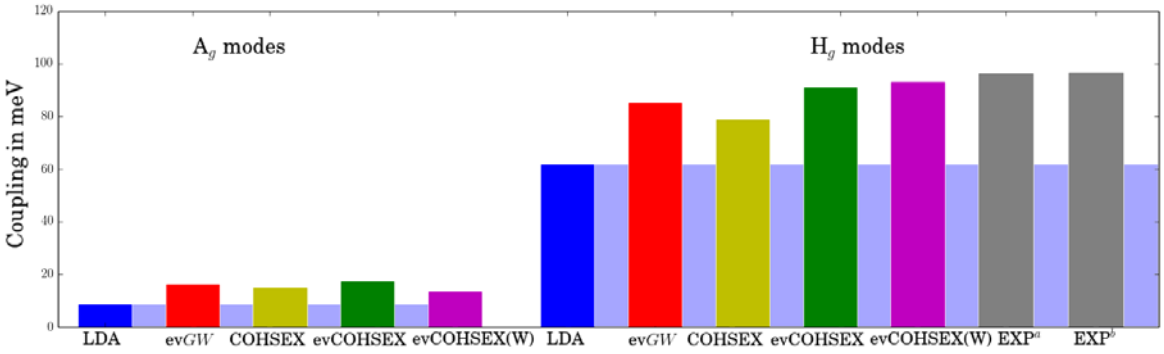

Table 3.6.: Mode-resolved V_ν^{ep} coupling potentials of the C_{60} lowest unoccupied molecular orbital and their V^{ep} totals (in meV). In addition, the totals are visualized in the lower panel, where the blue background represents the *DFT-LDA* value. For symmetry reasons, only the H_g and A_g vibrational modes can couple.
[a] Ref. [263], Table V;
[b] Ref. [262];

imation is observed here to systematically increase the coupling strength as compared to ev*GW*. On the contrary, the single-shot COHSEX approximation, starting from *DFT-LDA* eigenstates, approaches the reference ev*GW* value from below, with an error not larger than that induced by the evCOHSEX technique. This stems from a cancellation of errors between the COHSEX approximation and the lack of self-consistency, leading to an overscreening when building the screened Coulomb potential W directly from the *DFT-LDA* spectrum.

The case of graphene is of specific interest since, in great contrast to the semiconducting C_{60}, the gap reduces to zero in the equilibrium geometry and opens upon phonon distortions. For the optical phonon mode at the zone-center **Γ**-E_{2g}, the COHSEX approximation leads to an increase of 18% as compared to the G_0W_0 reference value. Such an error becomes much larger for the **K**-$A_1^{'}$ mode with a 29% increase of the EPC matrix element. We note that the error induced by the COHSEX approach remains smaller with respect to the 31% and 54% reduction observed upon using *DFT-LDA* instead of G_0W_0, but not negligible. As such, the validity of the COHSEX approximation in graphene is less encouraging than in the case

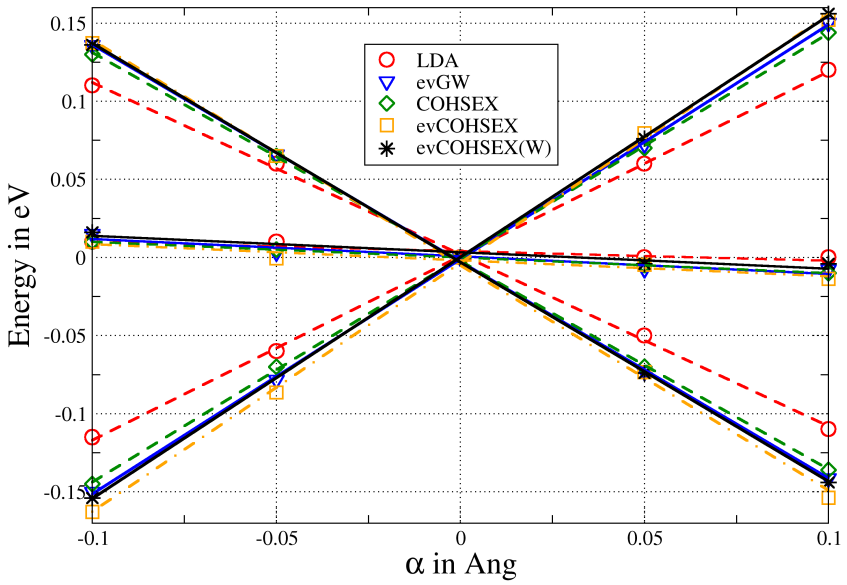

Figure 3.27.: Evolution of the 3-fold degenerate lowest-unoccupied molecular orbital in C_{60} with respect to a deformation α of $-0.1\,\text{Å} \geq \alpha \leq 0.1\,\text{Å}$ along the $HG07$ eigenmode, the strongest coupling mode. *DFT-LDA* (red circles) yields slopes and hence an electron-phonon potential which are much smaller than the corresponding evGW (blue downward triangles) calculations. COHSEX (green diamonds) and evCOHSEX (orange squares) are in very close agreement with evGW results. The evCOHSEX(W) approach (black stars) excellently reproduces the evCOHSEX results.

of C_{60}. This situation can be tentatively ascribed to the very peculiar nature of the Fermi surface and the presence of low-energy plasmons [282], which decreases the validity of the static approximation.

The constant screening approach The results of the constant screening approximation are compiled in Table (3.6) for C_{60} and in Table (3.7) for graphene. For C_{60}, where we test the constant screening approximation at the COHSEX level, an excellent agreement is obtained within evCOHSEX(W) compared to the corresponding evCOHSEX calculations. In total, evCOHSEX(W) agrees within 1.5% compared to evCOHSEX.

In the case of graphene, we remind that difficulties have been encountered at the COHSEX level. Concerning the constant screening approach, the coupling with the zone-center optical mode $\mathbf{\Gamma}$-E_{2g} provides the best results, with a 5% error when comparing $G_0W_0(W)$ to G_0W_0 and COHSEX(W) to COHSEX. For the coupling with the zone-corner $\mathbf{K}$-$A_1^{'}$ mode, discrepancies are not larger than 6% and 7%, applying the constant screening approximation to G_0W_0 and COHSEX, respectively. This is much smaller than the error induced by the standard *DFT-LDA* approach.

Clearly, among the two approximations tested above, the constant screening approach stands as a much better approximation than the static COHSEX one in the present case of electron-phonon coupling, in particular in the somehow pathological case of graphene.

Mode	*LDA*	G_0W_0	G_0W_0 (*W*)	COHSEX	COHSEX(*W*)
	Graphene				
Γ-E_{2g}	45	65.5 (62.8[a])	69	77	81
K-$A_1^{'}$	90	197 (193[a])	209	255	237

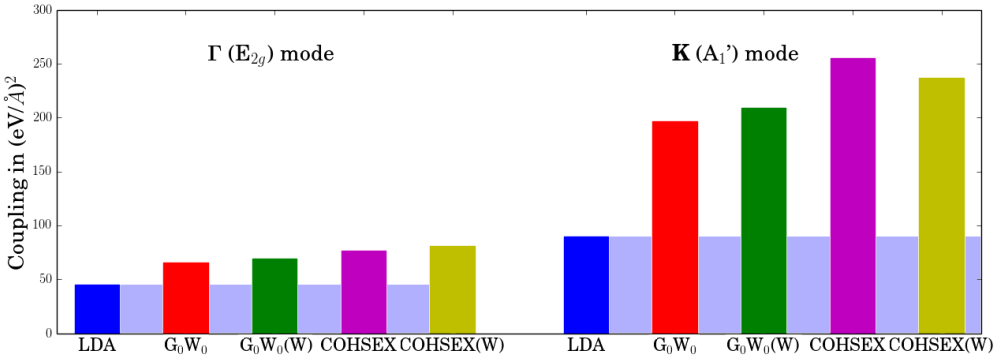

Table 3.7.: Calculated EPC for graphene, which corresponds to the splitting of the degenerate HOMO and LUMO π-levels at the Dirac point. Values given in $(eV/\text{Å})^2$. The lower panel provides a visualization of the EPC as calculated within the different approaches, where the blue background represents the *DFT-LDA* value.
[a] Ref. [51];

Coming back to the analogue approximations implemented in standard *GW/BSE* calculations, namely a static screened Coulomb potential W and $(\partial W/\partial G = 0)$, it is commonly assumed that the *GW/BSE* approach is much more resistant to approximations on the screened Coulomb potential W as compared to the *GW* approach for (charged) excitations. This is due to cancellations of errors between the electron-electron and electron-hole interactions. Namely, any error introduced in W is expected to affect excitonic interactions and quasiparticle gaps in opposite ways. Clearly, the present *GW* study of the variations of a given quasiparticle energy with respect to ionic positions cannot benefit from such cancellation of errors. Nevertheless, the constant screening approximation turns out to be a reliable approach, which allows to tremendously save on computational costs.

An important consequence of the present findings is that once the screened Coulomb potential $W(\mathbf{r}, \mathbf{r}'; \omega)$ is built for the equilibrium geometry, the calculation of the variations of the quasiparticle energies with respect to the perturbation (λ) only requires the evaluation of the variations of the Green's function G with respect to the perturbation. This can be straightforwardly performed within standard DFPT techniques, at least in the case of non-self-consistent G_0W_0 calculations, where the Green's function is directly constructed from input DFT eigenstates. This may invite, for molecular systems such as C_{60}, to rely on G_0W_0 calculations starting from DFT eigenstates obtained with hybrid functionals, which have been shown to be a better starting point for organic systems [48, 198], instead of carrying out self-consistent *GW* calculations.

3.4.4. Conclusion

Electron-phonon coupling plays a prominent role in organic semiconductors. As shown here above for several important systems, its accurate description from first principles necessitates to go beyond $DFT/DFPT$ with standard (semi)local functionals. GW clearly demonstrated to be a promising alternative, however, up to now, this approach is limited to small systems and zone-center phonons due to tremendous computational costs within the frozen-phonon technique. This points out the need for methods which are accurate and computationally reasonable at the same time. Inspired from the GW/BSE formalism, we tested two approaches, namely the static COHSEX approximation and the constant screening approach. Since the calculation of the W denotes the most expensive part of a GW calculation, this greatly reduces the computational effort.

Concerning the accuracy of the tested approaches, our findings suggest that the COHSEX approximation may not be reliable, in particular in the case of graphene. However, the constant screening hypothesis, namely assuming that W remains to first order constant with respect to small ionic displacements, seems to be valid. In the case of C_{60}, it introduces a small error of about 2%. Preliminary results on the extended semiconductor diamond confirm this excellent agreement. Concerning the paradigmatic case of graphene, where the phonon perturbation dramatically affects the Dirac cone and the semi-metallic character, a maximum discrepancy of 7% is found. The present results offer promising perspectives to carry on such many-body evaluations of the electron-phonon coupling gradients with much reduced computer costs on realistic systems. However, further studies are required both on a larger set of systems and physical observables in order to better assess the validity of the presented approach.

4 | Conclusion & Perspectives

Organic photovoltaics offers unique perspectives for a sustainable electricity generation from sun light. The assortment of appropriate organic semiconductors is vast and can be thereto largely increased by molecular engineering. However, the design of efficient organic solar cells is a highly non-trivial optimization problem, where material combinations with well matching electronic levels and optical gaps have to be found.

The present project aimed to assess the ability of the many-body perturbation theory GW/BSE formalism to describe electronic and optical properties of organic systems, in order to contribute to the understanding of fundamental microscopic processes and to actively steer experimental materials research. In this context, we studied the electronic and optical properties for molecules in the gas phase in order to assess the quality of the GW/BSE formalism for finite systems. On the electronic structure level, we chose a model dipeptide, a paradigmatic molecule which raised our interest due to significant discrepancies in the optical spectra within reference TDDFT and quantum chemistry methods [10, 47]. Already its electronic structure is an interesting study case, where large discrepancies between the starting DFT-LDA and the GW electronic structure are observed. The many-body GW correction not only opens the gap and shifts the occupied levels to lower energies, but important level crossings and changes in the level spacings can be noted. This is similar to the previously studied case of the DNA/RNA nucleobases [7] and demonstrates that a simple GW Scissor approach with an explicit correction of the HOMO and the LUMO only is not enough. Instead, the GW correction should be calculated self-consistently with an update of the eigenvalues (evGW approach) for several states around the gap. Since this approach quickly becomes expensive for large systems, we tested the quality of the inexpensive static COHSEX approximation. We showed that self-consistent COHSEX calculations, even though overestimating fundamental gaps, yield results in much better agreement with the final evGW electronic structure than DFT-LDA and thus offer an ideal starting point for inexpensive non-self-consistent G_0W_0 or GW Scissor operator calculations.

Concerning optical absorption properties, the model dipeptide is characterized by low-lying intramolecular charge-transfer excitations. As expected, TDDFT with (semi)local exchange-correlation functionals fails to reproduce the latter, drastically underestimating the electron-hole Coulomb interaction. TDDFT with range-separated hybrid functionals cures the problem and brings the CT excitations energies in good agreement with the higher-level correlated quantum chemistry reference. However, parameters are introduced which have to be adjusted for the respective problem. On the contrary, our combined GW/BSE approach comes in

close agreement with the quantum chemistry data, while being parameter-free and system-independent. As a second case study showing intramolecular charge-transfer excitations, we focused on the optical spectra of a family of coumarin dyes [11]. These molecules recently attracted much attention, namely as all-organic, transition metal free absorbers in Grätzel cells with very promising power-conversion efficiencies. Moreover, they are an impressive example of molecular design, where the gap and structural properties have been systematically optimized [28, 29]. Again, TDDFT with (semi)local exchange-correlation functionals has problems in reproducing the charge-transfer excitation energies from the quantum chemistry reference and range-separated hybrid functionals are needed. The tested GW/BSE approach, however, intrinsically adjusts the electron-hole Coulomb interaction and consequently gives charge-transfer excitation energies in good agreement with quantum chemistry calculations. As a further important issue, we could also assess the quality of GW/BSE oscillator strengths, in the interesting case of molecular systems, where not only the onset of absorption, but also the oscillator strength has been chemically engineered in order to optimize the matching with the solar spectrum.

After having carefully tested the accuracy of the presented GW/BSE approach for the electronic and optical properties of the model dipeptide and the coumarin dyes, we also studied its quality concerning the electron-phonon coupling (EPC). The latter takes a prominent place in organic semiconductors and an accurate calculation from first principles is indispensable for a realistic modeling. Even though DFT, and especially density functional perturbation theory ($DFPT$), provides a most efficient way to access the electron-phonon coupling, recent studies showed a clear underestimation of the EPC of up to 50% as compared to experiment when using standard (semi-)local exchange-correlation functionals. The problem is cured on the many-body GW level, where EPC strengths come in close agreement with experiment [12, 51, 52]. However, within GW, efficient techniques as in the case of $DFPT$ are not available and an expensive frozen-phonon approach with step-wise atomic displacements along the phonon modes has to be carried out. In this work, we tested two alternative many-body approaches for the calculation of the EPC, namely the static COHSEX and the constant screening approximation, which are supposed to yield much less demanding frozen-phonon calculations. We studied their validity range by means of the fullerene C_{60} and the popular two-dimensional semi-metal graphene. Concerning the static COHSEX approach, we demonstrated that it results in significant discrepancies as compared to the GW reference, especially in the case of graphene. The constant screening approach, where we neglect the variations of the screened Coulomb potential with respect to small deformations around the equilibrium structure, gives, however, results in excellent agreement with the corresponding GW reference. Even though this approach has still to be validated for a larger variety of systems, the obtained results are promising and open the door to an inexpensive and reliable many-body treatment of the electron-phonon coupling.

Embedding techniques The presented studies aimed at the validation of GW/BSE calculations for isolated molecular systems. Not only the accurate determination of electronic and optical excitation energies (ionization energy, electronic affinity, optical gap), but also the cal-

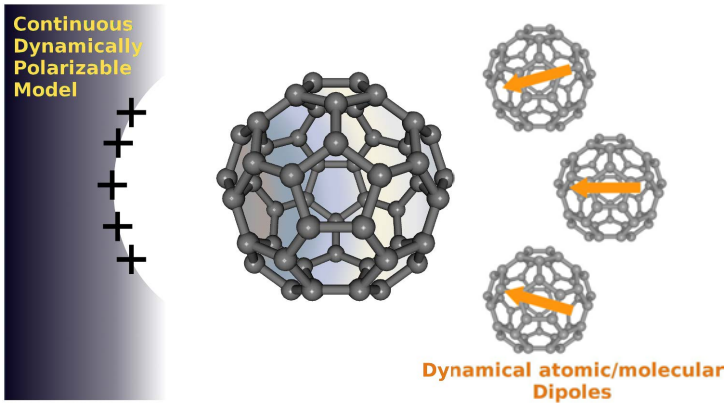

Figure 4.1.: Symbolic representation of embedding strategies: the full quantum mechanical GW/BSE study (center) is complemented by the effect of a continuous (left) and/or discrete (right) dynamically polarizable model with atomic or molecular dipoles.

culation of electron-phonon coupling strengths have been discussed. Nevertheless, there is still much to be done in order to simulate organic systems of the type used in organic photovoltaic cells, where the molecules are immersed in an environment of polarizable molecules.

The surrounding environment strongly renormalizes the electronic and optical properties of organic systems. By way of example, the fundamental gap of the Buckminster fullerene C_{60} is around 5 eV in the gas phase,[1] whereas it reduces to around 2.3-2.5 eV in the solid state packing form [283]. In organic semiconductors, due to the rather weak band dispersion, this renormalization originates only to a minor degree from the direct quantum mechanical interaction mediated by wave function overlaps. Instead, it mainly occurs through the classical interaction between dipoles on the neighboring polarizable molecules, induced when a charge or electron-hole pair is created. In further studies, we want to explore several strategies to account for such an interaction, relying on the fact that at moderate or long distance, the full quantum mechanical description reduces to a classical dipole interaction. Typically, we plan to study one molecule and its first shell of neighbors on a full quantum mechanical GW/BSE level, while all interactions beyond that layer will be described by fictitious atomic/molecular dipoles reproducing that of the real molecule (see Fig. 4.1). The implemented real-space Gaussian basis approach of the FIESTA package straightforwardly opens the way to such embedding techniques. As a mean to become familiar with the trade of code development, significant effort in this direction has been undertaken during my doctoral thesis, even though work remains still to be achieved. Alternatively to discrete embedding approaches, following standard techniques for ground state DFT calculations, the classical part of the system can be modeled by a continuous polarizable model. Here, the important difference compared to existing techniques is that for the planned excited states studies, the *dynamical* polarizability – and not the static one only – probably needs to be used. Promising results have been obtained along this line. This is a major step towards the study of realistic molecular and hybrid systems within the present GW/BSE formalism.

[1] Experimental data taken from the NIST chemistry webbook at: http://webbook.nist.gov/chemistry/.

A | Appendix: Details and derivations

A.1. Mathematical background and notation

Notation For the sake of clarity, a shorthand notation is introduced. Space and time coordinates are combined to natural numbers, e.g.

$$1^{(+)} \equiv \{\mathbf{r}_1, t_1 (+\eta)\},$$

where η is an infinitesimal positive time. The δ-function is represented by

$$\delta(1,2) = \delta(\mathbf{r}_1 - \mathbf{r}_2)\,\delta(t_1 - t_2)$$

and integrals are carried out like

$$\int d1 = \int d^3\mathbf{r}_1 \int_{-\infty}^{+\infty} dt_1.$$

Further,

$$v(1,2) = v(\mathbf{r}_1 - \mathbf{r}_2)\,\delta(t_1 - t_2) = \frac{1}{|\mathbf{r}_1 - \mathbf{r}_2|}\delta(t_1 - t_2)$$

is the bare Coulomb potential and the operator h_0 represents the single-particle Hamiltonian,

$$h_0 = -\frac{1}{2}\nabla^2 + V_{ext}(\mathbf{r}).$$

Functional derivatives For the following derivations, some mathematical background is needed, namely the theory of functional derivative. Usually, one deals with functions, which map one number x onto another number y:

$$f(x):\ x \to y.$$

In many-body theory, functionals one often encounters functionals, i.e. functions whose arguments themselves are functions:

$$F[f(x)]:\ f(x) \to y.$$

To differentiate between a function and a functional, square brackets are used. One prominent example for a functional is the ground state energy of a many-body system depending on the

ground state density which is in turn a function of $\mathbf{r}$: $E_0[n_0(\mathbf{r})]$. Derivatives can be carried out following:

$$\frac{dF[f(x)]}{df(x)} = \int dx \, \frac{\partial F[f(x)]}{\partial f(x)}.$$

A short overview of very useful relations follows [2]:

1. $\frac{\partial F(1)}{\partial F(2)} = \delta(1-2)$
2. The product rule denotes:

$$\frac{\partial}{\partial \Psi(2)} \left(F[\Psi(1)] G[\Psi(1)] \right) = \frac{\partial F[\Psi(1)]}{\partial \Psi(2)} G[\Psi(1)] + \frac{\partial G[\Psi(1)]}{\partial \Psi(2)} F[\Psi(1)]. \tag{A.1}$$

3. $\frac{\partial}{\partial \Psi(2)} \left(\frac{F[\Psi(1)]}{G[\Psi(1)]} \right) = \frac{1}{G[\Psi(1)]^2} \left(\frac{\partial F[\Psi(1)]}{\partial \Psi(2)} G[\Psi(1)] - \frac{\partial G[\Psi(1)]}{\partial \Psi(2)} F[\Psi(1)] \right)$
4. For $F[G[\Psi(1);2]]$ a chain rule exists:

$$\frac{\partial F}{\partial \Psi(1)} = \int d2 \, \frac{\partial F}{\partial G(2)} \frac{\partial G(2)}{\partial \Psi(1)}. \tag{A.2}$$

5. For $F[\Psi(1);2,3]$ being the inverse of $G[\Psi(1);2,3]$ it holds:

$$\int d4 \, F[\Psi(1);2,4] G[\Psi(1);4,3] = \delta(2-3).$$

6. Definition (5) can be used to derive a very useful relation:

$$\frac{\partial F[\Psi(1);2,3]}{\partial \Psi(6)} = -\int d4d5 \, F[\Psi(1);2,4] \frac{\partial G[\Psi(1);4,5]}{\partial \Psi(6)} F[\Psi(1);5,3]. \tag{A.3}$$

The derivation starts with $F(12) = \iint d3d4 F(13) G(34) F(42)$ which is a reformulation of definition (5). We proceed as follows:

$$\begin{aligned}
&\frac{\partial F(12)}{\partial \Psi(3)} = \\
= \quad & \frac{\partial \left(\iint d4d5 \, F(14) G(45) F(52) \right)}{\partial \Psi(3)} \\
= \quad & \iint d4d5 \frac{\partial F(14)}{\partial \Psi(3)} G(45) F(52) + \iint d4d5 F(14) \frac{\partial G(45)}{\partial \Psi(3)} F(52) + \iint d4d5 F(14) G(45) \frac{\partial F(52)}{\partial \Psi(3)} \\
= \quad & \int d4 \frac{\partial F(14)}{\partial \Psi(3)} \delta(4-2) + \iint d4d5 \, F(14) \frac{\partial G(45)}{\partial \Psi(3)} F(52) + \int d5 \, \delta(1-5) \frac{\partial F(52)}{\partial \Psi(3)} \\
= \quad & \frac{\partial F(12)}{\partial \Psi(3)} + \iint d4d5 \, F(14) \frac{\partial G(45)}{\partial \Psi(3)} F(52) + \frac{\partial F(12)}{\partial \Psi(3)} \\
\rightarrow \quad & \frac{\partial F(12)}{\partial \Psi(3)} = -\iint d4d5 \, F(14) \frac{\partial G(45)}{\partial \Psi(3)} F(52).
\end{aligned}$$

Field operators Field operators create ($\hat{\Phi}^\dagger(\mathbf{r},t)$) or annihilate ($\hat{\Phi}(\mathbf{r}',t')$) a particle at $(\mathbf{r},t)$ and $(\mathbf{r}',t')$, respectively [90]. Their commutation relations are given by:

$$\left[\hat{\Phi}(\mathbf{r}',t'),\hat{\Phi}^\dagger(\mathbf{r},t)\right]_+ = \delta(\mathbf{r}-\mathbf{r}')\delta\left(t-t'\right)$$

$$\left[\hat{\Phi}^{(\dagger)}(\mathbf{r},t),\hat{\Phi}^{(\dagger)}(\mathbf{r}',t')\right]_+ = 0.$$

These relations hold for fermions, for bosons the field operators commutate.

The Hamiltonian for a system of N interacting electrons,

$$\hat{H} = \sum_{i=1}^{N}\left[-\frac{1}{2}\nabla_i^2 + V_{ext}\left(\mathbf{r}_i\right)\right] + \frac{1}{2}\sum_{i\neq j} v\left(\mathbf{r}_i-\mathbf{r}_j\right),$$

can be expressed in field operator notation following the transformation rules for operators. Sums over 1-particle operators $\hat{O}\left(\mathbf{r}\right)$ are transformed by:

$$\sum_{i=1}^{N}\hat{O}\left(\mathbf{r}_i\right) = \int d^3\mathbf{r}\,\hat{\Phi}^\dagger(\mathbf{r},t)\hat{O}\left(\mathbf{r}\right)\hat{\Phi}(\mathbf{r},t).$$

Analogue, for 2-particle operators like he Coulomb potential, it holds:

$$\sum_{ij}^{N}\hat{O}\left(\mathbf{r}_i,\mathbf{r}_j\right) = \int d^3\mathbf{r}d^3\mathbf{r}'\,\hat{\Phi}^\dagger(\mathbf{r}',t)\hat{\Phi}^\dagger(\mathbf{r},t)\hat{O}\left(\mathbf{r},\mathbf{r}'\right)\hat{\Phi}(\mathbf{r},t)\hat{\Phi}(\mathbf{r}',t).$$

For the Hamiltonian we thus obtain:

$$\hat{H} = \int d^3\mathbf{r}\,\hat{\Phi}^\dagger(\mathbf{r})\,h_0\left(\mathbf{r}\right)\,\hat{\Phi}(\mathbf{r}) + \frac{1}{2}\iint d^3\mathbf{r}d^3\mathbf{r}'\,\hat{\Phi}^\dagger(\mathbf{r},t)\hat{\Phi}^\dagger(\mathbf{r}',t)\,v\left(\mathbf{r}-\mathbf{r}'\right)\,\hat{\Phi}(\mathbf{r}',t)\hat{\Phi}(\mathbf{r},t),$$

with $h_0\left(\mathbf{r}\right) = -\frac{1}{2}\nabla^2 + V_{ext}\left(\mathbf{r}\right)$.

We work in the Heisenberg representation, assuming that the Hamiltonian has no explicit time-dependence. The time-dependent field operators fulfill Heisenberg's equation of motion, i.e

$$i\hbar\frac{\partial\hat{\Phi}(\mathbf{r},t)}{\partial t} = \left[\hat{\Phi}(\mathbf{r},t),\hat{H}\right]_-$$

and

$$-i\hbar\frac{\partial\hat{\Phi}^\dagger(\mathbf{r},t)}{\partial t} = \left[\hat{H},\hat{\Phi}^\dagger(\mathbf{r},t)\right]_-,$$

respectively, which describes the time evolution of a Heisenberg operator in the same way that the time-dependent Schrödinger equation describes the time evolution of a wave function. Inserting $\hat{H}$ and using the commutation relations for field operators leads to an explicit expression for the equation of motion of an annihilation field operator:

$$i\hbar\frac{\partial\hat{\Phi}(\mathbf{r},t)}{\partial t} = h_0\left(\mathbf{r}\right)\hat{\Phi}(\mathbf{r},t) + \int d^3\mathbf{r}'\,v\left(\mathbf{r}-\mathbf{r}'\right)\hat{\Phi}^\dagger(\mathbf{r}',t)\hat{\Phi}(\mathbf{r}',t)\hat{\Phi}(\mathbf{r},t). \tag{A.4}$$

The two-body Green's function $\mathbf{G_2}$ An important conceptual quantity which will be needed in the following is the so-called two-particle Green´s function G_2 [2, 90]. Analogue to the definition of the one-electron Green's function G_1^e,

$$(i\hbar)^2\, G_2^e\,(1234) = \left\langle \Psi_0^N \right| \hat{\Phi}(\mathbf{r}_1,t_1)\hat{\Phi}(\mathbf{r}_2,t_2)\,\hat{\Phi}^\dagger(\mathbf{r}_4,t_4)\hat{\Phi}^\dagger(\mathbf{r}_3,t_3) \left| \Psi_0^N \right\rangle \theta\left(t-t'\right),$$

describes the probability of finding an electron at $(\mathbf{r}_1,t_1)$ and a second at $(\mathbf{r}_2,t_2)$ after the injection of two electrons at $(\mathbf{r}_3,t_3)$ and $(\mathbf{r}_4,t_4)$, respectively. Similar, a Green's function for the propagation o two holes, G_2^h, can be defined, which in turn is combined with G_2^e to the time-ordered two-particle Green's function G_2:

$$G_2\,(1234) = \frac{1}{(i\hbar)^2}\,\left\langle \Psi_0^N \right| T\left[\hat{\Phi}(\mathbf{r}_1,t_1)\hat{\Phi}(\mathbf{r}_2,t_2)\,\hat{\Phi}^\dagger(\mathbf{r}_4,t_4)\hat{\Phi}^\dagger(\mathbf{r}_3,t_3)\right] \left| \Psi_0^N \right\rangle. \tag{A.5}$$

As a reminder, we are working in second quantization, so that $\left\langle \Psi_0^N \right| \ldots \left| \Psi_0^N \right\rangle$ does not denote an integral $\int d^3\boldsymbol{r}$, but an averaging over Fock states.

G_2 is an important quantity giving direct access to many non-equilibrium properties like the electric conductivity or the magnetic susceptibility. It can be written in terms of the one-particle Green's function G_1 and a non-local external potential U_{ext} which is introduced in addition to the external core ion potential V_{ext} included in h_0. It is an artificially introduced external potential which will be set to zero in the end:

$$G_2\left(1,\mathbf{r}'t;2,\mathbf{r}t^+\right) = G_1\,(1,2)\,G_1\left(\mathbf{r}'t,\mathbf{r}t^+\right) - \frac{\partial G_1\,(1,2)}{\partial U_{ext}\,(\mathbf{r},\mathbf{r}',t)}. \tag{A.6}$$

For local potentials we find:

$$G_2\left(1,3,2,3^+\right) = G_1\,(1,2)\,G_1\left(3,3^+\right) - \frac{\partial G_1\,(1,2)}{\partial U_{ext}\,(3)}, \tag{A.7}$$

The one-particle Green's function thus generates higher-order Green's function under the influence of an external potential. The derivation of the above formulas starts by transforming G_1 from the Heisenberg representation into the interaction picture:

$$i\hbar G_1\,(1,2) = \frac{\left\langle \Psi_0^N \right| T\left[S_{ev}\,(\infty,-\infty)\;\hat{\Phi}(1)\,\hat{\Phi}^\dagger(2)\right] \left| \Psi_0^N \right\rangle}{\left\langle \Psi_0^N \right| T\left[S_{ev}\,(\infty,-\infty)\right] \left| \Psi_0^N \right\rangle},$$

where the time evolution operator S_{ev} is given by:

$$T\left[S_{ev}\,(\infty,-\infty)\right] = Te^{-i\int_{-\infty}^{\infty} dt \int d\mathbf{r}d\mathbf{r}'\;\hat{\Phi}^\dagger(\mathbf{r},t^+)U_{ext}(\mathbf{r},\mathbf{r}',t)\hat{\Phi}(\mathbf{r}',t)}.$$

The time-dependence of the field operators is still governed by the equilibrium Hamiltonian, while the time-dependence due to the additional potential is completely contained in S_{ev}. Differentiating G_1 in the interaction representation with respect to a local external field U_{ext}

and applying the product and chain rule, leads to:

$$
\begin{aligned}
i\hbar\tfrac{\partial G_1(1,2)}{\partial U_{ext}(3)} &= \\
&= \frac{\langle\Psi_0^N|T\left[\frac{\partial S_{ev}}{\partial U_{ext}(3)}\,\hat{\Phi}(1)\,\hat{\Phi}^\dagger(2)\right]|\Psi_0^N\rangle}{\langle\Psi_0^N|T[S_{ev}]|\Psi_0^N\rangle} - \frac{\langle\Psi_0^N|T\left[S_{ev}\,\hat{\Phi}(1)\,\hat{\Phi}^\dagger(2)\right]|\Psi_0^N\rangle}{\langle\Psi_0^N|T[S_{ev}]|\Psi_0^N\rangle^2}\left\langle\Psi_0^N\right|\frac{T[\partial S_{ev}]}{\partial U_{ext}(3)}\left|\Psi_0^N\right\rangle \\
&= \frac{\langle\Psi_0^N|T\left[\frac{\partial S_{ev}}{\partial U_{ext}(3)}\,\hat{\Phi}(1)\,\hat{\Phi}^\dagger(2)\right]|\Psi_0^N\rangle}{\langle\Psi_0^N|T[S_{ev}]|\Psi_0^N\rangle} - \frac{\langle\Psi_0^N|T\left[S_{ev}\,\hat{\Phi}(1)\,\hat{\Phi}^\dagger(2)\right]|\Psi_0^N\rangle}{\langle\Psi_0^N|T[S_{ev}]|\Psi_0^N\rangle}\frac{\langle\Psi_0^N|\frac{T[\partial S_{ev}]}{\partial U_{ext}(3)}|\Psi_0^N\rangle}{\langle\Psi_0^N|T[S_{ev}]|\Psi_0^N\rangle} \\
&= \frac{\langle\Psi_0^N|T\left[\frac{\partial S_{ev}}{\partial U_{ext}(3)}\,\hat{\Phi}(1)\,\hat{\Phi}^\dagger(2)\right]|\Psi_0^N\rangle}{\langle\Psi_0^N|T[S_{ev}]|\Psi_0^N\rangle} - i\hbar G_1\left(1,2\right)\frac{\langle\Psi_0^N|\frac{T[\partial S_{ev}]}{\partial U_{ext}(3)}|\Psi_0^N\rangle}{\langle\Psi_0^N|T[S_{ev}]|\Psi_0^N\rangle}.
\end{aligned}
$$

The derivation of time-evolution operator with respect to the external field obeys:

$$
\frac{T\left[\partial S_{ev}\right]}{\partial U_{ext}\left(3\right)} = \frac{1}{i\hbar}T\left[S_{ev}\,\hat{\Phi}^\dagger(3)\hat{\Phi}(3)\right].
$$

Consequently, we obtain:

$$
\begin{aligned}
i\hbar\tfrac{\partial G_1(1,2)}{\partial U_{ext}(3)} &= \\
&= \tfrac{1}{i\hbar}\frac{\langle\Psi_0^N|T\left[S_{ev}\hat{\Phi}^\dagger(3)\hat{\Phi}(3)\hat{\Phi}(1)\hat{\Phi}^\dagger(2)\right]|\Psi_0^N\rangle}{\langle\Psi_0^N|T[S_{ev}]|\Psi_0^N\rangle} - i\hbar G_1\left(1,2\right)\tfrac{1}{i\hbar}\frac{\langle\Psi_0^N|T\left[S_{ev}\,\hat{\Phi}^\dagger(3)\hat{\Phi}(3)\right]|\Psi_0^N\rangle}{\langle\Psi_0^N|T[S_{ev}]|\Psi_0^N\rangle} \\
&= -\tfrac{1}{i\hbar}\frac{\langle\Psi_0^N|T\left[S_{ev}\hat{\Phi}(1)\hat{\Phi}(3)\hat{\Phi}^\dagger(3)\hat{\Phi}^\dagger(2)\right]|\Psi_0^N\rangle}{\langle\Psi_0^N|T[S_{ev}]|\Psi_0^N\rangle} + i\hbar G_1\left(1,2\right)\tfrac{1}{i\hbar}\frac{\langle\Psi_0^N|T\left[S_{ev}\,\hat{\Phi}(3)\hat{\Phi}^\dagger(3)\right]|\Psi_0^N\rangle}{\langle\Psi_0^N|T[S_{ev}]|\Psi_0^N\rangle} \\
&= -i\hbar G_2\left(1,3,2,3^+\right) + i\hbar G_1\left(1,2\right)G_1\left(3,3^+\right) \\
\\
\rightarrow \quad & \tfrac{\partial G_1(1,2)}{\partial U_{ext}(3)} = -G_2\left(1,3,2,3^+\right) + G_1\left(1,2\right)G_1\left(3,3^+\right),
\end{aligned}
$$

where we introduced $3^+ = (\mathbf{r}_3, t_3 + \eta)$ with $\eta \to 0$ to ensure the right time order.

A.2. Lehmann representation of the one-particle Green's function

In the so-called Lehmann representation [90], the eigenfunctions $\left\{\left|\Psi_n^N\right\rangle\right\}$ of the many-body Hamiltonian $\hat{H}$, solutions to $\hat{H}\left|\Psi_n^N\right\rangle = E_n^N\left|\Psi_n^N\right\rangle$, are used as a basis set, in which the Green's function is expressed. This set contains for example the ground state wave function $\left|\Psi_0^N\right\rangle$. Since the Hamiltonian is a Hermitian operator, its eigenvalues E_n^N are real. In field operator notation, where $\hat{\Phi}^\dagger(\mathbf{r},t)$ creates and $\hat{\Phi}(\mathbf{r},t)$ annihilates a particle at $(\mathbf{r},t)$, $\hat{H}$ is given by:

$$
\hat{H} = \int d^3\mathbf{r}\;\hat{\Phi}^+(\mathbf{r})\,h_0\left(\mathbf{r}\right)\;\hat{\Phi}(\mathbf{r}) + \frac{1}{2}\iint d^3\mathbf{r}d^3\mathbf{r}'\;\hat{\Phi}^\dagger(\mathbf{r},t)\hat{\Phi}^\dagger(\mathbf{r}',t)\,v\left(\mathbf{r}-\mathbf{r}'\right)\;\hat{\Phi}(\mathbf{r}',t)\hat{\Phi}(\mathbf{r},t),
$$

where the one-particle potentials are collected in $h_0\left(\mathbf{r}\right) = -\frac{1}{2}\nabla^2 + V_{ext}\left(\mathbf{r}\right)$ and where $v\left(\mathbf{r}-\mathbf{r}'\right) = \frac{1}{|\mathbf{r}-\mathbf{r}'|}$ is the Coulomb potential.

In the following, we derive an expression for the time-ordered single-particle Green's function in this basis. The single-electron Green's function at non-zero temperature is defined as the following thermal average:

$$\begin{aligned} G^e(\mathbf{r}t,\,\mathbf{r}'t') &= -\tfrac{i}{\hbar}\left\langle \hat{\Phi}(\mathbf{r},t)\,\hat{\Phi}^\dagger(\mathbf{r}',t')\right\rangle \Theta\left(t-t'\right) \\ &= -\tfrac{i}{\hbar}\tfrac{1}{Z}\,\textstyle\sum_n \left\langle \Psi_n^N\right| e^{-\beta\hat{H}}\,\hat{\Phi}(\mathbf{r},t)\,\hat{\Phi}^\dagger(\mathbf{r}',t')\left|\Psi_n^N\right\rangle \,\Theta\left(t-t'\right), \end{aligned}$$

where Z is defined in the grand canonical ensemble as $Z=\sum_n e^{\beta E_n^N}$, with $\beta=1/k_BT$. For the sake of clarity, we already used a shorthand notation, where we defined $\hat{H}\equiv\hat{H}-\mu\hat{N}$ including the chemical potential μ and the number operator $\hat{N}$. Moreover, $\left\{\left|\Psi_n^N\right\rangle\right\}$ and E_n^N are eigenfunctions and eigenvalues to $\left(\hat{H}-\mu\hat{N}\right)$, the Hamiltonian of a system exchanging energy and particles with a reservoir, i.e. a grand canonical ensemble. Since $\left\{\left|\Psi_n^N\right\rangle\right\}$ are eigenfunctions of $\hat{H}$, we can use the property,

$$e^{\hat{H}}\left|\Psi_n^N\right\rangle = \sum_k \frac{H^k}{k!}\left|\Psi_n^N\right\rangle = \sum_k \frac{E_n^k}{k!}\left|\Psi_n^N\right\rangle = e^{E_n^N}\left|\Psi_n^N\right\rangle,$$

in order to obtain:

$$\begin{aligned} G^e(\mathbf{r}t,\,\mathbf{r}'t') &= -\tfrac{i}{\hbar}\tfrac{1}{Z}\,\textstyle\sum_n \left\langle \Psi_n^N\right| e^{-\beta E_n^N}\,\hat{\Phi}(\mathbf{r},t)\,\hat{\Phi}^\dagger(\mathbf{r}',t')\left|\Psi_n^N\right\rangle \,\Theta\left(t-t'\right) \\ &= -\tfrac{i}{\hbar}\tfrac{1}{Z}\,\textstyle\sum_n e^{-\beta E_n^N}\left\langle \Psi_n^N\right| \hat{\Phi}(\mathbf{r},t)\,\hat{\Phi}^\dagger(\mathbf{r}',t')\left|\Psi_n^N\right\rangle \,\Theta\left(t-t'\right). \end{aligned}$$

In the Heisenberg picture the time-dependence of an operator $\hat{O}$ is governed by the relation:

$$\hat{O}(t)=e^{i\hat{H}t}\hat{O}(t=0)e^{-i\hat{H}t},$$

yielding for the single-electron Green's function:

$$\begin{aligned} G^e(\mathbf{r}t,\,\mathbf{r}'t') &= -\tfrac{i}{\hbar}\tfrac{1}{Z}\,\textstyle\sum_n e^{-\beta E_n^N}\,\left\langle \Psi_n^N\right| e^{i\hat{H}t}\hat{\Phi}(\mathbf{r})e^{-i\hat{H}t}\,e^{i\hat{H}t'}\hat{\Phi}^\dagger(\mathbf{r}')e^{-i\hat{H}t'}\left|\Psi_n^N\right\rangle \,\Theta\left(t-t'\right) \\ &= -\tfrac{i}{\hbar}\tfrac{1}{Z}\,\textstyle\sum_n e^{-\beta E_n^N}\,\left\langle \Psi_n^N\right| e^{iE_n^Nt}\hat{\Phi}(\mathbf{r})e^{-i\hat{H}t}\,e^{i\hat{H}t'}\hat{\Phi}^\dagger(\mathbf{r}')e^{-iE_n^Nt'}\left|\Psi_n^N\right\rangle \,\Theta\left(t-t'\right). \end{aligned}$$

Extracting the exponentials from the expectation value and inserting the completeness relation, $\sum_m \left|\Psi_m\right\rangle\left\langle\Psi_m\right| = \bar{1}$, in between the field operators results in:

$$G^e(\mathbf{r}t,\,\mathbf{r}'t') =$$

$$= -\tfrac{i}{\hbar}\tfrac{1}{Z}\,\textstyle\sum_{n,m} e^{-\beta E_n^N}e^{iE_n^Nt}e^{-iE_n^Nt'}\,\left\langle \Psi_n^N\right| \hat{\Phi}(\mathbf{r})e^{-i\hat{H}t}\,\left|\Psi_m\right\rangle\left\langle\Psi_m\right|\,e^{i\hat{H}t'}\hat{\Phi}^\dagger(\mathbf{r}')\left|\Psi_n^N\right\rangle \,\Theta\left(t-t'\right)$$

$$= -\tfrac{i}{\hbar}\tfrac{1}{Z}\,\textstyle\sum_{n,m} e^{-\beta E_n^N}e^{iE_n^Nt}e^{-iE_n^Nt'}\,\left\langle \Psi_n^N\right| \hat{\Phi}(\mathbf{r})\,e^{-iE_mt}\left|\Psi_m\right\rangle\left\langle\Psi_m\right|e^{iE_mt'}\,\hat{\Phi}^\dagger(\mathbf{r}')\left|\Psi_n^N\right\rangle \,\Theta\left(t-t'\right)$$

$$= -\tfrac{i}{\hbar}\tfrac{1}{Z}\,\textstyle\sum_{n,m} e^{-\beta E_n^N}e^{i(E_n^N-E_m)t}e^{i(E_m-E_n^N)t'}\,\left\langle \Psi_n^N\right| \hat{\Phi}(\mathbf{r})\left|\Psi_m\right\rangle\,\left\langle\Psi_m\right|\hat{\Phi}^\dagger(\mathbf{r}')\left|\Psi_n^N\right\rangle \,\Theta\left(t-t'\right)$$

$$= -\tfrac{i}{\hbar}\tfrac{1}{Z}\,\textstyle\sum_{n,m} e^{-\beta E_n^N}e^{-i(E_m-E_n^N)\tau}\,\left\langle \Psi_n^N\right| \hat{\Phi}(\mathbf{r})\left|\Psi_m\right\rangle\,\left\langle\Psi_m\right|\hat{\Phi}^\dagger(\mathbf{r}')\left|\Psi_n^N\right\rangle \,\Theta\left(\tau\right),$$

where we introduced $\tau=t-t'$ and where we assumed that $\{\left|\Psi_m\right\rangle\}$ are also eigenfunctions of the Hamiltonian with corresponding eigenvalues E_m. From the last equality, we draw the conclusion that the $\{\left|\Psi_m\right\rangle\}$ have to be a basis of a $(N+1)$ Hilbert space. Bases of different Hilbert

spaces, i.e. describing systems of varying particle number, form the Fock space and are orthogonal, $\langle \Psi^N \left| \Psi^{P\neq N} \right\rangle = 0$. This would cause for example $\langle \Psi_m | \hat{\Phi}^\dagger(\mathbf{r}') \left| \Psi_n^N \right\rangle = \langle \Psi_m | \Psi^{N+1} \rangle$ to be zero. That means, the index m denotes both the number of particles in the system: $(N+1)$ and the configuration, i.e. representing e.g. the ground state $\left|\Psi_0^{N+1}\right\rangle$ or the first excited state of the $N+1$ particle system. For the sake of clarity, we use the notation $|\Psi_m\rangle \equiv \left|\Psi_m^{N+1}\right\rangle$ here and in the following. Likewise, E_m^{N+1} is the **total** energy of a $N+1$ particle system in configuration m. Both $\left\{\left|\Psi_n^N\right\rangle\right\}$ and $\left\{\left|\Psi_m^{N+1}\right\rangle\right\}$ can be solutions to the eigenvalue problem of H, since the latter is expressed in field operator notation, where the number of particles is not fixed. In exactly the same manner, the single-hole Green's function $G^h(\mathbf{r}'t',\, \mathbf{r}t)$ can be rewritten, giving:

$$G^h(\mathbf{r}', \mathbf{r}, \tau) = -\frac{i}{\hbar}\frac{1}{Z} \sum_{n,l} e^{-\beta E_n^N} e^{-i(E_n^N - E_l^{N-1})\tau} \left\langle \Psi_n^N \right| \hat{\Phi}^\dagger(\mathbf{r}') \left| \Psi_l \right\rangle \left\langle \Psi_l \right| \hat{\Phi}(\mathbf{r}) \left| \Psi_n^N \right\rangle \Theta(-\tau)\,,$$

where l stands for a state of a $N-1$ particle system.

Definitions In order to facilitate the notation, the following quantities are introduced:

- the Lehmann amplitude of the $(N+1)$ system: $f_m(\mathbf{r}) = \left\langle \Psi_m^{N+1} \right| \hat{\Phi}^\dagger(\mathbf{r}) \left| \Psi_n^N \right\rangle$ and $f_m^*(\mathbf{r}) = \left\langle \Psi_n^N \right| \hat{\Phi}(\mathbf{r}) \left| \Psi_m^{N+1} \right\rangle$
- the Lehmann amplitude of the $(N-1)$ system: $g_l(\mathbf{r}) = \left\langle \Psi_l^{N-1} \right| \hat{\Phi}(\mathbf{r}) \left| \Psi_n^N \right\rangle$ and $g_l^*(\mathbf{r}) = \left\langle \Psi_n^N \right| \hat{\Phi}^\dagger(\mathbf{r}) \left| \Psi_l^{N-1} \right\rangle$
- the excitation energy needed to insert an electron to the N particle system resulting in a state $\left|\Psi_m^{N+1}\right\rangle$: $\varepsilon_m = E_m^{N+1} - E_0^N$
- the excitation energy needed to remove an electron resulting in a state $\left|\Psi_l^{N-1}\right\rangle$: $\varepsilon_l = E_0^N - E_l^{N-1}$

Using these definitions, the Green's functions G^e and G^h can be written in a more compact form:

$$G^e(\mathbf{r}, \mathbf{r}', \tau) = -\frac{i}{\hbar}\frac{1}{Z} \sum_{n,m} e^{-\beta E_n^N} e^{-i(E_m^{N+1} - E_n^N)\tau} f_m^*(\mathbf{r}) f_m(\mathbf{r}')\, \Theta(\tau)$$

$$G^h(\mathbf{r}', \mathbf{r}, \tau) = -\frac{i}{\hbar}\frac{1}{Z} \sum_{n,l} e^{-\beta E_n^N} e^{-i(E_n^N - E_l^{N-1})\tau} g_l^*(\mathbf{r}') g_l(\mathbf{r})\, \Theta(-\tau)\,.$$

The Green's function at zero temperature T Since we are interested in the low temperature regime, where $k_B T \leqslant |E_i - E_0|$ holds, the thermal energy is not sufficient to excite the initial system and consequently we assume the system to be in its ground state. Thus, the sum over excited states n of the N particle system becomes redundant and only the sums over m and l remain, because the latter describe excitations caused by photons or other higher energy sources. For instance, the prefactor Z becomes: $Z = \sum_n e^{\beta E_n^N} \overset{T\simeq 0}{\longrightarrow} e^{\beta E_0^N}$. This simplifies the

above equations to:

$$G^e(\mathbf{r},\mathbf{r}',\tau) = -\frac{i}{\hbar}\sum_m e^{-i(E_m^{N+1}-E_0^N)\tau}\, f_m^*(\mathbf{r}) f_m(\mathbf{r}')\,\Theta(\tau)$$

$$G^h(\mathbf{r}',\mathbf{r},\tau) = -\frac{i}{\hbar}\sum_l e^{-i(E_0^N-E_l^{N-1})\tau}\, g_l^*(\mathbf{r}') g_l(\mathbf{r})\,\Theta(-\tau)\,.$$

and

$$G^e(\mathbf{r},\mathbf{r}',\tau) = -\frac{i}{\hbar}\sum_m e^{-i\varepsilon_m\tau}\, f_m^*(\mathbf{r}) f_m(\mathbf{r}')\,\Theta(\tau) \tag{A.8}$$

$$G^h(\mathbf{r}',\mathbf{r},\tau) = -\frac{i}{\hbar}\sum_l e^{-i\varepsilon_l\tau}\, g_l^*(\mathbf{r}') g_l(\mathbf{r})\,\Theta(-\tau)\,, \tag{A.9}$$

respectively.

Transformation into frequency space Having in mind photoemission experiments, where the energy is usually expressed in terms of $\hbar\omega$, it is suitable to transform equation (A.8) and (A.9) into frequency space using the Fourier transformation:

$$\begin{aligned} G(\mathbf{r},\mathbf{r}',\omega) &= \textstyle\int_{-\infty}^{\infty} d\tau\, e^{i\omega\tau} G(\mathbf{r},\mathbf{r}',\tau) \\ G(\mathbf{r},\mathbf{r}',\tau) &= \textstyle\frac{1}{2\pi}\int_{-\infty}^{\infty} d\omega\, e^{-i\omega\tau} G(\mathbf{r},\mathbf{r}',\omega). \end{aligned}$$

For the single-electron Green's function this gives:

$$\begin{aligned} G^e(\mathbf{r},\mathbf{r}',\omega) &= -\tfrac{i}{\hbar}\textstyle\int_{-\infty}^{\infty} d\tau\, e^{i\omega\tau}\,\Theta(\tau)\sum_m e^{-i\varepsilon_m\tau}\, f_m^*(\mathbf{r}) f_m(\mathbf{r}') \\ &= -\tfrac{i}{\hbar}\textstyle\sum_m f_m^*(\mathbf{r}) f_m(\mathbf{r}')\int_0^{\infty} d\tau\, e^{i(\omega-\varepsilon_m)\tau} \\ &= -\tfrac{i}{\hbar}\textstyle\sum_m f_m^*(\mathbf{r}) f_m(\mathbf{r}')\left[\frac{1}{i(\omega-\varepsilon_m)} e^{i(\omega-\varepsilon_m)\tau}\right]_{\tau=0}^{\infty}. \end{aligned}$$

At this point, a case-by-case analysis is necessary. For $\tau = 0$, we obviously get:

$$G^e(\mathbf{r},\mathbf{r}',\omega) = -\frac{1}{\hbar}\sum_m f_m^*(\mathbf{r}) f_m(\mathbf{r}')\,\frac{1}{\omega-\varepsilon_m}.$$

On the contrary, the problem does not converge for $\tau \to \infty$. Therefore, we have to introduce a factor $e^{i(i\delta)\tau}$ with $\delta \to 0$:

$$G(\mathbf{r},\mathbf{r}',\omega) = \int_{-\infty}^{\infty} d\tau\, e^{i(\omega+i\delta)\tau} G(\mathbf{r},\mathbf{r}',\tau).$$

Like this, we get:

$$\begin{aligned} G^e(\mathbf{r},\mathbf{r}',\omega) &= -\tfrac{i}{\hbar}\textstyle\sum_m f_m^*(\mathbf{r}) f_m(\mathbf{r}')\int_0^{\infty} d\tau\, e^{i(\omega-\varepsilon_m+i\delta)\tau} \\ &= -\tfrac{i}{\hbar}\textstyle\sum_m f_m^*(\mathbf{r}) f_m(\mathbf{r}')\int_0^{\infty} d\tau\, e^{i(\omega-\varepsilon_m)\tau} e^{-\delta\tau}. \end{aligned}$$

$$\Rightarrow G^e(\mathbf{r},\mathbf{r}',\omega) = \frac{1}{\hbar}\sum_m f_m^*(\mathbf{r}) f_m(\mathbf{r}')\,\frac{1}{\omega-\varepsilon_m+i\delta}.$$

An analogue calculation for the single-hole Green's function results in:

$$\Rightarrow G^h(\mathbf{r},\mathbf{r}',\omega) = -\frac{1}{\hbar}\sum_l g_l^*(\mathbf{r}') g_l(\mathbf{r})\,\frac{1}{\omega-\varepsilon_l-i\delta}.$$

Combining the last two equations yields the time-ordered one-particle Green's function in the Lehmann representation:

$$G^T(\mathbf{r},\mathbf{r}',\omega) = \frac{1}{\hbar}\sum_m^{unocc}\frac{f_m^*(\mathbf{r}) f_m(\mathbf{r}')}{\omega-\varepsilon_m+i\delta} + \frac{1}{\hbar}\sum_l^{occ}\frac{g_l^*(\mathbf{r}') g_l(\mathbf{r})}{\omega-\varepsilon_l-i\delta}.$$

We have to bear in mind that m stands for excitations, where an electron is inserted, and l for excitations, where an electron is removed from the N-particle system. Analogue, the retarded and advanced Green's functions are:

$$G^R(\mathbf{r},\mathbf{r}',\omega) = \frac{1}{\hbar}\sum_m^{unocc}\frac{f_m^*(\mathbf{r}) f_m(\mathbf{r}')}{\omega-\varepsilon_m+i\delta} + \frac{1}{\hbar}\sum_l^{occ}\frac{g_l^*(\mathbf{r}') g_l(\mathbf{r})}{\omega-\varepsilon_l+i\delta}$$

$$G^A(\mathbf{r},\mathbf{r}',\omega) = \frac{1}{\hbar}\sum_m^{unocc}\frac{f_m^*(\mathbf{r}) f_m(\mathbf{r}')}{\omega-\varepsilon_m-i\delta} + \frac{1}{\hbar}\sum_l^{occ}\frac{g_l^*(\mathbf{r}') g_l(\mathbf{r})}{\omega-\varepsilon_l-i\delta},$$

with poles only in the upper (for G^A) or lower half plane (for G^R). Moreover, G^A and G^R are complex conjugates of each other: $G^R = \left[G^A\right]^*$.

A.3. Hedin's equations

Equation of motion of the single-particle Green's function Differentiating the single-particle Green's function with respect to one of its two time variables reveals important properties of the latter [2, 90]. Starting from the time-ordered one-particle Green's function at zero temperature:

$$\begin{aligned} G(\mathbf{r}t,\mathbf{r}'t') &= \tfrac{1}{i\hbar}\left\langle\Psi_0^N\right| T\left[\hat\Phi(\mathbf{r},t)\,\hat\Phi^\dagger(\mathbf{r}',t')\right]\left|\Psi_0^N\right\rangle = G^e(\mathbf{r}t,\,\mathbf{r}'t') - G^h(\mathbf{r}'t',\,\mathbf{r}t),\\ &= \tfrac{1}{i\hbar}\left\langle\Psi_0^N\right|\hat\Phi(\mathbf{r},t)\,\hat\Phi^\dagger(\mathbf{r}',t')\left|\Psi_0^N\right\rangle\,\theta(t-t')\\ &- \tfrac{1}{i\hbar}\left\langle\Psi_0^N\right|\hat\Phi^\dagger(\mathbf{r}',t')\,\hat\Phi(\mathbf{r},t)\left|\Psi_0^N\right\rangle\,\theta(t'-t) \end{aligned}$$

and using the product rule, one obtains:

$$\begin{aligned} i\hbar\tfrac{\partial G(\mathbf{r}t,\mathbf{r}'t')}{\partial t} &= \left\langle\Psi_0^N\right|\hat\Phi(\mathbf{r},t)\,\hat\Phi^\dagger(\mathbf{r}',t')\left|\Psi_0^N\right\rangle\tfrac{\partial\theta(t-t')}{\partial t} - \left\langle\Psi_0^N\right|\hat\Phi^\dagger(\mathbf{r}',t')\,\hat\Phi(\mathbf{r},t)\left|\Psi_0^N\right\rangle\tfrac{\partial\theta(t'-t)}{\partial t} +\\ &\left\langle\Psi_0^N\right|\tfrac{\partial\hat\Phi(\mathbf{r},t)}{\partial t}\,\hat\Phi^\dagger(\mathbf{r}',t')\left|\Psi_0^N\right\rangle\,\theta(t-t') - \left\langle\Psi_0^N\right|\hat\Phi^\dagger(\mathbf{r}',t')\,\tfrac{\partial\hat\Phi(\mathbf{r},t)}{\partial t}\left|\Psi_0^N\right\rangle\,\theta(t'-t)\\ i\hbar\tfrac{\partial G(\mathbf{r}t,\mathbf{r}'t')}{\partial t} &= \delta(t,t')\left[\left\langle\Psi_0^N\right|\hat\Phi(\mathbf{r},t)\,\hat\Phi^\dagger(\mathbf{r}',t')\left|\Psi_0^N\right\rangle + \left\langle\Psi_0^N\right|\hat\Phi^\dagger(\mathbf{r}',t')\,\hat\Phi(\mathbf{r},t)\left|\Psi_0^N\right\rangle\right] +\\ &\left\langle\Psi_0^N\right|\tfrac{\partial\hat\Phi(\mathbf{r},t)}{\partial t}\,\hat\Phi^\dagger(\mathbf{r}',t')\left|\Psi_0^N\right\rangle\,\theta(t-t') - \left\langle\Psi_0^N\right|\hat\Phi^\dagger(\mathbf{r}',t')\,\tfrac{\partial\hat\Phi(\mathbf{r},t)}{\partial t}\left|\Psi_0^N\right\rangle\,\theta(t'-t), \end{aligned}$$

where we used the fact that the derivative of a step function is a δ-function:

$$\frac{\partial\theta(t-t')}{\partial t} = -\frac{\partial\theta(t'-t)}{\partial t} = \delta(t-t').$$

Further, using that

$$\left[\hat{\Phi}(\mathbf{r})\,\hat{\Phi}^{\dagger}(\mathbf{r}')\right]_{+} = \delta\left(\mathbf{r}-\mathbf{r}'\right)$$

for equal times t and t' [90], the first two terms of the above equation simplify to:

$$\delta\left(t,t'\right)\left\langle\Psi_0^N\right|\hat{\Phi}(\mathbf{r},t)\,\hat{\Phi}^{\dagger}(\mathbf{r}',t')+\hat{\Phi}^{\dagger}(\mathbf{r}',t')\,\hat{\Phi}(\mathbf{r},t)\left|\Psi_0^N\right\rangle=\delta\left(t,t'\right)\delta\left(\mathbf{r}-\mathbf{r}'\right).$$

Concerning the remaining two terms, they can be combined to:

$$\left\langle\Psi_0^N\right|T\left[\frac{\partial\hat{\Phi}(\mathbf{r},t)}{\partial t}\hat{\Phi}^{\dagger}(\mathbf{r}',t')\right]\left|\Psi_0^N\right\rangle.$$

Further, inserting expression (A.4) for the equation of motion of the annihilation operator results in:

$$\begin{aligned}
i\hbar\tfrac{\partial G(\mathbf{r}t,\mathbf{r}'t')}{\partial t} &= \delta\left(\mathbf{r}-\mathbf{r}'\right)\delta\left(t,t'\right)+\left\langle\Psi_0^N\right|T\left[\tfrac{\partial\hat{\Phi}(\mathbf{r},t)}{\partial t}\hat{\Phi}^{\dagger}(\mathbf{r}',t')\right]\left|\Psi_0^N\right\rangle\\
&= \delta\left(\mathbf{r}-\mathbf{r}'\right)\delta\left(t,t'\right)+\\
&\quad \tfrac{1}{i\hbar}\left\langle\Psi_0^N\right|T\left[\left\{h_0\left(\mathbf{r}\right)\hat{\Phi}(\mathbf{r},t)+\int d^3\mathbf{r}''\,v\left(\mathbf{r}-\mathbf{r}''\right)\hat{\Phi}^{\dagger}(\mathbf{r}'',t)\hat{\Phi}(\mathbf{r}'',t)\hat{\Phi}(\mathbf{r},t)\right\}\hat{\Phi}^{\dagger}(\mathbf{r}',t')\right]\left|\Psi_0^N\right\rangle\\
&= \delta\left(\mathbf{r}-\mathbf{r}'\right)\delta\left(t,t'\right)+\\
&\quad \tfrac{1}{i\hbar}\left\langle\Psi_0^N\right|T\left[h_0\left(\mathbf{r}\right)\hat{\Phi}(\mathbf{r},t)\hat{\Phi}^{\dagger}(\mathbf{r}',t')\right]\left|\Psi_0^N\right\rangle+\\
&\quad \tfrac{1}{i\hbar}\left\langle\Psi_0^N\right|T\left[\int d^3\mathbf{r}''\,v\left(\mathbf{r}-\mathbf{r}''\right)\hat{\Phi}^{\dagger}(\mathbf{r}'',t)\hat{\Phi}(\mathbf{r}'',t)\hat{\Phi}(\mathbf{r},t)\hat{\Phi}^{\dagger}(\mathbf{r}',t')\right]\left|\Psi_0^N\right\rangle.
\end{aligned}$$

Since $h_0\left(\mathbf{r}\right)$ and $v\left(\mathbf{r}-\mathbf{r}''\right)$ are just functions and no operators in second quantization, they can be put in front of the corresponding matrix elements:

$$\begin{aligned}
i\hbar\tfrac{\partial G(\mathbf{r}t,\mathbf{r}'t')}{\partial t} &= \delta\left(\mathbf{r}-\mathbf{r}'\right)\delta\left(t,t'\right)+\\
&\quad h_0\left(\mathbf{r}\right)\tfrac{1}{i\hbar}\left\langle\Psi_0^N\right|T\left[\hat{\Phi}(\mathbf{r},t)\hat{\Phi}^{\dagger}(\mathbf{r}',t')\right]\left|\Psi_0^N\right\rangle+\\
&\quad \int d^3\mathbf{r}''\,v\left(\mathbf{r}-\mathbf{r}''\right)\tfrac{1}{i\hbar}\left\langle\Psi_0^N\right|T\left[\hat{\Phi}^{\dagger}(\mathbf{r}'',t)\hat{\Phi}(\mathbf{r}'',t)\hat{\Phi}(\mathbf{r},t)\hat{\Phi}^{\dagger}(\mathbf{r}',t')\right]\left|\Psi_0^N\right\rangle\\
&= \delta\left(\mathbf{r}-\mathbf{r}'\right)\delta\left(t,t'\right)+h_0\left(\mathbf{r}\right)G(\mathbf{r}t,\mathbf{r}'t')+\\
&\quad \int d^3\mathbf{r}''\,v\left(\mathbf{r}-\mathbf{r}''\right)\tfrac{1}{i\hbar}\left\langle\Psi_0^N\right|T\left[\hat{\Phi}^{\dagger}(\mathbf{r}'',t)\hat{\Phi}(\mathbf{r}'',t)\hat{\Phi}(\mathbf{r},t)\hat{\Phi}^{\dagger}(\mathbf{r}',t')\right]\left|\Psi_0^N\right\rangle.
\end{aligned}$$

The time-ordered product containing four field operators governs the full electron-electron interaction. We can rewrite this term respecting that every exchange of field operators causes a minus sign:

$$\begin{aligned}
i\hbar\tfrac{\partial G(\mathbf{r}t,\mathbf{r}'t')}{\partial t} &= \delta\left(\mathbf{r}-\mathbf{r}'\right)\delta\left(t,t'\right)+h_0\left(\mathbf{r}\right)G(\mathbf{r}t,\mathbf{r}'t')\\
&\quad -\int d^3\mathbf{r}'\,v\left(\mathbf{r}-\mathbf{r}'\right)\tfrac{1}{i\hbar}\left\langle\Psi_0^N\right|T\left[\hat{\Phi}(\mathbf{r},t)\hat{\Phi}(\mathbf{r}'',t)\hat{\Phi}^{\dagger}(\mathbf{r}'',t)\hat{\Phi}^{\dagger}(\mathbf{r}',t')\right]\left|\Psi_0^N\right\rangle
\end{aligned}$$

and introduce the two-particle Green's function G_2 (A.5):

$$G_2\left(\mathbf{r}t;\mathbf{r}''t;\mathbf{r}',t';\mathbf{r}''t^+\right) = \frac{1}{(i\hbar)^2}\left\langle\Psi_0^N\right|T\left[\hat{\Phi}(\mathbf{r},t)\hat{\Phi}(\mathbf{r}'',t)\hat{\Phi}^\dagger(\mathbf{r}'',t^+)\hat{\Phi}^\dagger(\mathbf{r}',t')\right]\left|\Psi_0^N\right\rangle.$$

Finally one obtains for the equation of motion of the single-particle Green's function:

$$\left(i\hbar\frac{\partial}{\partial t_1} - h_0\left(\mathbf{r}_1\right)\right)G(11') + i\hbar\int d^3\mathbf{r}_2\, v\left(\mathbf{r}_1-\mathbf{r}_2\right)\, G_2\left(12,1'2^+\right) = \delta\left(1,1'\right). \tag{A.10}$$

Concerning the shorthand notation, 1 represents $(\mathbf{r},t)$, $1' \equiv (\mathbf{r}',t')$, $2 \equiv (\mathbf{r}'',t)$ and $2^+ \equiv (\mathbf{r}'',t+\eta)$, where η with $\eta \to 0$ is introduced to ensure the right time order.

The Dyson equation Following Schwinger's functional derivative approach for the derivation of Hedin's equations, we introduce a time-dependent external potential U_{ext}, which is set to zero at the end of the derivation. This way, the two-particle Green's function in equation (A.10) can be substituted by equation (A.7):

$$G_2\left(121'2^+\right) = G\left(11'\right)G\left(22^+\right) - \frac{\partial G\left(11'\right)}{\partial U_{ext}\left(2\right)}.$$

This results in:

$$\begin{aligned} i\hbar\tfrac{\partial G(11')}{\partial t_1} &= \delta\left(1,1'\right) + h_0\left(\mathbf{r}_1\right)G\left(1,1'\right) - i\hbar\textstyle\int d^3\mathbf{r}_2\, v\left(\mathbf{r}_1-\mathbf{r}_2\right)\, G_2\left(12,1'2^+\right) \\ &= \delta\left(1,1'\right) + h_0\left(\mathbf{r}_1\right)G\left(1,1'\right) \\ &\quad -i\hbar\left[\textstyle\int d^3\mathbf{r}_2\, v\left(\mathbf{r}_1-\mathbf{r}_2\right)\, G\left(22^+\right)\right]G\left(11'\right) + i\hbar\textstyle\int d^3\mathbf{r}_2\, v\left(\mathbf{r}_1-\mathbf{r}_2\right)\, \frac{\partial G(11')}{\partial U_{ext}(2)} \\ \Rightarrow\quad i\hbar\tfrac{\partial G(11')}{\partial t_1} &= \delta\left(1,1'\right) + h_0\left(\mathbf{r}_1\right)G\left(1,1'\right) + V_H\left(\mathbf{r}_1\right)G\left(11'\right) + \textstyle\int d2\,\Sigma\left(12\right)G\left(21'\right). \end{aligned} \tag{A.11}$$

For the last identity we introduced the Hartree potential $V_H\left(\mathbf{r}_1\right)$:

$$V_H\left(\mathbf{r}_1\right) = \int d^3\mathbf{r}_2\, v\left(\mathbf{r}_1-\mathbf{r}_2\right)\, G\left(22^+\right), \tag{A.12}$$

where we used that $-i\hbar G(22^+)$ equals the electron density $n(2)$, which is the expectation value of the density operator $\hat{n}(2) = \hat{\Phi}^\dagger(2)\hat{\Phi}(2)$ as defined in Chapter I of the Appendix. Moreover, we defined the self-energy Σ as:

$$\Sigma\left(12\right) = i\hbar\iint d3d4\, v\left(\mathbf{r}_1-\mathbf{r}_3\right)\frac{\partial G\left(14\right)}{\partial U_{ext}\left(3\right)}G^{-1}\left(42\right),$$

where we used that $\delta\left(12\right) = \int d3\, G^{-1}\left(13\right)G\left(32\right)$. The expression for Σ can be further modified considering equation (A.3) and (A.2), leading to:

$$\begin{aligned}\Sigma(12) &= -i\hbar \iiiint d3d4d5d6\, v(\mathbf{r}_1-\mathbf{r}_3)\, G(15)\, \tfrac{\partial G^{-1}(56)}{\partial U_{ext}(3)} G(64)\, G^{-1}(42) \\ &= -i\hbar \iint d3d5\, v(\mathbf{r}_1-\mathbf{r}_3)\, G(15)\, \tfrac{\partial G^{-1}(52)}{\partial U_{ext}(3)} \\ &= -i\hbar \iiint d3d4d5\, v(\mathbf{r}_1-\mathbf{r}_3)\, G(15)\, \tfrac{\partial G^{-1}(52)}{\partial V_{tot}(4)} \tfrac{\partial V_{tot}(4)}{\partial U_{ext}(3)} \qquad \text{(A.13)}\end{aligned}$$

$$\Rightarrow \quad \Sigma(12) = i\hbar \iint d4d5\, G(15)\, \Gamma(52;4)\, W(14),$$

where we introduced a total potential $V_{tot} = U_{ext} + V_{ind}$, the vertex function $\Gamma(52;4) = -\frac{\partial G^{-1}(52)}{\partial V_{tot}(4)}$ and the screened Coulomb potential $W(14) = \int d3\, v(\mathbf{r}_1-\mathbf{r}_3)\, \frac{\partial V_{tot}(4)}{\partial U_{ext}(3)}$.

Incorporating the Hartree potential in the one-particle operator ($H_0 = h_0 + V_H$), we can write the equation of motion (A.11) as follows :

$$\left(i\hbar\frac{\partial}{\partial t_1} - H_0(\mathbf{r}_1)\right) G(11') - \int d3\, \Sigma(13)\, G(31') = \delta(1,1'). \qquad \text{(A.14)}$$

For a non-interacting system ($\Sigma = 0$), the latter simplifies to:

$$\left(i\hbar\frac{\partial}{\partial t_1} - H_0(\mathbf{r}_1)\right) G_0(11') = \delta(1,1'), \qquad \text{(A.15)}$$

i.e.

$$G_0(1,1') = \delta(1,1') \left(i\hbar\frac{\partial}{\partial t_1} - H_0(\mathbf{r}_1)\right)^{-1}. \qquad \text{(A.16)}$$

Multiplying equation (A.14) by $G_0(21)$ from the left and integrating over $d1$ results in the Dyson equation:

$$\int d1\, \delta(21) \left(i\hbar\frac{\partial}{\partial t_2} - H_0(\mathbf{r}_2)\right)^{-1} \left(i\hbar\frac{\partial}{\partial t_1} - H_0(\mathbf{r}_1)\right) G(11') - \iint d3d1\, G_0(21)\, \Sigma(13)\, G(31')$$

$$= \int d1\, G_0(21)\, \delta(11')$$

$$G(21') - \iint d3d1\, G_0(21)\, \Sigma(13)\, G(31') = G_0(21')$$

$$G(21') = G_0(21') + \iint d3d1\, G_0(21)\, \Sigma(13)\, G(31'), \qquad \text{(A.17)}$$

which can be reformulated using $\delta(12) = \int d3\, G^{-1}(13)\, G(32)$ to:

$$G^{-1}(54) = G_0^{-1}(54) - \Sigma(54).$$

Using the fact that the Fourier transformation of a derivative $\frac{\partial}{\partial t}$ becomes $-i\omega$ and that δ-functions $\delta(\tau)$ give unity, we can readily transform the above equation to frequency space, yielding:

$$\begin{aligned}G^{-1}(\mathbf{r}_5\mathbf{r}_4,\omega) &= G_0^{-1}(\mathbf{r}_5\mathbf{r}_4,\omega) - \Sigma(\mathbf{r}_5\mathbf{r}_4,\omega) \\ &= \delta(\mathbf{r}_5\mathbf{r}_4)\left[\hbar\omega - H_0(\mathbf{r}_5)\right] - \Sigma(\mathbf{r}_5\mathbf{r}_4,\omega).\end{aligned}$$

Consequently, for the EOM expressed in terms of the self-energy, we obtain:

$$\int d\mathbf{r}_4\, G^{-1}\left(\mathbf{r}_5\mathbf{r}_4,\omega\right) G\left(\mathbf{r}_4\mathbf{r}_3,\omega\right) = \int d\mathbf{r}_4\, G_0^{-1}\left(\mathbf{r}_5\mathbf{r}_4,\omega\right) G\left(\mathbf{r}_4\mathbf{r}_3,\omega\right) - \int d\mathbf{r}_4\, \Sigma\left(\mathbf{r}_5\mathbf{r}_4,\omega\right) G\left(\mathbf{r}_4\mathbf{r}_3,\omega\right)$$

$$\delta\left(\mathbf{r}_5\mathbf{r}_3\right) = \int d\mathbf{r}_4\, \delta\left(\mathbf{r}_5\mathbf{r}_4\right)\left[\hbar\omega - H_0\left(\mathbf{r}_5\right)\right] G\left(\mathbf{r}_4\mathbf{r}_3,\omega\right) - \int d\mathbf{r}_4\, \Sigma\left(\mathbf{r}_5\mathbf{r}_4,\omega\right) G\left(\mathbf{r}_4\mathbf{r}_3,\omega\right),$$

$$\rightarrow \quad \left[\hbar\omega - H_0\left(\mathbf{r}_5\right)\right] G\left(\mathbf{r}_5\mathbf{r}_3,\omega\right) - \int d\mathbf{r}_4\, \Sigma\left(\mathbf{r}_5\mathbf{r}_4,\omega\right) G\left(\mathbf{r}_4\mathbf{r}_3,\omega\right) = \delta\left(\mathbf{r}_5\mathbf{r}_3\right). \tag{A.18}$$

Schwinger's functional derivative approach for the Hedin's equations The Dyson equation derived within Schwinger's functional derivative approach can be directly used to determine the irreducible vertex function Γ:

$$\Gamma(1,2;3) \equiv -\frac{\partial G^{-1}(1,2)}{\partial V_{tot}(3)} = -\frac{\partial G_0^{-1}(1,2)}{\partial V_{tot}(3)} + \frac{\partial \Sigma(1,2)}{\partial V_{tot}(3)},$$

where $\partial V_{tot} = \partial U_{ext} + \partial V_H$. It is important to keep in mind that G_0 originates from a system governed by the Hamiltonian $H_0 = -\frac{1}{2}\nabla^2 + V_{ext} + V_H$, where V_{ext} accounts for the core ion potential. Inserting expression (A.16) for G_0, applying the chain rule (A.2) and using relation (A.3) leads to:

$$\begin{aligned}
\Gamma(1,2;3) &= -\frac{\partial\left[\delta(1,2)\left(i\hbar\frac{\partial}{\partial t_1}+\frac{1}{2}\nabla^2-V_{ext}(1)-V_H(1)\right)\right]}{\partial V_{tot}(3)} + \iint d4d5\, \frac{\partial\Sigma(12)}{\partial G(45)}\frac{\partial G(45)}{\partial V_{tot}(3)} \\
&= \delta(1,2)\,\frac{\partial V_H(1)}{\partial V_H(3)} + \iint d4d5\, \frac{\partial\Sigma(12)}{\partial G(45)}\frac{\partial G(45)}{\partial V_{tot}(3)} \\
&= \delta(1,2)\,\delta(1,3) + \iint d4d5\, \frac{\partial\Sigma(12)}{\partial G(45)}\frac{\partial G(45)}{\partial V_{tot}(3)} \\
&= \delta(1,2)\,\delta(1,3) - \iint d4567\, \frac{\partial\Sigma(12)}{\partial G(45)} G(46)\,\frac{\partial G^{-1}(67)}{\partial V_{tot}(3)} G(75).
\end{aligned}$$

This finally results in the Hedin equation for the irreducible vertex function Γ:

$$\Rightarrow \quad \Gamma(1,2;3) = \delta(12)\delta(13) + \iiiint d4567\, \frac{\partial\Sigma(12)}{\partial G(45)} G(46)\,\Gamma(6,7;3)\,G(75). \tag{A.19}$$

Analogously, by using identity (A.3) and the definition of the vertex function Γ, the irreducible polarizability $P(1,2) \equiv \frac{\partial n_{ind}(1)}{\partial V_{tot}(2)}$ can be derived:

$$\begin{aligned}
P(1,2) &= -i\hbar\frac{\partial G\left(11^+\right)}{\partial V_{tot}(2)} \\
&= i\hbar \iint d3d4\, G(13)\,\frac{\partial G^{-1}(34)}{\partial V_{tot}(2)} G(41)
\end{aligned} \tag{A.20}$$

$$\Rightarrow \quad P(1,2) = -i\hbar \iint d3d4\, G(13)\,\Gamma(3,4;2)\,G(41).$$

After having derived the Dyson equation for the Green's function (A.17), an explicit expression for the self-energy (A.13), the irreducible vertex function (A.19) and the irreducible polarizability (A.20), we conclude this section by introducing the screened Coulomb potential W,

$$W(12) = \int d3\, \epsilon^{-1}(13)\, v(32).$$

Using the chain rule (A.2) and the definition of the Hartree potential (A.12), the inverse dielectric function can be expressed via:

$$\begin{aligned}\epsilon^{-1}(12) &\equiv \frac{\partial V_{tot}(1)}{\partial U_{ext}(2)} = \frac{(\partial U_{ext}(1)+\partial V_H(1))}{\partial U_{ext}(2)} \\ &= \delta(12) + \int d3\, v(13)\, \frac{\partial G\left(33^+\right)}{\partial U_{ext}(2)} \\ &= \delta(12) + \int d34\, v(13)\, \frac{\partial G\left(33^+\right)}{\partial V_{tot}(4)}\, \frac{\partial V_{tot}(4)}{\partial U_{ext}(2)} \\ &= \delta(12) + \int d34\, v(13)\, P(34)\, \epsilon^{-1}(42).\end{aligned}$$

From this, it follows for the screened Coulomb potential $W(12) = \int d3\, \epsilon^{-1}(13)\, v(32)$:

$$\begin{aligned}W(12) &= \int d3\, \delta(13)\, v(32) + \int d345\, v(14)\, P(45)\, \epsilon^{-1}(53)\ v(32), \\ \Rightarrow \quad W(12) &= v(12) + \iint d45\, v(14)\, P(45)\, W(52). \end{aligned} \tag{A.21}$$

A.4. The GW formalism

A.4.1. Introduction of the quasiparticle weight

The single-particle Green's function can be written in a diagonal single-particle Hartree basis as follows:

$$G_{ii}(\omega) \equiv \frac{1}{\omega - \varepsilon_{H,i} - \Sigma_{ii}(\omega)}.$$

Expanding the real part of the self-energy $Re\Sigma(\omega)$ around the quasiparticle poles ε_{qp} in a Taylor series and assuming $Im\Sigma(\omega) \to 0$,

$$Re\Sigma_{ii}(\omega) = Re\Sigma_{ii}(\varepsilon_{qp,i}) + \left.\frac{\partial Re\Sigma_{ii}(\omega)}{\partial\omega}\right|_{\omega=\varepsilon_{qp,i}} (\omega - \varepsilon_{qp,i}) + \dots,$$

yields for the Green's function a decomposition into a coherent and incoherent part:

$$\begin{aligned}G_{ii}(\omega) &= \frac{1}{\omega - \varepsilon_{H,i} - Re\Sigma_{ii}(\varepsilon_{qp,i}) - \left.\frac{\partial Re\Sigma_{ii}(\omega)}{\partial\omega}\right|_{\omega=\varepsilon_{qp,i}} (\omega-\varepsilon_{qp,i}) - \dots} \\ &= Z_{qp,i}\frac{1}{\omega - \varepsilon_{H,i} - Re\Sigma_{ii}(\varepsilon_{qp,i})} + (1 - Z_{qp,i})\, G_{inc}.\end{aligned}$$

The introduced quasiparticle weight $Z_{qp,i}$ is defined as

$$Z_{qp,i} \equiv \left(1 - \left.\frac{\partial Re\Sigma_{ii}(\omega)}{\partial\omega}\right|_{\omega=\varepsilon_{qp,i}}\right)^{-1},$$

following from:

$$\begin{aligned} G_{coh}^{-1}(\omega) &= Z_{qp,i}^{-1}\left(\tfrac{1}{\omega-\varepsilon_{H,i}-Re\Sigma_{ii}(\varepsilon_{qp,i})}\right)^{-1} \\ &= \left(1-\left.\tfrac{\partial Re\Sigma_{ii}(\omega)}{\partial\omega}\right|_{\omega=\varepsilon_{qp,i}}\right)(\omega-\varepsilon_{H,i}-Re\Sigma_{ii}(\varepsilon_{qp,i}))\,, \end{aligned}$$

$$\begin{aligned} G_{coh}^{-1}(\omega) &= \omega-\varepsilon_{H,i}-Re\Sigma_{ii}(\varepsilon_{qp,i})-\omega\left.\tfrac{\partial Re\Sigma_{ii}(\omega)}{\partial\omega}\right|+\varepsilon_{H,i}\left.\tfrac{\partial Re\Sigma_{ii}(\omega)}{\partial\omega}\right|+\left.\tfrac{\partial Re\Sigma_{ii}(\omega)}{\partial\omega}\right| \\ &= \omega-\varepsilon_{H,i}-Re\Sigma_{ii}(\varepsilon_{qp,i})-\left.\tfrac{\partial Re\Sigma_{ii}(\omega)}{\partial\omega}\right|(\omega-\varepsilon_{H,i}-Re\Sigma_{ii}(\varepsilon_{qp,i})) \\ &= \omega-\varepsilon_{H,i}-Re\Sigma_{ii}(\varepsilon_{qp,i})-\left.\tfrac{\partial Re\Sigma_{ii}(\omega)}{\partial\omega}\right|(\omega-\varepsilon_{qp,i})\,. \end{aligned}$$

A.4.2. The quasiparticle equation

In order to facilitate the derivation, we generalize all quantities from real frequency space ω to the complex plane $z\in\mathbb{C}$. Consequently, the biorthonormal representation of the single-particle Green's function is represented by [98]:

$$G^T(\mathbf{r},\mathbf{r}',z)=\sum_\lambda\frac{\psi_\lambda(\mathbf{r},z)\,\overline{\psi}_\lambda(\mathbf{r}',z)}{z-E_\lambda(z)}.$$

$\overline{\psi}_\lambda$ and ψ_λ are left and right eigenvectors of the non-Hermitian operator $\tilde{H}$,

$$\tilde{H}(z)=\hat{H}_0+\Sigma\left(\mathbf{r},\mathbf{r}',z\right)=-\frac{1}{2}\nabla^2+V_{ext}(\mathbf{r})+V_H(\mathbf{r})+\Sigma\left(\mathbf{r},\mathbf{r}',z\right),$$

and $E_\lambda(z)$ is the corresponding eigenvalue. $\hat{H}_0$ regroups the kinetic energy, the external potential V_{ext} arising from the ion cores and the Hartree potential V_H. Inserting this representation of the Green's function in the equation of motion (EOM) in frequency space (A.18) yields:

$$\begin{aligned} &[z-H_0(\mathbf{r})]\,G(\mathbf{r},\mathbf{r}',z)-\textstyle\int d\mathbf{r}''\,\Sigma(\mathbf{r},\mathbf{r}'',z)\,G(\mathbf{r}'',\mathbf{r}',z) &&= \delta(\mathbf{r}-\mathbf{r}') \\ &\textstyle\sum_\lambda\,[z-E_\lambda(z)]^{-1}\{\,[z-H_0(\mathbf{r})]\,\psi_\lambda(\mathbf{r},z)\,\overline{\psi}_\lambda(\mathbf{r}',z) \\ &-\overline{\psi}_\lambda(\mathbf{r}',z)\textstyle\int d\mathbf{r}''\,\Sigma(\mathbf{r},\mathbf{r}'',z)\,\psi_\lambda(\mathbf{r}'',z)\,\} &&= \delta(\mathbf{r}-\mathbf{r}') \\ &\textstyle\sum_\lambda\,[z-E_\lambda(z)]^{-1}\{\,[z-H_0(\mathbf{r})]\,\psi_\lambda(\mathbf{r},z)\textstyle\int d\mathbf{r}'\psi_\nu(\mathbf{r}',z)\,\overline{\psi}_\lambda(\mathbf{r}',z) \\ &-\textstyle\int d\mathbf{r}'\psi_\nu(\mathbf{r}',z)\,\overline{\psi}_\lambda(\mathbf{r}',z)\int d\mathbf{r}''\,\Sigma(\mathbf{r},\mathbf{r}'',z)\,\psi_\lambda(\mathbf{r}'',z)\,\} &&= \textstyle\int d\mathbf{r}'\psi_\nu(\mathbf{r}',z)\,\delta(\mathbf{r}-\mathbf{r}') \\ &\textstyle\sum_\lambda\,[z-E_\lambda(z)]^{-1}\{\,[z-H_0(\mathbf{r})]\,\psi_\lambda(\mathbf{r},z)\,\delta_{\nu\lambda} \\ &-\delta_{\nu\lambda}\textstyle\int d\mathbf{r}''\,\Sigma(\mathbf{r},\mathbf{r}'',z)\,\psi_\lambda(\mathbf{r}'',z)\,\} &&= \psi_\nu(\mathbf{r},z) \\ &[z-H_0(\mathbf{r})]\,\psi_\nu(\mathbf{r},z)-\textstyle\int d\mathbf{r}''\,\Sigma(\mathbf{r},\mathbf{r}'',z)\,\psi_\nu(\mathbf{r}'',z) &&= [z-E_\nu(z)]\,\psi_\nu(\mathbf{r},z) \\ &H_0(\mathbf{r})\,\psi_\nu(\mathbf{r},z)+\textstyle\int d\mathbf{r}''\,\Sigma(\mathbf{r},\mathbf{r}'',z)\,\psi_\nu(\mathbf{r}'',z) &&= E_\nu(z)\,\psi_\nu(\mathbf{r},z)\,. \end{aligned}$$

The obtained equation is still general and in order to arrive at the quasiparticle equation we only consider z at the complex quasiparticle energy ε_{qp}, i.e. the pole of

$$\omega - E_\nu(z) = 0 \implies \varepsilon_{qp} - E_\nu(\varepsilon_{qp}) = 0.$$

Defining the quasiparticle wave functions as:

$$\psi_\nu^{qp}(\mathbf{r}) \equiv \psi_\nu(\mathbf{r},\, z = \varepsilon_{qp}),$$

where we neglect the frequency dependency of the wave functions, and further imposing $z = \varepsilon_{qp}$, we obtain the quasiparticle equation:

$$H_0(\mathbf{r})\,\psi_\nu^{qp}(\mathbf{r}) + \int d\mathbf{r}''\,\Sigma\left(\mathbf{r},\mathbf{r}'',\varepsilon_{qp}\right)\psi_\nu^{qp}\left(\mathbf{r}''\right) = \varepsilon_{qp}\psi_\nu^{qp}(\mathbf{r}).$$

A.4.3. Approximation of the quasiparticle energy in a state-independent framework

The difficult part in calculating the quasiparticle energy following

$$\varepsilon_{qp,\nu} = \varepsilon_\nu^{KS} + \left\langle \psi_\nu^{KS}\right| \Sigma\left(\varepsilon_{qp,\nu}\right) - V_{xc} \left|\psi_\nu^{KS}\right\rangle \tag{A.22}$$

is the dependence of the self-energy Σ on the quasiparticle energy $\varepsilon_{qp,\nu}$ itself. An approximation is to expand Σ up to the linear term in a Taylor series around the known DFT Kohn-Sham energy ε_ν^{KS}:

$$\Sigma(\varepsilon_{qp,\nu}) \approx \Sigma(\varepsilon_\nu^{KS}) + \left.\frac{\partial\Sigma(\omega)}{\partial\omega}\right|_{\omega=\varepsilon_\nu^{KS}} (\varepsilon_{qp,\nu} - \varepsilon_\nu^{KS}).$$

Inserting the above expansion in equation (A.22) yields:

$$\varepsilon_{qp,\nu} \approx \varepsilon_\nu^{KS} + \left\langle \psi_\nu^{KS} \left| \Sigma(\varepsilon_\nu^{KS}) + \left.\frac{\partial\Sigma(\omega)}{\partial\omega}\right|_{\omega=\varepsilon_\nu^{KS}} (\varepsilon_{qp,\nu} - \varepsilon_\nu^{KS}) \; - V_{xc} \right| \psi_\nu^{KS} \right\rangle,$$

which can be transformed as follows:

$$\begin{aligned}
\varepsilon_{qp,\nu} &= \varepsilon_\nu^{KS} + \left\langle \psi_\nu^{KS} \left|\Sigma(\varepsilon_\nu^{KS}) - V_{xc}\right| \psi_\nu^{KS}\right\rangle + \left\langle \psi_\nu^{KS} \left| \left.\frac{\partial\Sigma(\omega)}{\partial\omega}\right|_{\omega=\varepsilon_\nu^{KS}} (\varepsilon_{qp,\nu} - \varepsilon_\nu^{KS}) \right| \psi_\nu^{KS}\right\rangle \\
&= \varepsilon_\nu^{KS} + \left\langle \psi_\nu^{KS} \left|\Sigma(\varepsilon_\nu^{KS}) - V_{xc}\right| \psi_\nu^{KS}\right\rangle + \left\langle \psi_\nu^{KS} \left| \left.\frac{\partial\Sigma(\omega)}{\partial\omega}\right|_{\omega=\varepsilon_\nu^{KS}} \right| \psi_\nu^{KS}\right\rangle (\varepsilon_{qp,\nu} - \varepsilon_\nu^{KS}) \\
&= \varepsilon_\nu^{KS} + \left\langle \psi_\nu^{KS} \left|\Sigma(\varepsilon_\nu^{KS}) - V_{xc}\right| \psi_\nu^{KS}\right\rangle + \left.\frac{\partial\left\langle \psi_\nu^{KS}|\Sigma(\omega)|\psi_\nu^{KS}\right\rangle}{\partial\omega}\right|_{\omega=\varepsilon_\nu^{KS}} (\varepsilon_{qp,\nu} - \varepsilon_\nu^{KS})
\end{aligned}$$

$$\left(\varepsilon_{qp,\nu} - \varepsilon_\nu^{KS}\right) - \left(\varepsilon_{qp,\nu} - \varepsilon_\nu^{KS}\right) \left.\frac{\partial\left\langle \psi_\nu^{KS}\left|\Sigma(\omega)\right|\psi_\nu^{KS}\right\rangle}{\partial\omega}\right|_{\omega=\varepsilon_\nu^{KS}} = \left\langle \psi_\nu^{KS}\left|\Sigma(\varepsilon_\nu^{KS}) - V_{xc}\right|\psi_\nu^{KS}\right\rangle$$

$$\left(\varepsilon_{qp,\nu} - \varepsilon_\nu^{KS}\right) = \left(1 - \left.\frac{\partial \left\langle \psi_\nu^{KS} \left| \Sigma(\omega) \right| \psi_\nu^{KS} \right\rangle}{\partial \omega}\right|_{\omega=\varepsilon_\nu^{KS}}\right)^{-1} \left\langle \psi_\nu^{KS} \left| \Sigma(\varepsilon_\nu^{KS}) - V_{xc} \right| \psi_\nu^{KS} \right\rangle$$

to the final equation:

$$\varepsilon_{qp,\nu} \approx \varepsilon_\nu^{KS} + Z_\nu^{KS} \left\langle \psi_\nu^{KS} \left| \Sigma(\varepsilon_\nu^{KS}) - V_{xc} \right| \psi_\nu^{KS} \right\rangle .$$

A.5. The COHSEX formulation

We want to derive an expression for the self-energy Σ, where the latter is separated into two terms, namely the Coulomb hole Σ^{COH} and screened exchange Σ^{SEX} contribution:

$$\Sigma(\mathbf{r}, \mathbf{r}', E) = \frac{i}{2\pi} \int_{-\infty}^{\infty} d\omega \, e^{i\eta\omega} G(\mathbf{r}, \mathbf{r}', E+\omega) W\left(\mathbf{r}, \mathbf{r}', \omega\right) = \Sigma^{\mathrm{SEX}} + \Sigma^{\mathrm{COH}}.$$

For the derivation, we use the non-interacting Green's function G_0,

$$G_0(\mathbf{r}, \mathbf{r}', \omega) = \sum_l^{occ} \frac{\phi_l^*\left(\mathbf{r}'\right) \phi_l\left(\mathbf{r}\right)}{\omega - \varepsilon_l - i\eta} + \sum_m^{unocc} \frac{\phi_m^*\left(\mathbf{r}\right) \phi_m\left(\mathbf{r}'\right)}{\omega - \varepsilon_m + i\eta},$$

and the screened Coulomb potential W in its Lehmann representation:

$$W\left(\mathbf{r}, \mathbf{r}', \omega\right) = v\left(\mathbf{r}, \mathbf{r}'\right) + \sum_k \frac{2\,\varepsilon_k\, V_k\left(\mathbf{r}\right) V_k^*\left(\mathbf{r}'\right)}{\omega^2 - \left(\varepsilon_k - i\delta\right)^2} = v\left(\mathbf{r}, \mathbf{r}'\right) + \sum_k \frac{2\,\varepsilon_k\, V_k\left(\mathbf{r}\right) V_k^*\left(\mathbf{r}'\right)}{\left(\omega + \varepsilon_k - i\delta\right)\left(\omega - \varepsilon_k + i\delta\right)},$$

where δ is an infinitesimal parameter and where $V_k\left(\mathbf{r}\right)$ represents fluctuation potentials,

$$V_k\left(\mathbf{r}\right) = \int d^3\mathbf{r}' \, v\left(\mathbf{r}, \mathbf{r}'\right) \left\langle N, k \right| \hat{n}\left(\mathbf{r}'\right) \left| N, 0 \right\rangle .$$

The neutral excitation energies are given by $\varepsilon_k = E_{N,k} - E_{N,0}$, where E_N denote total energies of the N-particle system.

The self-energy integral is transformed into a complex integral following $\omega \to \bar{\omega} = \omega' + i\omega'' = R\, e^{i\varphi}$ with $R^2 = \left(\omega'\right)^2 + \left(\omega''\right)^2$ and $\varphi = \arctan\left(\frac{\omega''}{\omega'}\right)$:

$$\Sigma(\mathbf{r}, \mathbf{r}', E) =$$

$$= \tfrac{i}{2\pi} \oint_C d\bar{\omega} \sum_k e^{i\eta\bar{\omega}} \left(\sum_l^{occ} \tfrac{\phi_l^*(\mathbf{r}')\phi_l(\mathbf{r})}{E+\bar{\omega}-\varepsilon_l-i\eta} + \sum_m^{unocc} \tfrac{\phi_m^*(\mathbf{r})\phi_m(\mathbf{r}')}{E+\bar{\omega}-\varepsilon_m+i\eta}\right) \left(v\left(\mathbf{r}, \mathbf{r}'\right) + \tfrac{2\,\varepsilon_k\, V_k(\mathbf{r}) V_k^*(\mathbf{r}')}{(\bar{\omega}+\varepsilon_k-i\delta)(\bar{\omega}-\varepsilon_k+i\delta)}\right)$$
$$= \tfrac{i}{2\pi} \oint_C d\bar{\omega}\, g\left(\bar{\omega}\right).$$

This is advantageous, since complex contour integration techniques can be used. A detailed overview of the theorems used in the following can be found in Appendix A.9. The residue theorem states that a closed path integral over a function $g(z)$ with $z \in \mathbb{C}$ yields:

$$\oint_C dz\, g\left(z\right) = \begin{cases} 0, & \text{if no poles are enclosed} \\ 2\pi i \sum_i \mathrm{Res}\left(g, z_i\right) & \text{if poles at } z_i \text{ are enclosed.} \end{cases}$$

The residue $\mathrm{Res}\,(g, z_i)$ can be calculated following:

$$\mathrm{Res}\,(g, z_i) = \frac{1}{(n-1)!}\frac{d^{n-1}}{dz^{n-1}}\left[(z-z_i)^n\, g\,(z)\right]_{z=z_i}, \tag{A.23}$$

where n is the order of the pole. Expanding $g\,(\bar{\omega})$ results in:

$$\begin{aligned}
& \oint_C d\bar{\omega}\, g\,(\bar{\omega}) = \\
& \oint_C d\bar{\omega} \sum_m e^{i\eta\bar{\omega}} \left(\frac{\phi_m^*(\mathbf{r})\phi_m(\mathbf{r}')}{E+\bar{\omega}-\varepsilon_m+i\eta}\right) v\,(\mathbf{r},\mathbf{r}') \\
+ \quad & \oint_C d\bar{\omega} \sum_{m,k} e^{i\eta\bar{\omega}} \left(\frac{\phi_m^*(\mathbf{r})\phi_m(\mathbf{r}')}{E+\bar{\omega}-\varepsilon_m+i\eta}\right)\left(\frac{2\,\varepsilon_k\, V_k(\mathbf{r})V_k^*(\mathbf{r}')}{(\bar{\omega}+\varepsilon_k-i\delta)(\bar{\omega}-\varepsilon_k+i\delta)}\right) \\
+ \quad & \oint_C d\bar{\omega} \sum_l e^{i\eta\bar{\omega}} \left(\frac{\phi_l^*(\mathbf{r}')\phi_l(\mathbf{r})}{E+\bar{\omega}-\varepsilon_l-i\eta}\right) v\,(\mathbf{r},\mathbf{r}') \\
+ \quad & \oint_C d\bar{\omega} \sum_{k,l} e^{i\eta\bar{\omega}} \left(\frac{\phi_l^*(\mathbf{r}')\phi_l(\mathbf{r})}{E+\bar{\omega}-\varepsilon_l-i\eta}\right)\left(\frac{2\,\varepsilon_k\, V_k(\mathbf{r})V_k^*(\mathbf{r}')}{(\bar{\omega}+\varepsilon_k-i\delta)(\bar{\omega}-\varepsilon_k+i\delta)}\right).
\end{aligned}$$

That means we can split the problem in four subproblems, following:

$$\oint_C d\bar{\omega}\, g\,(\bar{\omega}) = \oint d\bar{\omega}\, g_1\,(\bar{\omega}) + \oint d\bar{\omega}\, g_2\,(\bar{\omega}) + \oint d\bar{\omega}\, g_3\,(\bar{\omega}) + \oint d\bar{\omega}\, g_4\,(\bar{\omega}).$$

To arrive at the COHSEX representation, the closed contour is chosen to consist of the entire real axis and a semi-circle with infinite radius R in the upper half complex plane (see Fig. A.1):

$$\oint_C d\bar{\omega}\, g\,(\bar{\omega}) = \oint_{C_1} d\bar{\omega}\, g\,(\bar{\omega}) + \oint_{C_2} d\bar{\omega}\, g\,(\bar{\omega}).$$

Since g_1 has only poles in the third and fourth quadrant, the contour encloses no poles and consequently the integral vanishes. Concerning the remaining integrals g_{2-4}, the residues have to be calculated. Corresponding to Jordan's lemma, the integral along contour C_2 vanishes for $R \to \infty$ in the case of higher order poles $n > 1$. This holds both for contours in the upper and in the lower half plane and concerns g_2 and g_4. The integrand g_3 has poles of first order, however, corresponding to Jordan's Lemma, for $\eta > 0$ the factor $e^{i\eta\bar{\omega}}$ ensures that the integral along a semi-circle in the upper half plane vanishes.[1] Consequently, one finds:

$$\oint_{upper} d\bar{\omega}\, g\,(\bar{\omega}) = \sum_k \mathrm{Res}_2\,(g_2, \bar{\omega}_k) + \sum_l \mathrm{Res}_3\,(g_3, \bar{\omega}_l) + \sum_{kl} \mathrm{Res}_4\,(g_4, \bar{\omega}_l, \bar{\omega}_k).$$

In order to arrive at the COHSEX formulation, we proceed in that way that we calculate the individual residues which are then grouped together in contributions originating from

[1] Jordan's lemma states that for a factor $e^{i\omega t}$ and $t > 0$, the semi-circle has to be in the upper half plane. For a semi-circle in the lower half plane, the integral diverges. For the same reasons, a semi-circle in the lower half plane has to be chosen for $t < 0$.

poles of G_0 and poles of W, respectively. The function g_2,

$$g_2 = \sum_{m,k} e^{i\eta\bar{\omega}} \left(\frac{\phi_m^* (\mathbf{r}) \phi_m (\mathbf{r}')}{E + \bar{\omega} - \varepsilon_m + i\eta} \right) \left(\frac{2\,\varepsilon_k\, V_k (\mathbf{r})\, V_k^* (\mathbf{r}')}{(\bar{\omega} + \varepsilon_k - i\delta)\,(\bar{\omega} - \varepsilon_k + i\delta)} \right),$$

has single poles in the upper half plane at $\bar{\omega}_k = -\varepsilon_k + i\delta$ which solely stem from the W contribution. According to equation (A.23), the residue can be calculated as follows:

$$\begin{aligned} & \textstyle\sum_k \mathrm{Res}_2 (g_2, \bar{\omega}_k) = \\ = \; & \lim_{\bar{\omega}\to\bar{\omega}_k} \textstyle\sum_{m,k} e^{i\eta\bar{\omega}} \left(\frac{\phi_m^*(\mathbf{r})\phi_m(\mathbf{r}')}{E+\bar{\omega}-\varepsilon_m+i\eta} \right) \left(\frac{2\,\varepsilon_k\, V_k(\mathbf{r}) V_k^*(\mathbf{r}')(\bar{\omega}+\varepsilon_k-i\delta)}{(\bar{\omega}+\varepsilon_k-i\delta)(\bar{\omega}-\varepsilon_k+i\delta)} \right) \\ = \; & \textstyle\sum_{m,k} e^{i\eta\bar{\omega}_k} \left(\frac{\phi_m^*(\mathbf{r})\phi_m(\mathbf{r}')}{E+\bar{\omega}_k-\varepsilon_m+i\eta} \right) \left(\frac{2\varepsilon_k\, V_k(\mathbf{r}) V_k^*(\mathbf{r}')}{-2\varepsilon_k+i2\delta} \right). \end{aligned}$$

For the third integrand g_3,

$$g_3 = \sum_l e^{i\eta\bar{\omega}} \left(\frac{\phi_l^* (\mathbf{r}') \phi_l (\mathbf{r})}{E + \bar{\omega} - \varepsilon_l - i\eta} \right) v (\mathbf{r}, \mathbf{r}'),$$

one identifies single poles at $\bar{\omega}_l = \varepsilon_l - E + i\eta$ originating from the Green's function for occupied states. The residue is:

$$\begin{aligned} & \textstyle\sum_l \mathrm{Res}_3 (g_3, \bar{\omega}_l) = \\ = \; & \lim_{\bar{\omega}\to\bar{\omega}_l} \textstyle\sum_l e^{i\eta\bar{\omega}} \left(\frac{\phi_l^*(\mathbf{r}')\phi_l(\mathbf{r})(E+\bar{\omega}-\varepsilon_l-i\eta)}{E+\bar{\omega}-\varepsilon_l-i\eta} \right) v (\mathbf{r}, \mathbf{r}') \\ = \; & \textstyle\sum_l e^{i\eta\bar{\omega}_l}\, \phi_l^* (\mathbf{r}')\, \phi_l (\mathbf{r})\; v (\mathbf{r}, \mathbf{r}'). \end{aligned}$$

The fourth integrand g_4,

$$g_4 = \sum_{k,l} e^{i\eta\bar{\omega}} \left(\frac{\phi_l^* (\mathbf{r}') \phi_l (\mathbf{r})}{E + \bar{\omega} - \varepsilon_l - i\eta} \right) \left(\frac{2\,\varepsilon_k\, V_k (\mathbf{r})\, V_k^* (\mathbf{r}')}{(\bar{\omega} + \varepsilon_k - i\delta)\,(\bar{\omega} - \varepsilon_k + i\delta)} \right),$$

includes poles in the upper half plane both at $\bar{\omega}_k = -\varepsilon_k + i\delta$ from W and at $\bar{\omega}_l = \varepsilon_l - E + i\eta$ from the Green's function:

$$\begin{aligned} & \textstyle\sum_{kl} \mathrm{Res}_4 (g_4, \bar{\omega}_{k,l}) = \\ = \; & \textstyle\sum_i \mathrm{Res} (g_4, \bar{\omega}_k) + \sum_i \mathrm{Res} (g_4, \bar{\omega}_l) \\ = \; & \lim_{\bar{\omega}\to\bar{\omega}_k} \textstyle\sum_{k,l} e^{i\eta\bar{\omega}} \left(\frac{\phi_l^*(\mathbf{r}')\phi_l(\mathbf{r})}{E+\bar{\omega}-\varepsilon_l-i\eta} \right) \left(\frac{2\,\varepsilon_k\, V_k(\mathbf{r}) V_k^*(\mathbf{r}')(\bar{\omega}+\varepsilon_k-i\delta)}{(\bar{\omega}+\varepsilon_k-i\delta)(\bar{\omega}-\varepsilon_k+i\delta)} \right) \\ & + \lim_{\bar{\omega}\to\bar{\omega}_l} \textstyle\sum_{k,l} e^{i\eta\bar{\omega}} \left(\frac{\phi_l^*(\mathbf{r}')\phi_l(\mathbf{r})(E+\bar{\omega}-\varepsilon_l-i\eta)}{E+\bar{\omega}-\varepsilon_l-i\eta} \right) \left(\frac{2\,\varepsilon_k\, V_k(\mathbf{r}) V_k^*(\mathbf{r}')}{(\bar{\omega}+\varepsilon_k-i\delta)(\bar{\omega}-\varepsilon_k+i\delta)} \right) \\ = \; & \textstyle\sum_{k,l} e^{i\eta\bar{\omega}_k} \left(\frac{\phi_l^*(\mathbf{r}')\phi_l(\mathbf{r})}{E+\bar{\omega}_k-\varepsilon_l-i\eta} \right) \left(\frac{2\varepsilon_k\, V_k(\mathbf{r}) V_k^*(\mathbf{r}')}{-2\varepsilon_k+i2\delta} \right) + \sum_{k,l} e^{i\eta\bar{\omega}_l}\, \phi_l^* (\mathbf{r}')\, \phi_l (\mathbf{r})\, \frac{2\,\varepsilon_k\, V_k(\mathbf{r}) V_k^*(\mathbf{r}')}{(\bar{\omega}_l+\varepsilon_k-i\delta)(\bar{\omega}_l-\varepsilon_k+i\delta)}. \end{aligned}$$

Having evaluated the four residues, one finds for the self-energy:

$$\begin{aligned}\Sigma(\mathbf{r},\mathbf{r}',E) &= -\sum_{m,k} e^{i\eta\bar{\omega}_k}\left(\frac{\phi_m^*(\mathbf{r})\phi_m(\mathbf{r}')}{E+\bar{\omega}_k-\varepsilon_m+i\eta}\right)\left(\frac{2\varepsilon_k V_k(\mathbf{r})V_k^*(\mathbf{r}')}{-2\varepsilon_k+i2\delta}\right)\\ &\quad -\sum_l e^{i\eta\bar{\omega}_l}\,\phi_l^*(\mathbf{r}')\,\phi_l(\mathbf{r})\; v(\mathbf{r},\mathbf{r}')\\ &\quad -\sum_{k,l} e^{i\eta\bar{\omega}_k}\left(\frac{\phi_l^*(\mathbf{r}')\phi_l(\mathbf{r})}{E+\bar{\omega}_k-\varepsilon_l-i\eta}\right)\left(\frac{2\varepsilon_k V_k(\mathbf{r})V_k^*(\mathbf{r}')}{-2\varepsilon_k+i2\delta}\right)\\ &\quad -\sum_{k,l} e^{i\eta\bar{\omega}_l}\,\phi_l^*(\mathbf{r}')\,\phi_l(\mathbf{r})\,\frac{2\,\varepsilon_k V_k(\mathbf{r})V_k^*(\mathbf{r}')}{(\bar{\omega}_l+\varepsilon_k-i\delta)(\bar{\omega}_l-\varepsilon_k+i\delta)}.\end{aligned}$$

Reordering yields:

$$\begin{aligned}&\Sigma(\mathbf{r},\mathbf{r}',E) =\\ -\;&\sum_{k,l}^{occ} e^{i\eta\bar{\omega}_l}\,\phi_l^*(\mathbf{r}')\,\phi_l(\mathbf{r})\left(v(\mathbf{r},\mathbf{r}')+\frac{2\,\varepsilon_k V_k(\mathbf{r})V_k^*(\mathbf{r}')}{(\bar{\omega}_l+\varepsilon_k-i\delta)(\bar{\omega}_l-\varepsilon_k+i\delta)}\right)\\ -\;&\sum_{k,l,m} e^{i\eta\bar{\omega}_k}\left(\frac{2\varepsilon_k V_k(\mathbf{r})V_k^*(\mathbf{r}')}{-2\varepsilon_k+i2\delta}\right)\left(\frac{\phi_m^*(\mathbf{r})\phi_m(\mathbf{r}')}{E+\bar{\omega}_k-\varepsilon_m+i\eta}+\frac{\phi_l^*(\mathbf{r}')\phi_l(\mathbf{r})}{E+\bar{\omega}_k-\varepsilon_l-i\eta}\right).\end{aligned}$$

Setting η and δ to zero, this equals:

$$\begin{aligned}&\Sigma(\mathbf{r},\mathbf{r}',E) =\\ -\;&\sum_{l}^{occ}\phi_l^*(\mathbf{r}')\,\phi_l(\mathbf{r})\; W(\mathbf{r},\mathbf{r}',E-\varepsilon_l)\\ +\;&\sum_{k,o} V_k(\mathbf{r})\,V_k^*(\mathbf{r}')\,\frac{\phi_o^*(\mathbf{r})\phi_o(\mathbf{r}')}{E+\varepsilon_k-\varepsilon_o}\\ =\;&\Sigma^{\mathrm{SEX}}+\Sigma^{\mathrm{COH}},\end{aligned}$$

where we introduced the summation index o including occupied and unoccupied states and thus combining l and m.

A.6. Calculation of the bare exchange using contour deformation techniques

In the following, we demonstrate that the bare exchange contribution of the self-energy,

$$\Sigma^x(\mathbf{r},\mathbf{r}',\tau) = iG_0(\mathbf{r},\mathbf{r}',\tau)\,v(\mathbf{r}\mathbf{r}'),$$

is equivalent to the Fock exchange in Hartree-Fock theory,

$$\langle\phi_{k,0}|\,\hat{V}_F\,|\phi_{k,0}\rangle = -\sum_n^{occ}\int d\mathbf{r}d\mathbf{r}'\,\frac{\phi_{k,0}(\mathbf{r})\,\phi_{n,0}(\mathbf{r}')\,\phi_{k,0}^*(\mathbf{r}')\,\phi_{n,0}^*(\mathbf{r})}{|\mathbf{r}-\mathbf{r}'|}.$$

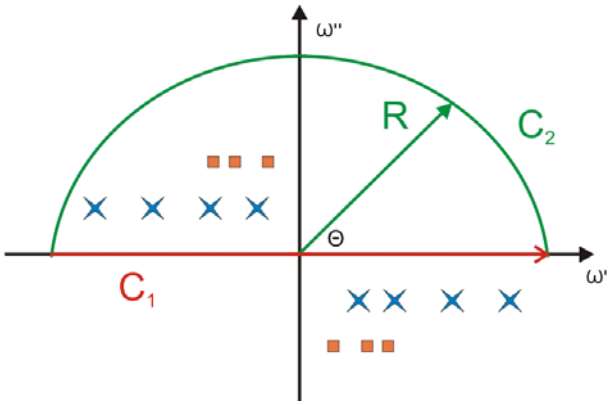

Figure A.1.: The complex integration along the contour C consists of a contour C_1 along the real axis and a semi-circle C_2. The poles of the non-interacting Green's function are at the real single-particle energies ε_l and ε_m (blue crosses), respectively. However, they are slightly shifted into the complex plane by the infinitesimal value $\pm\eta$. The poles of the screened Coulomb potential are found at the neutral excitation energies ε_k (orange squares), which are shifted by the infinitesimal value $\pm\delta$ in the complex plane. Only the poles of the Green's function for occupied states at $\bar{\omega}_l = \varepsilon_l + i\eta$ and the poles of W at $\bar{\omega}_k = -\varepsilon_k + i\delta$ are enclosed by the contour, whereas the remaining poles are not concerned.

Working in frequency space, the following integral has to be solved:

$$\Sigma^x(\mathbf{r},\mathbf{r}') = \frac{i}{2\pi} v(\mathbf{r},\mathbf{r}') \int_{-\infty}^{+\infty} d\omega\, e^{i\eta\omega} G_0(\mathbf{r},\mathbf{r}',\omega).$$

According to analytic continuation, we change to the complex plane ($\omega \to \bar{\omega} = \omega' + i\omega''$) and evaluate the complex integral

$$\Sigma^x(\mathbf{r},\mathbf{r}') = \frac{i}{2\pi} v\left(\mathbf{r},\mathbf{r}'\right) \oint_C d\bar{\omega}\, e^{i\eta\bar{\omega}} G_0(\mathbf{r},\mathbf{r}',\bar{\omega})$$

using contour deformation techniques. The contour C is chosen like depicted in figure (A.2), where the radius of the semi-circle R goes to infinity. Inserting the non-interacting Green's function G_0,

$$G_0(\mathbf{r},\mathbf{r}',\bar{\omega}) = \sum_l^{occ} \frac{\phi_l^*\left(\mathbf{r}'\right)\phi_l\left(\mathbf{r}\right)}{\bar{\omega} - \varepsilon_l - i\eta} + \sum_m^{unocc} \frac{\phi_m^*\left(\mathbf{r}\right)\phi_m\left(\mathbf{r}'\right)}{\bar{\omega} - \varepsilon_m + i\eta},$$

where η is an infinitesimal parameter, the pole structure of Σ^x can be evaluated. The latter has poles in the complex plane both at $\bar{\omega}_l = \varepsilon_l + i\eta$ and $\bar{\omega}_m = \varepsilon_m - i\eta$, however, only poles $\bar{\omega}_l$ for occupied states are enclosed by the contour. Using the same contour deformation rules

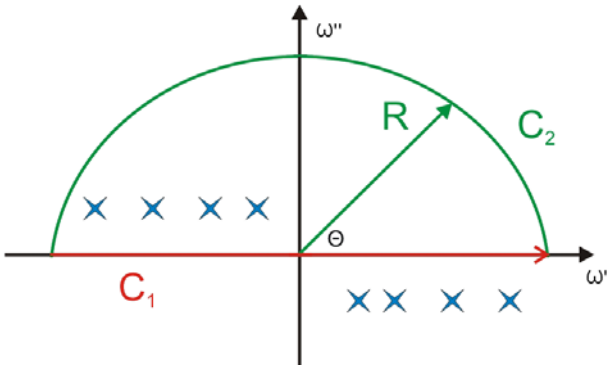

Figure A.2.: The complex integral is carried out along the contour C, which decomposes into an integration along C_1 and C_2. The poles of the Green's function are at the real excitation energies ε_m (blue crosses), however, they are slightly shifted into the complex plane by the infinitesimal value $\pm\eta$. Only the poles of the Green's function for occupied states at $\bar{\omega}_l = \varepsilon_l + i\eta$ are enclosed by the contour, whereas the poles for unoccupied states at $\bar{\omega}_m = \varepsilon_m - i\eta$ are outside.

as presented in the preceding section and in Appendix A.9, results in:

$$\begin{aligned}
\Sigma^x(\mathbf{r},\mathbf{r}') &= \tfrac{i}{2\pi} v(\mathbf{r},\mathbf{r}') \oint_C d\bar{\omega}\, e^{i\eta\bar{\omega}} G_0(\mathbf{r},\mathbf{r}',\bar{\omega}) \\
&= \tfrac{i}{2\pi} v(\mathbf{r},\mathbf{r}') \left[\int_{C_1} d\bar{\omega}\, e^{i\eta\bar{\omega}} G_0(\mathbf{r},\mathbf{r}',\bar{\omega}) + \int_{C_2} d\bar{\omega}\, e^{i\eta\bar{\omega}} G_0(\mathbf{r},\mathbf{r}',\bar{\omega}) \right] \\
&= \tfrac{i}{2\pi} v(\mathbf{r},\mathbf{r}') \cdot 2\pi i \sum_{\bar{\omega}_l} Res(G_0,\bar{\omega}_l) .
\end{aligned}$$

Corresponding to Jordan's lemma, the factor $e^{i\eta\bar{\omega}}$ ensures that integral along contour C_2 vanishes for $R \to \infty$. Consequently, one obtains:

$$\int_{C_1} d\bar{\omega}\, e^{i\eta\bar{\omega}} G_0(\mathbf{r},\mathbf{r}',\bar{\omega}) = 2\pi i \sum_{\bar{\omega}_l} Res(G_0,\bar{\omega}_l) .$$

Following equation (A.23), the residues of G_0 are calculated to:

$$\sum_{\bar{\omega}_l} Res(G_0,\bar{\omega}_l) = \sum_l \phi_l^*(\mathbf{r})\,\phi_l(\mathbf{r}') ,$$

where $\eta \to 0$. Finally, taking the expectation value of Σ^x with single-particle states $\phi_{k,0}$, one obtains:

$$\langle \phi_{k,0} | \Sigma^x | \phi_{k,0} \rangle = -\sum_l^{occ} \int d\mathbf{r} d\mathbf{r}' \, \frac{\phi_{k,0}(\mathbf{r})\,\phi_{l,0}(\mathbf{r}')\,\phi_{k,0}^*(\mathbf{r}')\,\phi_{l,0}^*(\mathbf{r})}{|\mathbf{r}-\mathbf{r}'|},$$

where $v(\mathbf{r},\mathbf{r}') = \frac{1}{|\mathbf{r}-\mathbf{r}'|}$ has been inserted. This is nothing else than the bare Fock exchange from Hartree-Fock theory.

A.7. Lehmann representation of the irreducible polarizability

In the following, the Lehmann representation for the irreducible polarizability $P\,(12)$ within *GW-RPA* is derived. In principle, P is a two-point quantity, however, we calculate with its four-point extension in order to draw direct conclusions for the quasi-independent-particle (QIP) polarizability:

$$L_{QIP}\left(1,2;1',2'\right) \equiv G\left(1,2'\right) G\left(2,1'\right).$$

The latter describes the independent propagation of an electron and its hole via the time-ordered one-particle Green's functions G. The notation "quasi-independent" refers to the fact that the two particles indeed propagate without interacting with each other, however, both are quasi-particles and interact with the surrounding medium. The independent-particle quantity L_{IP} can be obtained by inserting G_1^0 instead of G into the above equation:

$$L_{IP} \equiv G_1^0\left(1,2'\right) G_1^0\left(2,1'\right).$$

To come back to the actual problem, P^{GW} reads:

$$P^{GW}\left(\mathbf{r}_1,\mathbf{r}_2;\mathbf{r}_1^{'},\mathbf{r}_2^{'};t_1-t_2^{'};t_2-t_1^{'}\right) \equiv -iG\left(\mathbf{r}_1,\mathbf{r}_2^{'},t_1-t_2^{'}\right) G\left(\mathbf{r}_2,\mathbf{r}_1^{'},t_2-t_1^{'}\right).$$

Assuming that the electron and the hole propagate simultaneously, we set $t_1 = t_1^{'}$ and $t_2^{'} = t_2$. This yields:

$$P^{GW}\left(\mathbf{r}_1,\mathbf{r}_2;\mathbf{r}_1^{'},\mathbf{r}_2^{'};\tau\right) \equiv -iG\left(\mathbf{r}_1,\mathbf{r}_2^{'},\tau\right) G\left(\mathbf{r}_2,\mathbf{r}_1^{'},-\tau\right),$$

where $\tau = t_1 - t_2^{'}$. To derive the Lehmann representation, i.e. in order to express it in the basis spanned by the eigenfunctions of the Hamiltonian operator, we start by a Fourier transformation to frequency space. Further, we make use of the convolution theorem,

$$\begin{aligned} F\left(t\right) &= g_1\left(t\right) g_2\left(t\right) \\ F\left(E\right) &= \tfrac{1}{2\pi}\left[g_1 \star g_2\right]\left(E\right) = \tfrac{1}{2\pi}\int d\omega\, g_1\left(E-\omega\right) g_2\left(\omega\right), \end{aligned}$$

which states that the Fourier transform of a product of two functions is given by the convolution in Fourier space. Applied to P^{GW} we obtain:

$$P^{GW}\left(\mathbf{r}_1,\mathbf{r}_2;\mathbf{r}_1^{'},\mathbf{r}_2^{'};E\right) = -\frac{i}{2\pi}\int d\omega\, G\left(E+\omega\right) G\left(\omega\right).$$

Inserting the one-particle Green's function in its Lehmann representation gives:

$$\begin{aligned} P^{GW} &= -\tfrac{i}{2\pi}\textstyle\sum_{m,l}\int_{-\infty}^{\infty} d\omega \left(\frac{f_m(\mathbf{r}_1)f_m^*\left(\mathbf{r}_2^{'}\right)}{E+\omega-\varepsilon_m-i\eta} + \frac{f_l(\mathbf{r}_1)f_l^*\left(\mathbf{r}_2^{'}\right)}{E+\omega-\varepsilon_l+i\eta}\right)\left(\frac{f_m(\mathbf{r}_2)f_m^*\left(\mathbf{r}_1^{'}\right)}{\omega-\varepsilon_m-i\eta} + \frac{f_l(\mathbf{r}_2)f_l^*\left(\mathbf{r}_1^{'}\right)}{\omega-\varepsilon_l+i\eta}\right). \\ &= -\tfrac{i}{2\pi}\textstyle\sum_{m,l}\int_{-\infty}^{\infty} d\omega\, I\left(\mathbf{r}_1,\mathbf{r}_2;\mathbf{r}_1^{'},\mathbf{r}_2^{'};\omega\right). \end{aligned}$$

The integral can be solved by going to the complex plane according to analytic continuation ($\omega \to \bar{\omega} = \omega' + i\omega''$, $R = \sqrt{\left(\omega'\right)^2 + \left(\omega''\right)^2}$). As a consequence, a closed integral in the complex plane has to be evaluated using complex contour deformation theory. A detailed overview of

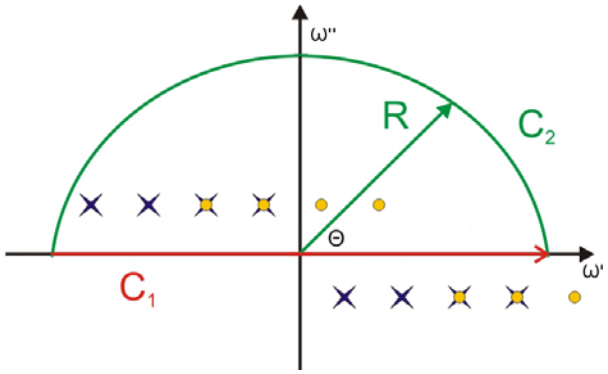

Figure A.3.: The complex integral is carried out along the contour C, which decomposes into an integration along C_1 and C_2. The poles of one Green's function occur at $\omega = \varepsilon_{m,l} \pm i\eta$ (blue crosses), while the poles of the other one (yellow dots) are at $\omega = \varepsilon_{m,l} - E \pm i\eta$. Only the poles for occupied states at $\bar{\omega}_1 = \varepsilon_{m1} + i\eta$ and $\bar{\omega}_2 = \varepsilon_{m2} - E + i\eta$ are enclosed by the contour, whereas the poles for unoccupied states are outlying.

the theorems used in the following can be found in Appendix A.9.

Expanding $I(\bar{\omega})$ results in:

$$\begin{aligned} I(\bar{\omega}) &= \left(\frac{f_m(\mathbf{r}_1)f_m^*(\mathbf{r}'_2)}{E+\bar{\omega}-\varepsilon_{m1}-i\eta}\right)\left(\frac{f_m(\mathbf{r}_2)f_m^*(\mathbf{r}'_1)}{\bar{\omega}-\varepsilon_{m2}-i\eta}\right) + \left(\frac{f_l(\mathbf{r}_1)f_l^*(\mathbf{r}'_2)}{E+\bar{\omega}-\varepsilon_{l1}+i\eta}\right)\left(\frac{f_m(\mathbf{r}_2)f_m^*(\mathbf{r}'_1)}{\bar{\omega}-\varepsilon_{m2}-i\eta}\right) \\ &\quad + \left(\frac{f_m(\mathbf{r}_1)f_m^*(\mathbf{r}'_2)}{E+\bar{\omega}-\varepsilon_{m1}-i\eta}\right)\left(\frac{f_l(\mathbf{r}_2)f_l^*(\mathbf{r}'_1)}{\bar{\omega}-\varepsilon_{l2}+i\eta}\right) + \left(\frac{f_l(\mathbf{r}_1)f_l^*(\mathbf{r}'_2)}{E+\bar{\omega}-\varepsilon_{l1}+i\eta}\right)\left(\frac{f_l(\mathbf{r}_2)f_l^*(\mathbf{r}'_1)}{\bar{\omega}-\varepsilon_{l2}+i\eta}\right) \\ &= I_1 + I_2 + I_3 + I_4. \end{aligned}$$

That implies that for each of the four summands, a closed integral has to be solved:

$$\oint_C d\bar{\omega}\, I(\bar{\omega}) = \sum_{i=1}^{4} \oint_C d\bar{\omega}\, I_i(\bar{\omega}).$$

The residue theorem states that a closed integral gives either zero, if no poles of the function are enclosed, or yields $2\pi i \sum_j \mathrm{Res}(I, \bar{\omega}_j)$ in the case when poles $\bar{\omega}_j$ of order n are contained. The closed contour C is chosen to consist of the entire real axis and a semi-circle in the upper half plane (see Fig. (A.2)) or a semi-circle in the lower half plane. Corresponding to Jordan's lemma, the integral along the semi-circle vanishes for $R \to \infty$ for higher order poles $n > 1$, both for contours in the upper and in the lower half plane. Since the above summands I_i only show higher order poles, one can freely choose either an integration in the upper or in lower half plane and one obtains:

$$\oint_C d\bar{\omega}\, I_{2,3}(\bar{\omega}) = \int_{-\infty}^{\infty} d\omega'\, I_{2,3}(\omega').$$

The choice of the contour depends on the position of the poles and one tries to avoid including the latter into the contour. Since I_1 and I_4 only have poles either in the upper or in the lower half plane, one can choose the path correspondingly, resulting in vanishing integrals. However,

since I_2 and I_3 have poles both in the upper and in the lower half plane, the residues have to be calculated:

$$\oint_C d\bar{\omega}\, I_{2,3}\left(\bar{\omega}\right) = \int_{-\infty}^{\infty} d\omega'\, I_{2,3}\left(\omega'\right) = 2\pi i \sum_j \mathrm{Res}\left(I_{2,3}, \bar{\omega}_j\right).$$

The latter can be obtained by solving:

$$\mathrm{Res}\left(I_{2,3}, \bar{\omega}_j\right) = \frac{1}{(n-1)!} \frac{d^{n-1}}{d\bar{\omega}^{n-1}} \left[\left(\bar{\omega} - \bar{\omega}_j\right)^n f\left(\bar{\omega}\right)\right]_{\bar{\omega}=\bar{\omega}_j}.$$

Choosing a semi-circle in the upper half plane, poles at $\bar{\omega}_{m2} = \varepsilon_{m2} + i\eta$ are enclosed for I_2. This yields for the residue:

$$\begin{aligned} Res\left(I_2, \bar{\omega}_{m2}\right) &= \frac{f_l(\mathbf{r}_1) f_l^*\left(\mathbf{r}_2'\right) f_m(\mathbf{r}_2) f_m^*\left(\mathbf{r}_1'\right)}{E + \bar{\omega}_{m2} - \varepsilon_{l1} + i\eta} \\ &= \frac{f_l(\mathbf{r}_1) f_l^*\left(\mathbf{r}_2'\right) f_m(\mathbf{r}_2) f_m^*\left(\mathbf{r}_1'\right)}{E + \varepsilon_{m2} + i\eta - \varepsilon_{l1} + i\eta} \\ &= \frac{f_l(\mathbf{r}_1) f_l^*\left(\mathbf{r}_2'\right) f_m(\mathbf{r}_2) f_m^*\left(\mathbf{r}_1'\right)}{E - (\varepsilon_{l1} - \varepsilon_{m2}) + 2i\eta}. \end{aligned}$$

For I_3, poles at $\bar{\omega}_{m1} = -E + \varepsilon_{m1} + i\eta$ are enclosed by a contour in the upper half plane, leading to:

$$\begin{aligned} Res\left(I_3, \bar{\omega}_{m1}\right) &= \frac{f_m(\mathbf{r}_1) f_m^*\left(\mathbf{r}_2'\right) f_l(\mathbf{r}_2) f_l^*\left(\mathbf{r}_1'\right)}{\bar{\omega}_{m1} - \varepsilon_{l2} + i\eta} \\ &= \frac{f_m(\mathbf{r}_1) f_m^*\left(\mathbf{r}_2'\right) f_l(\mathbf{r}_2) f_l^*\left(\mathbf{r}_1'\right)}{-E + \varepsilon_{m1} + i\eta - \varepsilon_{l2} + i\eta} \\ &= -\frac{f_m(\mathbf{r}_1) f_m^*\left(\mathbf{r}_2'\right) f_l(\mathbf{r}_2) f_l^*\left(\mathbf{r}_1'\right)}{E + (\varepsilon_{l2} - \varepsilon_{m1}) - 2i\eta}. \end{aligned}$$

Combining the obtained results leads to:

$$\begin{aligned} P^{GW}\left(\mathbf{r}_1, \mathbf{r}_2; \mathbf{r}_1', \mathbf{r}_2'; E\right) &= -2\pi i \tfrac{i}{2\pi} \textstyle\sum_{m,l} \frac{f_l(\mathbf{r}_1) f_l^*\left(\mathbf{r}_2'\right) f_m(\mathbf{r}_2) f_m^*\left(\mathbf{r}_1'\right)}{E - (\varepsilon_l - \varepsilon_m) + i\eta} - \frac{f_m(\mathbf{r}_1) f_m^*\left(\mathbf{r}_2'\right) f_l(\mathbf{r}_2) f_l^*\left(\mathbf{r}_1'\right)}{E + (\varepsilon_l - \varepsilon_m) - i\eta} \\ &= \textstyle\sum_{m,l} \frac{f_l(\mathbf{r}_1) f_l^*\left(\mathbf{r}_2'\right) f_m(\mathbf{r}_2) f_m^*\left(\mathbf{r}_1'\right)}{E - (\varepsilon_l - \varepsilon_m) + i\eta} - \frac{f_m(\mathbf{r}_1) f_m^*\left(\mathbf{r}_2'\right) f_l(\mathbf{r}_2) f_l^*\left(\mathbf{r}_1'\right)}{E + (\varepsilon_l - \varepsilon_m) - i\eta}, \end{aligned} \tag{A.24}$$

where we set $\varepsilon_{l1} = \varepsilon_{l2}$ and $\varepsilon_{m1} = \varepsilon_{m2}$, because the discrimination had only been introduced for the sake of clarity in the derivation.

From this result, the two-point irreducible polarizability within *GW-RPA* can be contracted:

$$P^{GW}\left(\mathbf{r}_1, \mathbf{r}_2; E\right) = \sum_{m,l} \frac{f_l\left(\mathbf{r}_1\right) f_l^*\left(\mathbf{r}_2\right) f_m\left(\mathbf{r}_2\right) f_m^*\left(\mathbf{r}_1\right)}{E - \left(\varepsilon_l - \varepsilon_m\right) + i\eta} - \frac{f_m\left(\mathbf{r}_1\right) f_m^*\left(\mathbf{r}_2\right) f_l\left(\mathbf{r}_2\right) f_l^*\left(\mathbf{r}_1\right)}{E + \left(\varepsilon_l - \varepsilon_m\right) - i\eta}.$$

Moreover, the Lehmann representation of P within the *RPA* can be readily deduced by replacing the Lehmann amplitudes $f_{m,l}$ and the excitation energies $\varepsilon_{m,l}$ by single-particle wave functions $\phi_{m,l}$ and energies $\varepsilon^0_{m,l}$:

$$P^{RPA}\left(\mathbf{r}_1, \mathbf{r}_2; E\right) = \sum_{m,l} \frac{\phi_l\left(\mathbf{r}_1\right) \phi_l^*\left(\mathbf{r}_2\right) \phi_m\left(\mathbf{r}_2\right) \phi_m^*\left(\mathbf{r}_1\right)}{E - \left(\varepsilon_l^0 - \varepsilon_m^0\right) + i\eta} - \frac{\phi_m\left(\mathbf{r}_1\right) \phi_m^*\left(\mathbf{r}_2\right) \phi_l\left(\mathbf{r}_2\right) \phi_l^*\left(\mathbf{r}_1\right)}{E + \left(\varepsilon_l^0 - \varepsilon_m^0\right) - i\eta}.$$

Furthermore, from equation (A.24), the quasi-independent-particle polarizability L_{QIP} as

needed for the Bethe-Salpeter equation can be readily obtained in its Lehmann representation by:

$$\begin{aligned} L_{QIP}\left(1,2;1',2';\tau\right) &= G\left(1,2';\tau\right)G\left(2,1';-\tau\right) = iP^{GW}\left(1,2;1',2';\tau\right) \\ L_{QIP}\left(\mathbf{r}_1,\mathbf{r}_2;\mathbf{r}_1',\mathbf{r}_2';E\right) &= iP^{GW}\left(\mathbf{r}_1,\mathbf{r}_2;\mathbf{r}_1',\mathbf{r}_2';E\right) \\ &= i\sum_{m,l}\frac{f_l(\mathbf{r}_1)f_l^*\left(\mathbf{r}_2'\right)f_m(\mathbf{r}_2)f_m^*\left(\mathbf{r}_1'\right)}{E-(\varepsilon_l-\varepsilon_m)+i\eta} - \frac{f_m(\mathbf{r}_1)f_m^*\left(\mathbf{r}_2'\right)f_l(\mathbf{r}_2)f_l^*\left(\mathbf{r}_1'\right)}{E+(\varepsilon_l-\varepsilon_m)-i\eta}. \end{aligned}$$

A.8. The Bethe-Salpeter equations

Derivation of the Bethe-Salpeter equation for L In order to account for excitonic effects in optical absorption, we introduce the two-particle correlation function L:

$$L(1,\mathbf{x}'t;2,\mathbf{x}t^+) = -G_2(1,\mathbf{x}'t;2,\mathbf{x}t^+) + G_1(1,2)G_1(\mathbf{x}'t,\mathbf{x}t^+),$$

which contains both the independent propagation of two particles through the one-particle Green's functions G_1 and their coupled motion through the two-particle Green's function G_2. From equation (A.6), we directly find:

$$L(1,\mathbf{x}'t;2,\mathbf{x}t^+) = \frac{\partial G_1\left(1,2\right)}{\partial U_{ext}\left(\mathbf{x},\mathbf{x}',t\right)}.$$

Using relation (A.3) yields:

$$L(1,\mathbf{x}'t;2,\mathbf{x}t^+) \;=\; -\int d3d4\, G_1\left(1,3\right)\frac{\partial G_1^{-1}(3,4)}{\partial U_{ext}(\mathbf{x},\mathbf{x}',t)}G_1\left(4,2\right).$$

From the Dyson equation:

$$G_1 = G_1^0 + G_1^0\left(M+U_{ext}\right)G_1,$$

where M is the mass operator containing all possible interactions and where G_1^0 is the one-particle Green's function for a system of non-interacting particles, we obtain:

$$G_1^{-1} = \left(G_1^0\right)^{-1} - \left(M+U_{ext}\right).$$

Inserting this in the equation for L gives:

$$\begin{aligned} & L(1,\mathbf{x}'t;2,\mathbf{x}t^+) = \\ = \;& -\int d3d4\, G_1\left(1,3\right)\left[\frac{\partial\left(G_1^0(3,4)\right)^{-1}}{\partial U_{ext}(\mathbf{x},\mathbf{x}',t)} - \frac{\partial M(3,4)}{\partial U_{ext}(\mathbf{x},\mathbf{x}',t)} - \frac{\partial U_{ext}(3,4)}{\partial U_{ext}(\mathbf{x},\mathbf{x}',t)}\right]G_1\left(4,2\right) \\ = \;& -\int d3d4\, G_1\left(1,3\right)\left[-\frac{\partial M(3,4)}{\partial U_{ext}(\mathbf{x},\mathbf{x}',t)} - \delta\left(\mathbf{x},\mathbf{x}_3\right)\delta\left(\mathbf{x}_4,\mathbf{x}'\right)\delta\left(t_3,t_4\right)\delta\left(t_4,t\right)\right]G_1\left(4,2\right) \\ = \;& \int d3456\, G_1\left(1,3\right)\frac{\partial M(3,4)}{\partial G_1(5,6)}\frac{\partial G_1(5,6)}{\partial U_{ext}(\mathbf{x},\mathbf{x}',t)}G_1\left(4,2\right) \\ & + \int d3d4\, G_1\left(1,3\right)\delta\left(\mathbf{x},\mathbf{x}_3\right)\delta\left(\mathbf{x}_4,\mathbf{x}'\right)\delta\left(t_3,t_4\right)\delta\left(t_4,t\right)G_1\left(4,2\right), \end{aligned}$$

where we applied the chain rule (A.2) for the derivation of M with respect to the external potential and where

$$\frac{\partial U_{ext}\left(3,4\right)}{\partial U_{ext}\left(\mathbf{x},\mathbf{x}',t\right)}=\delta\left(\mathbf{x},\mathbf{x}_3\right)\delta\left(\mathbf{x}_4,\mathbf{x}'\right)\delta\left(t_3,t_4\right)\delta\left(t_4,t\right)$$

and

$$\frac{\partial\left(G_1^0\left(3,4\right)\right)^{-1}}{\partial U_{ext}\left(\mathbf{x},\mathbf{x}',t\right)}=0,$$

since G_1^0 governs only unperturbed non-interacting systems with $h_0\left(\mathbf{r}\right)=-\frac{1}{2}\nabla^2+V_{ion}\left(\mathbf{r}\right)$. Simplifying the obtained equation even further, we finally arrive at a Dyson-like equation for L,

$$L(1,\mathbf{x}'t;2,\mathbf{x}t^+)=G_1\left(1,\mathbf{x}t\right)G_1\left(\mathbf{x}'t,2\right)+\int d3456\,G_1\left(1,3\right)G_1\left(4,2\right)\frac{\partial M\left(3,4\right)}{\partial G_1\left(5,6\right)}L(6,\mathbf{x}'t;5,\mathbf{x}t^+),$$

where the two-particle propagation is described by both the propagation of two quasi-independent particles and their motion coupled by an effective two-particle interaction, the so-called kernel K:

$$K\equiv\frac{\partial M\left(3,4\right)}{\partial G_1\left(5,6\right)}.$$

The Dyson-like equation for L has to be valid for arbitrary external time variables t and t', resulting in a compact notation:

$$L(1,2;1',2')=G_1\left(1,2'\right)G_1\left(2,1'\right)+\int d3456\,G_1\left(1,3\right)G_1\left(4,1'\right)\,K\left(3,5;4,6\right)\,L(6,2;5,2'),\tag{A.25}$$

which is known as the *Bethe-Salpeter equation for* L [2, 42, 43, 117, 118, 119]. Once the Bethe-Salpeter equation is solved, L is hence contracted to χ following $\chi\left(1,2\right)=-iL\left(1,2;1,2\right)$. This yields:

$$\begin{aligned}-iL(1,2;1,2) &= -iG_1\left(1,2\right)G_1\left(2,1\right)\\ &\quad+\int d3456\,\left[-iG_1\left(1,4\right)G_1\left(4,1\right)\right]\,iK\left(3,5;4,6\right)\left[-iL(6,2;6,2)\right]\\ \chi\left(1,2\right) &= P^{GW}\left(1,2\right)+\int d3456\,P^{GW}\left(1,4\right)\,iK\left(3,5;4,6\right)\,\chi\left(6,2\right),\end{aligned}\tag{A.26}$$

where $P^{GW}\left(1,2\right)=-iG_1\left(1,2\right)G_1\left(2,1\right)$.

Reducible and irreducible quantities In order to single out the Coulomb term from the effective two-particle interaction K, we split the mass operator into the Hartree term and the self-energy Σ:

$$M=V_H+\Sigma,$$

with $V_H(1,2) = \delta(1,2)\left[-i\int d3\, v(1,3)\, G_1(3,3^+)\right]$. Inserting this into the kernel K gives:

$$\begin{aligned} K &= \frac{\partial\Sigma(3,4)}{\partial G_1(5,6)} + \frac{\partial V_H(3,4)}{\partial G_1(5,6)} \\ &= \frac{\partial\Sigma(3,4)}{\partial G_1(5,6)} - i\delta(3,4)\int d7\, v(3,7)\, \frac{\partial G_1\left(7,7^+\right)}{\partial G_1(5,6)} \\ &= \frac{\partial\Sigma(3,4)}{\partial G_1(5,6)} - i\delta(3,4)\,\delta(5,6)\, v(3,5)\,. \end{aligned}$$

That means we can separate the kernel K into the Hartree term $K_H = -i\delta(3,4)\,\delta(5,6)\,v(3,5)$ and the remainder $K_R = \frac{\partial\Sigma(3,4)}{\partial G_1(5,6)}$. This splitting can be used to define the irreducible quantity $\tilde{L}$, which obeys:

$$\tilde{L}(1,2;1',2') = G_1\left(1,2'\right) G_1\left(2,1'\right) + \int d3456\, G_1(1,3)\, G_1\left(4,1'\right)\, K_R(3,5;4,6)\, \tilde{L}(6,2;5,2').$$

Having solved the integral equation for $\tilde{L}$, the reducible L can be obtained via:

$$L(1,2;1',2') = \tilde{L}(1,2;1',2') + \int d3456\, \tilde{L}(1,4;1',3)\, K_H(3,5;4,6)\, L(6,2;5,2').$$

The choice of the kernel So far, the kernel K accounts for all correlations and is hence a very complicated object. A possible simplification consists of approximating the self-energy Σ by its bare exchange part Σ^x:

$$\Sigma \approx \Sigma^x = iG(1,2,\tau)\, v(1,2)\,.$$

For the kernel, we thus have:

$$\begin{aligned} K^{TDHF}(3,5;4,6) &= \frac{\partial\Sigma^x(3,4)}{\partial G_1(5,6)} - i\delta(3,4)\,\delta(5,6)\, v(3,5) \\ &= i\frac{\partial G(3,4)}{\partial G_1(5,6)} v(3,4) - i\delta(3,4)\,\delta(5,6)\, v(3,5) \\ &= i\,\delta(3,5)\delta(4,6)\, v(3,4) - i\delta(3,4)\,\delta(5,6)\, v(3,5)\,. \end{aligned}$$

Inserting this into the Bethe-Salpeter equation yields:

$$L^{TDHF}(1,2;1',2') =$$

$$\begin{aligned} &= G_1(1,2')\, G_1(2,1') \\ &\quad + \int d3456\, G_1(1,3)\, G_1(4,1')\, \left[i\delta(3,5)\delta(4,6)\, v(3,4) - i\delta(3,4)\,\delta(5,6)\, v(3,5)\right] L(6,2;5,2') \\ &= G_1(1,2')\, G_1(2,1') \\ &\quad + i\int d56\, G_1(1,5)\, G_1(6,1')\, v(5,6)\, L(6,2;5,2') - i\int d46\, G_1(1,4)\, G_1(4,1')\, v(4,6)\, L(6,2;6,2'), \end{aligned}$$

which represents a time-dependent Hartree-Fock approach. The first summand accounts for the bare or Hartree-Fock exchange and the second for the classical Hartree contribution. Correlation is not taken into account.

Another approach, accounting also for screening effects, is to use the already introduced

GW approximation for Σ. For the kernel we thus get:

$$\begin{aligned} K^{TDSHF}(3,5;4,6) &= \frac{\partial \Sigma^{GW}(3,4)}{\partial G_1(5,6)} - i\delta(3,4)\,\delta(5,6)\,v(3,5) \\ &= \frac{\partial iG(3,4)W(3,4)}{\partial G_1(5,6)} - i\delta(3,4)\,\delta(5,6)\,v(3,5)\,. \end{aligned}$$

Applying the product rule (A.1), yields:

$$\begin{aligned} K^{TDSHF}(3,5;4,6) &= i\frac{\partial G_1(3,4)}{\partial G_1(5,6)}W(3,4) + iG_1(3,4)\frac{\partial W(3,4)}{\partial G_1(5,6)} - i\delta(3,4)\,\delta(5,6)\,v(3,5) \\ &\approx i\delta(3,5)\,\delta(4,6)\,W(3,4) - i\delta(3,4)\,\delta(5,6)\,v(3,5)\,, \end{aligned}$$

where - in addition to the GW approximation for the self-energy - we further neglected the dependence of the screened Coulomb potential on the propagation of the particle. Inserted into the Bethe-Salpeter equation,

$$\begin{aligned} & L^{TDSHF}(1,2;1',2') = \\ &= G_1(1,2')\,G_1(2,1') + \\ &\quad + \int d3456\, G_1(1,3)\,G_1(4,1')\left[i\delta(3,5)\,\delta(4,6)\,W(3,4) - i\delta(3,4)\,\delta(5,6)\,v(3,5)\right] L(6,2;5,2') \\ &= G_1(1,2')\,G_1(2,1') + \\ &\quad + i\int d56\, G_1(1,5)\,G_1(6,1')\; W(5,6)\; L(6,2;5,2') - i\int d46\, G_1(1,4)\,G_1(4,1')\,v(4,6)\,L(6,2;6,2') \\ &= L_{QIP}(121'2') + \\ &\quad + i\int d56\, L_{QIP}(161'5)\,W(5,6)\; L(6,2;5,2') - i\int d56\, L_{QIP}(151'5)\,v(5,6)\,L(6,2;6,2'), \end{aligned} \tag{A.27}$$

it is clear that we deal in this case with a time-dependent *screened* Hartree-Fock approach. The first summand accounts for the dynamical screened exchange, while the second term represents the Hartree contribution.

Fourier transformation to frequency space and the static approximation Since L is a four-point quantity, in principle it depends on four different time arguments. However, the Coulomb potential v is instantaneous,

$$v(1,2) = v(\mathbf{x}_1\mathbf{x}_2)\,\delta(t_1 - t_2)\,,$$

and also the one-particle Green's functions in equation (A.27) only depend on time differences. This suggests that the time arguments can be contracted to a single one in order to permit a straightforward Fourier transformation to frequency space. However, this is not possible without further ado and approximations are implied. First, one assumes translational time invariance and an isochronous propagation of the electron and the hole. [2] In addition, the dynamically screened interaction W is approximated within its static limit:

$$W(1,2) \approx W_{stat}(\mathbf{x}_1\mathbf{x}_2)\,\delta(t_1 - t_2)\,.$$

[2] For $L = L(1234)$, i.e. $L = L(t_1 - t_4; t_2 - t_3)$, we set $t_1 = t_3; t_2 = t_4$.

This significantly simplifies equation (A.27):

$$\begin{aligned}
& L\left(t_1 - t_2^{'}; t_2 - t_1^{'}\right) = \\
= \; & L_{QIP}\left(t_1 - t_2^{'}; t_2 - t_1^{'}\right) \\
& + i \int dt_3 t_4 \, L_{QIP}\left(t_1 - t_3; t_4 - t_1^{'}\right) W_{stat}\left(\mathbf{x}_3\mathbf{x}_4\right) \delta\left(t_3 - t_4\right) L\left(t_4 - t_2^{'}; t_2 - t_3\right) \\
& - i \int dt_3 t_4 \, L_{QIP}\left(t_1 - t_3, t_3 - t_1^{'}\right) v\left(\mathbf{x}_3\mathbf{x}_4\right) \delta\left(t_3 - t_4\right) L(t_4 - t_2^{'}, t_2 - t_4) \\
= \; & L_{QIP}\left(t_1 - t_2^{'}; t_2 - t_1^{'}\right) \\
& + i \int dt_4 \, L_{QIP}\left(t_1 - t_4; t_4 - t_1^{'}\right) W_{stat}\left(\mathbf{x}_3\mathbf{x}_4\right) L\left(t_4 - t_2^{'}; t_2 - t_4\right) \\
& - i \int dt_4 \, L_{QIP}\left(t_1 - t_4, t_4 - t_1^{'}\right) v\left(\mathbf{x}_3\mathbf{x}_4\right) L(t_4 - t_2^{'}, t_2 - t_4)
\end{aligned}$$

$$\begin{aligned}
& L\left(t_1 - t_2^{'}; t_2^{'} - t_1\right) = \\
= \; & L_{QIP}\left(t_1 - t_2^{'}; t_2^{'} - t_1\right) \\
& + i \int dt_4 \, L_{QIP}\left(t_1 - t_4; t_4 - t_1\right) W_{stat}\left(\mathbf{x}_3\mathbf{x}_4\right) L\left(t_4 - t_2^{'}; t_2^{'} - t_4\right) \\
& - i \int dt_4 \, L_{QIP}\left(t_1 - t_4, t_4 - t_1\right) v\left(\mathbf{x}_3\mathbf{x}_4\right) L(t_4 - t_2^{'}, t_2^{'} - t_4) \\
= \; & L_{QIP}\left(\tau; -\tau\right) \\
& + i \int d\tau' \, L_{QIP}\left(-\tau'; \tau'\right) W_{stat}\left(\mathbf{x}_3\mathbf{x}_4\right) L\left(\tau' + \tau; -\tau' - \tau\right) \\
& - i \int d\tau' \, L_{QIP}\left(-\tau'; \tau'\right) v\left(\mathbf{x}_3\mathbf{x}_4\right) L(\tau' + \tau, -\tau' - \tau)
\end{aligned}$$

$$\begin{aligned}
L\left(\tau; -\tau\right) &= L_{QIP}\left(\tau; -\tau\right) \\
&\quad + i \int d\tau' \, L_{QIP}\left(-\tau'; \tau'\right) W_{stat}\left(\mathbf{x}_3\mathbf{x}_4\right) L\left(\tau' + \tau; -\left(\tau' + \tau\right)\right) \\
&\quad - i \int d\tau' \, L_{QIP}\left(-\tau'; \tau'\right) v\left(\mathbf{x}_3\mathbf{x}_4\right) L\left(\tau' + \tau; -\left(\tau' + \tau\right)\right) \\
L\left(\tau\right) &= L_{QIP}\left(\tau\right) \\
&\quad + i \int d\tau' \, L_{QIP}\left(\tau'\right) L\left(\tau - \tau'\right) W_{stat}\left(\mathbf{x}_3\mathbf{x}_4\right) - i \int d\tau' \, L_{QIP}\left(\tau'\right) L\left(\tau - \tau'\right) v\left(\mathbf{x}_3\mathbf{x}_4\right),
\end{aligned}$$

where $\tau = t_1 - t_2^{'}$ and $\tau' = t_4 - t_1$. For the sake of clarity we used a simplified notation, where we dropped the space coordinates. We consequently simplified the time-dependent equation for L so far that we are now able to perform a straightforward Fourier transformation using the convolution theorem:

$$L\left(\omega\right) = L_{QIP}\left(\omega\right) + i L_{QIP}\left(\omega\right) L\left(\omega\right) W_{stat}\left(\mathbf{x}_3\mathbf{x}_4\right) - i L_{QIP}\left(\omega\right) L\left(\omega\right) v\left(\mathbf{x}_3\mathbf{x}_4\right).$$

We now reintroduce the space coordinates, yielding:

$$\begin{aligned}
L\left(\mathbf{x}_1\mathbf{x}_2; \mathbf{x}_1^{'}\mathbf{x}_2^{'}; \omega\right) &= L_{QIP}\left(\mathbf{x}_1\mathbf{x}_2; \mathbf{x}_1^{'}\mathbf{x}_2^{'}; \omega\right) \\
&\quad + i \int d\mathbf{x}_3\mathbf{x}_4 \, L_{QIP}\left(\mathbf{x}_1\mathbf{x}_4; \mathbf{x}_1^{'}\mathbf{x}_3; \omega\right) W_{stat}\left(\mathbf{x}_3\mathbf{x}_4\right) L\left(\mathbf{x}_4\mathbf{x}_2; \mathbf{x}_3\mathbf{x}_2^{'}; \omega\right) \\
&\quad - i \int d\mathbf{x}_3\mathbf{x}_4 \, L_{QIP}\left(\mathbf{x}_1\mathbf{x}_3; \mathbf{x}_1^{'}\mathbf{x}_3; \omega\right) v\left(\mathbf{x}_3\mathbf{x}_4\right) L\left(\mathbf{x}_4\mathbf{x}_2; \mathbf{x}_4\mathbf{x}_2^{'}; \omega\right) \\
&= L_{QIP}\left(\mathbf{x}_1\mathbf{x}_2; \mathbf{x}_1^{'}\mathbf{x}_2^{'}; \omega\right) \\
&\quad + \int d\mathbf{x}_3\mathbf{x}_4\mathbf{x}_5\mathbf{x}_6 \, L_{QIP}\left(\mathbf{x}_1\mathbf{x}_4; \mathbf{x}_1^{'}\mathbf{x}_3; \omega\right) L\left(\mathbf{x}_6\mathbf{x}_2; \mathbf{x}_5\mathbf{x}_2^{'}; \omega\right) \times \\
&\quad \times \left[i\delta\left(\mathbf{x}_5, \mathbf{x}_3\right) \delta\left(\mathbf{x}_6, \mathbf{x}_4\right) W_{stat}\left(\mathbf{x}_3\mathbf{x}_4\right) - i\delta\left(\mathbf{x}_3, \mathbf{x}_4\right) \delta\left(\mathbf{x}_5, \mathbf{x}_6\right) v\left(\mathbf{x}_3\mathbf{x}_5\right)\right],
\end{aligned}$$

with

$$L_{QIP}\left(\mathbf{x}_1\mathbf{x}_2;\mathbf{x}_1^{'}\mathbf{x}_2^{'};\omega\right)=\frac{1}{2\pi}\int d\omega'\,G_1\left(\mathbf{x}_1\mathbf{x}_2^{'};\omega+\omega'\right)G_1\left(\mathbf{x}_2\mathbf{x}_1^{'};\omega'\right)$$

being the Fourier transform of the already introduced quasi-independent two-particle correlation function L_{QIP}, where we also made use of the convolution theorem. In a short notation, we finally arrive at:

$$\begin{aligned}L\left(\mathbf{x}_1\mathbf{x}_2;\mathbf{x}_1^{'}\mathbf{x}_2^{'};\omega\right) &= L_{QIP}\left(\mathbf{x}_1\mathbf{x}_2;\mathbf{x}_1^{'}\mathbf{x}_2^{'};\omega\right)\\ &\quad+\int d\mathbf{x}_3\mathbf{x}_4\mathbf{x}_5\mathbf{x}_6\,L_{QIP}\left(\mathbf{x}_1\mathbf{x}_4;\mathbf{x}_1^{'}\mathbf{x}_3;\omega\right)K\left(\mathbf{x}_3\mathbf{x}_4;\mathbf{x}_5\mathbf{x}_6\right)L\left(\mathbf{x}_6\mathbf{x}_2;\mathbf{x}_5\mathbf{x}_2^{'};\omega\right),\end{aligned}\tag{A.28}$$

where

$$K\left(\mathbf{x}_3\mathbf{x}_4;\mathbf{x}_5\mathbf{x}_6\right)=i\delta\left(\mathbf{x}_5,\mathbf{x}_3\right)\delta\left(\mathbf{x}_6,\mathbf{x}_4\right)W_{stat}\left(\mathbf{x}_3\mathbf{x}_4\right)-i\delta\left(\mathbf{x}_3,\mathbf{x}_4\right)\delta\left(\mathbf{x}_5,\mathbf{x}_6\right)v\left(\mathbf{x}_3\mathbf{x}_5\right)$$

is the many-body perturbation theory kernel. We have to keep in mind that the Fourier transformation in the presented way is only possible due to the use of a static, i.e. strongly approximated, screened Coulomb potential W.

The effective two-particle problem Using the Lehmann representation of the Green's function in Fourier space, we can find an explicit expression for the quasi-independent two-particle correlation function L_{QIP} (see Appendix A.7):

$$-iL_{QIP}\left(\mathbf{x}_1\mathbf{x}_2;\mathbf{x}_1^{'}\mathbf{x}_2^{'};\omega\right)\approx\sum_{m,l}\frac{\phi_l\left(\mathbf{x}_1\right)\phi_m\left(\mathbf{x}_2\right)\phi_m^*\left(\mathbf{x}_1^{'}\right)\phi_l^*\left(\mathbf{x}_2^{'}\right)}{\omega-\left(\varepsilon_l-\varepsilon_m\right)+i\eta}-\frac{\phi_m^*\left(\mathbf{x}_2^{'}\right)\phi_l\left(\mathbf{x}_2\right)\phi_l^*\left(\mathbf{x}_1^{'}\right)\phi_m\left(\mathbf{x}_1\right)}{\omega+\left(\varepsilon_l-\varepsilon_m\right)-i\eta}.\tag{A.29}$$

Here, L_{QIP} is approximated by using single-particle wave functions $\phi_{m,l}$ instead of Lehmann amplitudes $f_{m,l}$. The energies $\varepsilon_{m,l}$ originate from a $DFT-KS$ calculation (i.e. $L_{QIP}\approx L_{IP}$) or can be quasiparticle energies obtained within a GW calculation. The index m denotes occupied, l unoccupied states. The form of L_{QIP} suggests to work in transition space, i.e. to define a two-particle excitonic basis $\{\psi^{exc}\}$,

$$\psi_i^{exc}\left(\mathbf{x}_1,\mathbf{x}_2\right)\equiv\sum_{n_1n_2}c_{i,n_1n_2}\phi_{n_1}\left(\mathbf{x}_1\right)\phi_{n_2}^*\left(\mathbf{x}_2\right),$$

based on the same single-particle basis functions $\phi_{m,l}$ as G_0 and L_{QIP}^{RPA}. The transformation of any four-point quantity $F\left(\mathbf{x}_1\mathbf{x}_2\mathbf{x}_3\mathbf{x}_4\right)$ to this basis follows:

$$F\left(\mathbf{x}_1\mathbf{x}_2;\mathbf{x}_3\mathbf{x}_4\right)=\sum_{n_1n_2n_3n_4}\phi_{n_1}\left(\mathbf{x}_1\right)\phi_{n_2}^*\left(\mathbf{x}_2\right)F^{n_1n_2n_3n_4}\phi_{n_3}\left(\mathbf{x}_3\right)\phi_{n_4}^*\left(\mathbf{x}_4\right)$$

with

$$F^{n_1n_2n_3n_4}=\int d\mathbf{x}_1\mathbf{x}_2\mathbf{x}_3\mathbf{x}_4\phi_{n_1}\left(\mathbf{x}_1\right)\phi_{n_2}^*\left(\mathbf{x}_2\right)F\left(\mathbf{x}_1\mathbf{x}_2;\mathbf{x}_3\mathbf{x}_4;\omega\right)\phi_{n_3}\left(\mathbf{x}_3\right)\phi_{n_4}^*\left(\mathbf{x}_4\right).$$

For the Bethe-Salpeter equation (A.28), we thus obtain:

$$\begin{aligned} L\left(\mathbf{x}_1\mathbf{x}_2;\mathbf{x}_3\mathbf{x}_4;\omega\right) &= \sum_{n_1n_2n_3n_4}\phi_{n_1}\left(\mathbf{x}_1\right)\phi^*_{n_2}\left(\mathbf{x}_2\right)L^{n_1n_2n_3n_4}\left(\omega\right)\phi_{n_3}\left(\mathbf{x}_3\right)\phi^*_{n_4}\left(\mathbf{x}_4\right) \\ &= \sum_{n_1n_2n_3n_4}\phi_{n_1}\left(\mathbf{x}_1\right)\phi^*_{n_2}\left(\mathbf{x}_2\right)L^{n_1n_2n_3n_4}_{QIP}\left(\omega\right)\phi_{n_3}\left(\mathbf{x}_3\right)\phi^*_{n_4}\left(\mathbf{x}_4\right)+ \\ &\quad \sum_{n_1n_2n_3n_4}\sum_{n_5n_6n_7n_8}\int d\mathbf{x}_5\mathbf{x}_6\mathbf{x}_7\mathbf{x}_8 \\ &\quad \phi_{n_1}\left(\mathbf{x}_1\right)\phi^*_{n_2}\left(\mathbf{x}_2\right)L^{n_1n_2n_5n_6}_{QIP}\left(\omega\right)\phi_{n_5}\left(\mathbf{x}_5\right)\phi^*_{n_6}\left(\mathbf{x}_6\right)\times \\ &\quad \phi_{n_5}\left(\mathbf{x}_5\right)\phi^*_{n_6}\left(\mathbf{x}_6\right)K^{n_5n_6n_7n_8}\phi_{n_7}\left(\mathbf{x}_7\right)\phi^*_{n_8}\left(\mathbf{x}_8\right)\times \\ &\quad \phi_{n_7}\left(\mathbf{x}_7\right)\phi^*_{n_8}\left(\mathbf{x}_8\right)L^{n_7n_8n_3n_4}\left(\omega\right)\phi_{n_3}\left(\mathbf{x}_3\right)\phi^*_{n_4}\left(\mathbf{x}_4\right) \end{aligned}$$

$$\rightarrow L^{n_1n_2n_3n_4}\left(\omega\right)=L^{n_1n_2n_3n_4}_{QIP}\left(\omega\right)+L^{n_1n_2n_5n_6}_{QIP}\left(\omega\right)K^{n_5n_6n_7n_8}L^{n_7n_8n_3n_4}\left(\omega\right),$$

which denotes in matrix notation:

$$\left[L\left(\omega\right)\right]=\left[L_{QIP}\left(\omega\right)\right]+\left[L_{QIP}\left(\omega\right)\right]\left[K\right]\left[L\left(\omega\right)\right].$$

At this point it is useful to multiply the Bethe-Salpeter equation with a factor $(-i)$ following equation (A.26), since in the end of the calculation one is interested in contracting L to χ:

$$\chi\left(1,2\right)=-iL(1,2;1^+,2^+).$$

One thus finds for the matrix equation:

$$\left[-iL\left(\omega\right)\right]=\left[-iL_{QIP}\left(\omega\right)\right]+\left[-iL_{QIP}\left(\omega\right)\right]\left[iK\right]\left[-iL\left(\omega\right)\right].$$

The quasi-independent polarizability L_{QIP} can be explicitly calculated in this basis starting from equation (A.29):

$$\begin{aligned} -iL^{n_1n_2n_3n_4}_{QIP}\left(\omega\right) &= -i\int d\mathbf{x}_1\mathbf{x}_1^{'}\mathbf{x}_2\mathbf{x}_2^{'}\phi_{n_1}\left(\mathbf{x}_1^{'}\right)\phi^*_{n_2}\left(\mathbf{x}_1\right)L_{QIP}\left(\mathbf{x}_1\mathbf{x}_2;\mathbf{x}_1^{'}\mathbf{x}_2^{'};\omega\right)\phi^*_{n_3}\left(\mathbf{x}_2\right)\phi_{n_4}\left(\mathbf{x}_2^{'}\right) \\ &= \int d\mathbf{x}_1\mathbf{x}_1^{'}\mathbf{x}_2\mathbf{x}_2^{'}\phi_{n_1}\left(\mathbf{x}_1^{'}\right)\phi^*_{n_2}\left(\mathbf{x}_1\right)\phi^*_{n_3}\left(\mathbf{x}_2\right)\phi_{n_4}\left(\mathbf{x}_2^{'}\right) \\ &\quad \times\left[\sum_{m,l}\frac{\phi_l(\mathbf{x}_1)\phi_m(\mathbf{x}_2)\phi^*_m\left(\mathbf{x}_1^{'}\right)\phi^*_l\left(\mathbf{x}_2^{'}\right)}{\omega-(\varepsilon_l-\varepsilon_m)+i\eta}-\frac{\phi^*_m\left(\mathbf{x}_2^{'}\right)\phi_l(\mathbf{x}_2)\phi^*_l\left(\mathbf{x}_1^{'}\right)\phi_m(\mathbf{x}_1)}{\omega+(\varepsilon_l-\varepsilon_m)-i\eta}\right] \\ &= \sum_{m,l}\frac{\delta(n_1,m)\delta(n_2,l)\delta(n_3,m)\delta(n_4,l)}{\omega-(n_2-n_1)+i\eta}-\sum_{m,l}\frac{\delta(n_1,l)\delta(n_2,m)\delta(n_3,l)\delta(n_4,m)}{\omega+(n_1-n_2)-i\eta}, \end{aligned}$$

where m stands for occupied and l for unoccupied states and where we assumed an orthogonal and complete basis:

$$\begin{aligned} \int d\mathbf{r}\phi^*_i\left(\mathbf{r}\right)\phi_j\left(\mathbf{r}\right) &= \delta\left(i,j\right) \\ \\ \sum_i\phi^*_i\left(\mathbf{r}\right)\phi_i\left(\mathbf{r}'\right) &= \delta\left(\mathbf{r}-\mathbf{r}'\right). \end{aligned}$$

We can draw an important conclusion from this result, namely that $[L_{QIP}]$ is diagonal in the transition basis ($n_1=n_3$, $n_2=n_4$). Moreover, only (occupied $\rightarrow$ unoccupied) or (unoccupied $\rightarrow$ occupied) transitions contribute, whereas (occupied $\rightarrow$ occupied) or (unoccupied $\rightarrow$

unoccupied) are not important. This can be depicted in a (n_1n_2, n_3n_4) matrix:

$$[-iL_{QIP}(\omega)] = \begin{array}{c|cccc} (n_1n_2)\ (n_3n_4) \rightarrow & mm & ll & ml & lm \\ \downarrow & & & & \\ mm & 0 & 0 & 0 & 0 \\ ll & 0 & 0 & 0 & 0 \\ ml & 0 & 0 & \frac{-1}{\Delta\varepsilon_{n_2n_1}-\omega} & 0 \\ lm & 0 & 0 & 0 & \frac{1}{\Delta\varepsilon_{n_2n_1}-\omega} \end{array}$$

where $\Delta\varepsilon_{n_2n_1} = \varepsilon_{n_2} - \varepsilon_{n_1}$ and $\Delta\varepsilon_{n_1n_2} = -\Delta\varepsilon_{n_2n_1}$. It is convenient to rewrite the matrix element $L_{QIP}^{n_1n_2n_3n_4}$ in a short notation using the occupation factors f_i ($f_m = 1$, $f_l = 0$):

$$-iL_{QIP}^{n_1n_2n_3n_4}(\omega) = \frac{(f_{n_2} - f_{n_1})\,\delta(n_1, n_3)\,\delta(n_2, n_4)}{\Delta\varepsilon_{n_2n_1} - \omega},$$

where zeros on the diagonal appear when $f_{n_2} = f_{n_1}$. From now on, we only work in the physical meaningful (ml, lm) subspace, where $[L_{QIP}]$ has no non-zero diagonal elements and is thus invertible. Moreover, we introduce an occupation matrix $[F]$,

$$F^{n_1n_2n_3n_4} = (f_{n_2} - f_{n_1})\,\delta(n_1, n_3)\,\delta(n_2, n_4),$$

which also has only non-zero elements in the chosen subspace. It follows:

$$[-iL_{QIP}(\omega)] = \left[-i\breve{L}_{QIP}(\omega)\right][F]$$

with

$$\left[-i\breve{L}_{QIP}(\omega)\right][F] = \begin{pmatrix} \frac{1}{\Delta\varepsilon_{n_2n_1}-\omega} & 0 \\ 0 & \frac{1}{\Delta\varepsilon_{n_2n_1}-\omega} \end{pmatrix} \begin{pmatrix} \underbrace{f(n_2 - n_1)}_{-1} & 0 \\ 0 & \underbrace{f(n_2 - n_1)}_{1} \end{pmatrix}.$$

Consequently, we can rewrite the Bethe-Salpeter matrix equation as follows:

$$\begin{aligned} [-iL(\omega)] &= \left[-i\breve{L}_{QIP}(\omega)\right][F] + \left[-i\breve{L}_{QIP}(\omega)\right][F][iK][-iL(\omega)] \\ &= \left(1 - \left[-i\breve{L}_{QIP}(\omega)\right][F][iK]\right)^{-1}\left[-i\breve{L}_{QIP}(\omega)\right][F] \\ &= \left(\left[-i\breve{L}_{QIP}(\omega)\right]^{-1} - [F][iK]\right)^{-1}[F]. \end{aligned}$$

Many mathematical simplifications follow from the fact that $\left[-i\breve{L}_{QIP}\right]$ is a diagonal matrix. For example, its inverse is readily calculated to:

$$\left[-i\breve{L}_{QIP}\left(\omega\right)\right]^{-1}=\left(\begin{array}{cc}\Delta\varepsilon_{n_2n_1}-\omega & 0\\ 0 & \Delta\varepsilon_{n_2n_1}-\omega\end{array}\right).$$

It is convenient to single out the frequency dependence:

$$\left[-i\breve{L}_{QIP}\left(\omega\right)\right]^{-1}=\left(\begin{array}{cc}\Delta\varepsilon_{n_2n_1} & 0\\ 0 & -\Delta\varepsilon_{n_2n_1}\end{array}\right)-\omega\left(\begin{array}{cc}1 & 0\\ 0 & 1\end{array}\right),$$

enabling us to define a frequency-independent two-particle effective Hamiltonian H^{2p}:

$$\begin{aligned}\left[H^{2p}\right] &= \left(\begin{array}{cc}\Delta\varepsilon_{n_2n_1} & 0\\ 0 & \Delta\varepsilon_{n_2n_1}\end{array}\right)-\left[F\right]\left[iK\right]\\ &= \left(\begin{array}{cc}\Delta\varepsilon_{n_2n_1} & 0\\ 0 & \Delta\varepsilon_{n_2n_1}\end{array}\right)+i\left(\begin{array}{cc}K_{ml,m'l'} & K_{ml,l'm'}\\ -K_{lm,m'l'} & -K_{lm,l'm'}\end{array}\right).\end{aligned}$$

In general, the two-particle effective Hamiltonian is non-hermitian and it denotes:

$$\left[H^{2p}\right]=\left(\begin{array}{cc}H^{res} & K^{coupl}\\ -\left(K^{coupl}\right)^{*} & -\left(H^{res}\right)^{*}\end{array}\right).$$

H^{res} is called resonant part, i.e. transitions between (occupied $\rightarrow$ unoccupied) states are treated. Contrary, $-\left(H^{res}\right)^{*}$ is an anti-resonant part, where transitions between (unoccupied $\rightarrow$ occupied) states and thus negative frequency transitions are considered. The K^{coupl} and $-\left(K^{coupl}\right)^{*}$ blocks couple the resonant to the anti-resonant part and include both (occupied $\rightarrow$ unoccupied) and (unoccupied $\rightarrow$ occupied) transitions. The matrix element $H^{res}_{ml,m'l'}=\Delta\varepsilon_{lm}\delta_{mm'}\delta_{ll'}+iK_{ml,m'l'}$ denotes in detail:

$$\begin{aligned}H^{res}_{ml,m'l'} &= \Delta\varepsilon_{lm}\delta_{mm'}\delta_{ll'}\\ &\quad +i\int d\mathbf{x}_1\mathbf{x}_1^{'}\mathbf{x}_2\mathbf{x}_2^{'}\phi_m\left(\mathbf{x}_1\right)\phi_l^{*}\left(\mathbf{x}_1^{'}\right)\phi_{m'}^{*}\left(\mathbf{x}_2\right)\phi_{l'}\left(\mathbf{x}_2^{'}\right)K\left(\mathbf{x}_1\mathbf{x}_2;\mathbf{x}_1^{'}\mathbf{x}_2^{'}\right)\\ &= \Delta\varepsilon_{lm}\delta_{mm'}\delta_{ll'}\\ &\quad +i\int d\mathbf{x}_1\mathbf{x}_1^{'}\mathbf{x}_2\mathbf{x}_2^{'}\phi_m\left(\mathbf{x}_1\right)\phi_l^{*}\left(\mathbf{x}_1^{'}\right)\phi_{m'}^{*}\left(\mathbf{x}_2\right)\phi_{l'}\left(\mathbf{x}_2^{'}\right)\\ &\quad \times\left[i\delta\left(\mathbf{x}_1,\mathbf{x}_2\right)\delta\left(\mathbf{x}_1^{'},\mathbf{x}_2^{'}\right)W_{stat}\left(\mathbf{x}_1\mathbf{x}_1^{'}\right)-i\delta\left(\mathbf{x}_1^{'},\mathbf{x}_1\right)\delta\left(\mathbf{x}_2^{'},\mathbf{x}_2\right)v\left(\mathbf{x}_1\mathbf{x}_2\right)\right]\\ &= \Delta\varepsilon_{lm}\delta_{mm'}\delta_{ll'}\\ &\quad +\int d\mathbf{x}_1\mathbf{x}_1^{'}\mathbf{x}_2\mathbf{x}_2^{'}\phi_m\left(\mathbf{x}_1\right)\phi_l^{*}\left(\mathbf{x}_1^{'}\right)\phi_{m'}^{*}\left(\mathbf{x}_2\right)\phi_{l'}\left(\mathbf{x}_2^{'}\right)\delta\left(\mathbf{x}_1^{'},\mathbf{x}_1\right)\delta\left(\mathbf{x}_2^{'},\mathbf{x}_2\right)v\left(\mathbf{x}_1\mathbf{x}_2\right)\\ &\quad -\int d\mathbf{x}_1\mathbf{x}_1^{'}\mathbf{x}_2\mathbf{x}_2^{'}\phi_m\left(\mathbf{x}_1\right)\phi_l^{*}\left(\mathbf{x}_1^{'}\right)\phi_{m'}^{*}\left(\mathbf{x}_2\right)\phi_{l'}\left(\mathbf{x}_2^{'}\right)\delta\left(\mathbf{x}_1,\mathbf{x}_2\right)\delta\left(\mathbf{x}_1^{'},\mathbf{x}_2^{'}\right)W_{stat}\left(\mathbf{x}_1\mathbf{x}_1^{'}\right)\\ &= H^{diag}_{ml,ml}+H^{exch}_{ml,m'l'}+H^{scr}_{ml,m'l'},\end{aligned}$$

where we split the resonant part into a diagonal, an electron-hole exchange and a screened electron-hole interaction part following:

$$\begin{aligned} H^{diag}_{ml,ml} &= \Delta\varepsilon_{lm}\delta_{mm'}\delta_{ll'}, \\ H^{exch}_{ml,m'l'} &= \int d\mathbf{x}_1\mathbf{x}_2\phi_m(\mathbf{x}_1)\,\phi^*_l(\mathbf{x}_1)\; v(\mathbf{x}_2\mathbf{x}_1)\;\phi^*_{m'}(\mathbf{x}_2)\,\phi_{l'}(\mathbf{x}_2), \\ H^{scr}_{ml,m'l'} &= -\int d\mathbf{x}_1\mathbf{x}_2\phi_m(\mathbf{x}_1)\,\phi^*_l(\mathbf{x}_2)\; W_{stat}(\mathbf{x}_1\mathbf{x}_2)\;\phi^*_{m'}(\mathbf{x}_1)\,\phi_{l'}(\mathbf{x}_2). \end{aligned}$$

A.9. Contour deformation techniques

In the following, a short overview of contour deformation techniques is provided. For a detailed derivation, the reader is referred to Ref. [284]. Assuming the following common type of an closed integral:

$$\oint_C dz\, I(z) = \oint_C dz\, \frac{f(z)\, e^{itz}}{(z-z_i)^n}, \tag{A.30}$$

where n is the order of the pole and $z = (x, y) \in \mathbb{C}$. The closed contour C can be freely chosen.

The residue theorem According to the residue theorem, a closed path integral over a function $f(z)$ yields:

$$\oint dz\, f(z) = \begin{cases} 0, & \text{if no poles are enclosed} \\ 2\pi i \sum_i \mathrm{Res}(f, z_i), & \text{if poles at } z_i \text{ are enclosed.} \end{cases}$$

$\mathrm{Res}(f, z_i)$ denotes the so-called residue of the function f at the enclosed pole z_i and it is the coefficient of the $(z - z_i)^{-1}$ summand in a Laurent expansion. It can be calculated following:

$$\mathrm{Res}(f, z_i) = \frac{1}{(n-1)!}\frac{d^{n-1}}{dz^{n-1}}\left[(z-z_i)^n f(z)\right]_{z=z_i}. \tag{A.31}$$

In this specific case, the contour C is chosen to consist of a counter-clockwise path along the entire real and a semi-circle with radius $R = \sqrt{x^2 + y^2}$ in the upper half or in the lower half plane (see Fig. (A.4)). In the former case, one deduces from the residue theorem:

$$\oint dz\, I(z) = \int_{-\infty}^{\infty} dx\, I(x) + \lim_{R\to\infty}\int_0^{\pi} d\varphi\, iRe^{i\varphi}\, I\left(Re^{i\varphi}\right) = 2\pi i \sum_i \mathrm{Res}(I, z_i)$$

and in the latter:

$$\oint dz\, I(z) = -\int_{-\infty}^{\infty} dx\, I(x) + \lim_{R\to\infty}\int_{\pi}^{2\pi} d\Theta\, iRe^{i\Theta}\, I\left(Re^{i\Theta}\right) = 2\pi i \sum_i \mathrm{Res}(I, z_i).$$

Jordan's lemma Analyzing the integral over the semi-circle for functions of the type A.30, one finds for the upper half plane with $z = Re^{i\varphi} = R\cos\varphi + iR\sin\varphi$ and $dz = iRe^{i\varphi}d\varphi$:

$$\int_0^{\pi} d\varphi\, iRe^{i\varphi}\, I\left(Re^{i\varphi}\right) = \int_0^{\pi} d\varphi\, iRe^{i\varphi}\, \frac{f\left(Re^{i\varphi}\right)}{\left(Re^{i\varphi} - z_i\right)^n}\, e^{itR\cos\varphi} e^{-tR\sin\varphi}$$

and for the limit, respectively:

$$\lim_{R\to\infty}\int_0^\pi d\varphi \ldots \frac{e^{-tR\sin\rho}}{R^{n-1}}.$$

The integral in the lower half plane from $\Theta = \pi \ldots 2\pi$ can be expressed in terms of $\varphi = 0 \ldots \pi$, following:

$$\begin{aligned}
\Theta &= \varphi + \pi \\
d\Theta &= d\varphi \\
Re^{i\Theta} &= R\cos(\varphi+\pi) + iR\sin(\varphi+\pi) \\
&= R\cos\varphi\cos\pi + R\sin\varphi\sin\pi + iR\sin\varphi\cos\pi + iR\cos\varphi\sin\pi \\
&= -R\cos\varphi - iR\sin\varphi \\
&= -Re^{i\varphi},
\end{aligned}$$

where we applied the addition theorem for sine and cosine. For the integral it follows with $z = -Re^{i\varphi}$:

$$\int_\pi^{2\pi} d\Theta\, iRe^{i\Theta}\, I\left(Re^{i\Theta}\right) = \int_0^\pi d\varphi\, iRe^{i\varphi}\, \frac{f\left(-Re^{i\varphi}\right)}{\left(-Re^{i\varphi}-z_i\right)^n}\, e^{-itR\cos\varphi} e^{+tR\sin\varphi}$$

and for the limit, respectively:

$$\lim_{R\to\infty}\int_0^\pi d\varphi \ldots \frac{e^{tR\sin\rho}}{R^{n-1}}.$$

Jordan's lemma now states that for poles of higher order ($n > 1$), the integral vanishes for $R \to \infty$. For poles of the order $n = 1$, a case-by-case analysis is necessary. For $t > 0$, the integral only vanishes for contours in the upper half plane, however, for contours in the lower half plane it diverges. Contrary, for $t < 0$, the integral vanishes for contours in the lower half plane and diverges for contours in the upper half plane. It is therefore crucial, to wisely choose the contour for a given problem.

Example: Step function The above theorems are applied to the step function Θ. In its integral form, the latter reads:

$$\Theta(t) = -\frac{1}{2\pi i}\int_{-\infty}^{\infty} d\omega'\, \frac{e^{-i\omega' t}}{\omega' + i\eta}.$$

The complex integral of interest is thus:

$$\oint_C d\bar{\omega}\, \frac{e^{-i\bar{\omega}t}}{\bar{\omega}+i\eta},$$

where $\bar{\omega} = \omega + i\omega''$ and $\eta \to 0$. One observes a pole of first order at $\bar{\omega}_0 = -i\eta$, i.e. in the lower half complex plane. Consequently, Jordan's Lemma has to be taken into account and one has to do a case-by-case study. For $t > 0$, the contour is chosen to consist of the entire

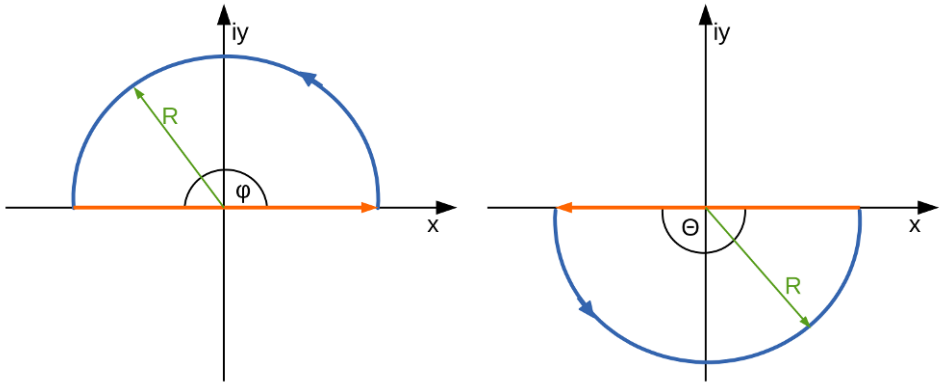

Figure A.4.: The chosen contour consists of the entire real axis and a semi-circle with radius $R \to \infty$ either in the upper or in the lower half plane.

real axis and a semi-circle in the lower-half plane, because this implies that the integral along the semi-circle vanishes. Along a semi-circle in the upper half plane it diverges. As a result, one finds:

$$\oint_C d\bar{\omega}\, \frac{e^{-i\bar{\omega}t}}{\bar{\omega} + i\eta} = \int_{-\infty}^{\infty} d\omega'\, \frac{e^{-i\omega' t}}{\omega' + i\eta} = -2\pi i Res\left(\bar{\omega}_0\right).$$

The residue is calculated to:

$$Res\left(\bar{\omega}_0\right) = \lim_{\eta \to 0} e^{-i(i\eta)t} = 1.$$

One thus obtains for $\Theta\left(t > 0\right)$:

$$\Theta\left(t > 0\right) = 1.$$

For $t < 0$, the contour has to consist of the entire real axis and a semi-circle in the upper half plane. Since no poles are enclosed, the integral vanishes and one obtains: $\Theta\left(t < 0\right) = 0$.

A.10. Gaussian function basis sets

A.10.1. Mathematical background

The Gaussian product theorem The Gaussian product theorem states that the product of two Gaussian functions centered on **A** and **B**, respectively, equals a Gaussian centered on a balance point **P**. This is in general valid, but for the sake of clarity, the product of two unnormalized primitive s-type Gaussian functions $G_1 = e^{-\gamma_1(\mathbf{r}-\mathbf{A})^2}$ and $G_2 = e^{-\gamma_2(\mathbf{r}-\mathbf{B})^2}$ is discussed here. The latter results in a third Gaussian G_3 which is centered at the balance point **P**, which has an exponential factor η being the sum of the two original exponential factors and which is multiplied by some constant factor C:

$$G_3 = C\, e^{-\eta(\mathbf{r}-\mathbf{P})^2},$$

with $\eta = \gamma_1 + \gamma_2$, $\mathbf{P} = \frac{\gamma_1\mathbf{A}+\gamma_2\mathbf{B}}{\eta}$ and $C = e^{-\frac{\gamma_1\gamma_2(\mathbf{A}-\mathbf{B})^2}{\gamma_1+\gamma_2}}$. The same is valid for two Gaussian functions with arbitrary angular momentum, but the multiplication constant becomes more sophisticated. Concerning products of several Gaussian functions, it is evident that the solution is again a Gaussian function, since the product can be evaluated two after two Gaussian functions resulting in a Gaussian function centered at the common balance point.

Gaussian integrals Integrals over Gaussian functions often reduce to simple analytic expressions and can be found in mathematical tables. They are of great use, since they can be solved straightforwardly. Some of these helpful relations, which are also used for derivations in this section, are the following:

$$\int_{-\infty}^{\infty} dx\, e^{-x^2} = \sqrt{\pi}, \qquad \int_{-\infty}^{\infty} dx\, e^{-c_1 x^2} = \sqrt{\frac{\pi}{c_1}}, \qquad \int_{-\infty}^{\infty} dx\, e^{-c_1(x+c_2)^2} = \sqrt{\frac{\pi}{c_1}}.$$

Normalization Since it is convenient to work in a normalized basis, one imposes to the so-called self-overlap SO:

$$SO = \int d^3\mathbf{r}\, \alpha_i^*(\mathbf{r})\, \alpha_i(\mathbf{r}) = 1$$

and introduces a normalization constant N for a Cartesian Gaussian function centered at the origin:

$$\alpha_i(\mathbf{r}) = N\, r_x^h r_y^i r_z^j\, e^{-\gamma \mathbf{r}^2}.$$

Thus, one obtains:

$$SO = N^2 \int d^3\mathbf{r}\, r_x^{2h} r_y^{2i} r_z^{2j}\, e^{-2\gamma \mathbf{r}^2} = 1.$$

This integral can be easily solved by separation and integration by parts:

$$SO = N^2 \int dr_x\, r_x^{2h} e^{-2\gamma r_x^2} \int dr_y\, r_y^{2i} e^{-2\gamma r_y^2} \int dr_z\, r_z^{2j} e^{-2\gamma r_z^2} = 1.$$

Consequently, one finds for the normalization constant of a primitive Gaussian function:

$$N = \left(\frac{2}{\pi}\right)^{\frac{3}{4}} \frac{2^l \gamma^{l/2}}{\left[(2h-1)!!\ (2i-1)!!\ (2j-1)!!\right]^{1/2}},$$

where $l = h + i + j$ is the angular momentum quantum number. For contracted Gaussian functions the normalization constant can be calculated in a similar way.

A.10.2. Calculation of Coulomb integrals in a Gaussian basis

Assume the interaction between two unnormalized s-like Gaussians centered at $\mathbf{A}$ and $\mathbf{B}$ with orbitals exponents κ and λ, the Coulomb integral $V_C = -\sum_n^{occ} \int d^3\mathbf{r} d^3\mathbf{r}'\, \frac{\alpha_i(\mathbf{r})\alpha_n(\mathbf{r})\alpha_n^*(\mathbf{r}')\alpha_j^*(\mathbf{r}')}{|\mathbf{r}-\mathbf{r}'|}$ reads in an auxiliary Gaussian basis $\{\beta_i\}$:

$$V_C^{s,s'} = \int\int d^3\mathbf{r}\, d^3\mathbf{r}'\, \frac{e^{-\kappa|\mathbf{r}-\mathbf{A}|^2} e^{-\lambda|\mathbf{r}'-\mathbf{B}|^2}}{|\mathbf{r}-\mathbf{r}'|}. \tag{A.32}$$

Due to the operator $1/|\mathbf{r}-\mathbf{r}'|$, the above integral does not factorize into products of x-, y- and z-components. To circumvent this problem, one uses the Fourier transform of the Coulomb potential instead of its representation in $\mathbf{r}$-space:

$$\frac{1}{|\mathbf{r}-\mathbf{r}'|} = \frac{4\pi}{(2\pi)^3}\int d^3\mathbf{q}\,\frac{e^{i\mathbf{q}(\mathbf{r}-\mathbf{r}')}}{\mathbf{q}^2}.$$

This is one of the key steps in treating integrals containing the Coulomb potential, allowing to separate the integral:

$$V_C^{s,s'} = \frac{4\pi}{(2\pi)^3}\int\int\int d^3\mathbf{q}\,d^3\mathbf{r}\,d^3\mathbf{r}'\,\frac{e^{i\mathbf{q}(\mathbf{r}-\mathbf{r}')}}{\mathbf{q}^2}e^{-\kappa|\mathbf{r}-\mathbf{A}|^2}e^{-\lambda|\mathbf{r}'-\mathbf{B}|^2}$$

$$V_C^{s,s'} = \frac{4\pi}{(2\pi)^3}\int d^3\mathbf{q}\;\frac{1}{\mathbf{q}^2}\int d^3\mathbf{r}\;e^{i\mathbf{q}\mathbf{r}}e^{-\kappa|\mathbf{r}-\mathbf{A}|^2}\int d^3\mathbf{r}'\;e^{-i\mathbf{q}\mathbf{r}'}e^{-\lambda|\mathbf{r}'-\mathbf{B}|^2}.$$

The integrations over $\mathbf{r}$ and $\mathbf{r}'$ can be carried out independently from each other applying the same solution scheme. One starts by introducing the vector $\boldsymbol{\mu} = \mathbf{r} - \mathbf{A}$ with $d^3\boldsymbol{\mu} = d^3\mathbf{r} = d\boldsymbol{\mu}_\mathbf{x}d\boldsymbol{\mu}_\mathbf{y}d\boldsymbol{\mu}_\mathbf{z}$:

$$\begin{aligned}
I_\mathbf{r} &= \int d^3\mathbf{r}\;e^{i\mathbf{q}\mathbf{r}}e^{-\kappa|\mathbf{r}-\mathbf{A}|^2}\\
&= e^{i\mathbf{q}\mathbf{A}}\int d^3\boldsymbol{\mu}\;e^{i\mathbf{q}\boldsymbol{\mu}}e^{-\kappa\boldsymbol{\mu}^2}\\
&= e^{i\mathbf{q}\mathbf{A}}\iiint d\mu_\mathbf{x}d\mu_\mathbf{y}d\mu_\mathbf{z}\;e^{i(q_x\mu_x+q_y\mu_y+q_z\mu_z)}e^{-\kappa(\mu_x^2+\mu_y^2+\mu_z^2)}\\
&= e^{i\mathbf{q}\mathbf{A}}I_\mathbf{r}^{q_x}I_\mathbf{r}^{q_y}I_\mathbf{r}^{q_z},
\end{aligned}$$

in order to separate the integration over $d\boldsymbol{\mu}$ into three independent integrals which are identical and which can be solved in the same manner. Exemplary, we give here the single steps for the calculation of $I_\mathbf{r}^{q_x}$:

$$\begin{aligned}
I_\mathbf{r}^{q_x} &= \int d\mu_\mathbf{x}\,e^{iq_x\mu_x}e^{-\kappa\mu_x^2}\\
&= e^{-\frac{q_x^2}{4\kappa}}\int d\mu_\mathbf{x}\,e^{-\kappa\left(\mu_x-\frac{iq_x}{2\kappa}\right)^2}\\
&= e^{-\frac{q_x^2}{4\kappa}}\sqrt{\frac{\pi}{\kappa}},
\end{aligned}$$

where we completed the square, $-\kappa\left(\mu_x^2 - 2\frac{iq_x\mu_x}{2\kappa}\right) = -\kappa\left[\left(\mu_x - \frac{iq_x}{2\kappa}\right)^2 - \left(\frac{iq_x}{2\kappa}\right)^2\right]$, and where we used essential properties of Gaussian integrals as presented in the preceding section. The same procedure is used to evaluate $I_\mathbf{r}^{q_y}$ and $I_\mathbf{r}^{q_z}$, respectively, and in total it follows for $I_\mathbf{r}$:

$$I_\mathbf{r} = e^{i\mathbf{q}\mathbf{A}}e^{-\frac{q_x^2+q_y^2+q_z^2}{4\kappa}}\left(\frac{\pi}{\kappa}\right)^{\frac{3}{2}} = \left(\frac{\pi}{\kappa}\right)^{\frac{3}{2}}e^{i\mathbf{q}\mathbf{A}}e^{-\frac{\mathbf{q}^2}{4\kappa}}.$$

We take advantage of the similarity of $I_\mathbf{r}$ and $I_{\mathbf{r}'} = \int d^3\mathbf{r}'\,e^{-i\mathbf{q}\mathbf{r}'}e^{-\lambda|\mathbf{r}'-\mathbf{B}|^2}$ and proceed in the same way by paying attention to the different signs. As a result, one obtains:

$$I_{\mathbf{r}'} = \left(\frac{\pi}{\lambda}\right)^{\frac{3}{2}}e^{-i\mathbf{q}\mathbf{B}}e^{-\frac{\mathbf{q}^2}{4\lambda}}.$$

Combining the obtained expression, yields for the Coulomb integral:

$$\begin{aligned} V_C^{s,s'} &= \tfrac{4\pi}{(2\pi)^3}\left(\tfrac{\pi}{\kappa}\right)^{\frac{3}{2}}\left(\tfrac{\pi}{\lambda}\right)^{\frac{3}{2}}\int d^3\mathbf{q}\,\tfrac{1}{\mathbf{q}^2}\,e^{i\mathbf{q}\mathbf{A}}e^{-\frac{\mathbf{q}^2}{4\kappa}}\,e^{-i\mathbf{q}\mathbf{B}}e^{-\frac{\mathbf{q}^2}{4\lambda}} \\ &= \tfrac{4\pi}{(2\pi)^3}\left(\tfrac{\pi}{\kappa}\right)^{\frac{3}{2}}\left(\tfrac{\pi}{\lambda}\right)^{\frac{3}{2}}\int d^3\mathbf{q}\,\tfrac{1}{\mathbf{q}^2}\,e^{i\mathbf{q}\mathbf{R}}e^{-\gamma\mathbf{q}^2} \\ &= \tfrac{4\pi}{(2\pi)^3}\left(\tfrac{\pi}{\kappa}\right)^{\frac{3}{2}}\left(\tfrac{\pi}{\lambda}\right)^{\frac{3}{2}}\int d^3\mathbf{q}\,\tfrac{1}{\mathbf{q}^2}\,e^{-\gamma\mathbf{q}^2+i\mathbf{q}\mathbf{R}}, \end{aligned}$$

where we defined $\mathbf{R}=\mathbf{A}-\mathbf{B}$ and $\gamma=\frac{1}{4\kappa}+\frac{1}{4\lambda}$. To solve the remaining integral over $d^3\mathbf{q}$, it is first differentiated and then reintegrated with respect to a variable τ. This allows to simplify the expression and to separate it:

$$I_{\mathbf{q}}(\tau)=\int d^3\mathbf{q}\,\frac{1}{\mathbf{q}^2}\,e^{-\tau\mathbf{q}^2+i\mathbf{q}\mathbf{R}}.$$

Here, τ corresponds to γ and we just renamed it in order to avoid confusion along the following procedure. Differentiation of $I_{\mathbf{q}}$ with respect to τ yields:

$$\begin{aligned} \tfrac{dI_{\mathbf{q}}}{d\tau} &= -\int d^3\mathbf{q}\,e^{-\tau\mathbf{q}^2+i\mathbf{q}\mathbf{R}} \\ &= -I_{\mathbf{q}}^{q_x}I_{\mathbf{q}}^{q_y}I_{\mathbf{q}}^{q_z}, \end{aligned}$$

$$\begin{aligned} I_{\mathbf{q}}^{q_x} &= \int dq_x\,e^{-\tau q_x^2+iq_xR_x} \\ &= e^{-\frac{R_x^2}{4\tau}}\int dq_x\,e^{-\tau\left(q_x-\frac{iR_x}{2\tau}\right)^2} \\ &= e^{-\frac{R_x^2}{4\tau}}\sqrt{\tfrac{\pi}{\tau}}. \end{aligned}$$

Proceeding in the same way for $I_{\mathbf{q}}^{q_y}$ and $I_{\mathbf{q}}^{q_z}$ and combining all results, gives:

$$\frac{dI_{\mathbf{q}}}{d\tau}=-e^{-\frac{\mathbf{R}^2}{4\tau}}\left(\frac{\pi}{\tau}\right)^{\frac{3}{2}}.$$

Integrating over this quantity holds an expression for $I_{\mathbf{q}}(\tau)$, since choosing wisely the integration limits, we get:

$$\int_{\gamma}^{\infty}\frac{dI_{\mathbf{q}}(\tau)}{d\tau}\,d\tau=I_{\mathbf{q}}(\infty)-I_{\mathbf{q}}(\gamma)=-I_{\mathbf{q}}(\gamma),$$

$$\rightarrow I_{\mathbf{q}}(\gamma)=-\int_{\gamma}^{\infty}\frac{dI_{\mathbf{q}}(\tau)}{d\tau}\,d\tau=\int_{\gamma}^{\infty}d\tau\,e^{-\frac{\mathbf{R}^2}{4x}}\left(\frac{\pi}{\tau}\right)^{\frac{3}{2}}.$$

This integral can be solved by substitution, where:

$$u^2=\tfrac{\mathbf{R}^2}{4\tau},\qquad x=\tfrac{\mathbf{R}^2}{4u^2},\qquad \tfrac{d\tau}{du}=-\tfrac{\mathbf{R}^2}{2u^3}.$$

Since τ goes from γ to ∞, u goes from $\sqrt{\frac{\mathbf{R}^2}{4\gamma}}$ to $\lim_{\tau\to\infty}\sqrt{\frac{\mathbf{R}^2}{4\tau}}=0$. It follows:

$$I_{\mathbf{q}}(\gamma) = -\int_{\sqrt{\frac{\mathbf{R}^2}{4\gamma}}}^{0} du\, \frac{\mathbf{R}^2}{2u^3}\, e^{-u^2}\, \frac{4u^3}{\mathbf{R}^3}\pi^{\frac{3}{2}},$$

$$I_{\mathbf{q}}(\gamma) = 4\pi^{\frac{3}{2}}\frac{1}{\mathbf{R}}\int_{0}^{\sqrt{\frac{\mathbf{R}^2}{4\gamma}}} du\, e^{-u^2}.$$

The integration over all space (A.32) has been replaced by a one-dimensional integration over a finite interval, which can be found in mathematical tables as error function erf(y):

$$\int_0^y du\, e^{-u^2} = \frac{\sqrt{\pi}}{2}\,\mathrm{erf}\,(y)\,.$$

This results in:

$$I_{\mathbf{q}}(\gamma) = 2\pi^2\frac{1}{\mathbf{R}}\mathrm{erf}\left(\sqrt{\frac{\mathbf{R}^2}{4\gamma}}\right).$$

Consequently, the Coulomb integral between two unnormalized s-like Gaussian functions can be calculated as:

$$V_C^{s,s'} = \left(\frac{\pi}{\kappa}\right)^{\frac{3}{2}}\left(\frac{\pi}{\lambda}\right)^{\frac{3}{2}}\frac{1}{\mathbf{R}}\mathrm{erf}\left(\sqrt{\frac{\mathbf{R}^2}{4\gamma}}\right). \tag{A.33}$$

The introduced error function is strongly related to the so-called Boys function F_n of order n [65, 131], obeying:

$$F_n(x) = \int_0^1 dt\, t^{2n} e^{-xt^2}$$

$$F_0(x) = \frac{\sqrt{\pi}}{2\sqrt{x}}\,\mathrm{erf}\left(\sqrt{x}\right),\ x > 0.$$

This function plays a key role in one- or two-electron integrals evaluation, since efficient evaluation methods based on upward/ downward recursion exist [**?**, 134]:

$$F_n(x) = \frac{1}{2x}\left[(2n{-}1)\,F_{n-1}(x){-}e^{-x}\right],$$

$$F_n(x) = \frac{1}{2n{+}1}\left[2x\,F_{n+1}(x){-}e^{-x}\right].$$

Rewriting the Coulomb integral for two s-like Gaussian functions (A.33) in terms of the Boys function gives:

$$V_C^{s,s'} = \frac{1}{\sqrt{\pi}\sqrt{\gamma}}\left(\frac{\pi}{\kappa}\right)^{\frac{3}{2}}\left(\frac{\pi}{\lambda}\right)^{\frac{3}{2}}F_0\left(\frac{\mathbf{R}^2}{4\gamma}\right). \tag{A.34}$$

This integral can not only be solved very efficiently, moreover it serves as a starting point for the calculation of the bare exchange interaction between the remaining orbitals. It can be demonstrated that it is not necessary to carry out the derivation from scratch, but solutions can be obtained based on $V_C^{s,s'}$. This is exemplary shown for the s-like and p_x-like Gaussian

$((r_x - C_x)\ e^{-\sigma|\mathbf{r}-\mathbf{C}|^2})$ Coulomb integral in the following:

$$\begin{aligned}\frac{d}{dA_x}V_C^{s,s'} &= 2\kappa \int\int d^3\mathbf{r}\, d^3\mathbf{r}'\, \frac{(r_x-A_x)e^{-\kappa|\mathbf{r}-\mathbf{A}|^2}e^{-\lambda|\mathbf{r}'-\mathbf{B}|^2}}{|\mathbf{r}-\mathbf{r}'|} \\ &= 2\kappa V_C^{s,p_x}.\end{aligned}$$

Consequently, V_C^{s,p_x} can be evaluated using (A.34):

$$\begin{aligned}V_C^{s,p_x} &= \frac{1}{2\kappa}\frac{d}{dA_x}V_C^{s,s'} \\ &= \frac{1}{2\kappa}\frac{1}{\sqrt{\pi}\sqrt{\gamma}}\left(\frac{\pi}{\kappa}\right)^{\frac{3}{2}}\left(\frac{\pi}{\lambda}\right)^{\frac{3}{2}}\frac{d}{dA_x}\left[F_0\left(\frac{\mathbf{R}^2}{4\gamma}\right)\right] \\ &= \frac{1}{2\kappa}\frac{1}{\sqrt{\pi}\sqrt{\gamma}}\left(\frac{\pi}{\kappa}\right)^{\frac{3}{2}}\left(\frac{\pi}{\lambda}\right)^{\frac{3}{2}}\frac{d}{dA_x}\left[\int_0^1 dt\, e^{-\frac{\mathbf{R}^2t^2}{4\gamma}}\right] \\ &= -\frac{1}{2\kappa}\frac{1}{\sqrt{\pi}\sqrt{\gamma}}\left(\frac{\pi}{\kappa}\right)^{\frac{3}{2}}\left(\frac{\pi}{\lambda}\right)^{\frac{3}{2}}\int_0^1 dt\, \frac{t^2}{2\gamma}\,(A_x - B_x)\, e^{-\frac{\mathbf{R}^2t^2}{4\gamma}} \\ &= -\frac{1}{\kappa}\frac{1}{\sqrt{\pi}}\gamma^{-\frac{3}{2}}\left(\frac{\pi}{\kappa}\right)^{\frac{3}{2}}\left(\frac{\pi}{\lambda}\right)^{\frac{3}{2}} R_x \int_0^1 dt\, t^2 e^{-\frac{\mathbf{R}^2t^2}{4\gamma}},\end{aligned}$$

$$V_C^{s,p_x} = -\frac{1}{\kappa}\frac{1}{\sqrt{\pi}}\gamma^{-\frac{3}{2}}\left(\frac{\pi}{\kappa}\right)^{\frac{3}{2}}\left(\frac{\pi}{\lambda}\right)^{\frac{3}{2}} R_x\ F_1\left(\frac{\mathbf{R}^2}{4\gamma}\right).$$

Following the same procedure and taking V_C^{s,p_x} as a starting point, we can derive an analytical expression for a p_x-like and p_y-like Gaussian $\left((r_y - C_y)\ e^{-\sigma|\mathbf{r}-\mathbf{C}|^2}\right)$ interaction:

$$\begin{aligned}\frac{d}{dB_y}V_C^{s,p_x} &= 4\kappa\lambda \int\int d^3\mathbf{r}\, d^3\mathbf{r}'\, \frac{(r_x-A_x)e^{-\kappa|\mathbf{r}-\mathbf{A}|^2}(r_y-B_y)e^{-\lambda|\mathbf{r}'-\mathbf{B}|^2}}{|\mathbf{r}-\mathbf{r}'|} \\ &= 4\kappa\lambda V_C^{p_x,p_y}.\end{aligned}$$

$$\begin{aligned}V_C^{p_x,p_y} &= \frac{1}{4\kappa\lambda}\frac{d}{dB_y}V_C^{s,p_x} \\ &= -\frac{1}{4\kappa^2\lambda}\frac{1}{\sqrt{\pi}}\gamma^{-\frac{3}{2}}\left(\frac{\pi}{\kappa}\right)^{\frac{3}{2}}\left(\frac{\pi}{\lambda}\right)^{\frac{3}{2}} R_x \frac{d}{dB_y}\left[F_1\left(\frac{\mathbf{R}^2}{4\gamma}\right)\right] \\ &= -\frac{1}{4\kappa^2\lambda}\frac{1}{\sqrt{\pi}}\gamma^{-\frac{3}{2}}\left(\frac{\pi}{\kappa}\right)^{\frac{3}{2}}\left(\frac{\pi}{\lambda}\right)^{\frac{3}{2}} R_x \frac{d}{dB_y}\left[\int_0^1 dt\, t^2 e^{-\frac{\mathbf{R}^2t^2}{4\gamma}}\right] \\ &= -\frac{1}{4\kappa^2\lambda}\frac{1}{\sqrt{\pi}}\gamma^{-\frac{3}{2}}\left(\frac{\pi}{\kappa}\right)^{\frac{3}{2}}\left(\frac{\pi}{\lambda}\right)^{\frac{3}{2}} R_x \int_0^1 dt\, \frac{t^4}{2\gamma}\,(A_y - B_y)\, e^{-\frac{\mathbf{R}^2t^2}{4\gamma}} \\ &= -\frac{1}{8\kappa^2\lambda}\frac{1}{\sqrt{\pi}}\gamma^{-\frac{5}{2}}\left(\frac{\pi}{\kappa}\right)^{\frac{3}{2}}\left(\frac{\pi}{\lambda}\right)^{\frac{3}{2}} R_x R_y \int_0^1 dt\, t^4 e^{-\frac{\mathbf{R}^2t^2}{4\gamma}}\end{aligned}$$

$$V_C^{p_x,p_y} = -\frac{1}{8\kappa^2\lambda}\frac{1}{\sqrt{\pi}}\gamma^{-\frac{5}{2}}\left(\frac{\pi}{\kappa}\right)^{\frac{3}{2}}\left(\frac{\pi}{\lambda}\right)^{\frac{3}{2}} R_x R_y\ F_2\left(\frac{\mathbf{R}^2}{4\gamma}\right).$$

Step by step, expressions for the different bare exchange interactions can be derived using the previous solutions following the demonstrated scheme. As a result, we get analytical expressions for the Coulomb integral containing Boys functions of different order. As already mentioned above, these can be efficiently evaluated applying recursion.

B | Appendix: List of publications and conference contributions

Publications

- Faber, C., Attaccalite, C., Olevano, V., Runge, E. and Blase, X., '*First- principles GW calculations for DNA and RNA nucleobases*', Phys. Rev. B, 83, 115123 (2011)
- Faber, C., Laflamme-Janssen, J., Côté, M., Runge, E. and Blase, X., '*Electron- phonon coupling in the C_{60} fullerene within the many-body GW approach*', Phys. Rev. B, 84, 155104 (2011)
- Ciuchi, S. et al., '*Molecular Fingerprints in the Electronic Properties of Crystalline Organic Semiconductors: From Experiment to Theory*', Phys. Rev. Lett., 108, 256401 (2012)
- Faber, C. et al., '*Electron-Phonon coupling and charge-transfer excitations in organic systems from many-body perturbation theory*', Journal of Materials Science, 47, 7472 (2012)
- Faber, C., Duchemin, I., Deutsch, T. and Blase, X., '*Many-body Green's function study of coumarins for dye-sensitized solar cells*', Phys. Rev. B, 86, 155315 (2012)
- Faber, C., Boulanger, P., Duchemin, I., Attaccalite, C. and Blase, X., '*Many- body Green's function GW and Bethe-Salpeter study of the optical excitations in a paradigmatic model dipeptide*', The Journal of Chemical Physics, 139, 194308 (2013)
- Faber, C., Blase, X. and Fratini, S., '*Electrons go green: Exploring organic semiconductors*', Institut Neel: Highlights 7 (2013)
- Faber, C., Boulanger, P., Attaccalite, C., Duchemin, I., and Blase, X., '*Excited states properties of organic molecules: from density functional theory to the GW and Bethe-Salpeter Green's function formalisms*', Phil. Trans. R. Soc. A 372 (2014)
- Faber, C., Boulanger, P., Attaccalite, C., and Blase, X., '*Approximations to the GW self-energy electron-phonon coupling gradients*', in preparation

Conference contributions

- Invited talks: GDR Electronique Organique (Grenoble, 2011)
- Oral conference contributions:

  ETSF Young Researcher Meeting 2012/2013/2014
  March Meeting of the German Physical Society 2011/2012/2014
  ETSF Conference (Zaragoza, 2014)

- Invited Group Seminars 2014:

  Materials Theory Group (Prof. N. Spaldin, ETH Zürich)
  Quantum Transport Group (Prof. M. Büttiker, University of Geneva)
  Theory of Dirac Fermion Materials Group (Prof. O. Yazyev, EPFL Lausanne)

- Posters: ETSF Conference 2011/2013, ElecMol (Grenoble, 2012)

Bibliography

[1] Hedin, L., 'New Method for Calculating the One-Particle Green's Function with Application to the Electron-Gas Problem', *Phys. Rev.*, **139**, A796 (1965).

[2] Strinati, G., 'Application of the Green's functions method to the study of the optical properties of semiconductors', *Rivista del nuovo cimento*, **11**, 1 (1988).

[3] Hybertsen, M.S. and Louie, S.G., 'Electron correlation in semiconductors and insulators: Band gaps and quasiparticle energies', *Phys. Rev. B*, **34**, 5390 (1986).

[4] Aryasetiawan, F. and Gunnarsson, O., 'The GW method', *Rep. Prog. Phys.*, **61**, 237 (1998).

[5] Aulbur, W.G., Jönsson, L. and Wilkins, J.W., 'Quasiparticle Calculations in Solids', in *Solid State Physics*, edited by H. Ehrenreich and F. Spaepen, Academic Press, London.

[6] Blase, X., Attaccalite, C. and Olevano, V., 'First-principles *GW* calculations for fullerenes, porphyrins, phtalocyanine, and other molecules of interest for organic photovoltaic applications', *Phys. Rev. B*, **83**, 115103 (2011).

[7] Faber, C., Attaccalite, C., Olevano, V., Runge, E. and Blase, X., 'First-principles *GW* calculations for DNA and RNA nucleobases', *Phys. Rev. B*, **83**, 115123 (2011).

[8] Blase, X. and Attaccalite, C., 'Charge-transfer excitations in molecular donor-acceptor complexes within the many-body Bethe-Salpeter approach', *Appl. Phys. Lett.*, **99**, 171909 (2011).

[9] Hedin, L., 'On correlation effects in electron spectroscopies and the GW approximation', *Journal of Physics: Condensed Matter*, **11**, R489 (1999).

[10] Faber, C., Boulanger, P., Duchemin, I., Attaccalite, C. and Blase, X., 'Many-body Green's function GW and Bethe-Salpeter study of the optical excitations in a paradigmatic model dipeptide', *The Journal of Chemical Physics*, **139**, 194308 (2013).

[11] Faber, C., Duchemin, I., Deutsch, T. and Blase, X., 'Many-body Green's function study of coumarins for dye-sensitized solar cells', *Phys. Rev. B*, **86**, 155315 (2012).

[12] Faber, C., Laflamme-Janssen, J., Côté, M., Runge, E. and Blase, X., 'Electron-phonon coupling in the C_{60} fullerene within the many-body *GW* approach', *Phys. Rev. B*, **84**, 155104 (2011).

[13] Benanti, T.L. and Venkataraman, D., 'Organic solar cells: An overview focusing on active layer morphology', *Photosynthesis research*, **87**, 73 (2006).

[14] Kippelen, B. and Bredas, J.L., 'Organic photovoltaics', *Energy Environ. Sci.*, **2**, 251 (2009).

[15] Su, Y.W., Lan, S.C. and Wei, K.H., 'Organic photovoltaics', *Materials Today*, **15**, 554 (2012).

[16] Mertens, K., *Photovoltaik - Lehrbuch zu Grundlagen, Technologie und Praxis*, Carl Hanser Verlag, München (2013).

[17] Zeman, M., 'Solar Cells', Lecture Notes, http://ocw.tudelft.nl/courses/microelectronics/solar-cells/readings/.

[18] Hull, R., *Properties of crystalline silicon*, The Institution of Electrical Engineers, London (1999).

[19] Shockley, W. and Queisser, H.J., 'Detailed balance limit of efficiency of p-n junction solar cells', *Journal of Applied Physics*, **32**, 510 (1961).

[20] Falk, F., 'Physik und Technologie der Solarzellen', Lecture Notes, http://www.ipht-jena.de/fileadmin/user_upload/redaktion/Lehre/Vorlesungsscripte/PVtot_deutsch.pdf.

[21] Bakulin, A.A. et al., 'The Role of Driving Energy and Delocalized States for Charge Separation in Organic Semiconductors', *Science*, **335**, 1340 (2012).

[22] Grancini, G. et al., 'Hot exciton dissociation in polymer solar cells', *Nature materials*, **12**, 29 (2013).

[23] M., S., 'Measuring internal quantum efficiency to demonstrate hot exciton dissociation', *Nature materials*, **12**, 594 (2013).

[24] Chidichimo, G. and Filippelli, L., 'Organic solar cells: problems and perspectives', *International Journal of Photoenergy*, **2010** (2010).

[25] Tang, C.W., 'Two-layer organic photovoltaic cell', *Applied Physics Letters*, **48**, 183 (1986).

[26] Hardin, B.E., Snaith, H.J. and McGehee, M.D., 'The renaissance of dye-sensitized solar cells', *Nature Photonics*, **6**, 162 (2012).

[27] O'Regan, B. and Graetzel, M., 'A low-cost, high-efficiency solar cell based on dye-sensitized colloidal TiO2 films', *Nature*, **353** (1991).

[28] Hara, K. et al., 'Molecular Design of Coumarin Dyes for Efficient Dye-Sensitized Solar Cells', *J. Phys. Chem. B*, **107**, 597 (2003).

[29] Hara, K. et al., 'Design of new coumarin dyes having thiophene moieties for highly efficient organic-dye-sensitized solar cells', *New J. Chem.*, **27**, 783 (2003).

[30] Hara, K. et al., 'Oligothiophene-Containing Coumarin Dyes for Efficient Dye-Sensitized Solar Cells', *The Journal of Physical Chemistry B*, **109**, 15476 (2005).

[31] Wang, Z.S. et al., 'A High-Light-Harvesting-Efficiency Coumarin Dye for Stable Dye-Sensitized Solar Cells', *Advanced Materials*, **19**, 1138 (2007).

[32] Hohenberg, P. and Kohn, W., 'Inhomogeneous Electron Gas', *Phys. Rev.*, **136**, B864 (1964).

[33] Kohn, W. and Sham, L.J., 'Self-Consistent Equations Including Exchange and Correlation Effects', *Phys. Rev.*, **140**, A1133 (1965).

[34] Jensen, F., *Introduction to Computational Chemistry*, Wiley, New York (2013).

[35] Runge, E. and Gross, E.K.U., 'Density-Functional Theory for Time-Dependent Systems', *Phys. Rev. Lett.*, **52**, 997 (1984).

[36] Marques, M.A.L. et al., *Time-Dependent Density Functional Theory*, Springer Verlag Berlin Heidelberg (2006).

[37] Caruso, D. and Troisi, A., 'Long-range exciton dissociation in organic solar cells', *Proc. Natl. Acad. Sci.*, **109**, 13498 (2012).

[38] Yost, S.R. and Van Voorhis, T., 'Electrostatic Effects at Organic Semiconductor Interfaces: A Mechanism for "Cold" Exciton Breakup', *J. Phys. Chem. C*, **117**, 5617 (2013).

[39] Sariciftci, N.S., Smilowitz, L., Heeger, A.J. and Wudl, F., 'Photoinduced Electron Transfer from a Conducting Polymer to Buckminsterfullerene', *Science*, **258**, 1474 (1992).

[40] Schmidt-Mende, L. et al., 'Self-Organized Discotic Liquid Crystals for High-Efficiency Organic Photovoltaics', *Science*, **293**, 1119 (2001).

[41] Hardin, B.E., Snaith, H.J. and McGehee, M.D., 'The renaissance of dye-sensitized solar cells', *Nat Photon*, **6**, 162 (2012).

[42] Onida, G., Reining, L. and Rubio, A., 'Electronic excitations: density-functional versus many-body Green's-function approaches', *Rev. Mod. Phys.*, **74**, 601 (2002).

[43] Bussi, G., 'Effects of the Electron-Hole Interaction on the Optical Properties of Materials: the Bethe-Salpeter Equation', *Physica Scripta*, **2004**, 141 (2004).

[44] Duchemin, I., Deutsch, T. and Blase, X., 'Short-Range to Long-Range Charge-Transfer Excitations in the Zincbacteriochlorin-Bacteriochlorin Complex: A Bethe-Salpeter Study', *Phys. Rev. Lett.*, **109**, 167801 (2012).

[45] Hüfner, S., *Photoelectron Spectroscopy - Principles and Applications*, Springer, Berlin Heidelberg, 3rd ed. (2003).

[46] Reinert, F. and Hüfner, S., 'Photoemission spectroscopy - from early days to recent applications', *New Journal of Physics*, **7**, 97 (2005).

[47] Serrano-Andres, L. and Fuelscher, M.P., 'Theoretical Study of the Electronic Spectroscopy of Peptides. III. Charge-Transfer Transitions in Polypeptides', *J. Am. Chem. Soc.*, **120**, 10912 (1998).

[48] Bruneval, F. and Marques, M.A.L., 'Benchmarking the Starting Points of the GW Approximation for Molecules', *J. Chem. Theory Comput.*, **9**, 324 (2013).

[49] Yanai, T., Tew, D.P. and Handy, N.C., 'A new hybrid exchange-correlation functional using the Coulomb-attenuating method (CAM-B3LYP)', *Chem. Phys. Lett.*, **393**, 51 (2004).

[50] Stein, T., Kronik, L. and Baer, R., 'Prediction of charge-transfer excitations in coumarin-based dyes using a range-separated functional tuned from first principles', *J. Chem. Phys.*, **131**, 244119 (2009).

[51] Lazzeri, M., Attaccalite, C., Wirtz, L. and Mauri, F., 'Impact of the electron-electron correlation on phonon dispersion: Failure of LDA and GGA DFT functionals in graphene and graphite', *Phys. Rev. B*, **78**, 081406 (2008).

[52] Antonius, G., Poncé, S., Boulanger, P., Côté, M. and Gonze, X., 'Many-Body Effects on the Zero-Point Renormalization of the Band Structure', *Phys. Rev. Lett.*, **112**, 215501 (2014).

[53] Hertz, H.R., 'Über einen Einfluß des ultravioletten Lichtes auf die electrische Entladung', *Ann. d. Physik und Chemie*, **31**, 983 (1887).

[54] Hallwachs, W., 'Über den Einfluß des Lichtes auf electrostatisch geladene Körper', *Ann. d. Physik und Chemie*, **33**, 301 (1888).

[55] Hedin, L., 'Electron correlation: Keeping close to an orbital description', *International Journal of Quantum Chemistry*, **56**, 445 (1995).

[56] Papalazarou, E. et al., 'Valence-band electronic structure of V_2O_3: Identification of V and O bands', *Phys. Rev. B*, **80**, 155115 (2009).

[57] Born, M. and Oppenheimer, R., 'Zur Quantentheorie der Molekeln', *Ann. d. Physik*, **84**, 457 (1927).

[58] Born, M., 'Theoretical investigations on the relation between crystal dynamics and x-ray scattering', *Rep. Progr. Physics*, **9**, 294 (1943).

[59] Koch, W. and Holthausen, M.C., *A Chemist's Guide to Density Functional Theory*, Wiley, New York, 2nd ed. (2001).

[60] Parr, R.G. and Yang, W., *Density-Functional Theory of Atoms and Molecules*, Oxford University Press, New York (1989).

[61] Lanczos, C., 'An Iteration Method for the Solution of the Eigenvalue Problem of Linear Differential and Integral Operators', *Journal of research of the National Bureau of Standards*, **45**, 255 (1950).

[62] Pulay, P., 'Convergence acceleration of iterative sequences. The case of SCF iteration', *Chemical Physics Letters*, **73**, 393 (1980).

[63] Fock, V., 'Näherungsmethode zur Lösung des quanten-mechanischen Mehrkörperproblems', *Z. Phys.*, **61**, 126 (1930).

[64] Slater, J.C., 'Note on Hartree's Method', *Phys. Rev.*, **35**, 210 (1930).

[65] Boys, S.F., 'Electronic Wave Functions. I. A General Method of Calculation for the Stationary States of Any Molecular System', *Proceedings of the Royal Society of London. Series A. Mathematical and Physical Sciences*, **200**, 542 (1950).

[66] Dykstra, C.E., *Ab initio calculation of the structures and properties of molecules*, Elsevier, Amsterdam (1988).

[67] Møller, C. and Plesset, M.S., 'Note on an Approximation Treatment for Many-Electron Systems', *Phys. Rev.*, **46**, 618 (1934).

[68] Shavitt, I. and Bartlett, R.J., *Many-Body Methods in Chemistry and Physics - MBPT and Coupled-Cluster Theory*, Cambridge University Press, Cambridge (2009).

[69] Szabo, A. and Ostlund, N.S., *Modern Quantum Chemistry - Introduction to Advanced Electronic Structure Theory*, Courier Dover Publications, Mineola, New York (2012).

[70] Gross, E.K.U. and Dreizler, R.M., *Density Functional Theory*, Springer, Berlin Heidelberg (1995).

[71] Perdew, J.P. and Zunger, A., 'Self-interaction correction to density-functional approximations for many-electron systems', *Phys. Rev. B*, **23**, 5048 (1981).

[72] Vosko, S.H., Wilk, L. and Nusair, M., 'Accurate spin-dependent electron liquid correlation energies for local spin density calculations: a critical analysis', *Can. J. Phys.*, **58**, 1200 (1980).

[73] Ceperley, D. and Alder, B., 'Ground State of the Electron Gas by a Stochastic Method', *Phys. Rev. Lett.*, **45**, 566 (1980).

[74] Perdew, J.P., Burke, K. and Ernzerhof, M., 'Generalized Gradient Approximation Made Simple', *Phys. Rev. Lett.*, **77**, 3865 (1996).

[75] Becke, A.D., 'A new mixing of Hartree-Fock and local density-functional theories', *J. Chem. Phys.*, **98**, 1372 (1993).

[76] Raghavachari, K., 'Perspective on 'Density functional thermochemistry. III. The role of exact exchange", *Theoretical Chemistry Accounts*, **103**, 361 (2000).

[77] Gunnarsson, O. and Jones, R.O., 'Density Functional Calculations for Atoms, Molecules and Clusters', *Physica Scripta*, **21**, 394 (1980).

[78] Moruzzi, V.L., Janak, J.F. and Williams, A.R., 'Calculations of electronic properties of metals', (1978).

[79] Yin, M.T. and Cohen, M.L., 'Theory of static structural properties, crystal stability, and phase transformations: Application to Si and Ge', *Phys. Rev. B*, **26**, 5668 (1982).

[80] Slater, J.C., *Quantum Theory of Molecules and Solids: Insulators, semiconductors, and metals*, vol. IV, McGraw-Hill, New York (1974).

[81] Janak, J.F., 'Proof that $\frac{\partial E}{\partial n} = \epsilon$ in density-functional theory', *Phys. Rev. B*, **18**, 7165 (1978).

[82] Kronik, L., Stein, T., Refaely-Abramson, S. and Baer, R., 'Excitation Gaps of Finite-Sized Systems from Optimally Tuned Range-Separated Hybrid Functionals', *J. Chem. Theory Comput.*, **8**, 1515 (2012).

[83] Kraisler, E. and Kronik, L., 'Fundamental gaps with approximate density functionals: The derivative discontinuity revealed from ensemble considerations', *The Journal of Chemical Physics*, **140**, 18A540 (2014).

[84] Perdew, J.P., Parr, R.G., Levy, M. and Balduz, J.L., 'Density-Functional Theory for Fractional Particle Number: Derivative Discontinuities of the Energy', *Phys. Rev. Lett.*, **49**, 1691 (1982).

[85] Levy, M., Perdew, J.P. and Sahni, V., 'Exact differential equation for the density and ionization energy of a many-particle system', *Phys. Rev. A*, **30**, 2745 (1984).

[86] Almbladh, C.O. and von Barth, U., 'Exact results for the charge and spin densities, exchange-correlation potentials, and density-functional eigenvalues', *Phys. Rev. B*, **31**, 3231 (1985).

[87] Jones, R.O. and Gunnarsson, O., 'The density functional formalism, its applications and prospects', *Rev. Mod. Phys.*, **61**, 689 (1989).

[88] Mahan, G.D., *Many-Particle Physics*, Springer, Berlin Heidelberg, 2nd ed. (1990).

[89] Gross, E.K.U., Runge, E. and Heinonen, O., *Many-particle theory*, A. Hilger, Bristol (1991).

[90] Bruus, H. and Flensberg, K., *Many-Body Quantum Theory in Condensed Matter Physics - An Introduction*, OUP Oxford, New York, London (2004).

[91] Friedrich, C. and Schindlmayr, A., 'Many-Body Perturbation Theory: The GW Approximation', in *NIC Series Volume 31: Computational Nanoscience: Do It Yourself!*, edited by D.M. J. Grotendorst S. Blügel, John von Neumann Institute for Computing, Jülich (2006).

[92] Galitskii, V. and Migdal, A., 'Application of quantum field theory methods to the many body problem', *Sov. Phys., JETP*, **7**, 96 (1958).

[93] Dyson, F.J., 'The Radiation Theories of Tomonaga, Schwinger, and Feynman', *Phys. Rev.*, **75**, 486 (1949).

[94] Dyson, F.J., 'The S Matrix in Quantum Electrodynamics', *Phys. Rev.*, **75**, 1736 (1949).

[95] Dirac, P.A.M., 'The Quantum Theory of the Emission and Absorption of Radiation', *Proceedings of the Royal Society of London. Series A*, **114**, 243 (1927).

[96] Fermi, E., *Nuclear Physics*, University of Chicago Press, Chigago (1949).

[97] Landau, L.D. and Lifshitz, E.M., *Statistical physics*, Pergamon Press, Oxford, 3rd ed. (1980).

[98] Layzer, A.J., 'Properties of the One-Particle Green's Function for Nonuniform Many-Fermion Systems', *Phys. Rev.*, **129**, 897 (1963).

[99] Schwinger, J., 'On the Green's functions of quantized fields. I', *Proceedings of the National Academy of Sciences*, **37**, 452 (1951).

[100] Martin, P.C. and Schwinger, J., 'Theory of Many-Particle Systems. I', *Phys. Rev.*, **115**, 1342 (1959).

[101] YU, P. and Cardona, M., *Fundamentals of Semiconductors - Physics and Materials Properties*, Springer, Berlin Heidelberg (2010).

[102] Schley, P., 'Optische Eigenschaften von InN und InN-basierten Halbleitern', *Ph.D. Thesis, Ilmenau University of Technology, Germany* (2010).

[103] Winzer, A., 'Optische und elektronische Eigenschaften von AlGaN/GaN-Heterostrukturen', *Ph.D. Thesis, Ilmenau University of Technology, Germany* (2008).

[104] Chuang, S.L., *Physics of Photonic Devices*, Wiley, New York (2012).

[105] Frenkel, J., 'On the Transformation of Light into Heat in Solids. II', *Phys. Rev.*, **37**, 1276 (1931).

[106] Wannier, G.H., 'The Structure of Electronic Excitation Levels in Insulating Crystals', *Phys. Rev.*, **52**, 191 (1937).

[107] Elliott, R.J., 'Intensity of Optical Absorption by Excitons', *Phys. Rev.*, **108**, 1384 (1957).

[108] Klingshirn, C.F., *Semiconductor Optics*, Springer, Berlin Heidelberg (2012).

[109] Wu, J. et al., 'Effects of the narrow band gap on the properties of InN', *Phys. Rev. B*, **66**, 201403 (2002).

[110] Fu, S.P. and Chen, Y.F., 'Effective mass of InN epilayers', *Appl. Phys. Lett.*, **85**, 1523 (2004).

[111] Vurgaftman, I. and Meyer, J.R., 'Band parameters for nitrogen-containing semiconductors', *Journal of Applied Physics*, **94**, 3675 (2003).

[112] Persson, C., da Silva, A.F., Ahuja, R. and Johansson, B., 'First-principle calculations of the dielectric function of zinc-blende and wurtzite InN', *Journal of Physics: Condensed Matter*, **13**, 8945 (2001).

[113] Grahn, H.T., *Introduction to Semiconductor Physics*, World Scientific, Singapur (1999).

[114] Adler, S.L., 'Quantum Theory of the Dielectric Constant in Real Solids', *Phys. Rev.*, **126**, 413 (1962).

[115] Wiser, N., 'Dielectric Constant with Local Field Effects Included', *Phys. Rev.*, **129**, 62 (1963).

[116] Ehrenreich, H., in *The Optical Properties of Solids*, edited by J. Tauc, Academic Press, New York, proc. internat. school of physics 'enrico fermi' ed. (1966).

[117] Sottile, F., 'Response functions of semiconductors and insulators: from the Bethe-Salpeter equation to time-dependent density functional theory', *Ph.D. Thesis, Ecole Polytechnique Paris, France* (2003).

[118] Bruneval, F., 'Exchange and Correlation in the Electronic Structure of Solids, from Silicon to Cuprous Oxide: GW Approximation and beyond', *Ph.D. Thesis, Ecole Polytechnique Paris, France* (2005).

[119] Rebolini, E., Toulouse, J. and Savin, A., 'Electronic excitation energies of molecular systems from the Bethe-Salpeter equation: Example of the H2 molecule', ArXiv:1304.1314 (2013).

[120] Onida, G., Reining, L., Godby, R.W., Del Sole, R. and Andreoni, W., 'Ab Initio Calculations of the Quasiparticle and Absorption Spectra of Clusters: The Sodium Tetramer', *Phys. Rev. Lett.*, **75**, 818 (1995).

[121] Rohlfing, M. and Louie, S.G., 'Excitons and Optical Spectrum of the Si(111) $-$ (2×1) Surface', *Phys. Rev. Lett.*, **83**, 856 (1999).

[122] Albrecht, S., Reining, L., Del Sole, R. and Onida, G., '*Ab Initio* Calculation of Excitonic Effects in the Optical Spectra of Semiconductors', *Phys. Rev. Lett.*, **80**, 4510 (1998).

[123] Benedict, L.X., Shirley, E.L. and Bohn, R.B., 'Optical Absorption of Insulators and the Electron-Hole Interaction: An *Ab Initio* Calculation', *Phys. Rev. Lett.*, **80**, 4514 (1998).

[124] Casida, M.E., in *Recent Advances in Density Functional Methods, Part I*, edited by D. Chong, World Scientific, Singapore (1995).

[125] Casida, M.E., 'Time-dependent density-functional theory for molecules and molecular solids', *J. Mol. Struct.: Theochem*, **914**, 3 (2009).

[126] Tiago, M.L. and Chelikowsky, J.R., 'Optical excitations in organic molecules, clusters, and defects studied by first-principles Green's function methods', *Phys. Rev. B*, **73**, 205334 (2006).

[127] Haydock, R., 'Recursive Solution of the Schroedinger Equation', in *Solid State Physics*, edited by H. Ehrenreich, Academic Press (1980).

[128] Press, W.H., Flannery, B.P., Teukolsky, S.A. and Vetterling, W.T., *Numerical Recipes in Fortran: The Art of Scientific Computing*, Cambridge University Press, 2nd ed. (1992).

[129] Hill, J.G., 'Gaussian basis sets for molecular applications', *International Journal of Quantum Chemistry*, **113**, 21 (2013).

[130] Ren, X. et al., 'Resolution-of-identity approach to Hartree-Fock, hybrid density functionals, RPA, MP2 and GW with numeric atom-centered orbital basis functions', *New Journal of Physics*, **14**, 053020 (2012).

[131] Boys, S., Cook, G., Reeves, C.M. and Shavitt, I., 'Automatic Fundamental Calculations of Molecular Structure', *Nature*, **178**, 1207 (1956).

[132] Clementi, E. and Davis, D., 'Electronic structure of large molecular systems', *Journal of Computational Physics*, **1**, 223 (1966).

[133] Ditchfield, R., Hehre, W. and Pople, J.A., 'Self-consistent Molecular-Orbital Methods. IX. An Extended Gaussian-Type Basis for Molecular Orbital Studies of Organic Molecules', *J. Chem. Phys.*, **54**, 724 (1971).

[134] Shavitt, I., in *Methods in Computational Physics*, edited by B. Alder, S. Fernbach and M. Rotenberg, Academic Press, New York (1963).

[135] Dunning, T.H., 'Gaussian basis sets for use in correlated molecular calculations. I. The atoms boron through neon and hydrogen', *J. Chem. Phys.*, **90**, 1007 (1989).

[136] Soler, J.M. et al., *J. Phys.: Condens. Matter*, **14**, 2745 (2002).

[137] Reeves, C.M. and Harrison, M.C., 'Use of Gaussian Functions in the Calculation of Wavefunctions for Small Molecules. II. The Ammonia Molecule', *The Journal of Chemical Physics*, **39**, 11 (1963).

[138] Cherkes, I., Klaiman, S. and Moiseyev, N., 'Spanning the Hilbert space with an even tempered Gaussian basis set', *Int. J. Quant. Chem.*, **109**, 2996 (2009).

[139] Aryasetiawan, F. and Gunnarsson, O., 'Product-basis method for calculating dielectric matrices', *Phys. Rev. B*, **49**, 16214 (1994).

[140] Foerster, D. and Koval, P., 'On the Kohn-Sham density response in a localized basis set', *The Journal of Chemical Physics*, **131**, 044103 (2009).

[141] Boulanger, P., Jacquemin, D., Duchemin, I. and Blase, X., 'Fast and Accurate Electronic Excitations in Cyanines with the Many-Body Bethe-Salpeter Approach', *Journal of Chemical Theory and Computation*, **10**, 1212 (2014).

[142] Valiev, M. et al., 'NWChem: A comprehensive and scalable open-source solution for large scale molecular simulations', *Computer Physics Communications*, **181**, 1477 (2010).

[143] Lundqvist, B.I., *Phys. Kondens. Mater.*, **6**, 206 (1967).

[144] Lundqvist, B.I., *Phys. Kondens. Mater.*, **6**, 193 (1967).

[145] Hedin, L. and Lundqvist, S., in *Solid State Physics*, edited by H. Ehrenreich, F. Seitz and D. Turnbull, Academic Press, New York (1969).

[146] von der Linden, W. and Horsch, P., 'Precise quasiparticle energies and Hartree-Fock bands of semiconductors and insulators', *Phys. Rev. B*, **37**, 8351 (1988).

[147] Hamada, N., Hwang, M. and Freeman, A.J., 'Self-energy correction for the energy bands of silicon by the full-potential linearized augmented-plane-wave method: Effect of the valence-band polarization', *Phys. Rev. B*, **41**, 3620 (1990).

[148] Engel, G.E. and Farid, B., 'Generalized plasmon-pole model and plasmon band structures of crystals', *Phys. Rev. B*, **47**, 15931 (1993).

[149] Godby, R.W., Schlüter, M. and Sham, L.J., 'Self-energy operators and exchange-correlation potentials in semiconductors', *Phys. Rev. B*, **37**, 10159 (1988).

[150] Schöne, W.D. and Eguiluz, A.G., 'Self-Consistent Calculations of Quasiparticle States in Metals and Semiconductors', *Phys. Rev. Lett.*, **81**, 1662 (1998).

[151] Bruneval, F., 'Ionization energy of atoms obtained from GW self-energy or from random phase approximation total energies', *J. Chem. Phys.*, **136**, 194107 (2012).

[152] Pickett, W.E., 'Density Functional theory in Solids: II. Excited States', *Comments Solid State Phys.*, **12** (1985).

[153] Louie, S., in *Electronic Structure, Dynamics, and Quantum Structural Properties of Condensed Matter*, edited by J.T. Devreese and P.V. Camp, Plenum Press, New York (1985).

[154] Mohr, S. et al., 'Daubechies wavelets for linear scaling density functional theory', *J. Chem. Phys.*, **140**, 204110 (2014).

[155] Skylaris, C.K., Haynes, P.D., Mostofi, A.A. and Payne, M.C., 'Introducing ONETEP: Linear-scaling density functional simulations on parallel computers', *The Journal of chemical physics*, **122**, 084119 (2005).

[156] Bachelet, G.B. and Christensen, N.E., 'Relativistic and core-relaxation effects on the energy bands of gallium arsenide and germanium', *Phys. Rev. B*, **31**, 879 (1985).

[157] Bechstedt, F., *Adv. Solid State Phys. 32*, **32** (1992).

[158] Pickett, W.E. and Wang, C.S., 'Local-density approximation for dynamical correlation corrections to single-particle excitations in insulators', *Phys. Rev. B*, **30**, 4719 (1984).

[159] Bechstedt, F. and Del Sole, R., in *Proc. 19th Internat. Conf. Phys. Semiconductors*, edited by W. Zawadzki, Institut of Physics, PAS, Warsaw (1988).

[160] Almbladh, C.O. and Pedroza, A.C., 'Density-functional exchange-correlation potentials and orbital eigenvalues for light atoms', *Phys. Rev. A*, **29**, 2322 (1984).

[161] Öğüt, S., Chelikowsky, J.R. and Louie, S.G., 'Quantum Confinement and Optical Gaps in Si Nanocrystals', *Phys. Rev. Lett.*, **79**, 1770 (1997).

[162] Godby, R.W. and White, I.D., 'Density-Relaxation Part of the Self-Energy', *Phys. Rev. Lett.*, **80**, 3161 (1998).

[163] Tiago, M.L., Idrobo, J.C., Öğüt, S., Jellinek, J. and Chelikowsky, J.R., 'Electronic and optical excitations in Ag_n clusters ($n = 1\tilde{}8$): Comparison of density-functional and many-body theories', *Phys. Rev. B*, **79**, 155419 (2009).

[164] Sharma, S., Dewhurst, J.K., Lathiotakis, N.N. and Gross, E.K.U., 'Reduced density matrix functional for many-electron systems', *Phys. Rev. B*, **78**, 201103 (2008).

[165] Chan, M.K.Y. and Ceder, G., 'Efficient Band Gap Prediction for Solids', *Phys. Rev. Lett.*, **105**, 196403 (2010).

[166] Ernzerhof, M. and Scuseria, G.E., 'Assessment of the Perdew-Burke-Ernzerhof exchange-correlation functional', *The Journal of Chemical Physics*, **110**, 5029 (1999).

[167] Refaely-Abramson, S., Baer, R. and Kronik, L., 'Fundamental and excitation gaps in molecules of relevance for organic photovoltaics from an optimally tuned range-separated hybrid functional', *Phys. Rev. B*, **84**, 075144 (2011).

[168] Savin, A., 'On Degeneracy, Near-degeneracy and Density Functional Theory', in *Recent Developments and Applications of Modern Density Functional Theory*, edited by J.M. Seminario, Elsevier (1996).

[169] Leininger, T., Stoll, H., Werner, H.J. and Savin, A., 'Combining long-range configuration interaction with short-range density functionals', *Chem. Phys. Lett.*, **275**, 151 (1997).

[170] Toulouse, J., Colonna, F. and Savin, A., 'Long-range/short-range separation of the electron-electron interaction in density-functional theory', *Phys. Rev. A*, **70**, 062505 (2004).

[171] Gerber, I.C., Ángyán, J.G., Marsman, M. and Kresse, G., 'Range separated hybrid density functional with long-range Hartree-Fock exchange applied to solids', *The Journal of Chemical Physics*, **127**, 054101 (2007).

[172] Okuno, K., Shigeta, Y., Kishi, R., Miyasaka, H. and Nakano, M., *J. Photochem. Photobiol.*, **A235**, 29 (2012).

[173] Krukau, A.V., Vydrov, O.A., Izmaylov, A.F. and Scuseria, G.E., 'Influence of the exchange screening parameter on the performance of screened hybrid functionals', *The Journal of Chemical Physics*, **125**, 224106 (2006).

[174] Tawada, Y., Tsuneda, T., Yanagisawa, S., Yanai, T. and Hirao, K., 'A long-range-corrected time-dependent density functional theory', *J. Chem. Phys.*, **120**, 8425 (2004).

[175] Iikura, H., Tsuneda, T., Yanai, T. and Hirao, K., 'A long-range correction scheme for generalized-gradient-approximation exchange functionals', *J. Chem. Phys.*, **115**, 3540 (2001).

[176] Baer, R. and Neuhauser, D., 'Density Functional Theory with Correct Long-Range Asymptotic Behavior', *Phys. Rev. Lett.*, **94**, 043002 (2005).

[177] Livshits, E. and Baer, R., 'A well-tempered density functional theory of electrons in molecules', *Phys. Chem. Chem. Phys.*, **9**, 2932 (2007).

[178] Hybertsen, M.S. and Louie, S.G., 'First-Principles Theory of Quasiparticles: Calculation of Band Gaps in Semiconductors and Insulators', *Phys. Rev. Lett.*, **55**, 1418 (1985).

[179] Godby, R.W., Schlüter, M. and Sham, L.J., 'Accurate Exchange-Correlation Potential for Silicon and Its Discontinuity on Addition of an Electron', *Phys. Rev. Lett.*, **56**, 2415 (1986).

[180] Chang, E.K., Blase, X. and Louie, S.G., 'Quasiparticle band structure of lanthanum hydride', *Phys. Rev. B*, **64**, 155108 (2001).

[181] Gonze, X. et al., 'ABINIT: First-principles approach to material and nanosystem properties', *Computer Physics Communications*, **180**, 2582 (2009).

[182] Deslippe, J. et al., 'BerkeleyGW: A massively parallel computer package for the calculation of the quasiparticle and optical properties of materials and nanostructures', *Computer Physics Communications*, **183**, 1269 (2012).

[183] Marini, A., Hogan, C., Gruning, M. and Varsano, D., 'Yambo: An ab initio tool for excited state calculations', *Comput. Phys. Comm.*, **180**, 1392 (2009).

[184] Shirley, E.L. and Martin, R.M., 'GW quasiparticle calculations in atoms', *Phys. Rev. B*, **47**, 15404 (1993).

[185] Rohlfing, M. and Louie, S.G., 'Electron-hole excitations and optical spectra from first principles', *Phys. Rev. B*, **62**, 4927 (2000).

[186] Grossman, J.C., Rohlfing, M., Mitas, L., Louie, S.G. and Cohen, M.L., 'High Accuracy Many-Body Calculational Approaches for Excitations in Molecules', *Phys. Rev. Lett.*, **86**, 472 (2001).

[187] Tiago, M.L. and Chelikowsky, J.R., 'First-principles GW-BSE excitations in organic molecules', *Solid State Communications*, **136**, 333 (2005).

[188] Dori, N. et al., 'Valence electronic structure of gas-phase 3,4,9,10-perylene tetracarboxylic acid dianhydride: Experiment and theory', *Phys. Rev. B*, **73**, 195208 (2006).

[189] Stan, A., Dahlen, N.E. and van Leeuwen, R., 'Fully self-consistent GW calculations for atoms and molecules', *EPL (Europhysics Letters)*, **76**, 298 (2006).

[190] Morris, A.J. et al., 'Vertex corrections in localized and extended systems', *Phys. Rev. B*, **76**, 155106 (2007).

[191] Bruneval, F., '*GW*', *Phys. Rev. Lett.*, **103**, 176403 (2009).

[192] Palummo, M., Hogan, C., Sottile, F., Bagala, P. and Rubio, A., 'Ab initio electronic and optical spectra of free-base porphyrins: The role of electronic correlation', *J. Chem. Phys.*, **131**, 084102 (2009).

[193] Rostgaard, C., Jacobsen, K.W. and Thygesen, K.S., 'Fully self-consistent GW calculations for molecules', *Phys. Rev. B*, **81**, 085103 (2010).

[194] Ke, S.H., 'All-electron *GW* methods implemented in molecular orbital space: Ionization energy and electron affinity of conjugated molecules', *Phys. Rev. B*, **84**, 205415 (2011).

[195] Foerster, D., Koval, P. and Sanchez-Portal, D., 'An O(N[sup 3]) implementation of Hedin's GW approximation for molecules', *J. Chem. Phys.*, **135**, 074105 (2011).

[196] Marom, N., Ren, X., Moussa, J.E., Chelikowsky, J.R. and Kronik, L., 'Electronic structure of copper phthalocyanine from G_0W_0 calculations', *Phys. Rev. B*, **84**, 195143 (2011).

[197] Samsonidze, G., Jain, M., Deslippe, J., Cohen, M.L. and Louie, S.G., 'Simple Approximate Physical Orbitals for *GW* Quasiparticle Calculations', *Phys. Rev. Lett.*, **107**, 186404 (2011).

[198] Marom, N. et al., 'Benchmark of *GW* methods for azabenzenes', *Phys. Rev. B*, **86**, 245127 (2012).

[199] Sharifzadeh, S., Tamblyn, I., Doak, P., Darancet, P. and Neaton, J., 'Quantitative molecular orbital energies within a G0W0 approximation', *Euro. Phys. J. B*, **85**, 1 (2012).

[200] Umari, P. and Fabris, S., 'Importance of semicore states in GW calculations for simulating accurately the photoemission spectra of metal phthalocyanine molecules', *J. Chem. Phys.*, **136**, 174310 (2012).

[201] Körzdörfer, T. and Marom, N., 'Strategy for finding a reliable starting point for G_0W_0 demonstrated for molecules', *Phys. Rev. B*, **86**, 041110 (2012).

[202] Caruso, F., Rinke, P., Ren, X., Scheffler, M. and Rubio, A., 'Unified description of ground and excited states of finite systems: The self-consistent *GW* approach', *Phys. Rev. B*, **86**, 081102 (2012).

[203] van Setten, M.J., Weigend, F. and Evers, F., 'The GW-Method for Quantum Chemistry Applications: Theory and Implementation', *J. Chem. Theory Comput.*, **9**, 232 (2013).

[204] Pham, T.A., Nguyen, H.V., Rocca, D. and Galli, G., '*GW* calculations using the spectral decomposition of the dielectric matrix: Verification, validation, and comparison of methods', *Phys. Rev. B*, **87**, 155148 (2013).

[205] Holm, B. and von Barth, U., 'Fully self-consistent GW self-energy of the electron gas', *Phys. Rev. B*, **57**, 2108 (1998).

[206] Ku, W. and Eguiluz, A.G., 'Band-Gap Problem in Semiconductors Revisited: Effects of Core States and Many-Body Self-Consistency', *Phys. Rev. Lett.*, **89**, 126401 (2002).

[207] Delaney, K., Garcia-Gonzalez, P., Rubio, A., Rinke, P. and Godby, R.W., 'Comment on 'Band-Gap Problem in Semiconductors Revisited: Effects of Core States and Many-Body Self-Consistency", *Phys. Rev. Lett.*, **93**, 249701 (2004).

[208] Faleev, S.V., van Schilfgaarde, M. and Kotani, T., 'All-Electron Self-Consistent *GW* Approximation: Application to Si, MnO, and NiO', *Phys. Rev. Lett.*, **93**, 126406 (2004).

[209] Bruneval, F., Vast, N. and Reining, L., 'Effect of self-consistency on quasiparticles in solids', *Phys. Rev. B*, **74**, 045102 (2006).

[210] Shishkin, M. and Kresse, G., 'Self-consistent *GW* calculations for semiconductors and insulators', *Phys. Rev. B*, **75**, 235102 (2007).

[211] Frisch, M.J. et al., 'Gaussian 09 Revision B.01', Gaussian Inc. Wallingford CT 2009.

[212] Troullier, N. and Martins, J.L., 'Efficient pseudopotentials for plane-wave calculations', *Phys. Rev. B*, **43**, 1993 (1991).

[213] Savin, A., 'Ground and low-lying excited states of interacting electron systems; A survey and some critical analyses', in *Electron Correlation in the Solid State*, edited by N. March, World Scientific, Singapore (1999).

[214] Vahtras, O., Almlöf, J. and Feyereisen, M., 'Integral approximations for LCAO-SCF calculations', *Chemical Physics Letters*, **213**, 514 (1993).

[215] Weigend, F. and Häser, M., 'RI-MP2: first derivatives and global consistency', *Theoretical Chemistry Accounts*, **97**, 331 (1997).

[216] Qian, X., Umari, P. and Marzari, N., 'Photoelectron properties of DNA and RNA bases from many-body perturbation theory', *Phys. Rev. B*, **84**, 075103 (2011).

[217] Vidal, J., Trani, F., Bruneval, F., Marques, M.A.L. and Botti, S., 'Effects of Electronic and Lattice Polarization on the Band Structure of Delafossite Transparent Conductive Oxides', *Phys. Rev. Lett.*, **104**, 136401 (2010).

[218] Vidal, J., Botti, S., Olsson, P., Guillemoles, J.F. and Reining, L., 'Strong Interplay between Structure and Electronic Properties in $CuIn(S,Se)_2$: A First-Principles Study', *Phys. Rev. Lett.*, **104**, 056401 (2010).

[219] Rangel, T. et al., 'Band structure of gold from many-body perturbation theory', *Phys. Rev. B*, **86**, 125125 (2012).

[220] Gatti, M., Bruneval, F., Olevano, V. and Reining, L., 'Understanding Correlations in Vanadium Dioxide from First Principles', *Phys. Rev. Lett.*, **99**, 266402 (2007).

[221] Korbel, S. et al., 'Benchmark Many-Body GW and Bethe-Salpeter calculations for small transition-metal molecules', *Journal of Chemical Theory and Computation*, accepted abstract online.

[222] Kurashige, Y., Nakajima, T., Kurashige, S., Hirao, K. and Nishikitani, Y., 'Theoretical Investigation of the Excited States of Coumarin Dyes for Dye-Sensitized Solar Cells', *J. Phys. Chem. A*, **111**, 5544 (2007).

[223] Wong, B.M. and Cordaro, J.G., 'Coumarin dyes for dye-sensitized solar cells: A long-range-corrected density functional study', *J. Chem. Phys.*, **129**, 214703 (2008).

[224] Sanchez-de Armas, R., San Miguel, M.A., Oviedo, J. and Sanz, J.F., 'Coumarin derivatives for dye sensitized solar cells: a TD-DFT study', *Phys. Chem. Chem. Phys.*, **14**, 225 (2012).

[225] Leszczynski, J., *Handbook of Computational Chemistry*, Springer, Berlin Heidelberg (2012).

[226] Wu, Q. and Van Voorhis, T., 'Constrained Density Functional Theory and Its Application in Long-Range Electron Transfer', *J. Chem. Theory Comput.*, **2**, 765 (2006).

[227] Ghosh, P. and Gebauer, R., 'Computational approaches to charge transfer excitations in a zinc tetraphenylporphyrin and C[sub 70] complex', *J. Chem. Phys.*, **132**, 104102 (2010).

[228] Dreuw, A., Weisman, J.L. and Head-Gordon, M., 'Long-range charge-transfer excited states in time-dependent density functional theory require non-local exchange', *J. Chem. Phys.*, **119**, 2943 (2003).

[229] Tozer, D.J., 'Relationship between long-range charge-transfer excitation energy error and integer discontinuity in Kohn-Sham theory', *J. Chem. Phys.*, **119**, 12697 (2003).

[230] Dreuw, A. and Head-Gordon, M., 'Failure of Time-Dependent Density Functional Theory for Long-Range Charge-Transfer Excited States: The Zincbacteriochlorin-Bacteriochlorin and Bacteriochlorophyll-Spheroidene Complexes', *J. Am. Chem. Soc.*, **126**, 4007 (2004).

[231] Mulliken, R.S., 'Structures of Complexes Formed by Halogen Molecules with Aromatic and with Oxygenated Solvents', *Journal of the American Chemical Society*, **72**, 600 (1950).

[232] Lange, A.W., Rohrdanz, M.A. and Herbert, J.M., 'Charge-Transfer Excited States in a pi-Stacked Adenine Dimer, As Predicted Using Long-Range-Corrected Time-Dependent Density Functional Theory', *J. Phys. Chem. B*, **112**, 6304 (2008).

[233] Stein, T., Kronik, L. and Baer, R., 'Reliable Prediction of Charge Transfer Excitations in Molecular Complexes Using Time-Dependent Density Functional Theory', *J. Am. Chem. Soc.*, **131**, 2818 (2009).

[234] Peach, M.J.G., Benfield, P., Helgaker, T. and Tozer, D.J., 'Excitation energies in density functional theory: An evaluation and a diagnostic test', *J. Chem. Phys.*, **128**, 044118 (2008).

[235] Akinaga, Y. and Ten-no, S., 'Range-separation by the Yukawa potential in long-range corrected density functional theory with Gaussian-type basis functions', *Chem. Phys. Lett.*, **462**, 348 (2008).

[236] Rocca, D., Lu, D. and Galli, G., 'Ab initio calculations of optical absorption spectra: Solution of the Bethe–Salpeter equation within density matrix perturbation theory', *J. Chem. Phys.*, **133**, 164109 (2010).

[237] Ma, Y., Rohlfing, M. and Molteni, C., 'Excited states of biological chromophores studied using many-body perturbation theory: Effects of resonant-antiresonant coupling and dynamical screening', *Phys. Rev. B*, **80**, 241405 (2009).

[238] Grüning, M., Marini, A. and Gonze, X., 'Exciton-Plasmon States in Nanoscale Materials: Breakdown of the Tamm-Dancoff Approximation', *Nano Lett.*, **9**, 2820 (2009).

[239] Giannozzi, P. et al., 'QUANTUM ESPRESSO: a modular and open-source software project for quantum simulations of materials', *Journal of Physics: Condensed Matter*, **21**, 395502 (2009).

[240] Baumeier, B., Andrienko, D., Ma, Y. and Rohlfing, M., 'Excited States of Dicyanovinyl-Substituted Oligothiophenes from Many-Body Green's Functions Theory', *J. Chem. Theory Comput.*, **8**, 997 (2012).

[241] Sangalli, D., Romaniello, P., Onida, G. and Marini, A., 'Double excitations in correlated systems: A many-body approach', *J. Chem. Phys.*, **134**, 034115 (2011).

[242] Hagfeldt, A., Boschloo, G., Sun, L., Kloo, L. and Pettersson, H., 'Dye-Sensitized Solar Cells', *Chemical Reviews*, **110**, 6595 (2010).

[243] Rehm, J.M. et al., 'Femtosecond Electron-Transfer Dynamics at a Sensitizing Dye-Semiconductor (TiO2) Interface', *The Journal of Physical Chemistry*, **100**, 9577 (1996).

[244] Gosar, P. and Choi, S.i., 'Linear-Response Theory of the Electron Mobility in Molecular Crystals', *Phys. Rev.*, **150**, 529 (1966).

[245] Fratini, S. and Ciuchi, S., 'Bandlike Motion and Mobility Saturation in Organic Molecular Semiconductors', *Phys. Rev. Lett.*, **103**, 266601 (2009).

[246] Ortmann, F., Bechstedt, F. and Hannewald, K., 'Theory of charge transport in organic crystals: Beyond Holstein's small-polaron model', *Phys. Rev. B*, **79**, 235206 (2009).

[247] Ciuchi, S. et al., 'Molecular Fingerprints in the Electronic Properties of Crystalline Organic Semiconductors: From Experiment to Theory', *Phys. Rev. Lett.*, **108**, 256401 (2012).

[248] Tamura, H., Ramon, J.G.S., Bittner, E.R. and Burghardt, I., 'Phonon-Driven Ultrafast Exciton Dissociation at Donor-Acceptor Polymer Heterojunctions', *Phys. Rev. Lett.*, **100**, 107402 (2008).

[249] Lautenschlager, P., Allen, P.B. and Cardona, M., 'Phonon-induced lifetime broadenings of electronic states and critical points in Si and Ge', *Phys. Rev. B*, **33**, 5501 (1986).

[250] Gopalan, S., Lautenschlager, P. and Cardona, M., 'Temperature dependence of the shifts and broadenings of the critical points in GaAs', *Phys. Rev. B*, **35**, 5577 (1987).

[251] Hebard, A.F. et al., 'Superconductivity at 18K in potassium-doped C60', *Nature*, **350**, 600 (1991).

[252] Gunnarsson, O., 'Superconductivity in fullerides', *Rev. Mod. Phys.*, **69**, 575 (1997).

[253] Ganin, A.Y. et al., 'Bulk superconductivity at 38K in a molecular system', *Nature Materials*, **7**, 367 (2008).

[254] Mitsuhashi, R. et al., 'Superconductivity in alkali-metal-doped picene', *Nature*, **464**, 76 (2010).

[255] Faber, C. and Fratini, S., 'Electrons go green: Exploring organic semiconductors', *Institut Neel: Highlights 7*, available under: http://neel.cnrs.fr/IMG/pdf/03.pdf (2013).

[256] Tiago, M.L., Northrup, J.E. and Louie, S.G., 'Ab initio', *Phys. Rev. B*, **67**, 115212 (2003).

[257] Yoshida, H. and Sato, N., 'Crystallographic and electronic structures of three different polymorphs of pentacene', *Phys. Rev. B*, **77**, 235205 (2008).

[258] Gonze, X. and Lee, C., 'Dynamical matrices, Born effective charges, dielectric permittivity tensors, and interatomic force constants from density-functional perturbation theory', *Phys. Rev. B*, **55**, 10355 (1997).

[259] Baroni, S., de Gironcoli, S., Dal Corso, A. and Giannozzi, P., 'Phonons and related crystal properties from density-functional perturbation theory', *Rev. Mod. Phys.*, **73**, 515 (2001).

[260] Laflamme-Janssen, J., Côté, M., Louie, S.G. and Cohen, M.L., 'Electron-phonon coupling in C_{60} using hybrid functionals', *Phys. Rev. B*, **81**, 073106 (2010).

[261] Yin, Z.P., Kutepov, A. and Kotliar, G., 'Correlation-Enhanced Electron-Phonon Coupling: Applications of *GW* and Screened Hybrid Functional to Bismuthates, Chloronitrides, and Other High-T_c Superconductors', *Phys. Rev. X*, **3**, 021011 (2013).

[262] Hands, I.D. et al., 'Vibronic interactions in the visible and near-infrared spectra of C60 anions', *Phys. Rev. B*, **77**, 115445 (2008).

[263] Iwahara, N., Sato, T., Tanaka, K. and Chibotaru, L.F., 'Vibronic coupling in C60 anion revisited: Derivations from photoelectron spectra and DFT calculations', *Phys. Rev. B*, **82**, 245409 (2010).

[264] Poncé, S. et al., 'Verification of first-principles codes: Comparison of total energies, phonon frequencies, electron-phonon coupling and zero-point motion correction to the gap between ABINIT and QE/Yambo', *Computational Materials Science*, **83**, 341 (2014).

[265] Antropov, V.P., Gunnarsson, O. and Liechtenstein, A.I., 'Phonons, electron-phonon, and electron-plasmon coupling in C_{60} compounds', *Phys. Rev. B*, **48**, 7651 (1993).

[266] Schlüter, M., Lannoo, M., Needels, M., Baraff, G.A. and Tománek, D., 'Electron-phonon coupling and superconductivity in alkali-intercalated C_{60} solid', *Phys. Rev. Lett.*, **68**, 526 (1992).

[267] Hellmann, H., *Einführung in die Quantenchemie* -, Deuticke, Leipzig (1937).

[268] Feynman, R.P., 'Forces in Molecules', *Phys. Rev.*, **56**, 340 (1939).

[269] Novoselov, K.S. et al., 'Electric field effect in atomically thin carbon films', *Science*, **306**, 666 (2004).

[270] Geim, A.K. and Novoselov, K.S., 'The rise of graphene', *Nature materials*, **6**, 183 (2007).

[271] Geim, A.K., 'Graphene: Status and Prospects', *Science*, **324**, 1530 (2009).

[272] Schwierz, F., 'Graphene transistors', *Nature nanotechnology*, **5**, 487 (2010).

[273] Bonaccorso, F., Sun, Z., Hasan, T. and Ferrari, A., 'Graphene photonics and optoelectronics', *Nature Photonics*, **4**, 611 (2010).

[274] Sun, Y., Wu, Q. and Shi, G., 'Graphene based new energy materials', *Energy & Environmental Science*, **4**, 1113 (2011).

[275] Wang, H., Sun, K., Tao, F., Stacchiola, D.J. and Hu, Y.H., '3D Honeycomb-Like Structured Graphene and Its High Efficiency as a Counter-Electrode Catalyst for Dye-Sensitized Solar Cells', *Angewandte Chemie*, **125**, 9380 (2013).

[276] Allen, M.J., Tung, V.C. and Kaner, R.B., 'Honeycomb Carbon: A Review of Graphene', *Chemical Reviews*, **110**, 132 (2010).

[277] Castro Neto, A.H., Guinea, F., Peres, N.M.R., Novoselov, K.S. and Geim, A.K., 'The electronic properties of graphene', *Rev. Mod. Phys.*, **81**, 109 (2009).

[278] Piscanec, S., Lazzeri, M., Mauri, F., Ferrari, A.C. and Robertson, J., 'Kohn Anomalies and Electron-Phonon Interactions in Graphite', *Phys. Rev. Lett.*, **93**, 185503 (2004).

[279] Kohn, W., 'Image of the Fermi Surface in the Vibration Spectrum of a Metal', *Phys. Rev. Lett.*, **2**, 393 (1959).

[280] Maultzsch, J., Reich, S., Thomsen, C., Requardt, H. and Ordejón, P., 'Phonon Dispersion in Graphite', *Phys. Rev. Lett.*, **92**, 075501 (2004).

[281] Rohlfing, M. and Louie, S.G., 'Excitonic Effects and the Optical Absorption Spectrum of Hydrogenated Si Clusters', *Phys. Rev. Lett.*, **80**, 3320 (1998).

[282] Trevisanutto, P.E., Giorgetti, C., Reining, L., Ladisa, M. and Olevano, V., 'Ab Initio GW Many-Body Effects in Graphene', *Phys. Rev. Lett.*, **101**, 226405 (2008).

[283] Shirley, E.L. and Louie, S.G., 'Electron excitations in solid C_{60}: Energy gap, band dispersions, and effects of orientational disorder', *Phys. Rev. Lett.*, **71**, 133 (1993).

[284] Sormann, H., 'Elektronentheorie des Festkörpers', Lecture Notes, http://itp.tugraz.ac.at/LV/sormann/TFKP4/.